

Investigations on ThMn_{12} -type and Mn-Al compounds as permanent magnet candidates

Zur Erlangung des akademischen Grades Doktor-Ingenieur (Dr.-Ing.)

Genehmigte Dissertation im Fachbereich Material- und Geowissenschaften von Fernando Maccari aus Tubarão, Brazil

Tag der Einreichung: 09. Dezember 2021, Tag der Prüfung: 11. März 2022

1. Gutachten: Prof. Dr. Oliver Gutfleisch (Technische Universität Darmstadt)

2. Gutachten: Prof. Dr. Karsten Durst (Technische Universität Darmstadt)

Darmstadt



TECHNISCHE
UNIVERSITÄT
DARMSTADT



Investigations on ThMn_{12} -type and Mn-Al compounds as permanent magnet candidates

Genehmigte Dissertation im Fachbereich Material- und Geowissenschaften von Fernando Maccari

1. Gutachten: Prof. Dr. Oliver Gutfleisch (Technische Universität Darmstadt)
2. Gutachten: Prof. Dr. Karsten Durst (Technische Universität Darmstadt)

Tag der Einreichung: 09. Dezember 2021

Tag der Prüfung: 11. März 2022

Darmstadt

Bitte zitieren Sie dieses Dokument als:

URN: urn:nbn:de:tuda-tuprints-211407

URL: <http://tuprints.ulb.tu-darmstadt.de/21140>

Dieses Dokument wird bereitgestellt von tuprints,

E-Publishing-Service der TU Darmstadt

<http://tuprints.ulb.tu-darmstadt.de>

tuprints@ulb.tu-darmstadt.de



Veröffentlicht unter CC BY-SA 4.0 International

<https://creativecommons.org/licenses/by-sa/4.0>

Erklärungen laut Promotionsordnung

§8 Abs. 1 lit. c PromO

Ich versichere hiermit, dass die elektronische Version meiner Dissertation mit der schriftlichen Version übereinstimmt.

§8 Abs. 1 lit. d PromO

Ich versichere hiermit, dass zu einem vorherigen Zeitpunkt noch keine Promotion versucht wurde. In diesem Fall sind nähere Angaben über Zeitpunkt, Hochschule, Dissertationsthema und Ergebnis dieses Versuchs mitzuteilen.

§9 Abs. 1 PromO

Ich versichere hiermit, dass die vorliegende Dissertation selbstständig und nur unter Verwendung der angegebenen Quellen verfasst wurde.

§9 Abs. 2 PromO

Die Arbeit hat bisher noch nicht zu Prüfungszwecken gedient.

Darmstadt, 09. Dezember 2021

F. Maccari

Contents

Acknowledgments	viii
Curriculum Vitae	x
List of Publications	xii
List of Figures	xvii
List of Tables	xix
Nomenclature	xxi
1 Introduction and Motivation	1
2 Fundamentals	5
2.1 Permanent magnets	5
2.1.1 Figures of merit and types of permanent magnets	5
2.1.2 Ferromagnetism and the role of <i>3d</i> elements	8
2.1.3 Magnetic hardening and the role of rare earth <i>4f</i> electrons	11
2.2 Magnetic Domain Structure	18
2.3 Microstructural effects on magnetic properties and Brown's paradox	21
2.4 The rare earth crisis - one decade later	27
2.5 The ThMn ₁₂ material system - Potential rare earth lean magnets	30
2.5.1 Extrinsic properties of Nd-based 1:12-type systems	32
2.5.2 Extrinsic properties in Sm-based 1:12	34
2.5.3 Properties in Ce-based 1:12	36
2.6 The Mn-Al material system - Potential rare earth-free gap magnet	37
3 Synopsis of Publications	43
3.1 Preamble of the synopsis	43
3.2 Publication A: Rapid solidification of Nd _{1+x} Fe ₁₁ Ti compounds: Phase formation and magnetic properties	46
3.3 Publication B: Correlating changes of the unit cell parameters and microstructure with magnetic properties in the CeFe ₁₁ Ti compound	49
3.4 Publication C: Twins – A weak link in the magnetic hardening of ThMn ₁₂ -type permanent magnets	53
3.5 Publication D: Microstructure and magnetic properties of Mn-Al-C permanent magnets produced by various techniques	57

4	Conclusions and Outlook	61
	Bibliography	65
5	Cumulative Part of the Thesis	85
5.1	Statement of Personal Contribution	85
5.2	Full-text of Selected Publications	87
5.2.1	Full-text of Selected Publication A	88
5.2.2	Full-text of Selected Publication B	98
5.2.3	Full-text of Selected Publication C	115
5.2.4	Full-text of Selected Publication D	134

Acknowledgments

I would like to thank **Prof. Oliver Gutfleisch** for supervising this PhD work and for giving me the opportunity to join the Functional Materials group. I really appreciate this period and the experience that I have gained throughout these years of research in the group. The possibility to meet and work with several experts in the field of magnetism and metallurgy greatly influenced my development.

In addition, I would like to thank **Prof. Karsten Durst** for agreeing to referee my dissertation.

A big thanks to all members of the *Functional Materials* group. It was a pleasure to work in a very productive atmosphere, to meet nice and good colleagues that were always willing to help and to share their experience. In detail, I would like to highlight the support by:

- **Dr. Iliya Radulov** for supervising my experimental work on the daily basis, helping in different processing and characterization techniques and devices that were very important during my research. The constant feedback and his experience have been of a great importance during the period of my PhD;
- **Dr. Konstantin Skokov** for helping a lot with his vast experience in magnetic materials, interpretation of results and for the many research ideas. Also, I appreciate the help with the pressure dependent magnetization measurements at the PPMS;
- **M.Sc. Lukas Schäfer** for all his help in all kind of experiments, for the collaboration in many different topics and material systems and, most important, for his friendship during this time;
- **Dr. Semih Ener**, who is always eager to discuss new ideas, share his experience and for the collaboration in many works. Moreover, I am thankful for his help on proofreading this dissertation;
- **Dr. Alex Aubert** for being a great lab partner, withstanding many difficulties and challenges that we have faced working on many different topics;
- **Dr. Léopold V. B. Diop**, who was always very patient to teach the fundamentals of magnetism and to share his immense expertise in the field;
- **M.Sc. Navid Shayanfar**, for the help with PPMS and MPMS measurements and for the support during stressful times;
- former colleagues and exchange students **Dr. Ahmed Talaat**, **Dr. Amin Davarpanah**, **Dr. Luís Moreno-Ramírez**, **Dr. Juan S. Trujillo** for making a fun and motivating environment for research, besides all the collaboration in various topics;
- my office mate and friend **Ing. Bernd Stoll**, who has helped me a lot on building/fixing devices, with LabView programming and many other tasks.

Apart from the *Functional Materials* group, I would like to extend my gratitude to all colleagues with whom I have collaborated at TU Darmstadt. A huge thanks to **Dr. Enrico Bruder** from the *Physical Metallurgy* research group for all the EBSD analysis, discussions and valuable advice during my PhD. In the same group, I extend my thanks to **Petra Neuhausel** and **Claudia Wasmund** (*in memoriam*) for all the assistance with metallographic preparation and chemical etching of challenging samples. In addition, I

thank **David Koch** from the *Structure Research* group for temperature dependent XRD measurements and discussions. Also to **Prof. Leopoldo Molina-Luna, M.Sc. Alexander Zintler** and **Ulrike Kunz** from the *Advanced Electron Microscopy Division* for the TEM and ACOM measurements and the interesting discussions, besides the help with the SEM operation.

I also had a great opportunity to be part of fruitful collaborations with many other universities and research institutes. In especial, I would like to emphasize the work with *Max Planck Institute for Iron Research* - **Dr. Dhanalakshmi Palanisamy, Dr. Baptiste Gault, M.Sc. Liuliu Han, Dr. Isnaldi R. Souza Filho, Halil I. Sözen, Dr. Tilmann Hickel** and **Prof. Dierk Raabe**; *Technion - Israel Institute of Technology* - **Dr. Vladimir V. Popov Jr., Dr. Alexey Kovalevsky, Dr. Alexander Katz-Demyanetz** and **Prof. Menahem Bamberger**.

I am thankful for the financial support of my PhD work by the DFG through the Priority Program "SPP1959 - Fields Matter". The project also gave me the opportunity to meet several researchers/colleagues, to establish collaborations and to learn different topics.

I would also thank my **family** and all my **friends** for the constant support. Finally, I thank my wife, my life partner, **Kamila Almeida de Oliveira** for always give me strength and for being on my side at all times.

Curriculum Vitae

Personal information

Name	Fernando Maccari
Date of birth	03 of May, 1990
Place of birth	Tubarão, Brazil
Citizenship	Brazilian

Education

2017 - 2021	Ph.D. student in Material Science Degree sought: Doctor of Engineering (Dr.-Ing.) Supervisor: Prof. O. Gutfleisch Technische Universität Darmstadt, Germany
2016	Research assistant Mechanical Engineering Department, Group of Magnetic Materials Synthesis and characterization of permanent magnets Federal University of Santa Catarina, Florianópolis-Brazil
2013 - 2016	Master Studies in Materials Science and Engineering Degree: Master of Science and Engineering (M.Sc.) Thesis: Study of the interaction between soldering alloys and Ni and Cu substrates Supervisor: Prof. P. A. P. Wendhausen Federal University of Santa Catarina, Florianópolis-Brazil
2008 - 2013	Bachelor Studies in Materials Engineering Degree: Engineer (Eng.) Thesis: Micropatterning of Large Areas and Complex-Shaped Ceramic Bodies via Modified μ -Molding Technique Supervisor: M. Sc. T. Halfer Federal University of Santa Catarina, Florianópolis-Brazil

2005 - 2007	Secondary School
Conference contributions and Workshops	<p data-bbox="475 309 1452 347">Escola Técnica de Comércio de Tubarão (ETCT), Brazil</p> <p data-bbox="475 510 1452 638">26th International Workshop on Rare Earth and Future Permanent Magnets and Their Applications (REPM) 2021, Baltimore, USA (Virtual Conference), Poster presentation</p> <p data-bbox="475 645 1452 728">Material Science and Engineering Congress (MSE) 2020, Darmstadt, Germany (Virtual Conference), Poster presentation</p> <p data-bbox="475 734 1452 817">2nd Electric Field Enhanced Processing of Advanced Materials Conference 2019, Tomar, Portugal, Poster presentation</p> <p data-bbox="475 824 1452 907">Material Science and Engineering Congress (MSE) 2018, Darmstadt, Germany, Poster presentation</p> <p data-bbox="475 913 1452 996">9th Joint European Magnetic Symposia (JEMS) 2018, Mainz, Germany, Poster presentation</p> <p data-bbox="475 1003 1452 1120">24th International Workshop on Rare Earth and Future Permanent Magnets and Their Applications (REPM) 2016, Darmstadt, Germany, Poster presentation</p>

List of Publications

- [1] A. Galler, S. Ener, **F. Maccari**, I. Dirba, K. P. Skokov, O. Gutfleisch, S. Birkman and L. Pourovskii, *Intrinsically weak magnetic anisotropy of cerium in potential hard-magnetic intermetallics*, npj Quantum Materials **6**, 2 (2021).
<https://doi.org/10.1038/s41535-020-00301-6>
- [2] M. T. Ghahfarokhi, A. Chirkova, **F. Maccari**, F. Casoli, S. Ener, K. P. Skokov, R. Cabassi, O. Gutfleisch and F. Abertini, *Influence of martensitic configuration on hysteretic properties of Heusler films studied by advanced imaging in magnetic field and temperature*, Acta Materialia **221**, 117356 (2021).
<https://doi.org/10.1016/j.actamat.2021.117356>
- [3] L. Han, Z. Rao, I. R. Souza, **F. Maccari**, Y. Wei, G. Wu, A. Ahmadian, X. Zhou, O. Gutfleisch, D. Ponge, D. Raabe and Z. Li, *Ultrastrong and Ductile Soft Magnetic High-Entropy Alloys via Coherent Ordered Nanoprecipitates*, Advanced Materials **33**, 2102139 (2021).
<https://doi.org/10.1002/adma.202102139>
- [4] L. Schäfer, K. P. Skokov, J. Liu, **F. Maccari**, T. Braun, S. Riegg, I. Radulov, J. Gassmann, H. Merschroth, J. Harbig, M. Weigold and O. Gutfleisch, *Design and Qualification of Pr-Fe-Cu-B Alloys for the Additive Manufacturing of Permanent Magnets*, Advanced Functional Materials **31**, 2102148 (2021).
<https://doi.org/10.1002/adfm.202102148>
- [5] S. Ener, K. P. Skokov, D. Palanisamy, T. Devillers, J. Fischbacher, G. G. Eslava, **F. Maccari**, L. Schäfer, L. V. B. Diop, I. Radulov, B. Gault, G. Hrkac, N. M. Dempsey, T. Schrefl, D. Raabe and O. Gutfleisch, *Twins – A weak link in the magnetic hardening of ThMn₁₂-type permanent magnets*, Acta Materialia **214**, 116968 (2021) - **Selected publication - PUBLICATION C**
<https://doi.org/10.1016/j.actamat.2021.116968>
- [6] V. V. Popov Jr., **F. Maccari**, I. Radulov, A. Kovalevsky, A. Katz-Demyanetz, and M. Bamberger, *Microstructure and magnetic properties of Mn-Al-C permanent magnets produced by various techniques*, Manufacturing Review **8**, 10 (2021) - **Selected publication - PUBLICATION D**
<https://doi.org/10.1051/mfreview/2021008>
- [7] A. Davarpanah, I. Radulov, N. Shayanfar, **F. Maccari**, K. P. Skokov, J. Amaral and O. Gutfleisch, *The impact of Pr and Nd substitution on structure, hysteresis and magnetocaloric properties of La_{1-x}(Pr,Nd)_xFe_{11.6}Si_{1.4}*, Journal of Physics D: Applied Physics **54**, 22 (2021).
<https://doi.org/10.1088/1361-6463/abea3c>
- [8] **F. Maccari**, S. Ener, D. Koch, I. Dirba, K. P. Skokov, E. Bruder, L. Schäfer and O. Gutfleisch, *Correlating changes of the unit cell parameters and microstructure with magnetic properties in the CeFe₁₁Ti compound*, Journal of Alloys and Compounds **867**, 158805 (2021) - **Selected publication - PUBLICATION B**
<https://doi.org/10.1016/j.jallcom.2021.158805>
- [9] D. Palanisamy, S. Ener, **F. Maccari**, L. Schäfer, K. P. Skokov, O. Gutfleisch, D. Raabe and B. Gault, *Grain boundary segregation, phase formation, and their influence on the coercivity of rapidly solidified SmFe₁₁Ti hard magnetic alloys*, Physical Review Materials **4**, 054404 (2020).
-

-
- <https://doi.org/10.1103/PhysRevMaterials.4.054404>
- [10] **F. Maccari**, D. Y. Karpenkov, E. Semenova, A. Y. Karpenkov, A. Y. Karpenkov, I. Radulov, K. P. Skokov and O. Gutfleisch, *Accelerated crystallization and phase formation in $Fe_{40}Ni_{40}B_{20}$ by electric current assisted annealing technique*, Journal of Alloys and Compounds **836**, 155338 (2020).
<https://doi.org/10.1016/j.jallcom.2020.155338>
- [11] I. Radulov, V. V. Popov Jr., A. Koptuyug, **F. Maccari**, A. Kovalevsky, S. Essel, J. Gassmann, K. P. Skokov and M. Bamberger, *Production of net-shape Mn-Al permanent magnets by electron beam melting*, Additive Manufacturing **30**, 100787 (2019). <https://doi.org/10.1016/j.addma.2019.100787>
- [12] **F. Maccari**, L. Schäfer, I. Radulov, L. V. B. Diop, S. Ener, E. Bruder, K. P. Skokov and O. Gutfleisch, *Rapid solidification of $Nd_{1+x}Fe_{11}Ti$ compounds: Phase formation and magnetic properties*, Acta Materialia **180**, 15-23 (2019) - **Selected publication - PUBLICATION A**
<https://doi.org/10.1016/j.actamat.2019.08.057>
- [13] D. Stadler, T. Brede, D. Schwarzbach, **F. Maccari**, T. Fischer, O. Gutfleisch, C. A. Volkert and S. Mathur, *Anisotropy control in magnetic nanostructures through field-assisted chemical vapor deposition*, Nanoscale Advances **1**, 4290-4295 (2019).
<https://doi.org/10.1039/C9NA00467J>
- [14] H. I. Sözen, S. Ener, **F. Maccari**, K. P. Skokov, O. Gutfleisch, F. Körmann, J. Neugebauer and T. Hickel, *Ab initio phase stabilities of Ce-based hard magnetic materials and comparison with experimental phase diagrams*, Physical Review Materials **3**, 084407 (2019).
<https://doi.org/10.1103/PhysRevMaterials.3.084407>
- [15] L. M. Moreno-Ramirez, C. Romero-Muniz, J. Y. Law, V. Franco, A. Conde, I. Radulov, **F. Maccari**, K. P. Skokov and O. Gutfleisch, *Tunable first order transition in $La(Fe,Cr,Si)_{13}$ compounds: Retaining magnetocaloric response despite a magnetic moment reduction*, Acta Materialia **175**, 406-414 (2019).
<https://doi.org/10.1016/j.actamat.2019.06.022>
- [16] D. Simon, H. Wuest, S. Hinderberger, T. Koehler, A. Maruszczyk, S. Sawatzki, L. V. B. Diop, K. P. Skokov, **F. Maccari**, A. Senyshyn, H. Ehrenberg and O. Gutfleisch, *Structural and magnetic properties of $Ce_{1-x}Sm_xFe_{11-y}Ti_1V_y$* , Acta Materialia **172**, 131-138 (2019).
<https://doi.org/10.1016/j.actamat.2019.04.006>
- [17] J. S. T. Hernandez, **F. Maccari**, L. G. Marshall, J. A. Tabares and G. A. P. Alcazar, *Exchange Coupling in MnAlC/ α -Fe Nanocomposite Magnets*, Journal of Superconductivity and Novel Magnetism **31**, 3941-3947 (2018).
<https://doi.org/10.1007/s10948-018-4661-4>
- [18] L. M. Moreno-Ramirez, C. Romero-Muniz, J. Y. Law, V. Franco, A. Conde, I. Radulov, **F. Maccari**, K. P. Skokov and O. Gutfleisch, *The role of Ni in modifying the order of the phase transition of $La(Fe,Ni,Si)_{13}$* , Acta Materialia **160**, 137-146 (2018).
<https://doi.org/10.1016/j.actamat.2018.08.054>
- [19] C. E. E. Naranjo, J. S. T. Hernandez, M. J. R. Salgado, J. A. Tabares, **F. Maccari**, A. Cortes and G. A. P. Alcazar, *Processing and characterization of $Nd_2Fe_{14}B$ microparticles prepared by surfactant-assisted ball milling*, Applied Physics A **124**, 564 (2018).
<https://doi.org/10.1007/s00339-018-1977-7>
- [20] **F. Maccari**, R. V. Well, G. Eller, M. S. T. Hoffmann, L. U. Lopes, H. Takiishi and P. A. P. Wendhausen, *Dry and Wet Milling Comparison of Nd-Fe-B Magnets Based on Strip Cast Alloys*, Materials Science Forum **899**, 567-571 (2017).
<https://doi.org/10.4028/www.scientific.net/MSF.899.567>

-
- [21] T. Staudt, T. Akinaga, L. U. Lopes, **F. Maccari**, and P. A. P. Wendhausen, *Impact Analysis of PM magnetization level on motor performance: simulations and experimental results*, *Journal of Microwaves, Optoelectronics and Electromagnetic Applications* **16**, 01 (2017).
<https://doi.org/10.1590/2179-10742017v16i1879>

Others

- [A] L. M. Moreno-Ramirez, J. Law, C. Romero-Muniz, V. Franco, A. Conde, **F. Maccari**, I. Radulov, K. P. Skokov and O. Gutfleisch, *Finding the Separation Between First-and Second-Order Phase transitions in La(Fe,Ni,Si)13 magnetocaloric materials*, 2018 IEEE International Magnetics Conference (INTERMAG) Proceedings, Singapore (2018).
<https://doi.org/10.1109/INTMAG.2018.8508032>
- [B] V. Popov, A. Koptug, I. Radulov, **F. Maccari** and G. Muller, *Prospects of additive manufacturing of rare-earth and non-rare-earth permanent magnets*, *Procedia Manufacturing* **21**, 100-108 (2018).
<https://doi.org/10.1016/j.promfg.2018.02.199>

List of Figures

2.1	Hysteresis loop of an ideal anisotropic permanent magnet.	6
2.2	Energy-product evolution for different permanent magnets.	7
2.3	Bethe-Slater curve and thermomagnetic response.	9
2.4	Formation of band structure and Slater-Pauling curve.	10
2.5	Magnetocrystalline anisotropy in Fe, Ni and Co.	12
2.6	Total magnetic moment of RE elements.	14
2.7	RE ⁺³ ion 4f real-space shape and effect of surrounding charges	15
2.8	Change of anisotropy upon nitrogenation in RE ₂ Fe ₁₇ compounds	16
2.9	Determination of anisotropy energy and field for Nd ₂ Fe ₁₄ B and SmCo ₅ single crystals . . .	17
2.10	Hardness parameter κ for different compounds	18
2.11	Magnetic domains and domain wall	19
2.12	Hysteresis loops based on intrinsic properties and the corresponding anisotropic and isotropic magnet	22
2.13	a) Hysteresis loops based on Stoner-Wohlfart model and b) coherent rotation	24
2.14	Hysteresis loops based on Stoner-Wohlfart model	28
2.15	Crystal structure and occupancy in the ThMn ₁₂ tetragonal structure and the relation with 2:17 and 1:5	31
2.16	Coercivity values related to the grain size for Sm-based 1:12 compounds in comparison to Nd-Fe-B	35
2.17	Mn-Al phase diagram and different representations of τ -phase	38
2.18	Extrinsic magnetic properties of Mn-Al produced by different methods	40
3.1	Microstructure length scales in correlation with intrinsic and extrinsic magnetic properties	43
3.2	Overview of magnetic properties of hard ferrite, Nd-Fe-B, Mn-Al and REFe ₁₁ Ti	45
3.3	Graphical abstract - Representation of microstructure, thermomagnetic and magnetic properties	46
3.4	Magnetic domain structure of NdFe ₁₁ Ti under applied magnetic field	49
3.5	Microstructural analysis of Ce _{1.20} Fe ₁₁ Ti sample annealed at 850°C	50
3.6	Anisotropy field of CeFe ₁₁ Ti under different conditions	51
3.7	HR-STEM HAADF of twin boundary in SmFe ₁₁ Ti	54
3.8	APT of twin boundary in SmFe ₁₁ Ti	55
3.9	Twin boundaries in different 1:12 compounds	56
3.10	Methods to obtain Mn ₅₂ Al ₄₄ C ₂ samples	57
3.11	Microstructure and magnetic properties of Mn ₅₂ Al ₄₄ C ₂ induction melted-cast sample	58
3.12	Hysteresis loops, at room temperature, of Mn ₅₂ Al ₄₄ C ₂ HPT samples	59

List of Tables

2.1	Magnetic moment per atom and magnetization values of selected pure elements.	10
2.2	Coercivity of Nd-based nitrogenated 1:12 compounds produced by different techniques. . .	34
3.1	Chemical composition of NdFe ₁₁ Ti (1:12), Nd ₂ (Fe,Ti) ₁₇ (2:17) and Nd ₃ (Fe,Ti) ₂₉ (3:29) phases.	47
5.1	Definitions according to Contributor Roles Taxonomy.	85

Nomenclature

α	Angle between the magnetization axis and the easy magnetization axis
α_ψ	Angular dependence of the coercivity used in the Kronmüller equation
α_j	Stevens coefficient
α_K	Microstructural parameter in the Kronmüller equation
δ_W	Domain wall thickness
γ	Domain wall energy density
κ	Magnetic hardness parameter
μ_0	Vacuum permeability
μ_B	Bohr magnetron
ϕ	Angle between adjacent atomic magnetic moments
θ	Angle between easy magnetization axis and the applied magnetic field
A	Exchange stiffness or exchange constant
a, b, c	Lattice constants
A_2^0	Crystal field parameter
a_s	Interatomic spacing
B	Induction
B_r	Remanent induction
d	Diameter of the 3d orbital
d_c	Critical diameter
E_A	Anisotropy energy
$E_{mstatic}$	Magnetostatic energy or stray field energy
E_{total}	Total energy
E_{Zeeman}	Zeeman energy
H_{appl}	External applied magnetic field strength
H_A	Anisotropy field

H_{cb}	Coercive field
H_{cj}	Intrinsic coercivity
H_c	Coercivity
H_d	Demagnetizing field
H_N	Nucleation field
H_{str}	Stray field
J	Magnetic polarization
J_{ex}	Exchange interaction
J_m	Total magnetic moment
J_r	Remanent polarization
J_s	Saturation polarization
K, K_n	Anisotropy constant, anisotropy constant of power of n
L	Orbital magnetic moment
L_{ex}	Ferromagnetic exchange length
M_s	Saturation magnetization
N_{eff}	Effect of demagnetizing fields (dipolar interaction) used in the Kronmüller equation
r_{4f}	Shell radius of $4f$ electrons
S, S_i, S_j	Spin magnetic moment
T_C	Curie temperature
V	Volume
Z	Atomic number
ΔK	Strength of the magnetic inhomogeneity
(BH_{max})	Energy-product
1:12	REFe ₁₂ -type compounds
2:17	RE ₂ Fe ₁₇ -type compounds
3:29	RE ₃ Fe ₂₉ -type compounds
APB	Antiphase boundary
APT	Atom probe tomography
bcc	body-centered cubic crystal structure
BSE	Backscatter electron

CRedit Contributor roles taxonomy
DFT Density functional theory
EBM Electron beam melting
EBSD Electron backscatter diffraction
EDX Energy-dispersive X-Ray spectroscopy
fcc face-centered cubic crystal structure
HAADF High-angle annular dark field
hcp hexagonal close packed crystal structure
HDDR Hydrogenation-disproportionation-desorption-recombination process
HPT High pressure torsion
HR-STEM High resolution scattering transmission electron microscopy
HRE Heavy rare earth
PM Permanent magnets
PPMS Physical property measurement system
PR Paramagnetic
RE Rare earth
RT Room temperature
SEM Scanning electron microscopy
SPS Spark plasma sintering
STEM Scanning transmission electron microscopy
TEM Transmission electron microscopy
TM Transition metal
VSM Vibrating sample magnetometry/magnetometer
XRD X-ray diffraction

1 Introduction and Motivation

Permanent magnets (PM) are key components on the emerging and growing technologies related to renewable energies and electromobility, besides the vast use in data storage, sensors, robotics and automatization and many other consumer technologies [1]. All these applications require optimization of the magnetic performance, in terms of materials selection and processing, allied with a redesign and miniaturization of devices while keeping the products competitive to the market. In this sense, magnetic materials development is tied with the evolution of modern technologies and the possible solutions for future ones. This shows that permanent magnets have many implications in society, going much far beyond then sticking holidays pictures or due bills on the refrigerator-even though these “less noble” use are still important on daily basis.

The current market of PMs is dominated by two major material systems: hexaferrites (Ba- and Sr-based) and Nd-Fe-B [2]. The hexaferrites has the highest market share in terms of weight, around 80%, owing to the low cost of the raw materials, high corrosion resistance and relatively simple production methods, being used in a variety of applications that requires low magnetic performance (small energy-product $(BH)_{max}$ values below 50 kJ/m^3) [1–3]. On the other hand, the rare earth Nd-Fe-B based compounds dominates the market in terms of costs and in performance, showing the highest BH_{max} values, at room temperature, from the known materials ($(BH)_{max} \approx 430 \text{ kJ/m}^3$ -N52 grade) [1, 3]. Even though this scenario has been prevailing during the past decade, one notices the big performance gap between these materials, which yields to the situation that for some applications Nd-Fe-B is used under its full potential [2].

Since it is foreseen that applications, such as automation and e-mobility, will grow substantially in the next years, the demand for PM will follow the same trend, especially for the rare earth (RE) based magnets [4]. This necessity brings challenges that goes further than the technical requirements, including geopolitical economy, supply chain stability and environmental/criticality aspects [5–7]. The fragility of this situation was observed in 2011 in the so called “rare earth crisis”, when the RE elements price have increased by a factor of 10 within months, as a result from the monopolistic market of which around 95% of the RE are mined and exported by China [8]. Despite the fact that the prices have decreased in the subsequent years, the possibility of new price fluctuation and instability, on top of the resources limitations of the RE elements, has emerged the necessity to overcome this issue, since many industrial branches rely on these materials [8]. Among the strategies directed to face these circumstances are the ones related to diversification of supply chain (open new mines in different countries), recycling of scrap magnets for further re-use and the research/development of alternative materials [6, 9].

The search for alternatives has manifold to several types of possibilities, including the optimization of the Nd-Fe-B magnets by partial substitution of Nd by Ce and La (more abundant and cheaper RE) and processing techniques to excel the current magnetic performance while avoiding/reducing the use of heavy RE (Tb and Dy) [10]. In addition, the pursuit and development of alternative compounds with less (RE-lean) and even without RE elements (RE-free) to substitute Nd-Fe-B permanent magnets, at least in some applications, has been a great importance [9, 10]. This necessity is not only to avoid the previously mentioned issues but also to obtain materials that are able to fill the magnetic performance gap existing between ferrites and Nd-Fe-B [2, 9].

Among the promising systems to fulfill these requirements, two of them received major attention, namely the RE-lean ThMn_{12} -type materials (will be referred as 1:12 for the rest of the dissertation) and the RE-free Mn-Al. These two material systems are dated and reported even before the 90's and had the attraction renewed based on their intrinsic potential and the growing demand for permanent magnets [11, 12]. For the 1:12 compounds, studies on Nd- and Sm-based systems have shown the possibility to achieve comparable intrinsic similar magnetic properties to Nd-Fe-B with less RE, while for Mn-Al the interest relies on the possibility outperform ferrites without using expensive raw materials.

Even though they are suitable candidates presenting intrinsic properties to fill the gap, is crucial to find ways to convert this potential to extrinsic properties [9]. Different approaches were reported, but still the obtained values are below the expected ones, especially coercivity, and the reason for this discrepancy is still not fully understood [13, 14]. In this dissertation, aspects related to phase stability, microstructural features (defects, secondary phases, grain size and others) and processing routes have been taken into consideration to give a better explanation for the reasons of observed extrinsic properties. With this aim, this dissertation will be focusing on the previous mentioned aspects for the two different material systems that are candidates to be “gap magnets”.

In the case of the ThMn_{12} -type material systems, results on $\text{REFe}_{11}\text{Ti}$ (RE: Nd, Ce, Sm) will be discussed, including the influence of the rare earth elements on the phase stability and the differences in magnetic properties. Despite the different RE element, similar microstructural features were observed and proved to be related to demagnetization mechanism, as observed by *in situ* optical Kerr analysis. Various characterization methods and simulations were used to understand this behavior, which proved to be a reason on why a large discrepancy between intrinsic and extrinsic magnetic properties is observed in $\text{REFe}_{11}\text{Ti}$ compounds.

As for the RE-free Mn-Al material system, one specific composition has been chosen and used as basis for different processing routes, including thermo and mechanical processes. A parallel between processing, microstructure and extrinsic magnetic properties could be draw. Understanding this correlation has made possible to elucidate important aspects that can be used to create strategies to improve the magnetic properties of Mn-Al alloys even further.

In this cumulative dissertation, the main principles of magnetism focusing on permanent magnets will be briefly covered in Chapter 2, including aspects of alloy design, magnetic properties and figures of merit. A specific description and more details on the ThMn_{12} and Mn-Al material systems will be presented in the last part of the chapter. After this literature overview, a synopsis of 4 selected peer reviewed and published

articles on the research carried out in both material systems is going to be shown in Chapter 3. From these 4 articles, 3 of them are related to REFe₁₁Ti (RE: Nd, Ce, Sm - one for each rare earth element) while the fourth is focused on Mn-Al. It worth mentioning that the author of this dissertation has been either first author or co-author of the selected publications. This will be followed by the summary and conclusions in Chapter 4. At the end, the cumulative chapter (Chapter 5) presents the personal contribution of all authors to the selected articles, followed by the replication of the full-text in its published format, including supplementary materials when applicable.

2 Fundamentals

This chapter focuses on the overview of current permanent magnet materials, including the main figures of merit and magnetic properties, a concise explanation of the underlying physics of these functional materials and how the relation with microstructural features might limit the magnetic performance. Moreover, the context will be expanded, beyond the technical requirements, to understand the necessity to develop new candidates to the current existing magnets. In this context, an overview of two selected promising materials systems (REFe₁₁Ti and Mn-Al) investigated in this dissertation will be given to elucidate their potential as permanent magnets candidates.

2.1 Permanent magnets

2.1.1 Figures of merit and types of permanent magnets

Permanent magnets can be seen as energy-stored devices, which are used to generate/provide a constant magnetic field in a particular volume in the surrounding space without the necessity of additional external stimuli or power input [8, 15]. These permanent magnets can, if properly handled and manufactured, retain its magnetism indefinitely. They can be demagnetized by either applying an opposing external magnetic field, in respect to its original magnetization direction, with a certain strength (intrinsic coercivity - H_{cj}), or when heated above a critical temperature which the ferromagnetic order is no longer preserved (Curie temperature - T_C). For this reason, it is important to understand the figures of merit and properties of permanent magnets in respect to an applied external magnetic field and temperature that limits the applicability and can be further used as selection criteria.

A schematic hysteresis loop of a typical anisotropic permanent magnet when measured along the easy magnetization direction is shown in Figure 2.1a . Since the majority of figures of merit of permanent magnets is taken in the second quadrant of the hysteresis loop, a magnified view with the principal properties are highlighted in Figure 2.1b The horizontal axis is the external applied magnetic field strength ($\mu_0 H_{appl}$) while the vertical axis is the response of the material (J - polarization) or a combination between the applied field and material response (B -induction), as given by the equation [15]:

$$B = \mu_0 H_{appl} + J \quad (2.1)$$

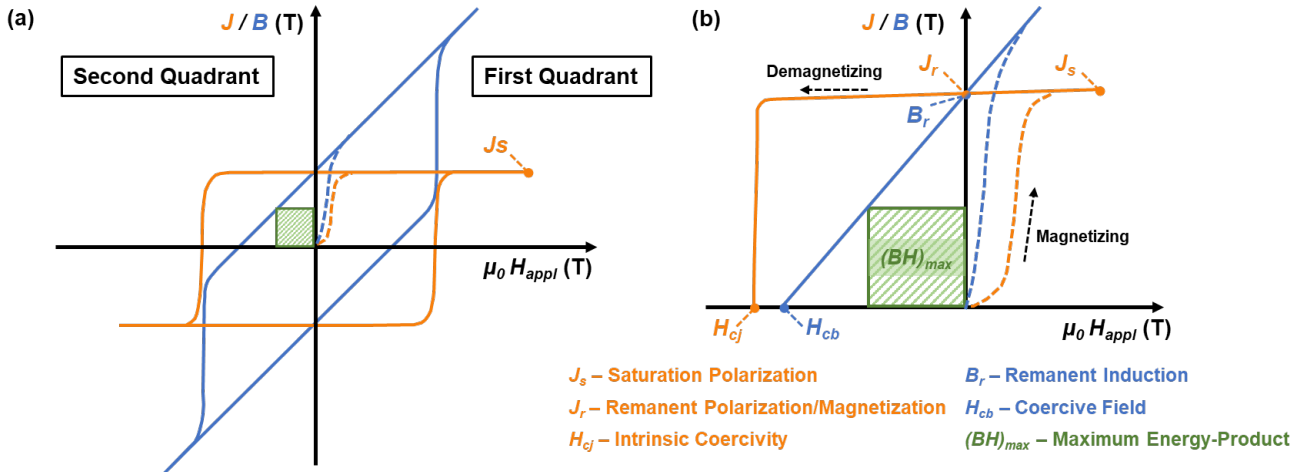


Figure 2.1: a) Hypothetical hysteresis loop of an ideal anisotropic permanent magnet measured along the easy magnetization direction; b) enlarged second quadrant of the hysteresis loop.

where μ_0 is permeability of vacuum.

Following the magnetization process as shown in Figure 2.1b, at first the material is demagnetized (net polarization is zero) and when the applied field is increased the magnetic polarization also increases until a certain threshold value (J_s -saturation polarization) that represents the maximum polarization possible for this material. Upon the removal of the magnetic field, it is obtained the remanent polarization (J_r) or remanent induction (B_r), that is the magnetic flux retained by the magnet without any external field influence. Reversing the direction of the magnetic field (negative/reversal magnetic field) and increasing its strength, it is possible to observe a abrupt decrease in polarization until reaches zero at the coercive field (H_{cj}), which brings the material to the demagnetized state. This property can be seen as the magnet resistance to demagnetization by external field, which is one of the main differences between hard magnetic materials and soft magnets ($H_c \approx 0$ -narrow hysteresis loop). Is worth mentioning that further increase in the negative field will lead to the magnetization in the reverse direction - see Figure 2.1a. More details about the hysteresis loops, comparing the theoretical, anisotropic and isotropic behavior will be presented in a later stage.

Following the induction (B) curve in the second quadrant, blue curve in Figure 2.1b, the decrease is linear until it reaches $B = 0$ at H_{cb} , that is the magnetic field necessary to nullify the magnetic flux given by the permanent magnet. Another very important figure of merit that can be derived from the $B - H_{appl}$ loop is the maximum energy-product ($(BH)_{max}$), which is the maximum energy stored in a magnet. This important property is graphically defined as the area of the rectangle that can be drawn in the the $B - H_{appl}$ loop as shown in Figures 2.1a and 2.1b. As both intrinsic and extrinsic magnetic properties are temperature dependent, it is essential to take into consideration the working temperature, for a given application, for the material selection.

Considering all the extrinsic magnetic properties of permanent magnets, a direct comparison between different material types is generally done by using the figure of merit $(BH)_{max}$, since it is related to both coercivity and remanence. Figure 2.2 shows the historical evolution of different permanent magnets in correspondence to their maximum energy-product values.

To give an easier understanding and visualization for the meaning of $(BH)_{max}$ values a schematic representation of different permanent magnet designs are shown in the figure as cylinders. The color coding of the cylinders corresponds to the different material systems and each cylinder has the same magnetic strength. As it can be seen from the size comparison the permanent magnets with higher energy products lead to smaller volume for the same magnetic flux density. This direct comparison indicates the importance of reaching high $(BH)_{max}$ for achieving miniaturization of devices. Considering the recent advances in different everyday life applications, e.g. headphones, hard-disc drives and others, the direct effect of Nd-Fe-B to the miniaturization can be seen.

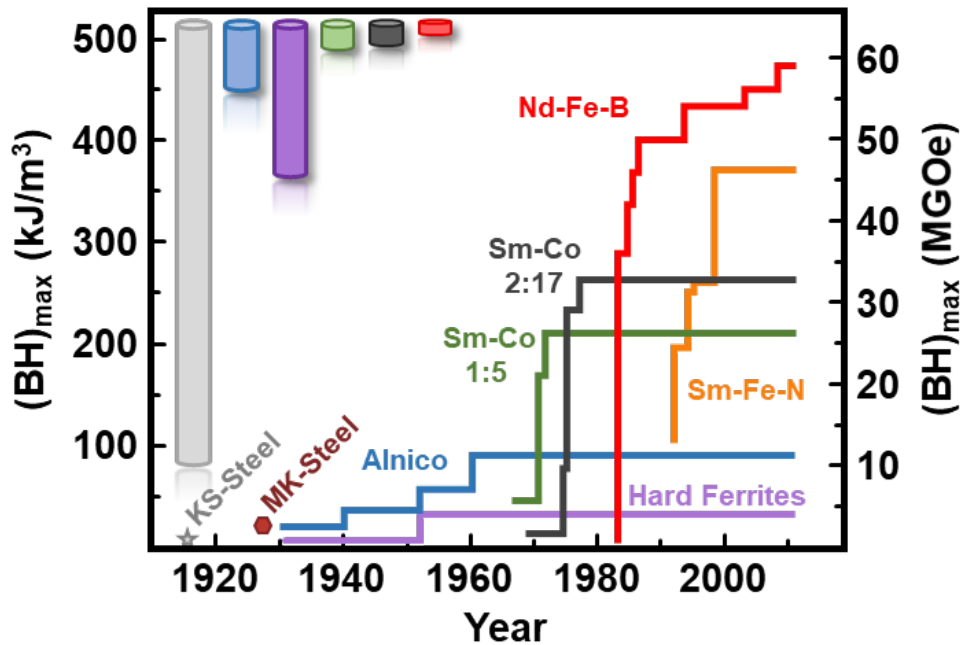


Figure 2.2: Evolution of the energy-product value ($(BH)_{max}$) for different compounds. Figure was adapted from [8, 16].

Three conclusions can be drawn from this figure: first is related to the abrupt jump in the energy-product values in compounds containing rare earth elements, starting from Sm-Co; the second is the increments of the $(BH)_{max}$ values for the same compounds throughout the years; the third is related to the gap between the energy-product values between Alnico and ferrites (below 100 and 50 kJ/m³, respectively) compare to the RE-based (above 200 kJ/m³) permanent magnets [8, 17]. From the first, it is possible to derive the importance of the RE elements in the development of permanent magnets, being associated with their characteristic electronic structure that affects the intrinsic properties [18–20]. The second point is related to

the optimization of manufacturing of such magnets, including alloy and microstructural design allied with different processing routes to obtain higher extrinsic properties, $(BH)_{max}$, H_{cj} and J_r . The third shows the importance searching for new hard magnetic compounds to fill the existing energy gap and/or, eventually, that could even excel the current values shown by Nd-Fe-B. Based on this three points, it is already possible to derive the necessity of finding materials with proper intrinsic magnetic properties and the importance to adopt and control processing routes to convert this intrinsic potential to extrinsic [1, 10, 21].

2.1.2 Ferromagnetism and the role of 3d elements

As could be observed in the historical evolution of $(BH)_{max}$, in terms of material system, the alloy chemistry plays an important role on the magnetic properties. In this section, the focus will be given to the intrinsic properties that are defined by the chemical composition and structure of the hard magnetic phase. Further alloying elements which are used for processing and extrinsic properties tailoring will be briefly discussed on a later stage.

To start the considerations about the reason of the magnetic properties in permanent magnets, we focus in one similarity for all the systems, the presence of 3d transition metals (TM) elements in the composition, more specific Fe, Co and/or Ni. These elements are known to be ferromagnetic at room temperature, meaning that atomic moments interact with the neighboring ones to promote parallel alignment, giving rise to a collective interaction as explained by quantum mechanics in the Heisenberg model [21]. This nearest neighbor interaction, also called exchange interaction (J_{ex}), leads to a potential energy (E_{ex}) related to the atomic moments (defined by the spin vector S - S_i and S_j are adjacent spins), and the angle between them ϕ , through the expression:

$$E_{ex} = -J_{ex}\vec{S}_i\vec{S}_j = -J_{ex}S_iS_j\cos\phi \quad (2.2)$$

The parallel alignment occurs for $J_{ex} > 0$, leading to ferromagnetic ordering, and antiparallel coupling for $J_{ex} < 0$, inducing antiferromagnetic behavior. The different exchange behavior arises from the interplay between the Pauli exclusion principle (fermionic nature of electrons) and the Coulomb interaction between electrons. Based on this, an empirical description of the exchange interaction related to interatomic spacing was deduced, the Bethe-Slater curve. For 3d transition metal solids, one must consider the overlap of the d-orbitals of the neighboring atoms, for this reason, the ratio between the interatomic spacing (a_s) and the 3d ionic radius is used. The Bethe-Slater curve is shown in Figure 2.3a. As can be seen, there are only four elements which present ferromagnetism at room temperature and, interestingly, iron can have both behaviors depending on the structure, i.e., interatomic spacing. As a side note, one can notice the possibility of changing the ordering of Mn in compounds if a proper atomic distance is achieved - this will be discussed in more detail in this dissertation on a later stage.

The exchange interaction energy in ferromagnets also sets the scale for the ferromagnetic ordering-disordering temperature. This means that above a certain critical temperature (Curie temperature - T_C) the thermal energy surpass the energy that keep the magnetic moments aligned and they become randomly

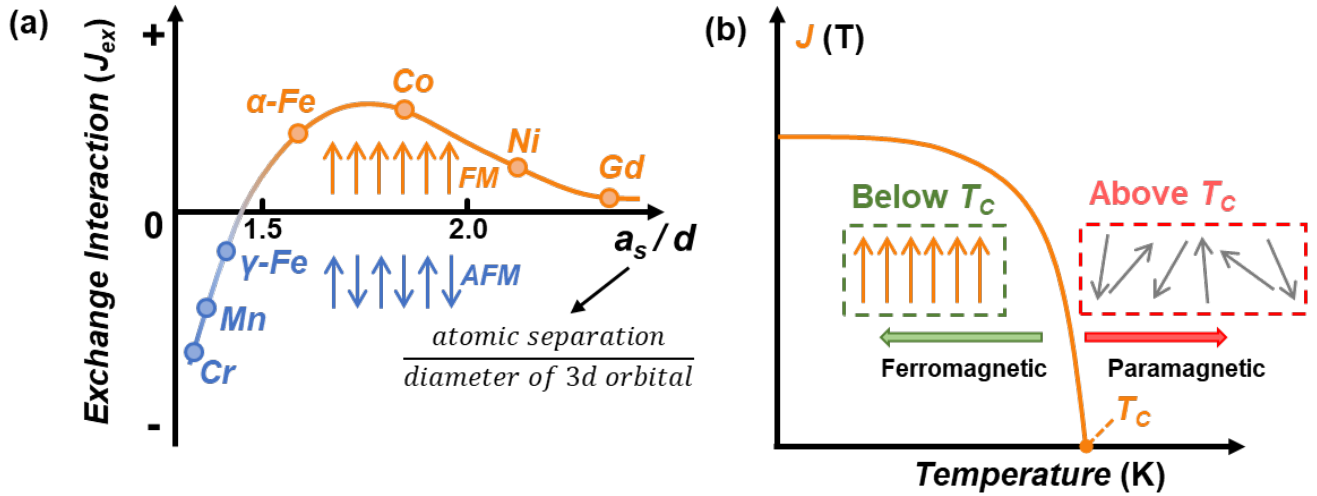


Figure 2.3: a) Bethe-Slater curve for different 3d elements showing ferromagnetic (FM) and antiferromagnetic (AFM) coupling and b) typical thermomagnetic curve of a ferromagnetic material showing the Curie temperature T_C . Figure a) was adapted from [21].

oriented (paramagnetic state). This is as schematically shown in Figure 2.3b.

With the combination of concepts given by the exchange energy and the relation with interatomic distance and T_C , alloying elements and disordering effects can be qualitatively understood and the reason why the magnetization of alloys based on Co are less sensitive to temperature variations - high J_{ex} leads to high T_C - as observed in Alnico and Sm-Co magnets. It worth mentioning and emphasize that the exchange interaction is mainly dependent on interatomic distances, not being necessary linked to any regularity of atomic positioning. For this reason it is possible to observe ferromagnetism in amorphous materials, even though the atomic distances distribution leads to fluctuations in the exchange interactions [15, 21].

Another, and equally important, characteristic necessary for magnetic materials is related to the magnitude of magnetic dipole moments and, therefore, the saturation magnetization. Considering isolated atoms, the electron distribution on the different electronic shells and subshells follows the Pauli exclusion principle, aiming to decrease the free energy of the system. Upon distribution, the unpaired spins in unfilled shells, usually in the outer shell, are the ones which contribute to the atomic moment [14]. However, when atoms are brought together, as in the case to form a solid, the quantized energy levels are severely modified when compared to free atoms. The assemble of atoms will cause a splitting of the energy levels, leading to a virtually continuous energy distribution that is allowed for the electrons to fulfill. This much complex scenario is studied through the band theory of solids, in which the analysis of spin-resolved energy bands (differences between spin up and spin down in terms of energy) and the density of states describes and resolves the atomic magnetic dipole, that can be further used to calculate the saturation magnetization (M_s) value of an alloy [15, 21]. A schematic representation of the 4s and 3d band formation

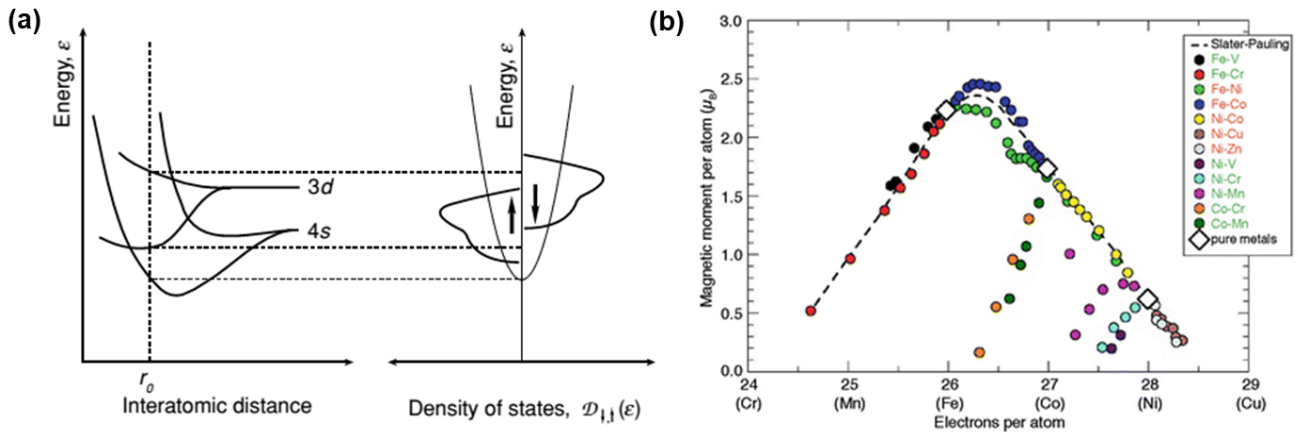


Figure 2.4: a) Formation of a band structure in a $3d$ transition metal and the energy splitting in spin up and spin down; b) Slater-Pauling curve for different $3d$ based alloys - magnetic moment in Bohr magneton (μ_B). Figure a) was adapted from [14] and Figure b) from [22].

Table 2.1: Magnetic moment per atom (μ_m), saturation polarization (J_s) at 0 K and room temperature (RT) and Curie temperature (T_C) for different elements - Para stands for paramagnetic state. The values were taken from [8, 14, 21, 23].

Element	μ_m at 0 K (μ_B)	J_s at 0 K (T)	J_s at RT (T)	T_C (K)
Fe	2.22	2.23	2.16	1043
Co	1.72	1.85	1.81	1388
Ni	0.60	0.65	0.63	627
Gd	7.63	3.90	≈ 0 - Para	292
Dy	10.2	2.65	≈ 0 - Para	88

and the corresponding density of states is shown in Figure 2.4a. It worth mentioning that depending on the chemical interaction and bonding type, like ionic or covalent bonding, the magnetism that might be annihilated, despite the magnetism of the individual atoms [14].

As previously mentioned, the contribution to the magnetic moment comes from unpaired spins of unfilled outer shells. For the TM $3d$ elements like Fe, Co and Ni, the contributing magnetic moments comes from the difference in the unbalanced spins (difference in spin up-spin down) in the $3d$ band. Based on the band theory calculations, it was possible to correlate with the experimental derived curve of Slater-Pauling, showing the magnetization per atom as a function of the number of electrons per atom, as depicted in Figure 2.4b. Some of these properties for selected elements are summarized in Table 2.1 for comparison.

2.1.3 Magnetic hardening and the role of rare earth 4f electrons

Through the analysis of the given theories and experimental validation so far, it is reasonable to assume the choice of Fe-Co based alloys, since it shows the highest magnetic moment per atom (near the top of Slater-Pauling curve), strong ferromagnetic behavior ($J_{ex} > 0$) and high Curie temperature (temperature stability). This alloy design is commonly applied for soft magnets, where high susceptibility (large change in magnetization at low applied magnetic fields) and the low switching field values (low coercivity) are desired, especially to avoid energy losses during high frequencies applications. However, for hard magnetic materials it is imperative to add the “magnetic hardness” to keep the material magnetized when there is no external applied field and to resist against the demagnetizing fields, i.e., it is necessary the development of coercivity (Figure 2.1). As the coercivity is an extrinsic property it can be tuned in different ways, but the upper theoretical limit for hard magnetic materials is defined by the intrinsic property called magnetic anisotropy. As the name suggests, the magnetic properties depend on the crystallographic directions. There are different kinds or ways to induce anisotropy, according to [15]:

1. Magnetocrystalline anisotropy
2. Shape anisotropy
3. Stress anisotropy
4. Anisotropy induced by
 - a) Magnetic annealing
 - b) Plastic deformation
 - c) Irradiation
5. Exchange anisotropy

Among these different types, only magnetocrystalline anisotropy is intrinsic, meaning that all the rest can be induced during processing (extrinsic). The present discussion will be restricted to the intrinsic origin of anisotropy, but the details of the anisotropy types and their examples can be found in [14, 15, 23–25]. It worth mentioning that among the commercially available permanent magnets, only Alnico relies on another type of anisotropy than magnetocrystalline anisotropy (shape anisotropy).

For the specific case of magnetocrystalline anisotropy, the anisotropy correlates the dependence of the magnetic properties to the different crystallographic axis in relation to the external applied magnetic field. Independently on the crystal symmetry, there is a certain crystallographic direction which saturates (all magnetic moments are aligned in the same direction) at small applied magnetic field, this is called easy magnetization axis. On the other hand, the direction which requires the highest applied field to saturate is denominated as the hard axis. From this simple observation, which has been shown experimentally for many different materials with different crystal structures, one can derive that there must be energy associated to the magnetization direction in respect to the different crystallographic axis. This is called anisotropy energy (E_A) and can be expressed, based on the crystal symmetry, in series of expansion which takes into consideration the angle between magnetization in relation to the crystal axis and the

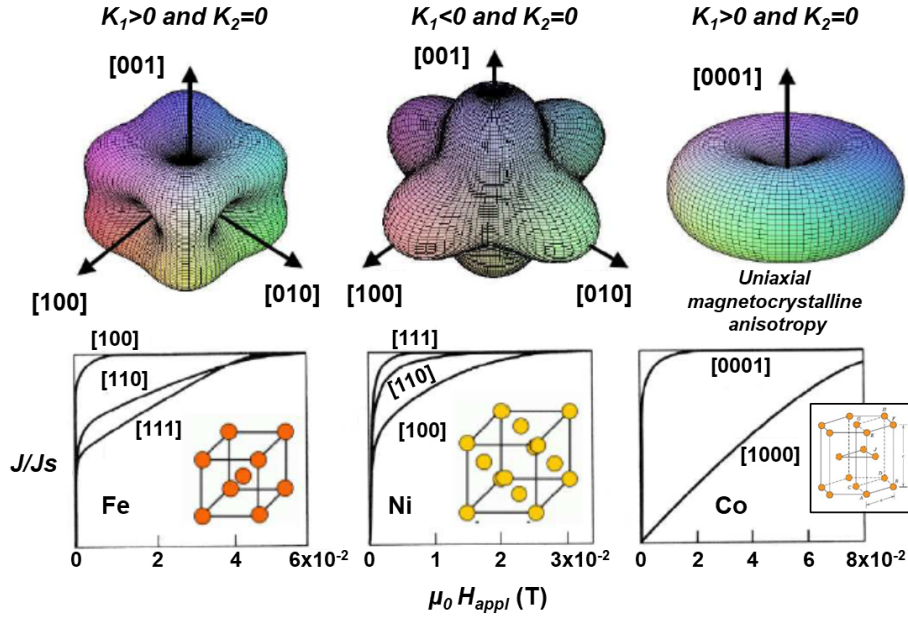


Figure 2.5: The E_A distribution for Fe (bcc structure), Ni (fcc structure) and Co (hcp structure) and the corresponding magnetization measurements along different axis. Figure was adapted from [14, 26, 27].

anisotropy constants values (K_n - where n is the power of the term K). The K_n values can be seen as anisotropy-energy density which are constant for a specific material at a defined temperature, which goes to zero at T_C [20]. In the absence of external magnetic field, the energy is dominated by the anisotropy energy and it is minimized when the magnetization lies along the easy axis. As an example, Figure 2.5 shows the magnetization measurements in different crystallographic directions and the associated E_A distribution for Fe (bcc structure), Ni (fcc structure) and Co (hcp structure)-note that the high E_A is along hard axis, while low E_A is along the easy one. However, if an magnetic field is applied, the magnetostatic energy (Zeeman energy) also plays a significant role in the system. If this magnetic field is applied in a different direction than the easy axis, an energy barrier must be surpassed in order to change the magnetization direction to the applied field direction. The energy barrier is maximum along the hard magnetization axis. From this analysis, it is possible to infer that for permanent magnets would be beneficial to have only one easy axis (uniaxial magnetocrystalline anisotropy), which is perpendicular to the hard axis, with a large energy difference from the other axis to prevent the change the magnetization direction (high K). To realize such energy difference between the crystallographic axis, one can notice constraints on the choice of crystal symmetry, since in high symmetry structures the energy difference between the axis are small to be exploited for possible permanent magnets, as in the case of cubic crystals. For this reason, crystals with only one different axis (hexagonal and tetragonal) or with three equal axes but one different angle between them (rhombohedral) are the symmetries of choice to meet this condition [9, 14, 23].

Considering an uniaxial magnetocrystalline anisotropy material, the E_A can be expressed in a simplified

and lower order as [20]:

$$E_A = K_1 V \sin^2 \theta + K_2 V \sin^4 \theta \quad (2.3)$$

Where θ is the angle between the magnetization and the crystallographic easy axis and V is the volume of the material/crystal/magnet. In general, for permanent magnets, the expression is reduced to only the first term, since K_1 is positive and dominates over K_2 . For comparison, the K_1 value at room temperature for Fe is 0.05 MJ/m³, for Co is 0.5 MJ/m³ and for the rare-earth based hard magnetic intermetallic phases Nd₂Fe₁₄B (tetragonal) and SmCo₅ (hexagonal) are 5.0 and 17.0 MJ/m³, respectively [20]. This pronounced difference in anisotropy-energy density is one of the key factors that has paved the evolution of magnets and established the high performance rare earth permanent magnets. The high anisotropy observed in these magnets is mainly related to the lanthanides 4*f* electrons and its spatial distribution which results in a combination of strong spin-orbit coupling and interactions with the electrostatic crystal field, as will be further discussed.

The 4*f* electrons are very close to the heavy atomic nuclei of the rare earth element and experience the spin-orbit coupling ($S - L$ coupling). The strength of this coupling is proportional to the atomic number Z . In short, this interaction can be seen as the coupling between the electron spin and the magnetic field created by its own orbital motion around the nucleus [28]. This means that the total magnetic moment of such elements is no longer only related to the spin magnetic moment (S), as in the case of 3*d*-metal elements, and an addition of the orbital magnetic moment (L) has to be included in this expression. The summation of both contributions follow the Hund's rules to minimize the free energy associated to the combination of S and L to the total magnetic moment J_m , therefore J_m becomes a good quantum number to describe these systems. In the case of light RE, the total magnetic moment is the absolute value of the difference between the orbital and the spin part, while for heavy RE is the sum of these two parts [29]. The values of S , L and J_m for the different RE elements are shown in Figure 2.6. In comparison, the 3*d* electrons of Co and Fe occupy the conductive energy band in the outer shell and they will mainly adapt to the electronic charges in the crystal structure (crystal field). As result, the orbital moment and magnetic anisotropy expectation values are nearly zero, i.e., "almost fully quenched" crystal field states [20].

Since the 4*f* electrons are located near the RE nuclei, well-screened from the surrounding environment, the crystal field (A_2^0 -describe the electronic charges in the crystal environment) generally only causes small perturbations to the anisotropy, since the main contribution comes from the $S - L$ coupling. Nevertheless, the shape of the 4*f* orbitals in the RE ions (RE⁺³) also plays a role, since when placed in the crystalline environment it will tend to accommodate itself to decrease the electrostatic energy, thus defining the direction of the 4*f* orbital [31]. The Stevens coefficient (α_J) is used to describe the shape of the 4*f* electrons into oblate ($\alpha_J < 0$), prolate ($\alpha_J > 0$) or spheric format ($\alpha_J = 0$), as exemplified in Figure 2.7a. Taking a $\alpha_J > 0$ ion and placed it in a negatively charged environment as example, the "tip" of the prolate ion will avoid pointing towards the negative charges to avoid electrostatic repulsion with the 4*f* electrons. In a cubic environment, Figure 2.7b, the prolate can be pointing towards any of the faces of the cube,

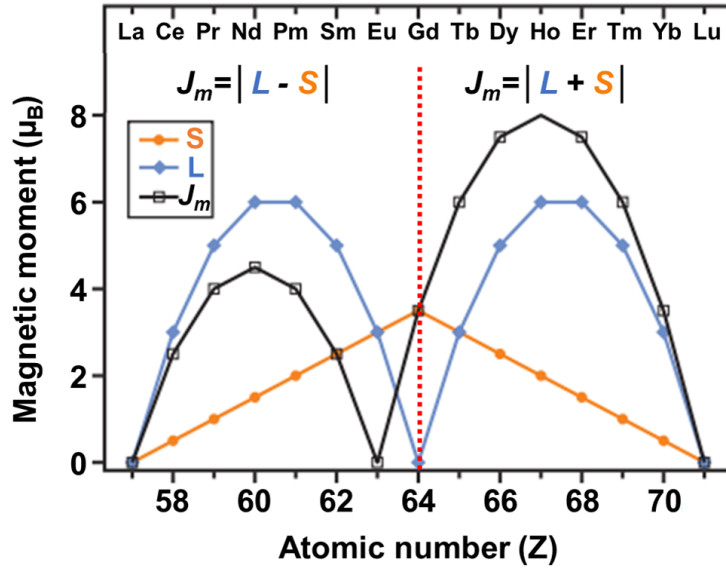


Figure 2.6: The contribution of the spin (S) and orbital (L) magnetic moments to the total magnetic moment (J_m). Figure was adapted from [30].

leading to isotropic behavior. However, when placed in a tetragonal environment, like in Figure 2.7c, the “tip” will be preferably pointing along the vertical axis (c direction), which leads to uniaxial anisotropy ($K_1 > 0$). In the case of another tetragonal environment with opposing A_2^0 parameter compared to the previous example, Figure 2.7d, the prolate “tip” will tend to point along the $a - b$ plane, leading to easy plane anisotropy ($K_1 < 0$) - not applicable to produce permanent magnets.

To summarize and account all these complex factors on the rare-earth anisotropy, which were simplified previously, the following expression can be used:

$$K_1 = -\frac{3}{2}\alpha_J r_{4f}^2 A_2^0 (2J_m^2 - J_m) \quad (2.4)$$

Where r_{4f}^2 is the squared $4f$ shell radius and has approximate value of $(0.05 \text{ nm})^2$. This expression gives insights on the possible change of RE element in determined compounds, as in the case of $\text{Nd}_2\text{Fe}_{14}\text{B}$ -easy axis by $\text{Pr}_2\text{Fe}_{14}\text{B}$ -easy axis and why to avoid $\text{Sm}_2\text{Fe}_{14}\text{B}$ -easy plane - see Figure 2.7. In addition, changes in crystal field parameter related to the additional charges, caused by interstitial atoms (like nitrogen), that can change the anisotropy from easy plane to easy axis in $\text{Sm}_2\text{Fe}_{17}$. The same does not happen to other RE^{+3} elements, as schematically demonstrated in Figure 2.8.

However, the use of rare earth also leads to technical challenges, including the low ordering temperature and paramagnetic response at around room temperature - despite having higher saturation magnetization at low temperatures than Fe-Co alloys, e.g., at 4 K holmium shows M_s of 3.8 T ($T_C = 20 \text{ K}$) while $\text{Fe}_{65}\text{Co}_{35}$ presents 2.5 T ($T_C > 1350 \text{ K}$). Also, when combined with ferromagnetically ordered $3d$ transition metal

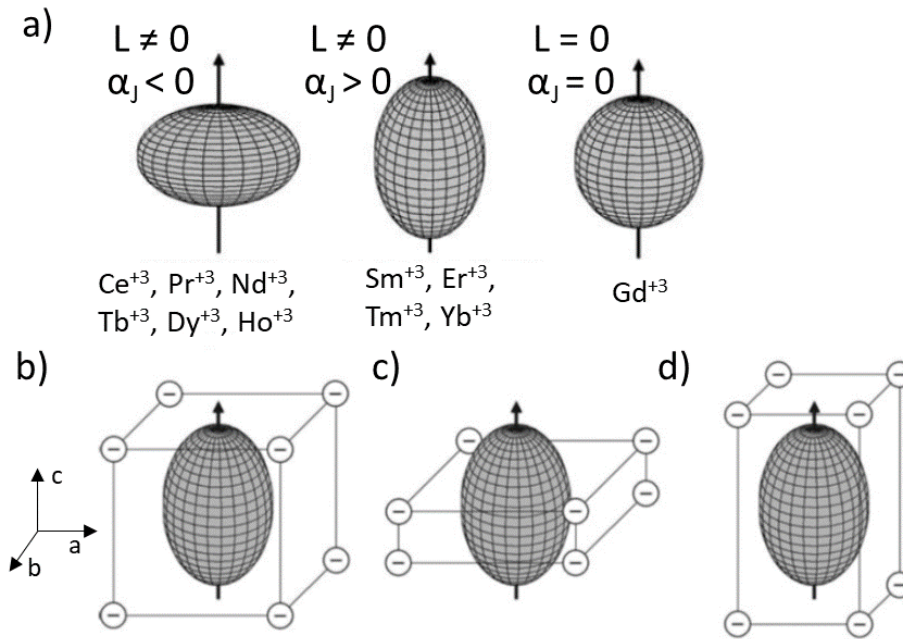


Figure 2.7: a) Shape of the 4f electron cloud for the different RE^{+3} elements and the corresponding Stevens coefficient; b) Prolate 4f RE ion in a cubic and in two tetragonal environments c) and d) with opposing A_2^0 values. Figure was adapted from [20, 27].

elements, the total magnetic moment (J_m) of heavy RE elements is coupled antiparallel to the moment of the 3d metals, which leads to a decrease in the overall saturation magnetization when compared to compounds with light RE instead, which presents parallel coupling with 3d elements [29]. For this reason, an alloy design has to be carefully carried out to account all the factors and to take the best advantage given by the 3d transition metals and the lanthanides to produce intermetallic, or intermediate, compounds for permanent magnets applications.

In a nutshell, the RE elements are responsible for the anisotropy while the ferromagnetic 3d elements ensure the magnetization and stabilizes the anisotropy constant at finite temperatures. In addition, the 3d elements also maintain high Curie temperatures, which is related to the $d-d$ exchange interaction, with an yield correction given by the indirect $d-f$ exchange (3d and RE) that also stabilizes the RE anisotropy against thermal fluctuations [20].

As an example, Figure 2.9 shows magnetization measurements along easy (parallel to c -axis) and hard (perpendicular to c -axis) magnetization directions of $\text{Nd}_2\text{Fe}_{14}\text{B}$ and SmCo_5 single crystals to determine: anisotropy energy E_A , anisotropy constant K_1 , saturation magnetization/polarization M_S or J_S and anisotropy field H_A . The anisotropy field is the magnetic field necessary to reach saturation when measuring along the hard magnetization axis, as in the exemplified case, perpendicular to c axis. The values of H_A and J_S can be directly obtained from the graph while for the anisotropy energy it is necessary to integrate the area between both curves - easy and hard magnetization axis, as indicated by the highlighted areas.

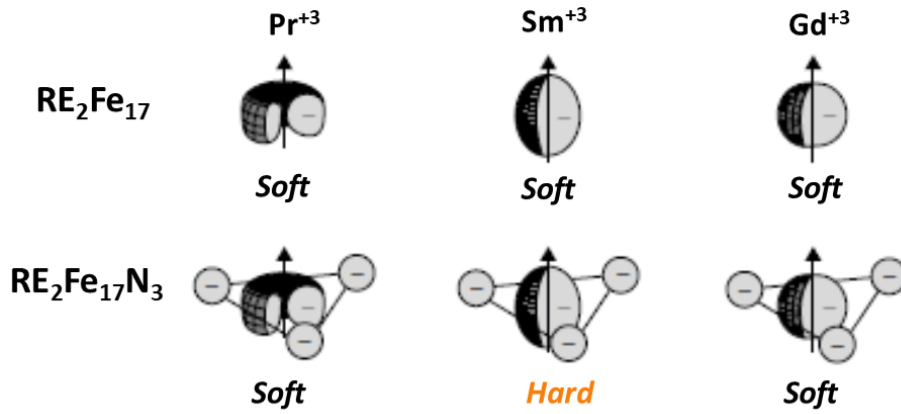


Figure 2.8: Schematic showing the influence of nitrogenation on the negative charges surrounding the RE^{+3} and the magnetic behavior of different $\text{RE}_2\text{Fe}_{17}$ compounds. Figure was adapted from [27].

The following equation which relates the H_A to K_1 and J_S can be used to obtain the theoretical anisotropy constant:

$$H_A = \frac{2K_1}{J_S} \quad (2.5)$$

As mentioned previously, for permanent magnets is beneficial to maximize J_S (extrinsic: high J_r and $(BH)_{max}$) along with K_1 and H_A (extrinsic: high H_{cj}), even though it seems contradictory since anisotropy field and saturation polarization are inversely proportional. With this in mind, the magnetic hardness parameter κ can be used to correlate the intrinsic properties according to the magnetic behavior into hard ($\kappa > 1$), semihard ($0.1 < \kappa < 1$) and soft ($\kappa < 0.1$) through the following equation (written in different forms) [32]:

$$\kappa = \sqrt{\frac{\mu_0 K_1}{J_S^2}} = \sqrt{\frac{2\mu_0 H_A}{J_S}} = \sqrt{\frac{2H_A}{M_S}} \quad (2.6)$$

This parameter indicates the potential for a material to be developed into a permanent magnet independently on the shape when $\kappa > 1$ and with shape/dimension limitations for semihard alloys (as in the case for Alnico) [32]. For comparison, different compounds are shown in Figure 2.10 according to K_1 and J_S relative to the corresponding κ value denoted by the solid and dashed lines [32].

As a short summary, in this section was discussed the ferromagnetic behavior (positive exchange energy) that leads to parallel alignment of spins and how in $3d$ transition metal atoms the magnetic moment is related to unpaired spins moments upon electronic configuration. The concept was expanded from isolated atoms to solids (assemble of atoms), in which the formation of band structure and the uneven electronic distribution to the corresponding splitting in spin up and spin down energy states give rise to

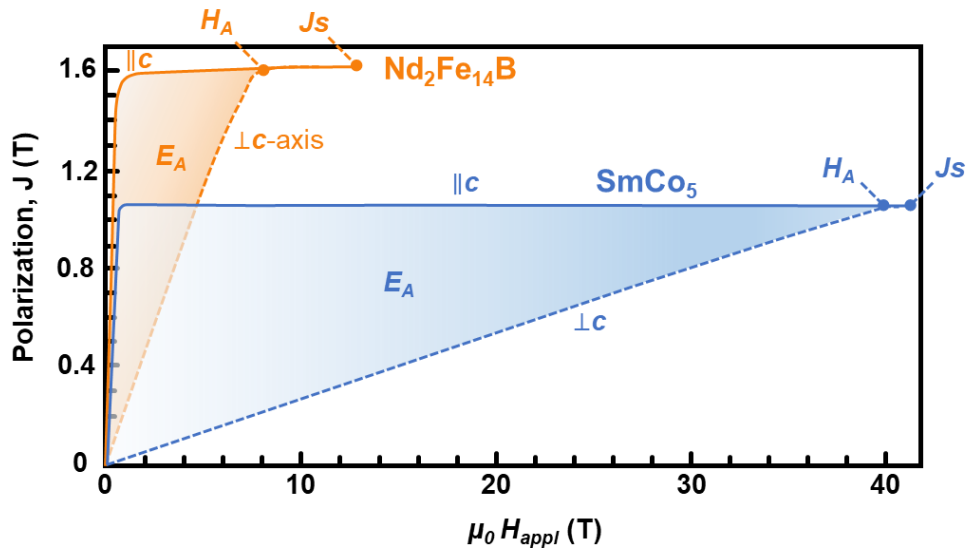


Figure 2.9: Determination of anisotropy energy E_A , anisotropy field H_A and polarization saturation J_S for $\text{Nd}_2\text{Fe}_{14}\text{B}$ and SmCo_5 single crystals. Figure was adapted from [13].

the magnetization of alloys. However, high magnetic anisotropy is also necessary to develop permanent magnets, since is the intrinsic key for the development of “magnetic hardness” (coercivity). The high performance permanent magnets are based on magnetocrystalline anisotropy, which can be achieved through the combination of the $3d$ elements with rare earths, since the former shows a strong spin-orbit coupling as the main reason for the high anisotropy observed in these compounds. Constraints on the crystal structure were also discussed in terms of anisotropy energy and the necessity to have material systems with uniaxial magnetocrystalline anisotropy for permanent magnets to prevent an easy change in the magnetization direction. All the intrinsic magnetic properties (J_S , H_A , K_1 and T_C) are important to determine the potential of a compound to be a permanent magnet, as demonstrated by the parameter κ .

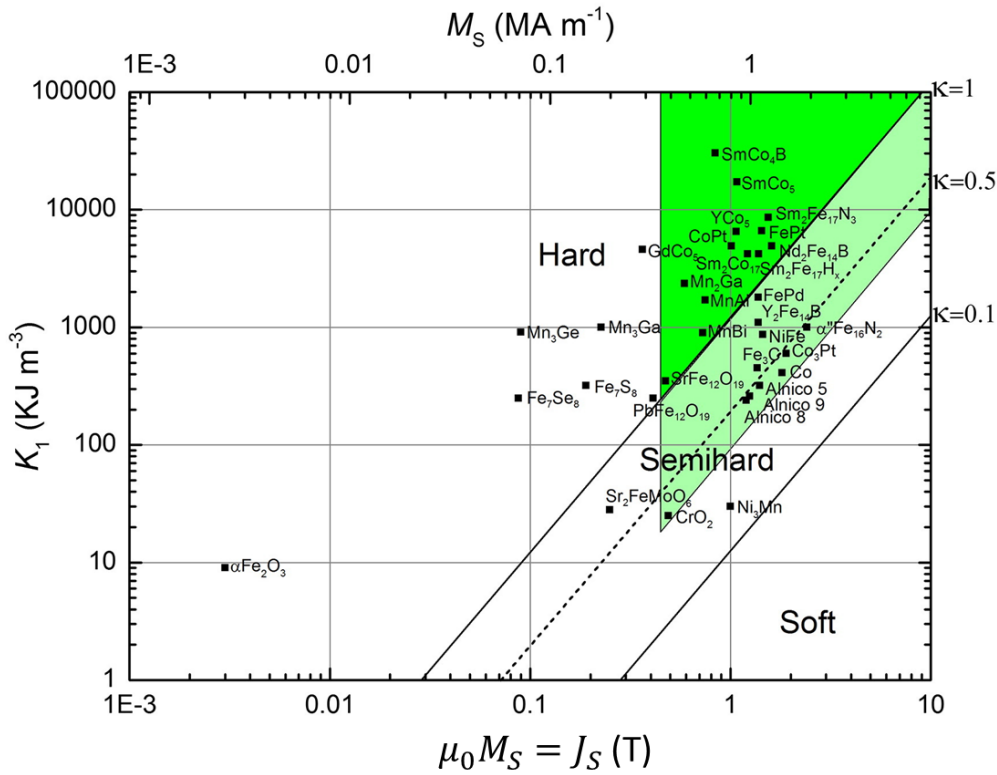


Figure 2.10: Anisotropy constant (K_1) in function of saturation polarization (J_S) for different compounds. The lines indicate different hardness parameter values (κ). Hard magnetic materials in the bright green area can be used for magnet production without shape constraints. Semihard materials located in the pale green area can also be used to produce magnets, but with severely shape-limited energy product. Figure was adapted from [32].

2.2 Magnetic Domain Structure

Going one step further on important concepts surrounding permanent magnets, the discussion will move towards ferromagnetism in a larger scale to further correlate with the overall hysteresis behavior shown by permanent magnets. Considering a ferromagnet and the magnetic energies discussed so far, the magnetic moments would be preferably parallel, to avoid increase the exchange energy (E_{ex}), and the magnetization vector being along the easy magnetization axis to reduce the magnetocrystalline anisotropy energy (E_A). If only these two energies were acting in the ferromagnetic material, would be beneficial that the magnetization would be maximized along the easy axis. However, when magnetized or in a saturated configuration, a ferromagnet have a high magnetostatic energy (also known as stray field energy), that can be expressed by:

$$E_{mstatic} = -\frac{1}{2}\mu_0 \int_{sample} H_d M dV = \frac{1}{2}\mu_0 \int_{space} H_{str}^2 dV \quad (2.7)$$

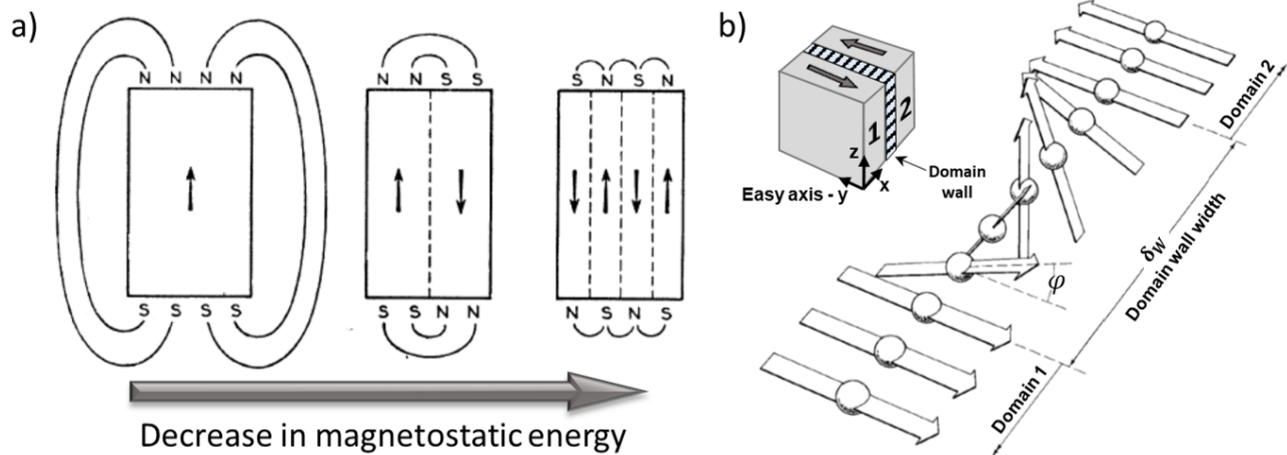


Figure 2.11: a) Magnetic domains in the highest Determination of anisotropy ; b) structure of a 180° domain wall. Figure a) was adapted from [13] and b) from [15].

where H_d is the demagnetizing field of the sample, H_{str} is the stray field in the space surrounding the sample and dV is the infinitesimal volume of the sample or the encircling space and M is the magnetization. To minimize the magnetostatic energy, it is advantageous to decrease the stray field by dividing the material into smaller magnetic volumes, so called magnetic domains. These domains are macroscopic volumes where the atomic moments are aligned, because of the ferromagnetic exchange interaction, and each domain has a saturation magnetization magnitude which lies along the easy axis, in the case of uniaxial anisotropy, or one of the easy axes, for non-uniaxial materials. For a uniaxial anisotropy material, subdividing these volumes into antiparallel magnetized domains of equal volume, the stray field around the sample would be minimized and, consequently, the $E_{mstatic}$ energy. This subdivision can be repeated to reduce the stray field energy even further, but at each time a domain is divided an interfacial region is created, known as domain wall. The existence of domain wall is associated with an additional energy term, for this reason the ultimate number and size of magnetic domains which will yield to lower total energy is a balance between volume, magnetostatic and interfacial domain wall energies. Within the domain wall, the magnetic moments are gradually changing the orientation until it reaches the configuration of the adjacent domain, in the exemplified case it is antiparallel, i.e., 180° Bloch type domain wall. The rotation of the magnetic moment across the domain wall can either be parallel (Bloch wall - common in bulk materials) or perpendicular to the domain wall (Néel wall - common in thin films). The schematic depicted in Figure 2.11a shows the subdivision of magnetic domains that leads to a decrease in the stray field, meaning that the magnetic flux is concentrated mainly at the surface instead of the surrounding volume of the sample. In Figure 2.11b is shown a 180° domain wall and how the magnetic moments gradually change the direction between the two domains.

Recalling the exchange energy equation, assuming identical spins (S), and expanding this expression to

calculate the exchange energy of a continuum instead of individual atoms, one can reach to the following expression:

$$E_{ex} = -2A \cos\left(\frac{d\phi}{dx}\right) \quad (2.8)$$

The term $A = \left(\frac{nJS^2}{a}\right)$ is the exchange stiffness, or exchange constant, that is related to the number of atoms per unit cell n and the lattice parameter a . The $\frac{d\phi}{dx}$ correspond to the moment angular variation in respect to the x direction, according to Figure 2.11b. Applying this equation for ferromagnetic materials, the exchange energy would be maximized if adjacent spin are antiparallel ($\phi = 180^\circ$), making it advantageous to reorient the spins across a large distance (small $\left(\frac{d\phi}{dx}\right)$), which would lead a large domain wall thickness (δ_W). However, in terms of anisotropy energy the opposite behavior is expected, since across the domain wall the magnetic moments would be along different axis which are not the easy magnetization one, implying on higher E_A . To minimize the E_A the spins should be along the easy axis, either parallel or antiparallel, resulting in a decrease the δ_W . Considering the competition of these two energies in a uniaxial anisotropy material, the domain wall width is a compromise between both, leading an expression that is dependent on A and K_1 :

$$\delta_W = \pi \sqrt{\frac{A}{K_1}} \quad (2.9)$$

In addition, the energy density associated with the 180° Bloch domain wall can be expressed as:

$$\gamma = 4\sqrt{AK_1} \quad (2.10)$$

Based on these competing energies and the spin rotation across the domain wall, it is important to introduce the concept of the ferromagnetic exchange length L_{ex} , which is the critical length scale where the exchange energy balances the anisotropy energy [13]. It can also be seen as the distance over which the perturbation caused by a switching of a single spin decays, meaning that above the L_{ex} the moments are magnetically decoupled [21, 33]. The exchange length is defined by the equation [13]:

$$L_{ex} = \sqrt{\frac{A}{\mu_0 M_s^2}} = \sqrt{\frac{\mu_0 A}{J_s^2}} \quad (2.11)$$

Since there is an energy associated with the domain wall, it is possible to hinder its creation by decreasing the size of the ferromagnet, or the grain size composing the ferromagnet, below a certain critical size (d_c). In this way, the energy penalty involved on the domain wall creation is higher than the gain related to the decrease in magnetostatic energy. For the simple case of isolated spherical particle with uniaxial magnetic anisotropy, the critical diameter size can be calculated using the expression [34]:

$$d_c = 18 \frac{\delta_W}{\mu_0 M_s^2} \quad (2.12)$$

For particles/grains with diameter larger than d_c , the presence of domains is favorable (multidomain state) while for smaller size the single domain state is energetically advantageous.

The existence of magnetic domains, along with the interactions given by exchange length, gives crucial insights and understanding on the magnetization and demagnetization processes of magnets, being an important link to correlate the overall hysteresis loop behavior and microstructure. The direct observation of domain wall nucleation and movement by *in situ* techniques, such as Kerr and magnetic force microscopy, give valuable insights that can be used to create strategies to improve extrinsic properties, as will be discussed in the next section.

2.3 Microstructural effects on magnetic properties and Brown's paradox

Based on the concepts discussed previously, it is possible to have a glimpse on the complex hierarchy and the different length scales involving magnetic materials, starting from the magnetism in atomic level and interactions/coupling, moving to intrinsic properties of permanent magnets and the formation of magnetic domain structures. The discussion so far was kept focused on ferromagnetic materials and, more specifically, on permanent magnets, showing requirements in terms of chemical composition and crystal structure to obtain intrinsic magnetic properties of potential hard magnetic compounds. The intrinsic properties can be seen as the ultimate theoretical limit for the extrinsic magnetic properties. However, to convert even part of this potential into magnets it is a challenge task, which must be adapted and optimized for each material system. Nevertheless, some general and common features can be derived and be used as a starting point in this optimization process.

To deepen the discussion, and explicitly show the existing gap between intrinsic and extrinsic properties, it worth to recall the hysteresis loop of an anisotropic magnet in comparison to the intrinsic loop (based on the intrinsic properties) and in an isotropic material (randomly oriented grains). These three loops are shown in Figure 2.12. The loops were based on the known properties/behavior of Nd-Fe-B magnets reported by Sawatzki [35], however no explicitly value is given since the general trend can be extrapolated for other material systems.

Starting the comparison from the saturation polarization/magnetization of the intrinsic-based curve (J'_s) and both anisotropic and isotropic magnets (J_s), it is generally observed that for magnets the polarization values are overall lower ($J_s < J'_s$), even though this is an intrinsic property. This occurs because the microstructure of a magnetic is not only composed of the hard magnetic phase, from which is the expected J'_s value. The additional phases are usually “non-magnetic” or with lower saturation than the main hard magnetic phase, in both cases the magnetization value would be reduced, since the measurements are the average value of the whole sample/magnet. An exception case is the spring-exchange magnets, where the chemical composition and microstructure are designed to have a soft magnetic phase with high J_s dispersed in a hard magnetic matrix in a compromised way to obtain higher magnetization without losing the magnetic hardness. Although the additional phases can be seen as detrimental at first glance, it is

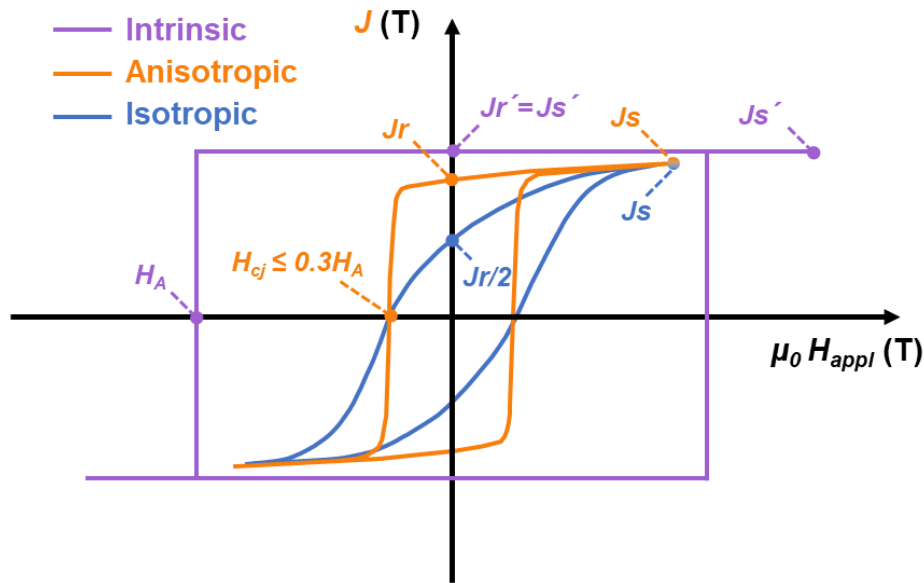


Figure 2.12: Hysteresis loops of hard magnetic materials illustrating the the upper limit (intrinsic) and the corresponding anisotropic and isotropic “real feasible magnets”. Figure was adapted from [35].

not always the case since they can be used for processing and microstructure optimization, leading to an enhancement of other properties, like coercivity. As an example, in sintered Nd-Fe-B magnets, the microstructure is composed of the hard magnet phase $\text{Nd}_2\text{Fe}_{14}\text{B}$ and Nd-rich grain boundary phase, which usually also contains Cu, Al, Ga in commercial alloys. The grain boundary phase has low melting point, which is beneficial for densification through liquid phase sintering, in addition, when well dispersed along the grain boundaries, this phase helps to improve coercivity despite reducing the overall magnetization. If the Nd-rich grain boundary is unevenly distributed, or in the worst case absent, the coercivity is drastically reduced - this will be discussed when comparing H_A and H_{cj} . The optimization of a permanent magnetic is not only related to the hard magnetic phase, but other factors play an important role in terms of processing, microstructure and extrinsic properties, which will be even more evident on the other figures of merit.

Following the decrease of field strength in the first quadrant of the hysteresis loop, we reach to the remanent polarization J_r , remanence in short. As the upper limit, the J_r' would be equal to J_s' , meaning that even in absence of applied magnetic field all magnetic domains are aligned and saturated in only one direction along the easy axis, this would provide the highest magnetic flux/stray field possible. Comparatively, in anisotropic magnets a slight difference is observed leading to J_r lower than J_s . To understand this difference is necessary to correlate the remanence with microstructure and grain arrangement. A high remanence is obtained through grain alignment/texture along the crystallographic easy magnetization axis, which would create a situation energetically favorable that the magnetization would lie along a single axis of the magnet as well, even when the applied field is removed. But during the manufacturing process,

the degree of alignment deviates from the ideal and not all the grains are perfectly aligned. This fraction of misoriented grains is the main reason that the J_r is slightly below J_s . Anisotropic magnets, when optimized, can have remanence of around 90-97% of the J_s value [36]. On the other hand, if the sample is isotropic (absence of texture), each crystal (each individual grain in this case) would have the easy magnetization direction randomly distributed across the magnet. This will average the contribution of the grains, creating a situation that the magnetic properties of the magnet will be isotropic along all axis and the obtained remanence will be around half of the remanence of a anisotropic magnet [37].

For the high performance rare-earth based magnets, where the second quadrant of the B-H loop is linear and $J_r = H_{cb}$, the maximum energy-product can be estimated through the expression:

$$(BH)_{max} = \frac{J_r^2}{4\mu_0} \quad (2.13)$$

This shows that an anisotropic magnet, with high degree of texture, is required to maximize the J_r - B_r along one of the axes and, consequently, $(BH)_{max}$. With this configuration, the magnet shows higher magnet flux along the textured direction, when compared to isotropic magnet, and almost no flux perpendicular to it.

The texture is induced during the manufacturing process and it is dependent on the process route of the magnet. For industrial sintered Nd-Fe-B for example, this happens after jet milling, when each micrometer-sized particle, consisted of monocrystalline $\text{Nd}_2\text{Fe}_{14}\text{B}$, can be rotated and aligned in a magnetic field along the c axis-the easy magnetization axis. This magnetic alignment can be combined with the uniaxial pressing or before cold isostatic pressing step, leading to a preservation of the texture after densification through sintering [24, 38]. A different processing route, also used for Nd-Fe-B, is related to hot deformation-die upsetting of nanocrystalline (melt spun ribbon-rapidly quenched) precursor. The mechanical deformation allied with anisotropic growth and the solution-precipitation mechanism are the reason for the texture development, along the pressing direction, in nanocrystalline Nd-Fe-B [35, 39, 40]. As an alternative route, it is possible to use gas-solid state reaction to promote grain refinement and texturing by decomposing and recombining the hard magnetic $\text{Nd}_2\text{Fe}_{14}\text{B}$ phase in hydrogen atmosphere. This process, HDDR (hydrogenation disproportionation - desorption recombination), involves different metallurgical aspects and kinetics to achieve the desirable fine and textured microstructure which goes beyond the scope of this thesis, but more information can be found in [38, 40, 41]. Despite giving examples for Nd-Fe-B, these processes are/can be used for other rare earth based magnets, especially the powder metallurgy-sintering route, which is widely applied in industry for large scale production. As for RE-free magnets, sintering is also the standard process for anisotropic hard ferrites, while for Alnico a combination of heat treatment under applied magnetic field induces shape anisotropy of FeCo precipitates in the Al-Ni matrix through spinodal decomposition reaction. Hot deformation, by hot extrusion, have been used in the past to produce anisotropic Mn-Al based magnets [42].

To summarize, the difference in J_r and J'_r can be attributed to additional phases in the microstructure and misorientation of grains. However, different grades of the same material system can be tuned to

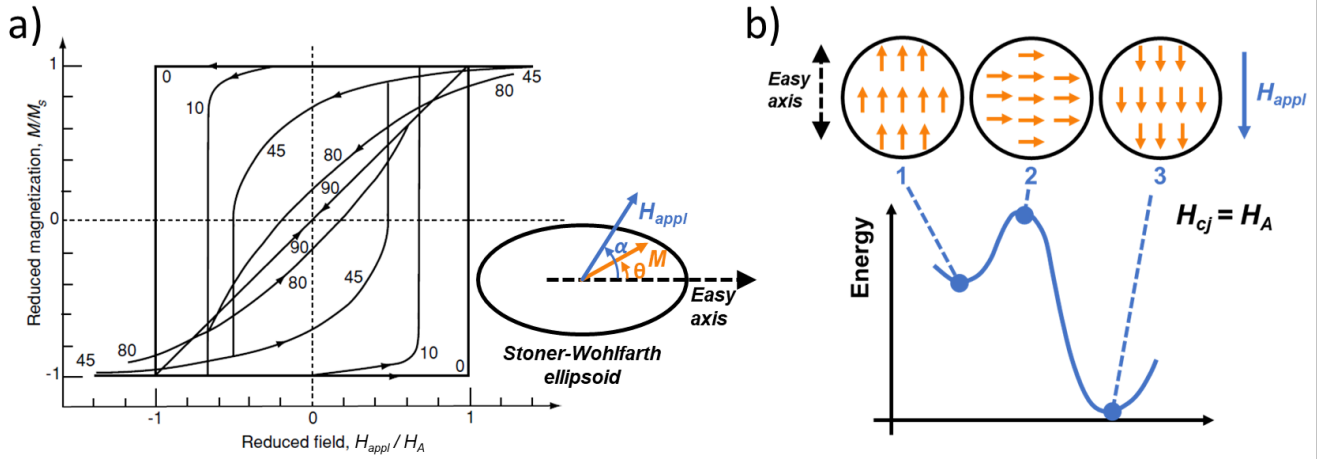


Figure 2.13: a) Hysteresis loops based on Stoner-Wohlfarth model for different applied field angles and the schematic of a ellipsoid particle that fulfill the criteria of the model. Figure was adapted from [14]. b) Coherent rotation of magnetization and the energy landscape path during the rotation process. Figure was adapted from [43, 44].

decrease this difference at expenses of other properties, like coercivity. This common trade-off is used for the different Nd-Fe-B grades, the upper limit for J_r (J'_s) is 1.61 T and magnets can be produced with remanence as high as 1.49 T (N55 - commercial grade), but with lower coercivity than other grades that shows lower remanence and, consequently, lower $(BH)_{max}$.

Moving along the hysteresis loop and entering in the second quadrant, where the applied magnetic field is reversed and opposite to the initial magnetization direction of the magnet, we have the property of coercivity H_{cj} . As explained previously, coercivity is the necessary applied magnetic field to demagnetize the magnet, $J = 0$. By comparison in Figure 2.12, and the previous discussion regarding the saturation and remanence, it is clear that coercivity is the extrinsic property that differs the most compared to the intrinsic counterpart H_A . To understand this large deviation, it is important to understand why the upper limit for H_{cj} is H_A . This derives from the Stoner-Wohlfarth model of magnetization reversal process, which only takes into consideration the mechanism of uniform rotation of the magnetic moments. In this model, it is considered for an uniform magnetized ellipsoid particle, with uniaxial anisotropy, where the magnetization is forming an angle α with the easy axis and an external magnetic field is applied on an angle θ with respect to the easy axis, as shown in the schematic in Figure 2.13a.

It is considered two energies in this system, the anisotropy energy (E_A - only the first term is used for simplification) and the energy related to the applied field (Zeeman energy - E_{Zeeman}), that is associated with the tendency to align the magnetic moments along the field direction. Combining these two contributions to the total energy E_{tot} , will give the expression:

$$E_{tot} = E_A + E_{Zeeman} = K_1 \sin^2 \theta + H_{appl} \mu_0 M_S \cos(\alpha - \theta) \quad (2.14)$$

Minimizing the total energy in respect to θ , and varying the applied field in a specific α angle, gives the hysteresis loops presented in Figure 2.13. As can be seen, for $\alpha = 0^\circ$ the hysteresis has square shape with coercivity equals to the anisotropy field, which is the highest value possible. When $\alpha = 90^\circ$, meaning that the field is applied along the hard magnetization direction, the hysteresis is reduced to a straight line with $H_c = 0$ that reaches saturation at H_A , similar to observed for single crystals of $\text{Nd}_2\text{Fe}_{14}\text{B}$ and SmCo_5 previously shown in Figure 2.9. The Stoner-Wohlfarth model takes into consideration a homogeneous isolated particle (no interaction between particles) without defects, in which only coherent rotation of the magnetic moments is allowed as magnetization reversal mechanism. However, these boundary conditions are far from real magnets and because of these differences, the coercivity values are substantially lower than H_A , reaching, in the best case scenario, around 20-30% of this value (Figure 2.12 for commercially available magnets - this observed discrepancy is often called Brown's paradox in literature. It worth mentioning that these values were achieved after intensive research and microstructural engineering, taking into consideration alloy design and processing optimization. Nevertheless, there are values reported in the literature that are actually above this threshold and close to H_A , as in the case of stress-free single domain Ba-ferrites particles (coercivity around 90% of H_A) and anisotropic FePt thin film (around 75% of H_A) [45–47]. These exceptions can be seen as goal values, which shows that it is possible to exceed the current obtained coercivity, however there is not yet a method to reproduce similar results in bulk magnets [10].

The reason for the disparity between H_{cj} and H_A can be attributed to other magnetization reversal mechanism than the coherent rotation used for the Stoner-Wohlfahrt model [43]. For the coherent rotation, all the moments that are align have to rotate collectively to follow the field direction. In the case that the magnetic field applied along the easy magnetization axis ($\alpha = 0^\circ$ - square shaped loop), going from positive to negative applied field, the domains would need to rotate 180° to follow the field direction. This means that the domains would go from the easy axis (lowest anisotropy energy), passing through different θ angles, including the hard axis (highest anisotropy energy - $\theta = 90^\circ$), until it reaches again the easy axis with reverse orientation. An schematic of the coherent rotation is displayed in Figure 2.13b. The reversal through this mechanism would cause a large energy penalty related to the anisotropy, since the moments would be in other directions than the easy axis (lowest energy) during the rotation.

As alternative to coherent rotation, there is the nucleation and growth of reverse magnetic domains. Through this mechanism, a region of the material that shows discontinuities/defects with different local magnetic properties (e.g. K_1), or magnetic moment arrangement, would act as a nucleation center for these reversal magnetic domains. Upon increasing the reversed applied magnetic field, the domain wall propagates throughout the grain, growing the magnetic reversed region, until reaches the demagnetized state (coercivity) and, eventually, saturate the sample in the opposite direction. The total energy required to nucleate the Bloch wall is proportional to the whole surface of the domain wall, thus, since the nucleation occurs in a small volume, the energy required is considerably lower than the energy involved in the coherent

rotation mechanism.

The nucleation of a reversed domain generally takes place at defected regions upon externally applied magnetic field in a different direction than the initial magnetization or even, in extreme cases, the nucleation can be spontaneously. Taking these magnetic inhomogeneities regions of low anisotropy into consideration, Kronmüller has developed a generalized relation for the nucleation field (H_N) based on the micromagnetic equations as follows [48, 49]:

$$H_N = \alpha_K(\Delta K, r_0)\alpha_\psi \frac{2K_1}{M_S} - N_{eff}M_S \quad (2.15)$$

where α_K and N_{eff} are microstructural parameters that describe the inhomogeneity of local anisotropy, by either nucleate or pin domain wall, and the effect of demagnetizing fields (dipolar interaction), respectively. The α_K parameter is a function of the strength (ΔK) and the width ($2r_0$) of the magnetic inhomogeneity, while N_{eff} takes into consideration grain size and shape in addition to non-magnetic phases that can generate local demagnetization stray fields. The other parameter on the first term, α_ψ , is linked to the angular dependence of the coercivity convoluted with the angular distribution of different grains composing the microstructure of the magnet [43, 49]. This equation shows the relevance of microstructural features on scaling down the intrinsic potential coercivity H_A to the obtained extrinsic counterpart for different permanent magnets.

There are two fundamental types of magnets regarding the magnetization and demagnetization in respect of reversal domain growth and domain wall propagation: nucleation and pinning type magnets. On the nucleation type, the domain wall motion within the grain is relatively easy and, in general, should be pinned at the grain boundary to avoid the propagation through different grains, otherwise a single nucleated wall would cause complete reversal of an entire magnet. Making a parallel to what has been discussed previously on Nd-Fe-B, the non-magnetic Nd-rich phase is the main responsible to pin the domain wall at the boundaries and to exchange-decoupled adjacent grains, preventing the unrestrained propagation through grains [50–53]. For the pinning type magnets, the coercivity is controlled based on the pinning of the domain wall movement within the grains. This mechanism is realized though inhomogeneities present within the grains that hinder the wall motion preventing further demagnetization. Wall displacement can only occur when the applied field is strong enough to overcome the pinning field strength, also called de-pinning field. This mechanism is observed in $\text{Sm}_2\text{Co}_{17}$ -type magnets, in which the domain walls are strongly pinned at the cell boundaries of the 1-5 phase located within the 2-17 matrix grains [54, 55]. The same behavior is observed in $\text{Sm}(\text{Co}_{1-x}\text{Cu}_x)_5$ and $\text{Ce}(\text{Co}_{1-x}\text{Cu}_x)_5$, where the Cu-rich precipitates are also hindering the domain wall propagation through pinning in a non-magnetic inclusion [19, 56].

Taking into consideration the equation derived by Kronmüller 2.15 and the given examples, it is possible to notice the importance of defects on the coercivity and the mechanism behind. Even though the word “defect” has a negative connotation, it does not necessarily imply that is something to be avoided. Each type of defect can impact differently the coercivity depending on the material system. As an example which can be taken to demonstrate the positive effect is related to interstitial atoms. Strictly speaking,

interstitial atoms are considered “interstitial defects” and when applied in $\text{Sm}_2\text{Fe}_{17}$ to form nitrides, it changes the behavior from soft magnetic (easy plane anisotropy) to hard magnetic with high uniaxial anisotropy. Another example is the strategy applied to improve coercivity by reducing grain size. It is reported that smaller grains would statistically decrease the probability to have critical defects at the surface of the grains and areas with high stray field (N_{eff}), also would prevent inhomogeneities with enough size to decrease significantly the nucleation field for reversal domains [14, 40, 57]. Moreover, the grain size reduction can also induce different magnetization/demagnetization behavior and, consequently, change the coercivity, as demonstrated by hot deformed Nd-Fe-B magnets reported by K. Hioki and correlate with the threshold between multidomain (above critical domain size- d_c) and single domain state grains (below d_c) [14, 39, 58]. But, accompanied with grain size refinement is the increase of area of grain boundaries, which is by definition is a planar defect that can contain other defects and chemical segregation [59, 60]. These are some examples how different defects can play either a positive or negative role in the magnetic properties of permanent magnets.

It is important to emphasize that defects are inherently present in real materials and real magnets. For this reason it is necessary to identify the types of defects existing in a particular material system and evaluate their impact on the coercivity. This would indicate if and which defect is the “weak link” in the microstructure that will be responsible for nucleation of reversal domains (smaller H_N) [61, 62]. With this knowledge, microstructural engineering, alloy design and process optimization can be used to overcome the weak link/links. Successfully adopting these strategies would lead to the augment of α_K and α_ψ while minimizing the effect of N_{eff} , resulting in a higher H_N that can be translated to a higher H_{cj} .

Identifying and correlating the microstructural features to the overall hysteresis is the main point to understand the extrinsic magnetic properties and to obtain information on how to improve permanent magnets. Nevertheless, it is a challenging task, since defects can exist in different length scales and have different impact on the magnetic properties for each specific material systems. Even for well-known materials, like Nd-Fe-B, there are still open questions regarding coercivity and the effects of microstructural features, since this compound can be processed through different techniques resulting in a different microstructure and still retain high magnetic performance [53, 63]. For developing new compounds as permanent magnets, this must be taken into consideration to gain knowledge about the material and its peculiarities regarding the coercivity-microstructure relation, allowing tailoring the magnetic properties to reach as close as possible to the upper limit given by the intrinsic properties.

2.4 The rare earth crisis - one decade later

The discussion so far was focused on the technical aspects of permanent magnets, including the choice of elements, intrinsic properties, main figures of merit and the microstructural effect on the extrinsic properties. These characteristics are indeed very important to understand and to further optimize permanent magnets, especially considering the key role of these materials on the technologies related to the transition from fossil fuels towards renewable energies, including electromobility and wind turbine generators, and application

on miniaturization of electronic components allied industrial automation [4, 6]. Consequently, there is a rise in the economic importance and a higher demand for these functional materials, leading to the scenario that other factors, besides the magnetic performance, also become relevant [64].

Based on the discussion so far, it is clear the role of rare earth elements and its importance for high performance magnet production. Nevertheless, these elements are categorized as “critical materials” by different global resource organizations [4, 7]. This means that the rare earth elements will face risks regarding supply because of geopolitical or sustainable development issues in respect to the growing demand [5, 6]. In this context, the majority of the global RE mining is done in China and this is seen as a supply-risk for governments and industries along with possible high price fluctuation.

This sequence of events already happen in 2010-2011, in a episode called “RE crisis”, in which the prices abruptly increased by an order of magnitude within few months, as shown in Figure 2.14, because of the limited exports of these elements imposed by the Chinese government [8]. The clear dominance of China in the global RE production is also represented in Figure 2.14. The price fluctuation had substantial impact on the Nd-Fe-B magnet market, since the costs have also increased because of the Nd and Dy prices. Dysprosium is a vital alloying element for high temperature applications, since it replaces Nd on the main hard magnetic phase leading to an increase in anisotropy field and, consequently, coercivity.

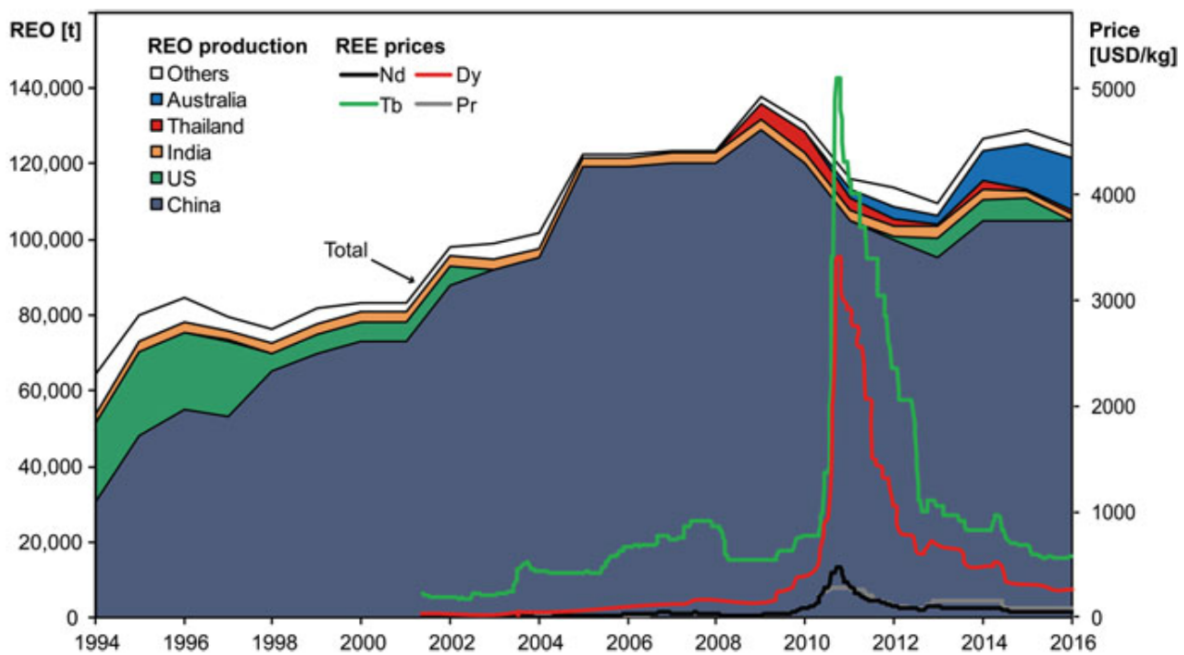


Figure 2.14: Global production of rare-earth oxides by country and the price development of Nd, Dy, Tb, and Pr (metal prices FOB China) around the time of rare earth crisis. Figure was taken from [8].

In face of such crisis, numerous strategies were stimulated to reduce the dependence from China. Among these, the diversification of supply chain was initiated to include recycling of scrap magnets and the (re-)opening of mines in different countries with high RE abundance, like Australia and USA [6, 8, 65, 66].

However, these solutions are still under development since it creates new challenges to be addressed. As in the case of recycling, the lack of collection logistics and the limited amount of information about the quantity of RE elements available for this procedure are the main issues that need development [65]. The opening of new mines and reopening of closed ones, along with process of reduction and separation, are also ongoing, but issues with environmental laws, proper waste management and the social impacts of these activities must be taken into consideration [8, 67].

Another additional pillar on the RE crisis strategy was revisiting Nd-Fe-B magnets in terms of chemical composition and process optimization. Different studies were focused to reduce and even avoid the use of heavy rare earths (HRE) in Nd-Fe-B magnets for high temperature applications, including grain boundary diffusion and similar processes, where the amount required of HRE was significantly reduced without detriment to the magnetic properties [68–72]. In the same direction, the substitution of Nd by the light rare earths La and Ce is still also extensively studied, since these two elements are in higher abundance and lower cost when compared to the former [73–77]. It worth mentioning that some of these developed strategies for Nd-Fe-B are already implemented as commercial products, as in the case of different grades of powders manufactured by the company Magnequench Co. - largest producer of Nd-Fe-B-based magnetic powder.

Apart from the previous actions, another important branch developed as a result from this situation was the search for new compounds and the re-evaluation of ideas from the 1980s and 1990s regarding hard magnetic phases, preferably containing less amount (RE-lean) or even without rare earth (RE-free) [9, 78]. By looking closer again to these old ideas, it is possible to reassess and might even improve their potential as permanent magnets [79]. Furthermore, the knowledge acquired during the research of other material systems, regarding coercivity mechanism and processing routes, can be implemented as strategies to develop an alloy with microstructure that can deliver useful extrinsic properties [9]. However, to be attractive for applications, these prominent permanent magnets have to be produced at low cost in industrial scale using less or none critical elements, avoid using toxic raw materials and to be based on raw elements with a stable supply with multiple sources worldwide, avoiding prohibitive price fluctuations [8].

Looking back to the comparison of energy-product presented in Figure 2.2, and having the requirements mentioned previously, is beneficial to have new materials that can either replace the existing magnets or that can fill the existing performance gap, especially between the Nd-Fe-B and ferrites. It is important to emphasize that the magnetic performance of new permanent magnets candidates do not have necessarily to be superior to Nd-Fe-B - but of course would be a major breakthrough if this was the case. Concerning the development of new materials, it is important to remember all the necessary ingredients to create a potential system, with proper intrinsic magnetic properties, and the realization to extrinsic ones by optimizing microstructure [9]. These are major challenges, quoting Prof. J. M. D. Coey - well known researcher and author of many books and articles in magnetism [9]: *“It all takes time, persistence, and determination; in permanent magnetism, there are no home runs.”* Considering this context, the candidates based on the RE-lean RETM_{12} and the RE-free Mn-Al compounds are often highlighted choices because of their potential to become relevant in the field of permanent magnets. Both material systems are the

main focus of this dissertation, more specific information and a overview will be presented in the following sections.

2.5 The ThMn₁₂ material system - Potential rare earth lean magnets

The compounds based on the ThMn₁₂-type structure (hereafter 1:12) in which rare earth elements are combined with 3d transition metal (TM) have been reported in the 1960s and 1970s for the composition RE₄TM₁₂ [80–82]. Despite knowing the system, only in the late 1980s it was found that these compounds are also formed with higher TM concentration, leading to the possibility to use ferromagnetic elements to increase the magnetization and, potentially, to be used as permanent magnets [83–85]. It worth noting the ratio between the RE and TM, Fe and Co mainly, for the different hard magnetic phases: SmCo₅ (1:5), Nd₂Fe₁₄B (2:14), Sm₂Fe₁₇N₃ and Sm₂Co₁₇ (2:17) [86]. As mentioned previously, the magnetization and Curie temperature are mainly determined by the 3d metal, since this ratio is lower for the ThMn₁₂-type it is to expect high polarization saturation and high T_C for such systems. This was confirmed by Hirayama *et al.* when reported about the intrinsic properties of NdFe₁₂N_x (x-unknown concentration) thin films, that have shown $J_s \approx 1.66$ T, $T_C \approx 823$ K and anisotropy field $\mu_0 H_A \approx 8.0$ T [87, 88]. As a follow up work, Hirayama *et al.* reported on the values for Sm(Fe_{0.8}Co_{0.2})₁₂ thin films, showing $J_s \approx 1.78$ T, $T_C \approx 860$ K and $\mu_0 H_A \approx 12.0$ T [89]. The results for Nd-based systems are very close to the ones of Nd-Fe-B with higher T_C (Nd₂Fe₁₄B - $T_C \approx 587$ K), while for the Sm-based with Co substitution all the intrinsic properties are higher than the benchmark ternary Nd-Fe-B.

Despite these interesting and promising intrinsic properties demonstrated in thin films reported recently, the 1:12 compounds are not stable in its binary REFe₁₂ in the form of bulk samples. To obtain the tetragonal 1:12 phase in bulk samples it is necessary to introduce an additional element to form a ternary compound with general formula REFe_{12-x}M_x with $x \geq 1$, where M can be Ti, V, Mo, Cr, Si, W, Al and Mn [81, 90]. The addition of non-magnetic elements leads to a reduction of the saturation polarization, which scales down the values reported by Hirayama *et al.* - see Slater-Pauling curve Figure 2.4b. This was one of the reasons that the 1:12 system was studied in the beginning of 1990s but faded into oblivion in the following years. The lost of interest at that time was also caused by the Nd-Fe-B ascendancy, in terms of magnetic performance, while only modest coercivity values were reported for 1:12. However, the RE crisis and the necessity to reduce the use of critical elements has again put this material system in the spotlight, also intensified by the encouraging recent results reported by Hirayama *et al.*

The ThMn₁₂ structure is tetragonal ($I4/mmm$ space group) and it derived from the common frame founded in the RECo₅ compounds (CaCu₅ type structure) as in the case of 2:17 types (Th₂Ni₁₇ and Th₂Zn₁₇), as schematically presented in Figure 2.15 [11, 90–92]. In addition, there is another related structure that can be seen as a stack of 1:12 and 2:17 types, forming the RE₃(Fe,M)₂₉ [91]. The Fe atoms in the 1:12 structure can be replaced by the M elements in the three possible Wyckoff positions $8f$, $8j$ and/or $8i$ which are related to different Fe-Fe distances, 0.251, 0.259 and 0.271 nm, respectively [90]. When compared to the atomic radius of Fe, 0.126 nm, the distance of the Fe-Fe dumbbell (0.252 nm) is smaller than found in

the $8i$, which according to Kobayashi *et al.* is one the reasons why the binary REFe_{12} is not stable and the necessity to add non-magnetic elements [90, 93]. Also because of the differences in Fe-Fe distance, each M atom have preferential site substitution. For Ti, V and Mo the preferential site is the $8i$ while Cr can be placed in any of the Fe sites - more information about the occupancy can be found in [81, 90, 92]. Among the different M atoms, Ti has received major attention because it can stabilize the 1:12 phase with the least amount of substitution, $\text{REFe}_{11}\text{Ti}$ (7.7 at.%), meaning higher concentration of Fe and, consequently, higher magnetization [81, 94]. Further studies on alloy design have shown that partially replacing Nd with Zr, at $2a$ site, leads to the possibility to decrease the concentration of Ti by 50% while still retaining the 1:12 phase in bulk form [95]. Since Zr is smaller than Nd, it shrinks the surrounding structure and partially solves the mismatch between the 3 different Fe sites, reducing the Ti content to stabilize the phase [96]. Similar effect was also observed for Sm-Fe-Ti based system [97, 98].

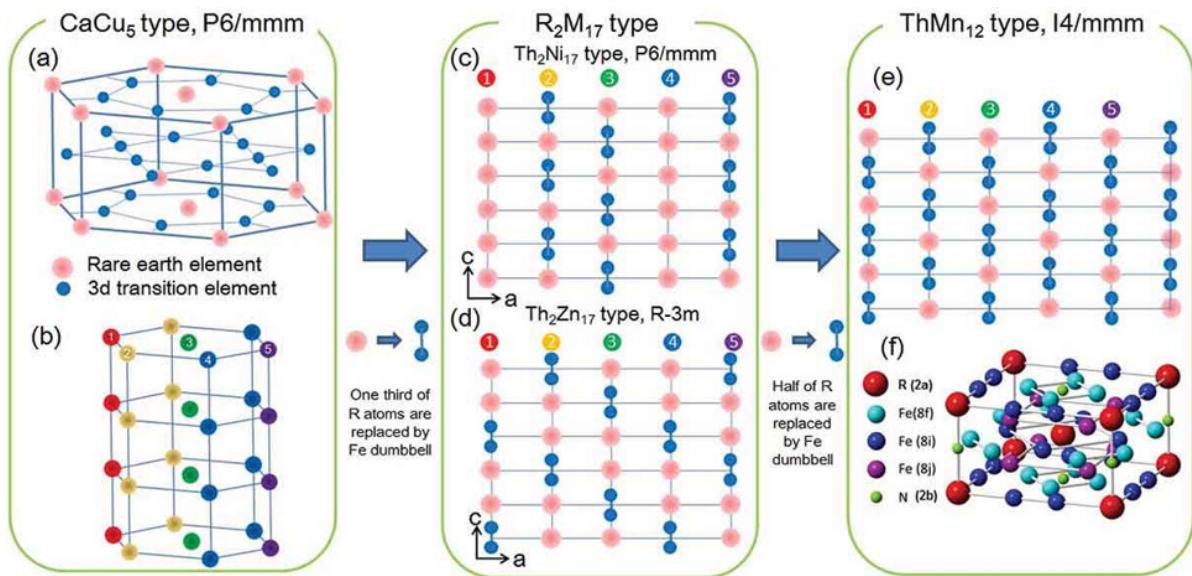


Figure 2.15: Crystal structures of RECo_5 (a,b) and its relation with the two 2:17 types and with the ThMn_{12} tetragonal structure. The occupancy is also shown in addition to the interstitial nitrogen in the $2b$ site of the ThMn_{12} structure. Figure was taken from [90].

Knowing this limitation to stabilize the phase in bulk form, it is necessary to understand and evaluate the intrinsic potential of $\text{REFe}_{12-x}\text{M}_x$ compounds to be developed as permanent magnets. Because of the several possible combinations between RE and M elements, neglecting the cases where Co is partially replacing Fe, we can draw general trends, as reported in [92]:

1. the average magnetic moment of Fe is in between $1.35\text{-}1.93 \mu_B$;
2. lower content of stabilizing elements is preferable to obtain higher polarization saturation;
3. the Curie temperatures varies in the range $400\text{-}650$ K, except when Mo is the stabilizing element, which brings the T_C to values between $260\text{-}500$ K;

The magnetic anisotropy is rather complex for this material system, for this reason is treated more specifically according to the RE element. When comparing the crystal field parameter (A_2^0 -crystalline environment) between $\text{REFe}_{12-x}\text{M}_x$ and $\text{RE}_2\text{Fe}_{14}\text{B}$ we observe opposite values, negative A_2^0 for former and positive for the latter. This means that the RE sublattice contributes to the uniaxial anisotropy only for RE elements with positive Stevens coefficient ($\alpha_J > 0$), i.e., the shape of the $4f$ electrons must be prolate - see equation 2.4. This would imply choosing between Sm, Er or Tm, however these last two are heavy RE elements, meaning that they couple antiparallel to the Fe sublattice, decreasing the expected magnetization for these compounds [81]. With these constraints, only Sm seems eligible to form 1:12 compounds for permanent magnets application [81, 99]. As for the other RE, with $\alpha_J < 0$, the compounds, like the Nd-based 1:12, that exhibits uniaxial anisotropy coming exclusively from the Fe sublattice. This rather weak anisotropy limits the anisotropy field to values below 2 T, resulting in compounds with hardness parameter lower than 1, being inappropriate candidates for permanent magnets [81, 92]. Nevertheless, it is possible to apply the same strategy used in $\text{Sm}_2\text{Fe}_{17}$ and completely reverse the sign of the RE sublattice anisotropy by changing the A_2^0 from negative to positive in the 1:12 compounds [81, 92, 100]. This is done by introducing interstitial nitrogen to the 1:12 lattice ($2b$ site as shown in Figure 2.15), which not only change the A_2^0 of the RE, but also increase the T_C up to 200 K of the corresponding 1:12 phase [81]. In theory, considering the single ion anisotropy approach (RE^{+3} - Figure 2.8), this effect of nitrogen uptake opens the possibility to use also Ce, Pr and/or Nd in $\text{REFe}_{12-x}\text{M}_x\text{N}_y$ as permanent magnet candidates. For comparison, the anisotropy field of $\text{NdFe}_{11}\text{Ti}$ is reported between 0.6-1 T that increases upon nitrogenation to values of around 8-10 T [87, 101–104]. Other nitrogenated Nd-based 1:12 compounds stabilized with Mo ($\mu_0 H_A \approx 13.0$ T) and V ($\mu_0 H_A \approx 10.0$ T) also exhibit similar behavior [8, 104].

Focusing in two systems to describe intrinsic properties, we have at room temperature:

$\text{SmFe}_{11}\text{Ti}$: $J_s \approx 1.17$ T; $\mu_0 H_A \approx 10.5$ T; $T_C \approx 570$ K; theoretical $(BH)_{max} \approx 270$ kJ/m³; hardness value of 2.1 [105–108];

$\text{NdFe}_{11}\text{TiN}_x$: $J_s \approx 1.4$ T; $\mu_0 H_A$ between 8.0-10.0 T; $T_C \approx 720$ K; theoretical $(BH)_{max} \approx 390$ kJ/m³; hardness value of ≈ 2.0 [87, 104, 107, 109, 110] - the values for the intrinsic properties are scattered in different studies, an average average value is given.

For both Nd- and Sm-based material systems, the intrinsic properties show potential to be applied as potential magnets. It worth mentioning that the anisotropy field of $\text{SmFe}_{11}\text{Ti}$ and the T_C of $\text{NdFe}_{11}\text{TiN}_x$ are higher than those of $\text{Nd}_2\text{Fe}_{14}\text{B}$ ($\mu_0 H_A$ of 7.5 T and T_C around 587 K). However, the saturation polarization is lower, giving also lower theoretical energy-product but still further alloy design can be explored to decrease the content of non-magnetic stabilizing element, as shown by Zr substitution, along and small additions of Co to improve saturation polarization [11, 90, 96, 109].

2.5.1 Extrinsic properties of Nd-based 1:12-type systems

Even though the intrinsic properties of these compounds show promising possibilities, converting this potential to extrinsic properties requires proper processing and microstructure optimization, as discussed

previously in section 2.3. Starting with Nd-based systems, there is the constraint that these compounds have to be nitrogenated, which limits the processing window to temperatures that are below the decomposition of the nitride phase. For $\text{NdFe}_{11}\text{TiN}_x$, according to the results reported by Hirayama *et al.*, the decomposition temperature is around 550°C , leading to the formation of $\alpha\text{-Fe}$ [87, 88]. As for $(\text{Nd}_{0.75}\text{Pr}_{0.25})\text{Fe}_{10.5}\text{Mo}_{1.5}\text{N}_x$, recent *in-situ* neutron studies by Aubert *et al.* have indicated that the decomposition occurs around 650°C [111]. Despite the higher decomposition temperature of Mo-stabilized nitrides, the temperature range is still rather low for conventional powder metallurgy processing routes, that normally involves densification by sintering at temperatures close to 2/3 of the melting temperature (typically around $900\text{--}1100^\circ\text{C}$). Because of this limitation, the extrinsic properties values are usually reported for powder or in polymer and metal bonded samples.

Table 2.2 shows a literature survey on coercivity values for nitrogenated Nd- and Pr-based 1:12 obtained by different techniques. For each study, different alloy compositions, processing techniques and nitrogenation condition were used, which will eventually impact the microstructure and possibly the nitrogen content, but a general trend can be discussed. Higher coercivity values are related to processing routes that leads to small grain size, like melt spinning, mechanical alloying, HDDR and mechanochemical synthesis. Even though not all works reported on the grain size, from the general knowledge about the mentioned techniques, it is reasonable to assume that they lead to submicrometer sized grains. As a consequence, it is statistically less probable that the grains will have defects that can nucleate reversal domains, as discussed previously. The amount of RE content also seems to influence, especially considering the work on HDDR of different alloys reported by Tang *et al.*, the rapid quenched reported by Aubert *et al.* and the mechanochemical synthesis of Sanchez *et al.* [112–114]. According to Tang *et al.*, the hyperstoichiometric composition reduces/eliminate the formation of $\alpha\text{-Fe}$. The highest reported coercivity value was from Yang *et al.* for fast quenched Mo stabilized alloy, giving $\mu_0 H_{cj}$ of 1.08 T [115]. In summary, it is necessary to combine a highly pure 1:12 phase precursor with elements that do not undergo decomposition reactions, submicrometric sized grains (close to the critical diameter, typically below 500 nm [8, 116]) and fully nitrogenated (maximum H_A).

Complimentary to the research focusing on developing extrinsic properties of Nd-based 1:12, other investigations on structural and microstructural characteristics have been performed. On the work of Chin *et al.*, it was reported the presence of antiphase boundaries (APB) in $\text{NdFe}_{11}\text{Ti}$ non-nitride probed by transmission electron microscopy (TEM), but no correlation was drawn between APB and magnetic properties or domain wall motion [122]. Nunes *et al.* investigated the magnet domain structure in non-nitrided mixed phase $\text{NdFe}_{11}\text{Ti}/\text{Nd}_2(\text{Fe},\text{Ti})_{17}$, by means of Lorentz microscopy, and observed planar defects related to the fine intergrowth of $\text{Th}_2\text{Zn}_{17}$ -type within ThMn_{12} -type structures [123, 124]. A relation between the two crystal structures was discussed and no pinning effect was observed at the planar defects.

Despite the results reported, the coercivity is still below the potential of these material systems, even when considered the limitation of 30% of H_A established by the Brown's paradox. This opens possibilities that other microstructure features might be responsible for the observed discrepancy, however, no systematic evaluation was reported yet.

Table 2.2: Coercivity (H_{cj}) at room temperature (RT) of Nd-based nitrogenated 1:12 compounds produced by different techniques - two examples of Pr-based are also given for comparison.

Parent alloy	Production Method	$\mu_0 H_{cj}$ (T) @ RT	Reference
Nd(Fe, Ti) ₁₂	Thin film-rf sputtering	0.53	Navarathna <i>et al.</i> [104]
Nd(Fe, Mo) ₁₂	Thin film-rf sputtering	0.72	Navarathna <i>et al.</i> [104]
NdFe ₁₁ Ti	Mechanical alloying	0.23	Tang <i>et al.</i> [112]
NdFe _{10.6} V _{1.2} Ti _{0.2}	Mechanical alloying	0.60	Tang <i>et al.</i> [112]
NdFe _{10.5} V _{1.5}	Mechanical alloying	0.88	Tang <i>et al.</i> [112]
NdFe ₁₁ Ti	HDDR	0.05	Tatsuki <i>et al.</i> [117]
Nd _{1.3} Fe ₁₀ V ₂	HDDR	0.22	Tatsuki <i>et al.</i> [117]
Nd _{1.3} Fe ₁₀ Mo ₂	HDDR	0.35	Tatsuki <i>et al.</i> [117]
Nd _{1.3} Fe ₁₀ TiV	HDDR	0.30	Tatsuki <i>et al.</i> [117]
Nd _{1.3} Fe ₁₀ TiMo	HDDR	0.18	Tatsuki <i>et al.</i> [117]
Nd _{1.3} Fe ₁₀ VMo	HDDR	0.58	Tatsuki <i>et al.</i> [117]
Nd _{1.2} Fe _{10.6} Mo _{1.4}	Melt spinning	0.60	Aubert <i>et al.</i> [113]
NdFe _{10.5} Mo _{1.5}	Melt spinning	1.04	Yang <i>et al.</i> [115]
NdFe _{10.75} Mo _{1.25}	Induction melted and ball milled	0.64	Hu <i>et al.</i> [118]
NdFe ₁₀ Mo ₂	Arc melted and milled	0.10	Anagnostou <i>et al.</i> [119]
Nd _{1.1} Fe ₁₀ CoTi	Mechanochemical	0.52	Sanchez <i>et al.</i> [114]
NdFe ₈ Co ₃ Ti	Induction melted and jet milled	0.51	Inoue and Suzuki [120]
PrFe _{10.5} Mo _{1.5}	Melt spinning	0.45	Tang <i>et al.</i> [115]
PrFe ₁₀ VMo	HDDR	0.38	Tang <i>et al.</i> [121]

2.5.2 Extrinsic properties in Sm-based 1:12

The compounds based on Sm possess high uniaxial magnetic anisotropy without the necessity of interstitial modification, meaning that makes it a promising material for the production of anisotropic bulk and fully dense permanent magnets by conventional processing routes [106]. Nevertheless, other technical and practical aspects involving Sm evaporation during melting and high temperature annealing and the development of liquid phase for sintering needs to be addressed for this objective [125]. Similarly to Nd-based system, large part of the reported extrinsic properties of Sm-based 1:12 is related to melt spinning (rapid quenched - fine microstructure) and by a variety of other methods that results in powder form samples. Only recently more research has been done to produce Sm-based 1:12 bulk magnets by sintering and hot pressing/hot deformation [11, 90].

In Figure 2.16, the coercivity values of Sm(Fe,X)₁₂ and the benchmark Nd-Fe-B as a function of the grain size for different processing routes are shown [106]. As can be seen, bulk Nd-Fe-B with coercivity up to 1.9 T have been reported and even higher values for melt spun ribbons and thin films, reaching 2.9 T - roughly the upper limit of the Brown's paradox for the ternary Nd-Fe-B. While for Sm-based 1:12 the highest reported value is for mechanochemical synthesized (Sm_{0.815}Zr_{0.185})(Fe_{0.81}Co_{0.19})_{11.19}Ti_{0.81} particles reaching 1.26 T reported by Gabay *et al.* (dashed blue line), followed by Sm(Fe_{0.8}Co_{0.2})₁₂B_{0.5} thin film with $\mu_0 H_{cj}$ of 1.2 T from the work of Sepehri-Amin *et al.* [97, 126].

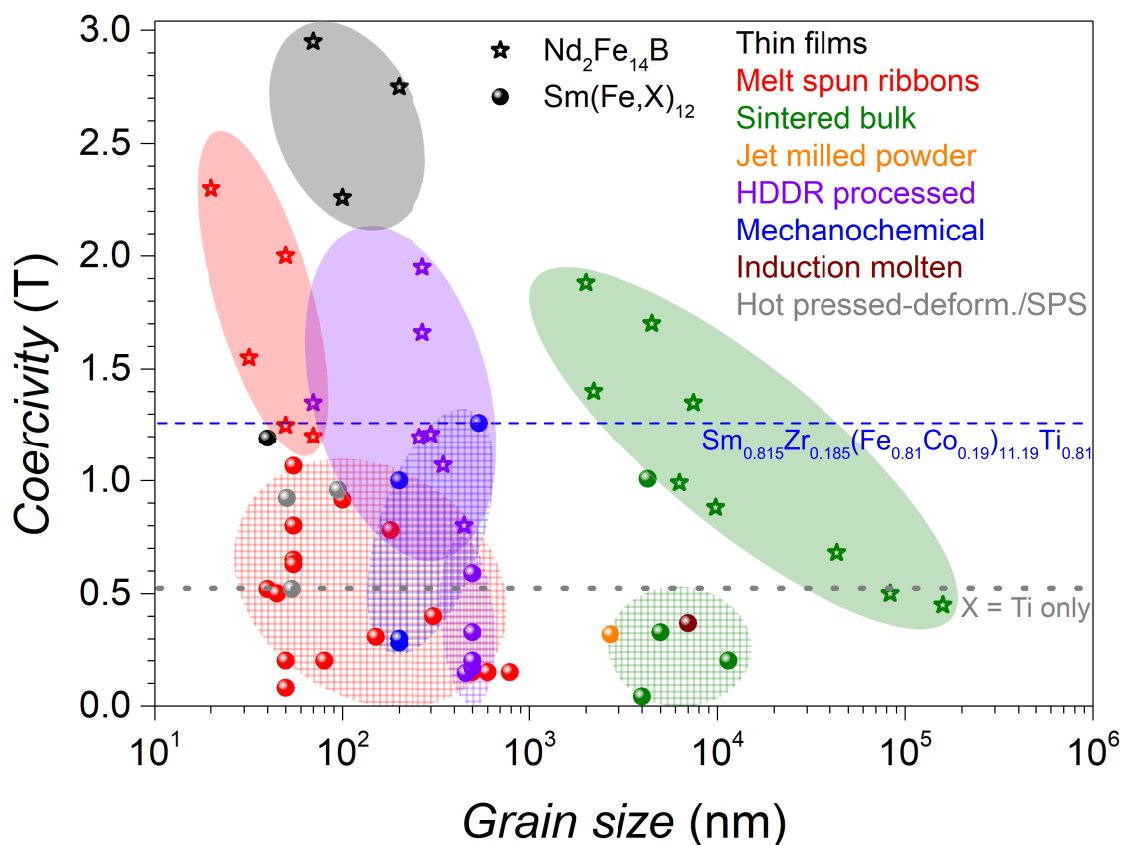


Figure 2.16: Comparison of reported coercivity values as a function of grain size between Nd-Fe-B and $\text{Sm}(\text{Fe},\text{X})_{12}$ systems. Different colors correspond to different production methods and shaded areas are guides to the eye. The highest reported coercivity of Sm-based 1:12 is shown by the blue dashed line [97]. The highest reported coercivity for a ternary $\text{Sm}(\text{Fe},\text{Ti})_{12}$ sample is shown by the grey dotted line [127]. Figure was adapted/updated from Ener *et al.* [106] to include the results from hot pressed/deformed/SPS processes [127–130].

As for bulk samples, consolidation of $\text{SmFe}_{11}\text{Ti}$ and $\text{SmFe}_{10}\text{V}_{1.5}\text{Ti}_{0.5}$ nanocrystalline powders were reported by Saito *et al.* using spark plasma sintering method, resulting in isotropic magnets with coercivity values of 0.52 T and 0.92 T, respectively [127, 128]. Alternatively to SPS, hot compaction and die upsetting of nanocrystalline $\text{Sm}_{12}\text{Fe}_{74}\text{V}_{12}\text{Cu}_2$ powders was reported by Schönhöbel *et al.* resulting in a isotropic magnet with coercivity of 0.96 T [129]. Two interesting aspects in this study apart from the magnetic properties: i) the detailed microstructure characterization has shown that the Cu hindered the grain growth and created a $\text{Sm}_{17.5}\text{Fe}_{71.5}\text{V}_8\text{Cu}_3$ grain boundary phase, which has contributed to the coercivity enhancement; ii) despite being subjected to hot deformation, the magnet has not shown texture development and remained isotropic. The second point demonstrated that conventional hot deformation process is not suitable to produce anisotropic magnets as in the case of Nd-Fe-B, as also discussed in detail by Simon *et al.* [90, 131, 132].

Alternatively to nanocrystalline precursor, Zhang *et al.* reported on the jet-milled micrometer sized

powder, consolidated by conventional liquid sintering process, to obtain anisotropic bulk sintered magnets of composition $\text{Sm}_8\text{Fe}_{73.5}\text{Ti}_8\text{V}_8\text{Ga}_{0.5}\text{Al}_2$ [130]. The resulting properties of the anisotropic magnets combined high remanence $J_r = 0.62$ T with coercivity of 1.0 T resulting in a $(BH)_{max}$ of 74 kJ/m^3 . From the magnetic domain analysis, combined with high resolution TEM, the authors attribute the relative high coercivity to the domain wall pinning at the grain boundary phase. The amorphous grain boundary phase is rich in Sm, Al and Ga with thickness around 3 nm, in the order of the exchange length (L_{ex}), and it is the reason for the magnetic decoupling of adjacent grains [90, 130]. It worth mentioning that the polarization saturation is rather low, compared to ternary systems, since the Fe content of the alloy is diluted by the many non-magnetic elements.

Despite the recent advances in producing bulk and anisotropic samples, the results revealed the necessity to understand the phase diagram of the Sm-based alloys, including the competing phases, and the effect of additional elements. As mentioned, the chemical composition of bulk samples are moving towards more complex multi-elements systems, incorporating the knowledge of common “additives” used for Nd-Fe-B magnets, like: Ga, Al, Cu and hypertoichiometric RE compositions [51–53, 90, 130, 133, 134]. The stabilizing element also seems to play a role, since the phase diagrams with V and Ti differs, leading to changes in the equilibrium phases with the 1:12 [135, 136]. The lack of non-magnetic phase in the Sm-Fe-Ti based system might be one of the reasons for the lower coercivity reported ($\mu_0 H_{cj}$ of 0.52 T - grey dotted line in Figure 2.16), as observed by the magnetic coupled grains in the work of Palanisamy *et al.* [137]. Moreover, the mechanochemical synthesis process reported by Gabay and Hadjipanayis show that the absence of structural defects on the particle surface, allied with the small crystalline size and separation, it is the responsible for the highest coercivity value reported so far [97]. These results shows that not only the exchange coupling of grains but also structural and microstructural defects of the 1:12 phase have to be addressed to excel the current reported coercivity values.

2.5.3 Properties in Ce-based 1:12

Cerium is a very appealing RE element, since it has high abundance and is relatively cheap, which is a good combination for permanent magnets. Nevertheless, the RE anisotropy is normally related to the single ion RE^{+3} contribution, as previously discussed, but Ce generally exhibits a mixed-valence state due to the co-existence of 3+ and 4+ states. This leads to the scenario that if in +4 state, there will be no contribution from the Ce-4*f* electron to magnetism in Ce-based compounds. However the valence state depends on the steric volume, i.e. on the local environment, meaning that one can vary the unit cell volume by interstitial/substitutional elements (chemical pressure) or even by applying external mechanical pressure [138, 139]. The valence manipulation of Ce has been reported for (Nd,Ce,La)-Fe-B where an increase of magnetization was observed when the valence was shifted towards +3 [140].

Few attempts to produce Ce-based 1:12 hard magnetic compounds have been reported, mainly focusing on intrinsic properties, studies on the effect of Co and Zr doping and interstitial modification with hydrogen and nitrogen [11, 141–145]. Different works show that the anisotropy field of $\text{CeFe}_{11}\text{Ti}$ is in the range of

1.8-2.5 T, which is to be expected since the main contribution comes from the Fe atoms [11, 146]. But contrary to what happens in Nd-based systems, interstitial modification with nitrogen slightly decreases H_A to values around 1.5-2.0 T, while increases the T_C by 240 K [146, 147]. The same trend is also seen for hydrogen modification, meaning that the Ce atoms do not contribute significantly to the anisotropy field and only the exchange interaction between Fe-Fe atoms is increased, resulting in a higher Curie temperature [143, 148]. As for extrinsic properties, Zhou *et al.* has reported coercivity of 0.13 T for melt spun $\text{CeFe}_{11}\text{Ti}$ with TiC precipitates [149]. The coercivity was attributed to the small grain size caused by a combination of fast solidification and the evenly distributed precipitates. Other approach to use Ce in 1:12 compounds is to partially substitute other RE elements, aiming to decrease the costs of possible magnets. This concept was investigated for (Ce,Nd)-Fe-Mo nitrides, in which was shown a decrease in coercivity with increasing Ce content because of the lower anisotropy field [150]. Simon *et al.* reported on a bulk magnet produced by hot compaction and hot deformation of $\text{Ce}_{0.5}\text{Sm}_{0.5}\text{Fe}_{10}\text{TiVGa}_{0.5}$ nanocrystalline powder, resulting in isotropic magnet with $\mu_0 H_{cj}$ of 0.53 T [132].

Even though the intrinsic properties of Ce-based 1:12 reported so far are lower than for other RE, there are still possibilities and studies being carried to change the rare earth sublattice contribution to the magnetism, among other related issues regarding phase stability and further alloying elements [138, 139, 146]. Experimental efforts are still scarce to understand these relations and also to correlate microstructure and extrinsic properties

2.6 The Mn-Al material system - Potential rare earth-free gap magnet

Mn is an interesting element to be used for new magnets development, first of all because it is an abundant element: Mn is the 12th most abundant element in the Earth's crust [9]. Furthermore, Mn forms ferromagnetic alloys having a relative high Curie temperature, which is beneficial for most of applications of permanent magnets. The atomic moment of Mn can be higher than that of Fe or Co, arising from its electronic configuration $[\text{Ar}] 4s^2 3d^5$, the $3d$ is half-filled with spins oriented parallel to each other, following the Hund's rules to maximize the spin moment. However, Mn tends to order antiferromagnetic because of short interatomic distance, whereas it orders ferromagnetically for distances above 2.9 Å [32] - see Bethe-Slater curve Figure 2.3a. Thus, alloying Mn with other elements, like Al, Bi and Ga, is necessary to form a ferromagnetic compound and to obtain uniaxial magnetocrystalline anisotropy [151, 152]. Among the different options, the binary Mn-Ga is not often considered since the price of Ga is prohibitive to develop this compound for permanent magnets applications [2, 9, 32]. Mn-Bi may be a good candidate with an affordable price per kilogram, but Bi is a rare element which is a by-product of lead, and the production of such magnets would then increase the demand and price of this element [2, 4, 32]. On the opposite, Al is very abundant, low-cost and has a stable supply including a well developed recycling industry [4, 9]. In addition, the saturation magnetization of the Mn-Bi and Mn-Ga are lower than in Mn-Al compound [2, 32]. Thus, Mn-Al is the main choice among the Mn-based compounds as a rare earth free candidate as permanent magnet [10, 153-155].

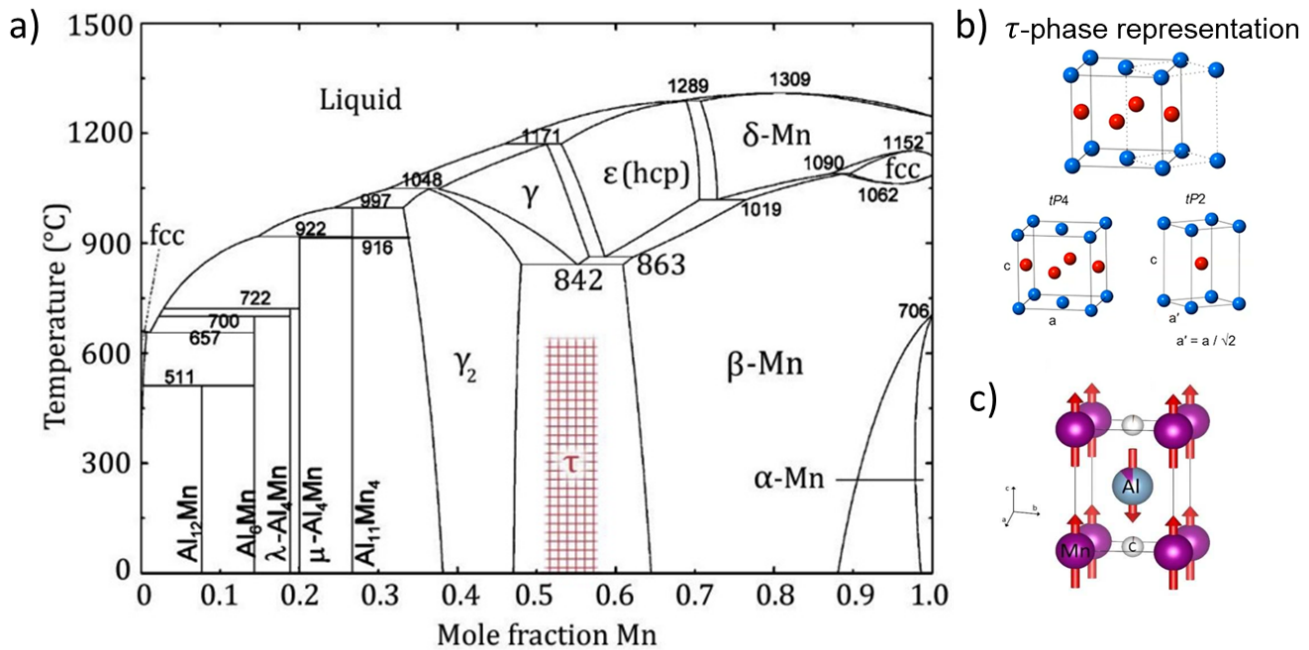


Figure 2.17: a) Mn-Al phase diagram highlighting the metastable τ -phase; b) different representation of the tetragonal τ -phase ($L1_0$ structure) and c) magnetic moments in the ferromagnetic phase. Figure a) was taken from [12]; b) and c) were adapted from [156].

The only ferromagnetic phase in the Mn-Al material system is the τ -phase, which is metastable and with composition range between 51-58 at.% Mn, as presented in the phase diagram Figure 2.17a [12, 157]. It possesses a tetragonal $L1_0$ chemically ordered structure (see Figure 2.17b), which can be represented in two ways: $tP2$ and $tP4$. For $tP2$ representation, 2 sites exist: $1a$ (0,0,0) and $1d$ ($\frac{1}{2}, \frac{1}{2}, \frac{1}{2}$). All $1a$ sites are occupied by Mn atoms and $1d$ sites are occupied by Al atoms as well as the excess Mn, since the composition is hyperstoichiometric in Mn. The atomic radius of Al is greater than that of Mn with 1.43 Å versus 1.37 Å, respectively, leading to a larger c unit cell parameter. From the literature data, the moments carried by the Mn atoms of the $1a$ sites are directed along the c axis and that these moments are ferromagnetically coupled (see Figure 2.17c) [158, 159]. However, the second Mn sublattice couples antiferromagnetically with the original Mn-sites due to the small interatomic distance (2.659 Å), leading to a lowering of the total saturation. This has been observed by neutron powder diffraction, where the magnetic moment of the Mn-site was refined to be $2.43(5) \mu_B$, while the magnetic moment of the Mn fraction on the Al-site was $-2.37(6) \mu_B$. Adequately choosing the composition is necessary to optimize the magnetic properties [151, 157, 160].

Melting techniques are often the preferred synthesis route for the production of τ -MnAl, but this usually leads to an undesirable non-ferromagnetic phase mixtures ($\tau + \beta\text{-Mn} + \gamma_2$) [158, 160–164]. The τ -MnAl is typically obtained by controlled cooling from the ϵ -phase region on the phase diagram

or by quenching the ϵ -phase phase followed by short annealing at temperatures in the range of 673–823 K [12, 165]. Two mechanisms have been proposed to explain the ϵ to τ transformation, one is based on diffusional “massive” transformation whereas the other one is a plate-like modification formed by a shear reaction, said “displacive” [12, 164–168]. Both have been observed simultaneously and the mechanisms is known to depend on various aspect of the process like composition, microstructure and annealing procedure [12, 164, 169].

Since the τ -phase is metastable, the processing window of these alloys have to be carefully taking into consideration to avoid decomposition to the stable non-magnetic β -Mn and γ_2 phases [162, 164]. One way to improve the stability of the τ -phase is to add an interstitial doping element, i.e. carbon (see Fig.2 b). The addition of C has been proved to suppress the decomposition of the τ -phase while increases the saturation magnetization [3, 12, 170]. However, the T_C is reduced by the this interstitial modification, depending on the C concentration, it can decrease from ≈ 640 K to ≈ 540 K [3, 12]. This decrease is associated with reduction of the exchange interaction because carbon decreases the unit cell parameter a , which leads to a shorter Mn-Mn distance in the $a - b$ crystallographic planes [159].

The composition influences the intrinsic magnetic properties of the Mn-Al(C) compounds. Typical values obtained for $\text{Mn}_{54}\text{Al}_{44}\text{C}_2$ are $M_S = 118 \text{ Am}^2/\text{kg}$ ($J_s \approx 0.75 \text{ T}$), $T_C = 540 \text{ K}$ and $H_A = 4.2 \text{ T}$ and $K_1 \approx 1.5 \text{ MJ/m}^3$, values taken from [12]. Theoretical $(BH)_{max}$ values of between 95 and 133 kJ/m^3 (12 - 16.8 MGOe) were reported in the literature for τ -MnAlC [3, 12]. Recalling the typical $(BH)_{max}$ values presented in Figure 2.2, it is possible to notice that the predicted energy-product for this RE-free permanent candidate lies in the gap range between ferrites and Nd-Fe-B, making this material system a prominent “gap magnet” [2].

From the experimental point of view, several approaches and techniques have been used to get the best from this alloys in terms of alloying elements, phase purity and extrinsic magnetic properties [12]. The remanence and coercive field of Mn-Al compounds obtained by different techniques are summarized in the Figure 2.18.

As can be seen, the extrinsic properties are highly dependent on the processing route, since each technique induces different effects on the microstructure. For this system, the coercivity is usually associated with domain wall nucleation and pinning, both are dependent on the defect type and defect density [12]. It was reported different types of defects for τ -MnAl-phase occurring in different length scales, including: stacking faults, antiphase boundaries, dislocations and twins (micro and nanoscale) [171–178]. Different studies have shown how complex is the relation between these microstructural defects and coercivity, since the defects can play different roles in the demagnetization behavior. In addition, the coexistence of these various defects makes difficult to experimentally assess and study them individually.

A recent study from Jia *et al.* partially clarified some of these issues by comparing samples with and without twins, which was shown that the coercivity decreases by half when twins are present, from 0.25 T to 0.12 T [172]. It was demonstrated that twin boundaries act as nucleation center for reversal magnetic domains and the domain walls are only weakly pinned at these defects, which would give a net negative impact on the coercivity. Similar trend was also reported previously by experiment and micromagnetic

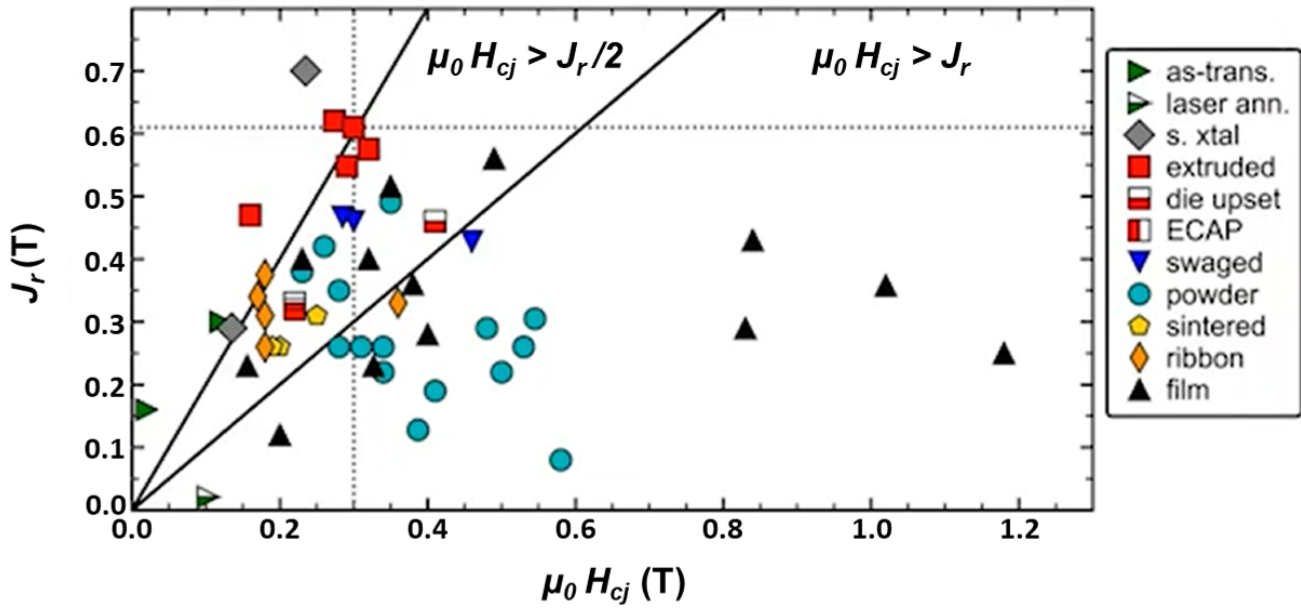


Figure 2.18: Remanence and coercivity for Mn-Al compounds produced by different techniques. Figure was taken from [156].

studies from Bittner *et al.* and theoretical calculations from Gusenbauer *et al.* [176, 179]. On the other hand, studies from Palanisamy *et al.* have demonstrated, through electron holography observation, that the domain wall is strongly pinned at twin boundaries [174]. This was combined with theoretical calculations that has shown a decrease in the domain wall energy along the twin boundary and hence the pinning effect. Also contributing to this pinning behavior it is the chemical segregation along the twin boundary, an enrichment of around 8 at.% Mn was observed which also affected the local magnetic properties [174, 180]. The contrast between these reported results show the controversy on this topic and, it worth mentioning that the alloy composition on these studies is also different, the one reported by Jia *et al.* is Mn-Al-C while the one from Palanisamy *et al.* is only binary Mn-Al. This difference can also be relevant, since the observed chemical segregation and even the formation of the twins during the formation of τ -phase might be affected by the alloy composition [166].

Regarding the effect of dislocations, in the same study comparing twinned versus twin free samples, Jia *et al.* showed the pinning effect of dislocations to the domain wall motion and the increase of the de-pinning field with increasing the dislocation density [172]. It is discussed that the size of dislocation is in the same range as the domain wall width ($\delta_W \approx 12.5$ nm), which makes dislocation suitable candidates as pinning centers. According to the authors, there is a change in the magnetization/demagnetization mechanism from nucleation to pinning controlled behavior as consequence of high density of dislocations. Despite having induced polytwins within the fine microstructure resulting from the high pressure torsion process (HPT-severe plastic deformation), the high dislocation density has increased the coercivity up to 0.53 T.

However, the lattice distortion caused by the plastic deformation causes a decrease in magnetization because of the shorter Mn-Mn interatomic distances and, consequently, higher antiferromagnetic interaction. The same trend of results was reported by other authors also using HPT [165, 181, 182] and other methods which induces high dislocation density, like ball milling [183–186], cold rolling [175, 187], equal channel angular extrusion [188], swaging [189], die upsetting [185] and hot extrusion [42, 190]. This trend of plastic deformation/dislocation density on increasing coercivity can be also visualize in Figure 2.18, showing coercivity values above 0.2 T, that is normally the threshold for as-cast and annealed states with fine microstructure - lower coercivity for coarse grains [165, 172, 176, 191].

The antiphase boundaries (APB) are reported to act as nucleation center for reversal domains and also pinning centers because of the antiferromagnetic coupling at the interface of the APB (short Mn-Mn distance) [173, 189]. However, according to the micromagnetic simulations reported by Arapan *et al.*, the nucleation field is strongly reduced when the number of APB is increased, showing that this defect is deleterious for coercivity [173]. As for the stacking faults, it was observed through Lorentz microscopy that the domain walls tend to be pinned at this defect, as reported by Zijlstra and Haanstra and reinforced by the works of McCurrie *et al.* and Jakubovics and Jolly [177, 192, 193].

The balance between the types and density of defects appears to be the key factor for coercivity and the mechanism behind it (nucleation and pinning) in τ -MnAl(C). Many of these defects are originated during the nucleation and growth of τ -phase and can be further modified depending on the chemical composition and processing route, as described previously and qualitatively reported by Zhao *et al.* [171]. Even though coercivity values close to 0.6 T were reported for highly deformed samples, this value is far below the ones observed for thin films, that can reach above 1.0 T [194] - see Figure 2.18. Taking into consideration the anisotropy field values for these alloys, between 4.0 T to 5.0 T depending on the composition, and considering the Brown's paradox that shows coercivity values up to 30% of H_A , it is reasonable to expect H_{cj} values in the range of the ones reported for thin films also for bulk samples. This difference shows that this system can still be further developed, even though has a rather complex relation between microstructure and coercivity, different studies are unveiling the path towards optimization. The knowledge that is being gathered can be linked to the nucleation field (H_A) equation 2.15, more specific to the α_K parameter. Showing how beneficial is to find defects to increase the domain wall pinning strength and increase the nucleation field for reversal domains, thus increasing α_K .

The other important figure of merit represented in Figure 2.18 is the remanence. As described previously, the J_r ($\mu_0 M_r$) is dependent on the texture along the easy magnetization axis, the c axis in the τ -phase tetragonal structure. The existence of twins is detrimental for achieving highly textured samples, since the misorientation angle of the twin variants would lead to the situation that the easy magnetization axis of each of the variants would be pointing along different directions, therefore resembling isotropic behavior [195]. For this reason, it is difficult to obtain monocrystalline particles that can be further aligned in magnetic field, prior consolidation, to obtain anisotropic samples. On the study reported by Zhang *et al.*, twin-free τ -phase particles were obtained by a complex process starting from a ϵ -phase single crystal and pressure assisted annealing to induce a single variant during the τ -phase formation [195].

Nevertheless, a more feasible and industrially standard process that can be used to obtain anisotropic samples is through hot extrusion, as can be observed by the high remanence values reported in Figure 2.18. This process was used in the late 1970s by the Japanese company Matsushita Electric Industrial Company and later by the company Sanyo Special Steels to commercially-produce anisotropic magnets [42, 190]. It worth mentioning that Sanyo was using gas atomized powder as feedstock material while Matsushita was extruding bulk ingots, and both added small amount of Ni to the ternary Mn-Al-C composition to facilitate the deformation and the extrusion process [190]. This combination has yield to a remanence value of 0.61 T (for reference $J_s \approx 0.75$ T) for the hot extruded magnets, which combined with $\mu_0 H_{cj} \approx 0.3$ T has given a $(BH)_{max}$ of 55 kJ/m³ [42]. This $(BH)_{max}$ value was higher than ferrites ($(BH)_{max}$ below 38 kJ/m³) and remained as the “state of the art” for the Mn-Al material system. Despite showing interesting and useful properties, the commercial production was discontinued two decades ago. Only recently similar results were reported by Feng *et al.*, in which $(BH)_{max}$ of 46 kJ/m³ was achieved [190]. It was also shown, by different characterization methods, the microstructural features resulting from hot extrusion, including the grain refinement caused by dynamic recrystallization in a large fraction of the sample that led to the decrease of twin density when compared to non-recrystallized grains, leading to coercivity values around 0.3 T. Other processing routes, like die upsetting and swaging, also show some degree of texture, however below the values reported for hot extrusion, as can be observed in Figure 2.18.

As discussed previously, the Mn-Al(C) has a great potential as gap magnet with $(BH)_{max}$ between ferrites and Nd-Fe-B. Other aspects regarding price, abundance of the raw materials and possibility for large scale production also highlight this prominent system as a important and interesting system to be studied. However, the complex microstructural arrangement of the ferromagnetic metastable phase, and the different types of defects, appears to be the main issue to be addressed for developing samples/magnets with high τ -phase fraction (high magnetization) with reasonable coercivity, remanence and, consequently, $(BH)_{max}$. Characterization and quantification of defects and micromagnetic simulations are helping to elucidate the role of defects on the overall hysteresis behavior, either improving or deteriorating the magnetic properties. There are still challenges to be overcome, features to be comprehend and room for optimization to develop Mn-Al(C) permanent magnets.

3 Synopsis of Publications

3.1 Preamble of the synopsis

The discussion so far has emphasize the complex relation between magnetism and metallurgical variables to optimize and obtain permanent magnets, starting from the magnetism of a single atom and exchange interactions in a solid up to the magnetic hysteresis of a bulk magnet. Across this path, different length scale variables can extensively influence the extrinsic magnetic properties. A parallel between typical microstructural features of an engineering material and a corresponding simplified version of the magnetic counterpart is summarized in Figure 3.1. The interplay between microstructural features, especially defects, and coercivity has been the object of many studies and the importance has been demonstrated on the micromagnetic equation proposed by Kronmüller, Equation 2.15. Since each material system can present distinguished features and behavior in face of such defects, the specificity for each compound needs to be taken into consideration.

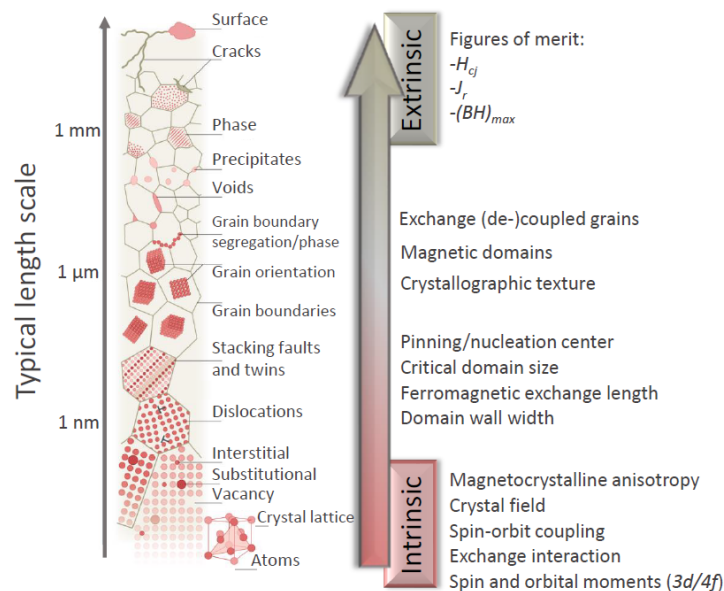


Figure 3.1: Microstructure length scales in correlation with intrinsic and extrinsic magnetic properties. Figure was modified from [196] and from [197].

Figure 3.2 shows the comparison between different intrinsic and the extrinsic properties reported for the two material systems studied in this dissertation, Mn-Al and REFe₁₁Ti compounds, in respect to the well established hard ferrites and Nd-Fe-B. From Figure 3.2a, one notices that Mn-Al and both REFe₁₁Ti compounds can be manufactured to have $(BH)_{max}$ in the range between hard ferrites (H-Ferrites) and Nd-Fe-B, i.e., potential gap magnets. Despite having the theoretical energy-product above the gap magnet region, the 1:12 compounds have constraints related to chemical composition/alloy design and processing routes. As mentioned previously, the nitrogen modification in Nd-based systems is necessary to obtain high magnetic anisotropy, however the temperature stability of the nitrogenated compound limits the processing window range to values below 823 K. However, within this temperature range it is unlikely to produce fully dense magnets, since the sintering temperature is expected to be around 1273 K, i.e., between 1/2 to 2/3 of the melting temperature. Alternatively, it is possible to manufacture Nd-based 1:12 bonded magnets, which would significantly dilute the volume of hard magnetic phase, implying that the maximum energy-product is expected to fall in the lower threshold of the gap magnet window. In the case of Sm-based compounds, it is possible to produce fully dense materials, as already reported by Zhang *et al.* for Sm₈Fe_{73.5}Ti₈V₈Ga_{0.5}Al₂ [130]. Nevertheless, the lack of perfect crystallographic texture and possible adjustments in composition by non-magnetic elements, to promote liquid phase sintering and to enhance coercivity, would inevitably reduce the total polarization of the alloy and $(BH)_{max}$, as demonstrated by Gabay and Hadjipanayis (cross symbol in Figure 3.2a) [97]. Based on this realistic scenario, Mn-Al and Nd-based 1:12 can possibly be produced with energy-product in the lower range of the gap magnet region, close to 100 kJ/m³, while Sm-based 1:12 have the potential to be between middle and the upper value of this range. If this assumption proves to be true, it would be possible to replace bonded and isotropic Nd-Fe-B magnets by these RE-lean and RE-free compounds.

Apart from the feasible $(BH)_{max}$ based solely on the crystallographic texture (maximum J_r), it is imperative to develop coercivity in these materials to ensure the condition of $H_{cj} \geq J_r$, that is an requirement in many applications [8]. Comparing the ratio between anisotropy field and coercivity values, Figure 3.2b, one can estimate how close the value is in respect to the Brown's paradox and how far the coercivity is from the ideal case given by the Stoner-Wohlfarth model. For optimized and commercially available ferrites and Nd-Fe-B, the ratio is around $0.2H_A$, in especial cases and processing methods, the values can exceed the usual paradox threshold, reaching $H_A \approx H_{cj}$ in utmost condition [8, 10, 14, 53]. In contrast, REFe₁₁Ti compounds shows ratio below 0.07 for the majority of processing techniques reported so far. Complimentary, when using processing methods that results in lower defect concentration, as mechanochemical synthesis in this case, the highest value reported reaches 0.12 [97]. To further emphasize the role of processing-microstructure, the ratio of Mn-Al is presented in two values for bulk samples, one being related to hot extruded magnets 0.07 (highest energy-product) and the other is for severely deformed sample, reaching 0.13 (result from Publication D) [42, 165, 190].

The observed disparity between H_A and H_{cj} highlights the necessity of studies to correlate intrinsic properties, microstructure and extrinsic properties to gain insight about each and specific material system. Having this knowledge is the first step to create strategies and adapt processing routes that can, through

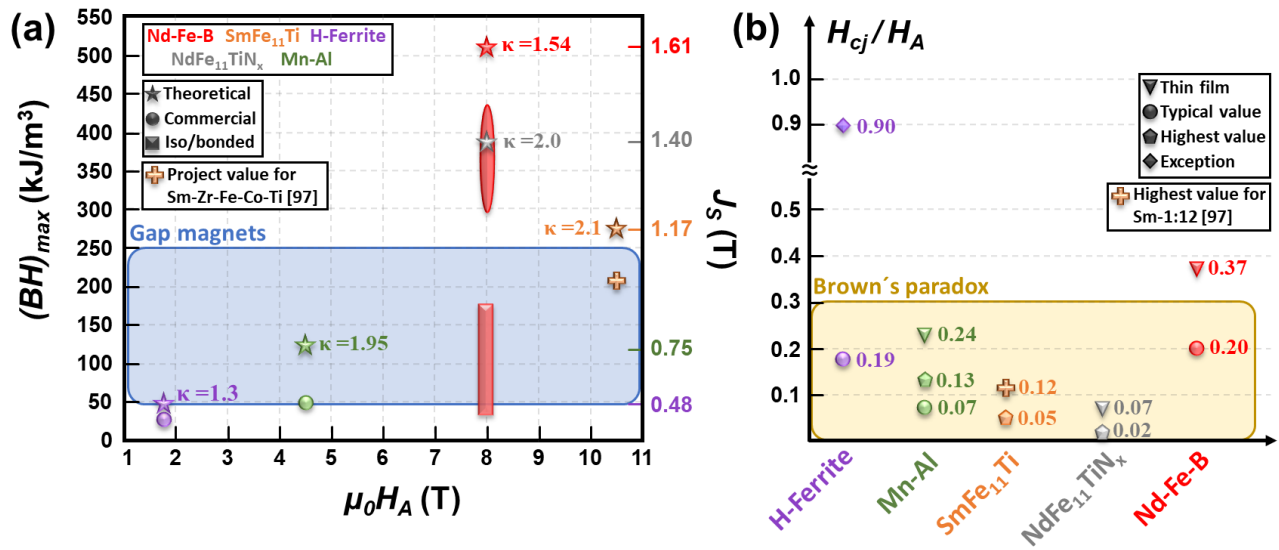


Figure 3.2: (a) Comparison of $(BH)_{max}$ values based on the theoretical (star symbols), commercially available (circle-anisotropic and rectangle-isotropic and/or bonded magnets) and one reference projected value for Sm-based 1:12 (cross symbol) compounds/magnets. The anisotropy field (H_A), saturation polarization (J_S) and magnetic hardness parameter (κ) are also given. The shaded blue area is a guide to the eye for the so called gap magnet energy-product region. (b) Ratio between coercivity (H_{cj}) and H_A of thin films samples, typical values for commercial magnets and the highest reported for Mn-Al and 1:12 material system - see text for further information. The shaded yellow area is a guide to the eye with the usual threshold given by the Brown's paradox. One exception value is also given for the hard-ferrite (H-Ferrite) that far exceeds the paradox threshold. The values were taken from multiple sources [8, 10, 14, 32, 53, 106, 107, 165].

microstructural engineering, better translate the intrinsic potential to extrinsic magnetic properties. In this light, the present research was carried out to identify the possible reasons for the such discrepancy, focusing on the correlation of phase stability, microstructure and magnetic properties. In the following, a brief summary and the main results of the four selected publications covered in this dissertation will be presented. The first three publications are related to the RE-lean ThMn₁₂-type material system and the fourth is about the RE-free Mn-Al material system. The full-text of the four publications will be provided at the end of the dissertation.

3.2 Publication A: Rapid solidification of $\text{Nd}_{1+x}\text{Fe}_{11}\text{Ti}$ compounds: Phase formation and magnetic properties

Authors: **Fernando Maccari**, Lukas Schäfer, Iliya A. Radulov, Léopold V. B. Diop, Semih Ener, Enrico Bruder, Konstantin P. Skokov and Oliver Gutfleisch

Journal: *Acta Materialia*, 180 (2019), p.15-23 - DOI: 10.1016/j.actamat.2019.08.057

Aiming to understand the formation and to obtain high purity $\text{NdFe}_{11}\text{Ti}$ samples, the effects of Nd content and annealing procedure (temperature and time) of rapidly solidified $\text{Nd}_{1+x}\text{Fe}_{11}\text{Ti}$ ($x=0.05, 0.10, 0.15$ and 0.20) alloys were investigated. The choice for rapid solidification using suction casting is the advantage to obtain bulk samples with fine microstructure, as shown in Figure 3.3a. The refined microstructure can be beneficial either to obtain high temperature phases already in the as-casted state or to reduce the annealing time to obtain the equilibrium phases, as demonstrated by our previous study in other material system [198]. Several samples of these four compositions were produced and annealed under different temperatures, varying from 700 up to 1200°C. The temperature interval was selected based on the values listed in literature and on the limited information regarding the corresponding ternary phase diagram. [93, 110, 147, 199].

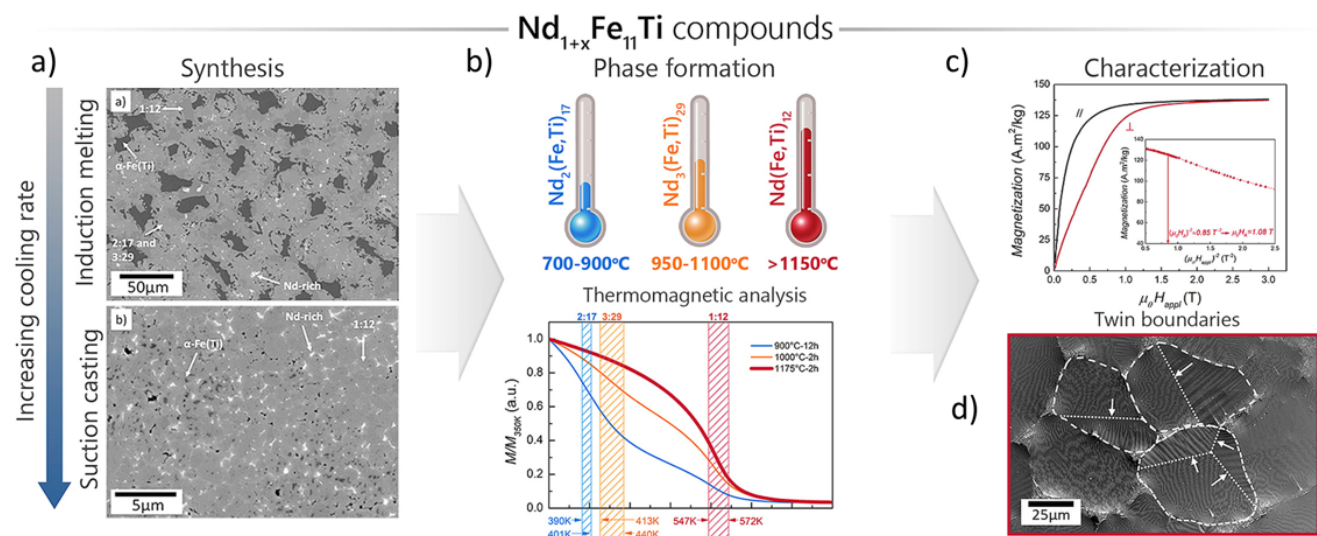


Figure 3.3: Graphical abstract showing a) comparison in the as-cast state of samples subjected to suction casting and induction melted; b) influence of annealing temperature on the thermomagnetic response; c) Kerr micrograph of $\text{Nd}_{1.15}\text{Fe}_{11}\text{Ti}$ sample annealed at 1175 °C highlighting the twin boundaries in one grain and d) Isothermal magnetization measurement of textured powder and the corresponding calculated anisotropy field H_A .

The phases were identified using a combined approach of scanning electron microscopy (SEM), coupled with energy-dispersive x-ray spectroscopy (EDX), and thermomagnetic analysis (temperature dependent

magnetization). The standard method of phase identification using x-ray diffraction (XRD) was also employed, however because of the similarities between the structures and corresponding diffraction patterns of $\text{NdFe}_{11}\text{Ti}$ (1:12-tetragonal), $\text{Nd}_2(\text{Fe,Ti})_{17}$ (2:17-rhombohedral) and $\text{Nd}_3(\text{Fe,Ti})_{29}$ (3:29-monoclinic), the accuracy to identify the present phases in the samples becomes challenging. This is even more critical if these phases coexists, as stressed and explained in the manuscript. Using the EDX and SEM-BSE (backscattered electron contrast) it was possible to detect the presence α -Fe and Fe_2Ti Laves phase in comparison to the previously mentioned ternary phases. For the 1:12, 2:17 and 3:29, it was identified that the Nd and Ti content of each phase lies in a different range, according to the average values shown exemplified in Table 3.1. The compositional range is in agreement with those reported by Margarian *et al.* [199]. Complimentary thermomagnetic measurements were performed to ensure and validate the results obtained from SEM-BSE-EDX analysis, since the different T_C values can be used as a fingerprint of the corresponding ternary phases, as represented in Figure 3.3b.

Table 3.1: Chemical composition obtained by EDS analysis for the ternary phases in $\text{Nd}_{1.15}\text{Fe}_{11}\text{Ti}$. Ten points were measured for each phase and for calculation of standard deviation.

Phase	Composition (at.%)		
	Nd	Fe	Ti
$\text{Nd}(\text{Fe,Ti})_{12}$	8.1 ± 0.1	balance	7.7 ± 0.1
$\text{Nd}_2(\text{Fe,Ti})_{17}$	10.9 ± 0.1	balance	3.7 ± 0.1
$\text{Nd}_3(\text{Fe,Ti})_{29}$	9.8 ± 0.1	balance	5.0 ± 0.2

Through the combined characterization methods, the phase formation and phase stability condition were determined. In short, only for the samples $\text{Nd}_{1.15}\text{Fe}_{11}\text{Ti}$ and $\text{Nd}_{1.20}\text{Fe}_{11}\text{Ti}$ it was possible to obtain pure 1:12 phase after annealing within the temperature range 1150-1200°C for 2 hours and quenched in water. Interestingly, annealing at lower temperatures can lead to mixed-phase state samples either with 2:17 (from 700-900°C) or 3:29 (from 950-1100°C). The results demonstrate the necessity to have hyperstoichiometric Nd composition to avoid secondary phases, especially the soft magnetic α -Fe. The 1:12 phase is a high temperature phase which is stable as single phase state in a small temperature window. Based on the obtained results, the composition $\text{Nd}_{1.15}\text{Fe}_{11}\text{Ti}$ was selected to be the focus of the study, including a complete description of the phases according to the annealing temperature and, for further characterization, the sample annealed at 1175°C, single 1:12 phase.

The room temperature intrinsic properties of saturation magnetization M_S and anisotropy field H_A were estimated, based on isothermal magnetization measurements of textured powder along parallel and perpendicular direction in relation to the texture axis, as displayed in Figure 3.3c. The results revealed M_S of $137 \text{ Am}^2\text{kg}^{-1}$ ($J_S \approx 1.30 \text{ T}$) and H_A of 1.08 T. As expected, the anisotropy field is rather low because it is limited to the Fe sublattice contribution, since the Stevens coefficient of Nd is negative ($\alpha_J < 0$). This means that for the case of $\text{NdFe}_{11}\text{Ti}$ compound, the Nd does not contribute to magnetic anisotropy. As a side note, the anisotropy field can be further improved by changing the crystal field sign, upon nitrogenation, leading to a change in the Nd sublattice that would contribute to magnetic anisotropy - this topic was not covered in the present publication.

Moreover, the magnetic domain structure of the NdFe₁₁Ti compound was investigated by means of Kerr microscopy, revealing typical domains of uniaxial magnetocrystalline anisotropy materials, as exemplified in the Figure 3.3d. Besides the domain structure, it was possible to notice the presence of twin boundaries, showing a misorientation of $57^\circ \pm 1^\circ$ (measured by electron backscatter diffraction - EBSD). This type of planar defect has been previously reported by Skokov *et al.* for Gd-Fe-Ti 1:12 system, but no correlation with magnetic behavior was drawn [200].

To investigate the contribution of this defect on the magnetization/demagnetization behavior, Kerr analysis using in plane magnetic field was performed. A region with a grain with in-plane magnetization (low demagnetization factor) was analyzed, where the magnetization makes a significant angle with the surface (high demagnetization factor). The sequence of Kerr micrographs (Figure 3.4a to 3.4d shows, in detail, a grain that is divided in two parts by a twin boundary. For this reason, part of the grain presents dark contrast and the other part shows bright contrast in saturated state when a magnetic field of 380 mT is applied (Figure 3.4a). Decreasing the applied field to 150 mT (Figure 3.4b), it is possible to observe the nucleation of reversal domains starts at the twin boundary (highlighted by the arrow) growing towards the grain boundary with further decreasing of the applied field. As shown in the sequence of micrographs, the nucleation and growth of reversal domains take place without the presence of pinning centers. Another interesting result from the Kerr analysis is when the magnetic field is decrease to 50 mT (Figure 3.3c), the reversal domains from the twinned grain directly affect the adjacent grain, shown by the dashed arrow, indicating a magnetic coupling between neighboring grains.

For the first time, correlation established between the microstructure and the magnetic domain analysis revealed that twins are acting as nucleation centers for reversal magnetic domains in NdFe₁₁Ti system. These findings can be one of the reasons why only low coercivity values were achieved so far (maximum reported was 0.23 T), even in the nitrogenated compound, which has a high H_A of 8 T. In addition to the twins, magnetic domain analysis revealed magnetic coupling between the grains, which is also has to be reduced or eliminated for coercivity development. In this way would be possible to eliminate microstructural features that decreases the nucleation field, leading to higher coercivity values and enabling the potential use of magnets based on NdFe₁₁Ti.

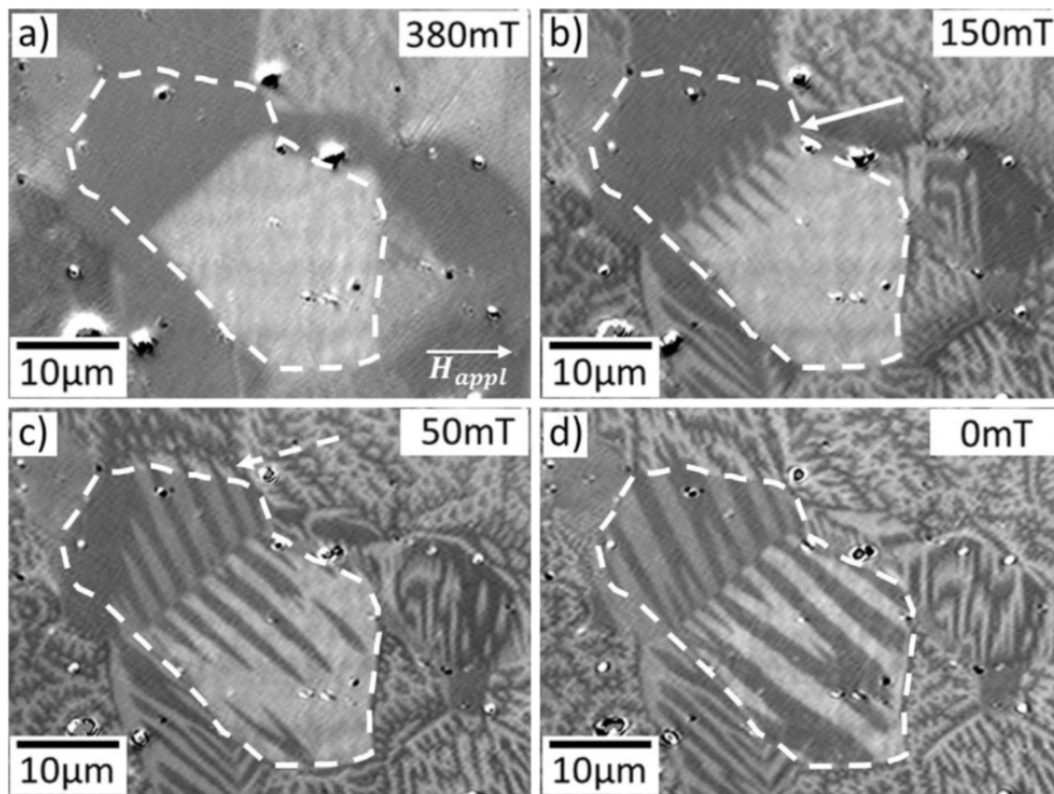


Figure 3.4: Kerr analysis from 380 mT (a) applied magnetic field (grains with twin boundary saturated) down to 0 mT (d-demagnetized state). The arrow showing the nucleation at the twin boundary with applied field of 150 mT (b) and the coupling between adjacent grains at 50 mT (c-dashed arrow).

3.3 Publication B: Correlating changes of the unit cell parameters and microstructure with magnetic properties in the $\text{CeFe}_{11}\text{Ti}$ compound

Authors: **Fernando Maccari**, Semih Ener, David Koch, Imants Dirba, Konstantin P. Skokov, Enrico Bruder, Lukas Schäfer and Oliver Gutfleisch

Journal: *Journal of Alloys and Compounds*, 867 (2021) 158805 - DOI: 10.1016/j.jallcom.2021.158805

The study of the Ce-Fe-Ti system followed similar methodology than the one of Nd-Fe-Ti (Publication A), including the synthesis, annealing procedure and most of the characterization methods. However, only the compositions with higher rare earth were evaluated ($\text{Ce}_{1.15}\text{Fe}_{11}\text{Ti}$ and $\text{Ce}_{1.20}\text{Fe}_{11}\text{Ti}$), since it has shown better results in terms of phase purity in the previous work on Nd-Fe-Ti system - Publication A.

Based on the annealing procedure and characterization, the highest amount of 1:12 phase was obtained at the temperature interval 850-950°C for both compositions. For the optimized condition, a mixture

between $\text{CeFe}_{11}\text{Ti}$ and CeFe_2 Laves phase was obtained, with phase fraction of around 93wt% and 7wt%, respectively. Higher annealing temperatures led to the decomposition of the desired 1:12 phase and formation of $\alpha\text{-Fe}$, while at lower annealing temperatures Fe_2Ti was observed. The phase fractions and microstructure are for all annealing conditions are given in the main manuscript and in the supplementary material - all are provided in the last chapter of this dissertation.

A closer look on the structural changes of the $\text{CeFe}_{11}\text{Ti}$ compound, in the optimum annealed sample, revealed an Invar-type anomaly, as observed by the unit cell parameter variation close to the T_C , around 485 K. The reason can be attributed to the large magnetostrictive deformation of the magnetically ordered lattice, originating from the magnetic anisotropy and magnetic exchange interactions of the rare-earth elements and $3d$ transition metals. The values of lattice variation in function of temperature obtained in this study had a good agreement with the theoretical models of magnetostriction.

Further characterization of the optimized sample using Kerr microscopy showed typical domain structure of uniaxial magnetocrystalline materials and the presence of twin boundaries (similar to $\text{NdFe}_{11}\text{Ti}$), as confirmed by EBSD as exemplified in Figure 3.5. The misorientation angle was found to be $58^\circ \pm 2^\circ$, indicating that the consistency of this specific angle is a strong indication that a lower energy of the twin boundaries is achieved in this configuration for Nd- and Ce-based 1:12 systems [59]. It worth noting that comparatively to $\text{NdFe}_{11}\text{Ti}$ samples from Publication A, the smaller grain size of the Ce-based samples lead to the reduction in twin boundary density. This might be a strategy to develop a microstructure composed of fine grains to diminish the amount of twin boundaries.

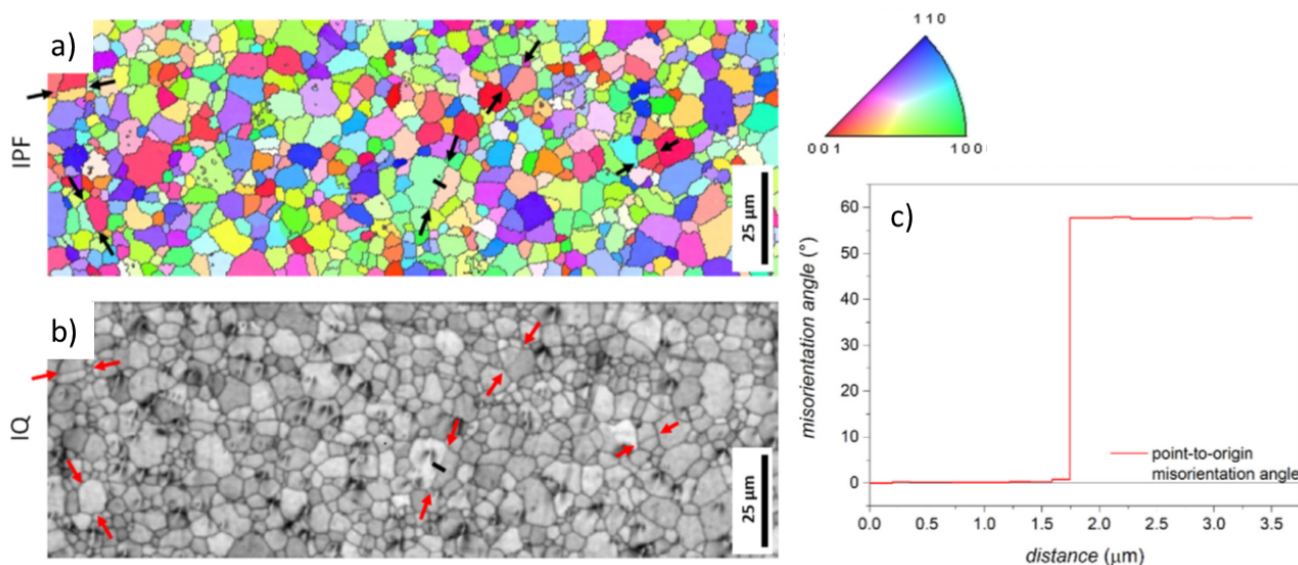


Figure 3.5: Microstructural analysis of the $\text{Ce}_{1.20}\text{Fe}_{11}\text{Ti}$ sample annealed at 850°C samples with a) inverse pole figure (IPF) and b) the image quality (IQ) contrast image. Observed twins are highlighted with arrows. c) Point-to-origin misorientation angle measurement through the twin boundary, $58^\circ \pm 2^\circ$, where the measurement line is indicated in IQ and IPF images with black line.

Magnetic characterization, focusing on the anisotropy field determination, was performed and yield to a value of 2.57 T for CeFe₁₁Ti at room temperature, similar to results reported elsewhere [11, 143, 147]. To probe the effect of unit cell compression and expansion on the magnetic properties, isothermal magnetization was carried out under hydrostatic pressure and after hydrogenation for different temperatures. A slight reduction is observed for the measured anisotropy field under 0.45 GPa hydrostatic pressure in the temperature interval of 10–300 K, which is consistent with the small increase detected for the hydrogenated compound. The anisotropy field values are given in Figure 3.6. As a comparison, literature values on the nitrogenated compound also show a reduction in the H_A [146].

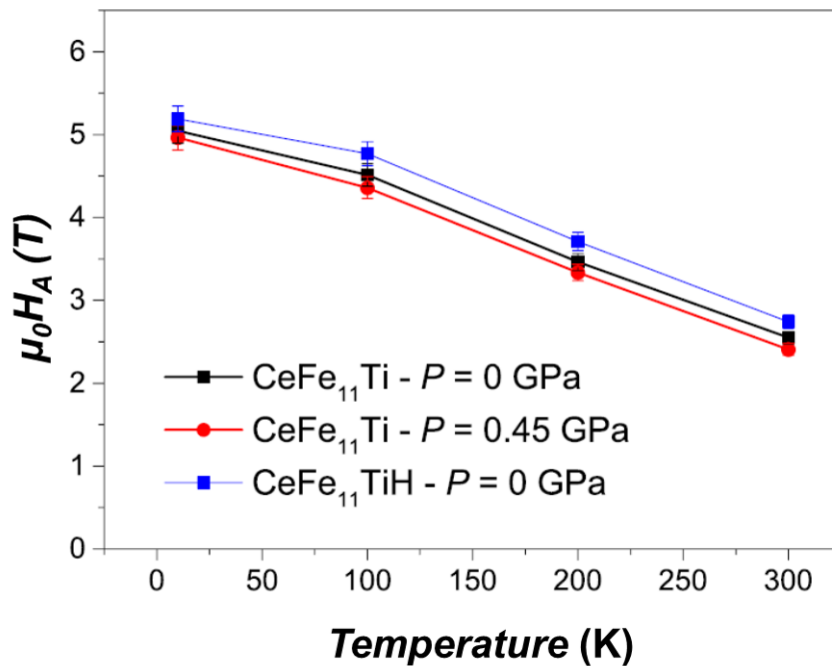


Figure 3.6: The anisotropy field values for CeFe₁₁Ti compound under 0 GPa and 0.45 GPa external hydrostatic pressure together with hydrogenated CeFe₁₁Ti sample.

Different than observed for Nd-based 1:12, a change in the crystal field parameter does not seem to affect the Ce sublattice anisotropy. As confirmed by other works, it is most probable that Ce is not contributing significantly to the overall magnetic anisotropy of the 1:12 phase because of its mixed valence state [143, 201]. Since the valence state depends on the steric volume, it was expected to be modified by changing the unit cell volume by chemical pressure (interstitial hydrogen-unit cell expansion) and/or by applying hydrostatic mechanical pressure (unit cell compression). However, the methods used in this study did not promote significant change on the valence state. Nevertheless, the study has shown the limitations of CeFe₁₁Ti compound in terms of intrinsic magnetic properties, determination of the 1:12 phase stability region and the correlation with microstructure, including the presence of twin boundaries. Additional investigations are still necessary to improve the intrinsic potential of Ce-based 1:12, especially the low anisotropy field, and also to overcome the microstructural features, that might limit the extrinsic properties.

Both conditions are necessary to make CeFe₁₁Ti appealing as permanent magnet candidate.

Other works which were developed in cooperation with other researchers and research institutes, that are directly related to the one presented here, can be found in the publications from Halil *et al.* [139] and Galler *et al.* [146], touching aspects regarding phase stability and the Ce magnetism by experimental and DFT methods (density functional theory) - both are co-authored by F. Maccari. In addition, the effect of a fourth element in Ce-Fe-Ti alloys on the 1:12 phase stability was also studied experimentally and theoretically within the framework of the dissertation of Halil İbrahim Sözen, presented the Ruhr University of Bochum, that can be found in [138].

3.4 Publication C: Twins – A weak link in the magnetic hardening of ThMn₁₂-type permanent magnets

Authors: Semih Ener, Konstantin P. Skokov, Dhanalakshmi Palanisamy, Thibaut Devillers, Johann Fischbacher, Gabriel Gomez Eslava, **Fernando Maccari**, Lukas Schäfer, Léopold V. B. Diop, Iliya A. Radulov, Baptist Gault, Gino Hrkac, Nora M. Dempsey, Thomas Schrefl, Dierk Raabe and Oliver Gutfleisch

Journal: *Acta Materialia*, 214 (2021) 116968 - DOI: 10.1016/j.actamat.2021.116968

The present publication follows the main microstructural feature observed for the Nd- and Ce-based 1:12, being specifically focused on the effect of twin boundaries as a nucleation center for reversal magnetic domains. Differently from the other two previously mentioned material systems, this work is based on SmFe₁₁Ti that shows a high anisotropy field $H_A \approx 10.5$ T, as the Sm has positive Stevens coefficient ($\alpha_J > 0$) and contributes to the magnetic anisotropy. As a consequence of the high H_A , it would be reasonable to expect coercivity values as high as 3.5 T, according to the upper limit of Brown's paradox. However, the values are often below 0.6 T for the ternary Sm-Fe-Ti, as shown previously in Figure 2.16 and Figure 3.2.

To understand this notorious discrepancy, investigations were performed in different samples, ranging from thin films, single crystals and polycrystalline samples. In all these length scales, twin boundaries were observed. Comparatively, Nd-Fe-B single crystal and polycrystalline samples were also prepared and characterized, however no twin boundaries were observed for the Nd-Fe-B samples. The investigation of the twin boundary has shown again the same misorientation angle of 57°, as similar to what has been obtained for NdFe₁₁Ti and CeFe₁₁Ti, indicating that the twins are intrinsic to the ThMn₁₂-type material systems.

High resolution characterization, using STEM (scanning TEM) and atom probe tomography (APT), of the twin boundary was done in order to observe the atomic arrangement and the coherency between the twin variants. The HR-STEM characterization using HAADF (high-angle annular dark field), which provides signal intensity proportional to atomic number (heavy atoms are brighter), is shown in Figure 3.7a-c. The atomic resolution images revealed that the twin boundary is in zig-zag configuration, as marked with black dashed lines in Figure 3.7b. Figures 3.7c and 3.7d show the (011) twinning plane and a schematic representation, respectively.

Additionally, APT analysis of the same area shown in Figure 3.7 was performed, as can be observed in Figure 3.8. The bright-field electron micrograph of the whole specimen is shown in Figure 3.8a and in 3.8b the corresponding APT reconstruction with the distribution of Fe, Ti, Sm atoms and a Sm 9 at.% iso-composition surface, highlighting the location of the twin boundary. Figure 3.8c shows the Sm compositional map evidencing the local enrichment of Sm (2 at.%) and Fe (0.7 at.%) and a depletion of Ti (2.7 at.%) at the twin boundary. This local chemical variation leads to the approximate stoichiometry of Sm_{9.8}Fe₈₅Ti_{5.2}. The observed stoichiometry falls exactly in the range of the 3:29 phase observed for Nd-based system (Publication A) as previously reported in Table 3.1.

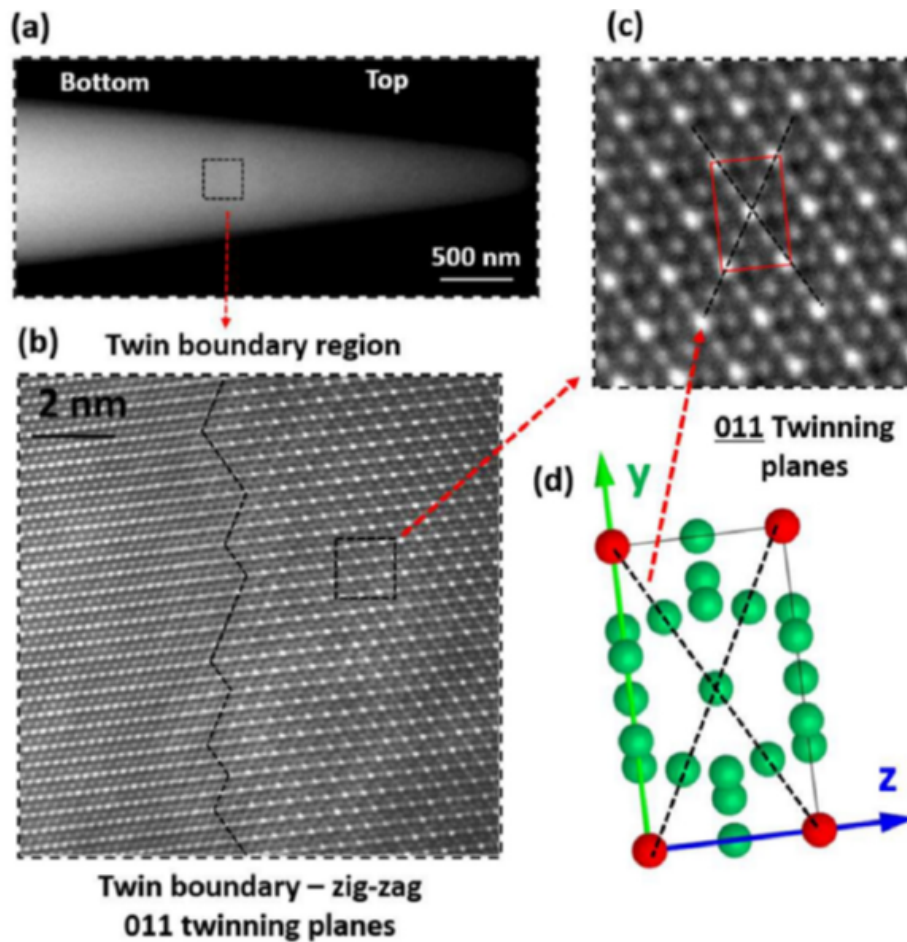


Figure 3.7: (a) Low magnification HAADF image of $\text{SmFe}_{11}\text{Ti}$ at the twin boundary region; (b) High-resolution HAADF image of the interface region of the twin along the $[100]$ zone axis; (c) High magnification of the twin boundary region and (d) schematic representation of the (011) twinning planes with Sm atoms in green and Fe/Ti in red.

The chemical segregation leading to the $\text{Sm}_3(\text{Fe,Ti})_{29}$ phase in the twin boundary region is an important information to understand why this defect is a nucleation center for reversal domains, since it has different intrinsic properties than the $\text{SmFe}_{11}\text{Ti}$ matrix. The anisotropy constant K_1 of the 3:29 phase has the value approximately 1/3 of the corresponding 1:12 phase, as reported by Wirth *et al.* [106]. The difference in anisotropy constant and the existence of twin boundaries were taken into consideration for micromagnetic simulation analysis. Using this method it was possible to compare the coercivity values between the benchmark Nd-Fe-B and the Sm-Fe-Ti systems by applying the different boundary conditions to the model, mimicking the experimentally observed microstructural features. Different conditions were evaluated, but the main outcome is that the formation of twins reduces the estimated coercivity values to 38% of the expected coercivity without twins. The result obtained by micromagnetic simulations are in agreement to the experimental observation. The results can be further extended to other 1:12 systems with different

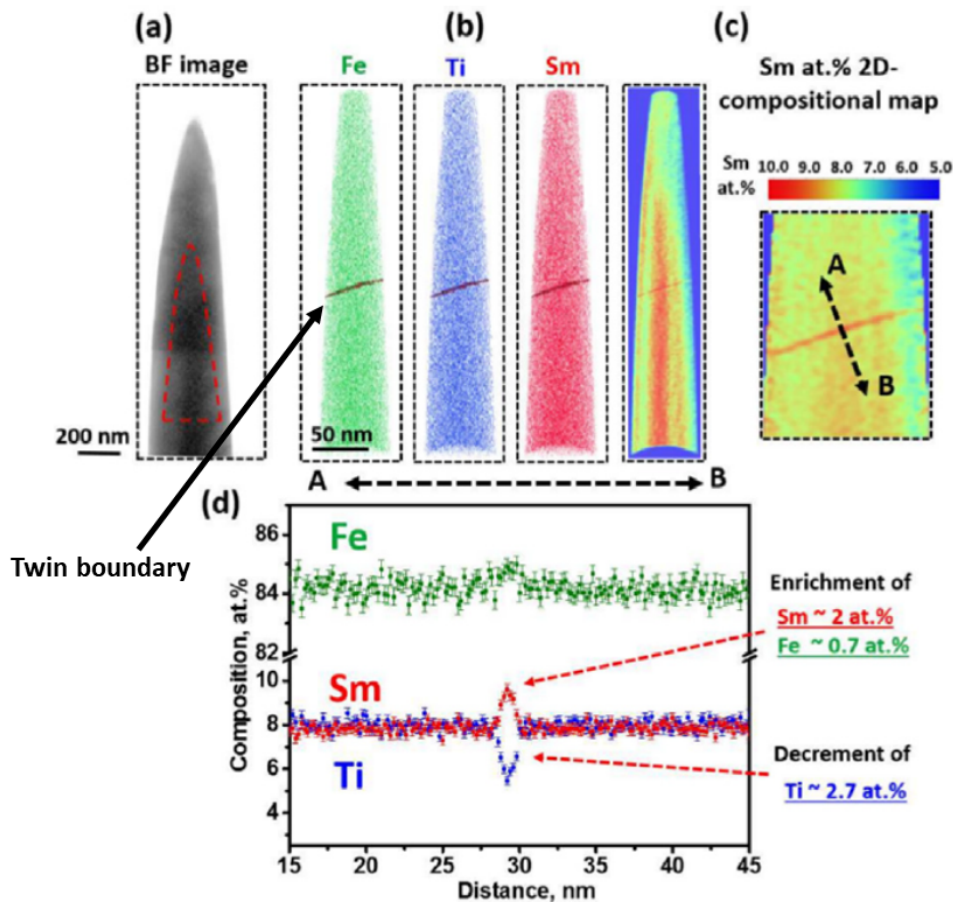


Figure 3.8: (a) Bright-field image of one of the investigated APT specimens. (b) Atom probe tomography reconstruction of the elemental distribution of Sm, Fe and Ti. (c) 2D compositional map of Sm and (d) chemical composition distribution at the twin boundary region.

RE and the stabilizing element, since twin boundaries were also observed for: $\text{NdFe}_{10.5}\text{Mo}_{1.5}$, $\text{NdFe}_{10}\text{V}_2$, $(\text{Nd}_{0.75}\text{Pr}_{0.25})\text{Fe}_{10.5}\text{Mo}_{1.5}$, $(\text{Nd}_{0.5}\text{Y}_{0.5})\text{Fe}_{10}\text{Ti}$, as highlighted in Figure 3.9 - these complimentary results are not part of any publication.

The existence of twin boundaries has been typically observed in alloys with low stacking fault energy and is commonly related to deformation caused by internal or external stresses [202]. To understand the reason behind the formation, *ab initio* molecular dynamics calculations were conducted. Results indicated that the twin formation energies are low and the competition between the formation energies of a twin boundary and a grain boundary are strongly dependent on the grain size and geometry. The calculations predict that the twin formation is more energetically favorable for grains with size above $1 \mu\text{m}$, which would explain the higher coercivity values obtained in nanocrystalline Sm-based 1:12.

Given the major impact of twin boundaries, it is clear that one needs to find a way to eliminate the formation of this defect. As the molecular dynamics calculations have shown, limiting the grain size to

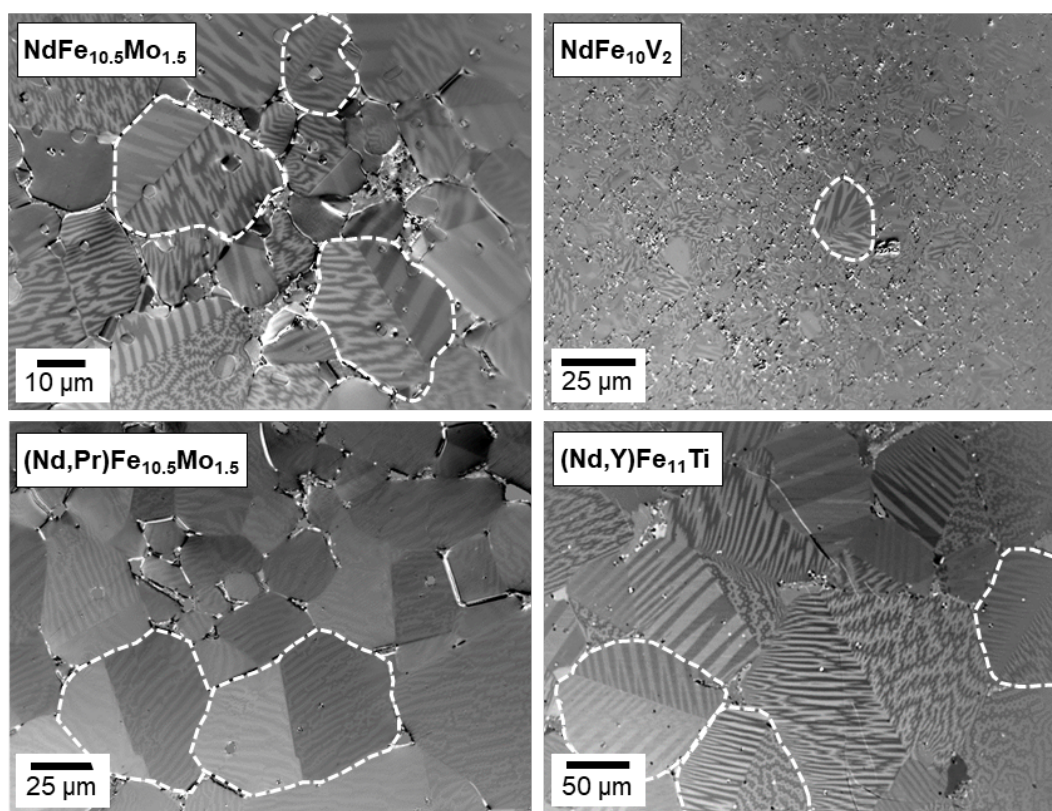


Figure 3.9: Kerr analysis of different 1:12 compounds with different RE and stabilizing elements: $\text{NdFe}_{10.5}\text{Mo}_{1.5}$, $\text{NdFe}_{10}\text{V}_2$, $(\text{Nd}_{0.75}\text{Pr}_{0.25})\text{Fe}_{10.5}\text{Mo}_{1.5}$, $(\text{Nd}_{0.5}\text{Y}_{0.5})\text{Fe}_{10}\text{Ti}$. Grains containing twin boundaries are marked with white dashed lines.

value in the submicrometer range might be one alternative, as also indirectly shown from the coercivity values found in the literature and from the qualitative observations presented in Publication B. However, this might also bring challenges to make anisotropic magnets, since obtaining monocrystalline particles and avoid excessive grain growth would be required.

Complimentary to this publication, additional work on $\text{SmFe}_{11}\text{Ti}$ was reported by Palanisamy *et al.* (co-authored by F. Maccari), focusing on the grain boundary phases and correlation with coercivity in rapid solidified samples [137]. Aspects of chemical segregation and magnetic coupling between adjacent grains, also observed for $\text{NdFe}_{11}\text{Ti}$ (Publication A), are discussed and addressed.

The combination of all these works show the importance to understand the defects, especially twins, on the 1:12 phase, regardless the RE or the stabilizing element. Moreover, other aspects regarding phase stability, grain boundary phases and magnetic coupling of grains also have to be considered to optimize the microstructure for enhancing coercivity.

3.5 Publication D: Microstructure and magnetic properties of Mn-Al-C permanent magnets produced by various techniques

Authors: Vladimir V. Popov. Jr., **Fernando Maccari**, Iliya A. Radulov, Aleksey Kovalevsky, Alexander Katz-Demyanetz and Menahem Bamberger - Both V.V.P. and F.M. equally contributed to this work.

Journal: *Manufacturing Review*, 8, 10 (2021) - DOI: 10.1051/mfreview/2021008

This work focused on the effect of different processing routes on the microstructure and extrinsic magnetic properties of RE-free $Mn_{52}Al_{44}C_2$ compound. Aiming to understand these effects, processing routes involving heat treatment and plastic deformation were performed while keeping the chemical composition fixed, as summarized in the schematic shown in Figure 3.10.

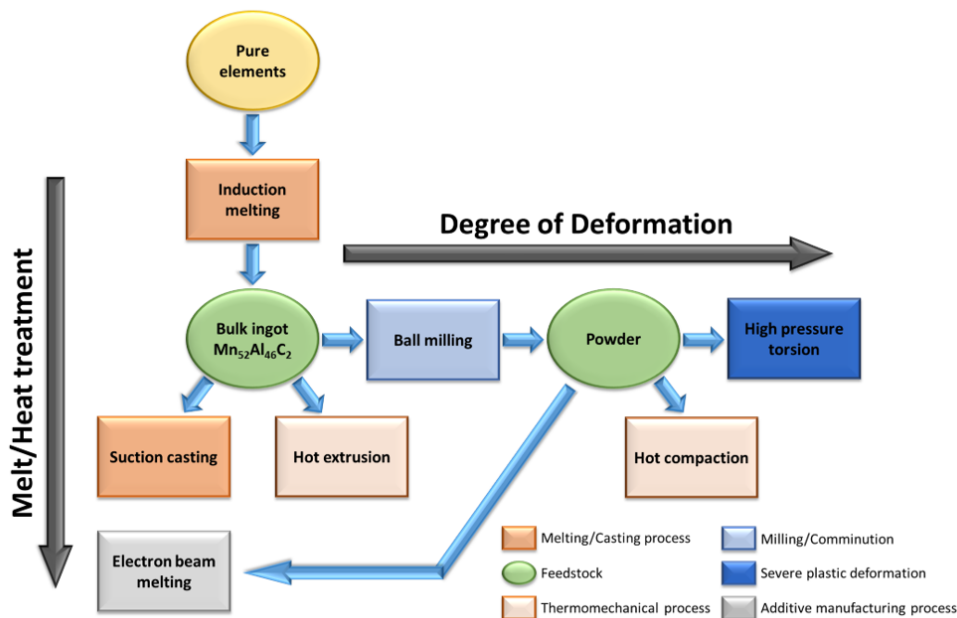


Figure 3.10: Overview of the methods used to prepare $Mn_{52}Al_{44}C_2$ samples and the relation with degree of deformation and melting/heat treatment.

After induction melting the pure elements and casting into graphite crucible, the cooling rate was fast enough to avoid the equilibrium phases, β -Mn and γ_2 , but not too fast to obtain the high temperature ϵ phase, resulting in an isotropic microstructure consisted of only the desired ferromagnetic metastable τ -phase. The coarse τ -phase microstructure exhibits a high number of twin boundaries, as revealed by the Kerr microscopy analysis exemplified in Figure 3.11a. The combination of pure ferromagnetic phase and the coarse microstructure with twin boundaries led to the high magnetization value at 3 T applied field (M_{3T}), around $100 \text{ Am}^2/\text{kg}$, and the low coercivity value, below 0.03 T, as shown in Figure 3.11b. It

worth mentioning that the magnetization value scales with the fraction of the ferromagnetic phase and is affected by internal stresses that can be induced during processing. The internal stresses cause a lattice strain and changes in the interatomic spacing, which might lead to an approximation of Mn atoms and, consequently, antiferromagnetic coupling. As for coercivity, as explained in the Section 2.6, it is mainly determined by defect type and density in combination with grain size. This justifies the value obtained in the as cast state and similar to the ones reported by Bittner *et al.*, since it has a coarse microstructure with defects that nucleate reversal domains, like twin boundaries. [176]

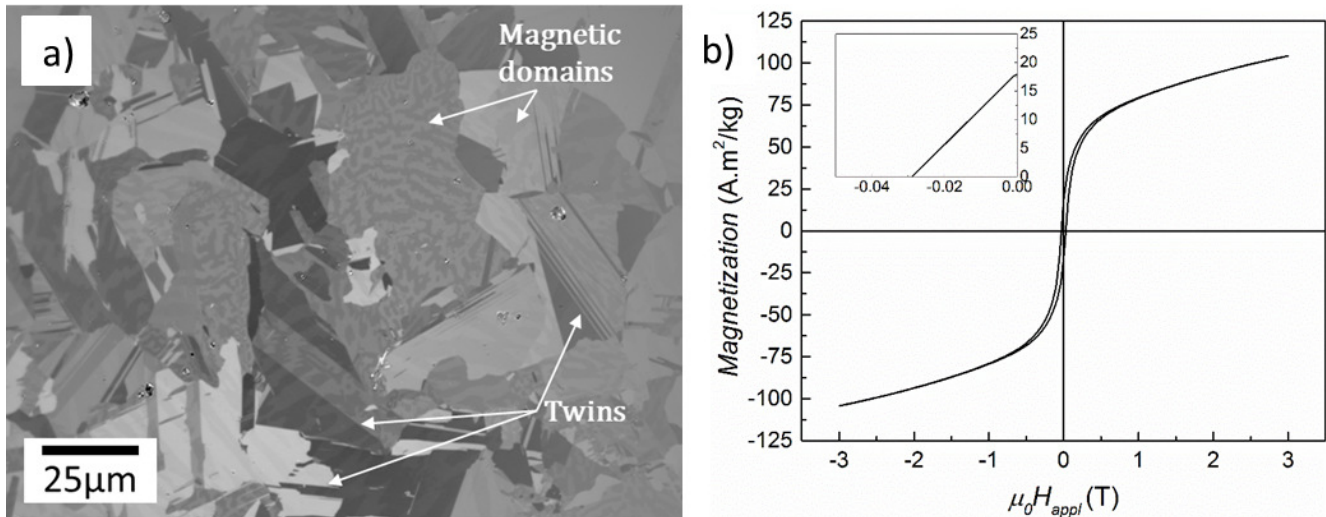


Figure 3.11: a) Kerr micrograph and b) magnetization measurement of the induction melted-cast $\text{Mn}_{52}\text{Al}_{44}\text{C}_2$ sample. The microstructure shows pure τ -phase, highlighting twin boundaries and the magnetic domain structure.

A microstructural refinement of the τ -phase was attempted by using two other melting methods with higher cooling rate: suction casting and electron beam melting (EBM). However, the microstructure was composed of different phases, being necessary a post annealing treatment to increase the τ -phase fraction, consisted of homogenization at high temperatures, 1100°C , followed by annealing at moderate temperature, $500\text{-}550^\circ\text{C}$. By using these methods, a slight enhancement on the coercivity value has been obtained, reaching values of 0.06 T and 0.04 T for EBM and suction casted samples, respectively. Despite having double the coercivity when compared to the as casted state, the obtained values are far below the anisotropy field ($H_A \approx 4.5\text{ T}$) and the expected one when considering the upper limit of the Brown's paradox, that would be around 1 T . However, as discussed previously and exemplified in Figure 2.18, aside from microstructural refinement, processing routes that induce plastic deformation tend to enhance the coercivity. Based on this, a combination of ball milling followed by hot pressing was evaluated using the bulk sample produced through induction melting as precursor. As expected, the coercivity has improved from a value below 0.03 T to 0.12 T after ball milling and up to 0.21 T after hot pressing. The microstructure has shown a significant grain refinement after hot compaction when compared to the as cast precursor.

Moreover, the combination of deformation (milling and hot compaction) and the exposure to moderate temperatures during the pressing step (450°C for 20 minutes), led to the decomposition of the metastable ferromagnetic phase. The decrease in the τ -phase fraction and appearance of the non-magnetic γ_2 -phase, along with the possible strain in the ferromagnetic phase, contributed to the decrease of M_{3T} value from 100 Am²/kg, in the precursor, to 50 Am²/kg after hot pressing. These results show that following this processing route, enhancement of coercivity is occurring in detriment of phase purity and, consequently, magnetization.

With the aim to increase the deformation and possibly prevent the phase decomposition, a severe plastic deformation method using high pressure torsion (HPT) was used. For this, powder size below 80 μm was used in between two anvils under applied pressure of 4 GPa to create a disc shaped sample for further HPT experiment. Subsequently, the sample was subjected to 50 revolutions using 1 RPM to induce the plastic deformation. The process was performed at room temperature and the tools were kept below 50°C during the entire process. The strain/deformation generated within the sample is proportional to the radius, meaning that the edges of the disc is deformed than the center, leading to a possible inhomogeneous microstructure, as reported in the literature [203]. In the case of heterogeneous microstructure, a gradient of magnetic properties throughout the edge of disc sample is expected. For this reason, three regions of the sample were evaluated: center (R_0), half radius ($R_{0.5}$) and on the edge (R_1); corresponding to the regions where it is expected to be subjected to lower, medium and higher deformation, respectively.

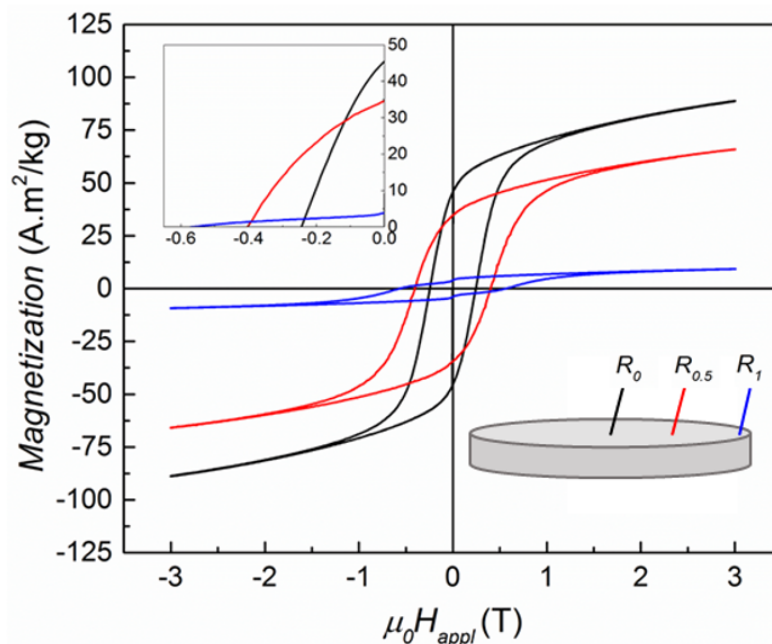


Figure 3.12: Isothermal magnetization curves of $\text{Mn}_{52}\text{Al}_{44}\text{C}_2$ obtained by HPT at different regions of the sample, as indicated by the schematic.

The hysteresis loops presented in Figure 3.12 confirm the gradient of magnetic properties, showing an

increase of coercivity while a decrease in magnetization towards the edge of the sample. The change in the values are pronounced, in which the coercivity varies from 0.25 T at the center up to 0.58 T at the edge, while the M_{3T} value decreases from 90 Am²/kg down to 10 Am²/kg at the center and edge, respectively. To understand the reason for such differences, microstructural characterization was performed using SEM, in which was revealed the changes in grain and particle morphology and the appearance of secondary phase in the very edge of the sample, caused by the decomposition of the metastable τ -phase. To gain more information at smaller length scale, TEM was also used to draw a comparison between the sample in the as-cast state, powder precursor and after HPT. It was observed a grain refinement allied with the substantial increase of dislocations, as expected from upon plastic deformation. The combination of these two characteristics led to the substantial increase in coercivity, in agreement with results reported in the literature and is among the highest reported so far for bulk samples [172, 176, 181]. On the other hand, the strain and the partial decomposition of the ferromagnetic phase are, more likely, the cause of the low magnetization after HPT. By optimizing the deformation during HPT or introducing an additional post annealing step to partially release internal stresses, a compromise between coercivity and magnetization might be established. However, as a main limitation of the HPT technique, the absence of induced texture still remains a challenge for increasing remanence and, consequently, the energy-product $(BH)_{max}$.

In this work, the comparison of different processing techniques has shown that the phase purity of the samples is important, but not the only factor that determines the magnetic properties of Mn-Al-C compound. Beside the amount of metastable τ -phase, the density and the type of microstructural defects can significantly affect the extrinsic magnet properties of this material system. In summary, it was observed that processing techniques that induce plastic deformation are recommended to increase coercivity, but can degrade magnetization, while techniques involving melting/casting and annealing result in higher magnetization but lower coercivity. Nevertheless, the absence of texture in the obtained samples (isotropic samples) is also an important point that has to be overcome to maximize the remanence and the overall magnetic performance of Mn-Al based magnets.

The results and discussion carried out in the framework of this publication have contributed to the understanding of the complex relationship between processing, microstructure and magnetic properties of Mn-Al-C. By keeping the composition fixed, a direct comparison could be drawn between the processing techniques in relation with phase stability and decomposition of the ferromagnetic metastable τ -phase, that also plays a role in the extrinsic magnetic properties.

4 Conclusions and Outlook

In the last decades, magnetic materials became an important part of the everyday life. Most of us are using soft and hard magnetic materials on daily basis without recognizing their existence. Among the magnetic materials, hard magnetic ones are having a great importance as they significantly impact commercial goods leading to a miniaturization of devices like headphones, portable equipment and others. In addition, with the recent developments in the hard magnetic materials and permanent magnets, new technologies took part of our lives as electro-mobility, power generation, etc. The combination of this scenario highlights the observed increase in the high-performance magnets demand that will grow in the following years. However, even though these key components are considered the main solution of such developments, they are also in the center of concerns and uncertainty. The rare earth elements used to obtain the high magnetic properties are very sensitive to market and price fluctuations, as shown by RE crisis in 2011. Additionally, the use of RE elements face risks regarding supply because of geopolitical or sustainable development issues. In this context, finding suitable compounds that show promising magnetic properties, while overcoming these issues, is of a great importance. Motivated by this necessity, the research done in the context of this dissertation has focused on two different material systems that are considered exponent candidates for new permanent magnet materials: the ThMn_{12} -type and MnAl-based material systems.

Both material systems show interesting intrinsic magnetic properties which is prerequisite for a hard magnetic material. However the conversion of this potential to extrinsic properties is not straightforward. The challenges and the reasons for such discrepancy were in detail discussed in this dissertation. Systematic studies on $\text{REFe}_{11}\text{Ti}$ (RE: Nd, Ce and Sm) and in $\text{Mn}_{52}\text{Al}_{46}\text{C}_2$ were carried out, taking into consideration of phase formation and stability together with magnetic properties in correlation with processing parameters and microstructure.

On the $\text{REFe}_{11}\text{Ti}$ material system, (Publication A) the effects of rare earth content and different annealing regimes on $\text{Nd}_{1+x}\text{Fe}_{11}\text{Ti}$ were studied to understand the stable 1:12 phase space and its competition with the possible secondary phases. It was found that hyperstoichiometric compositions, Nd content above 1.15, are necessary to avoid the formation of α -Fe, which would be detrimental for eventual permanent magnets because of the soft magnetic behavior of this phase. Moreover, low temperature annealing, between 700-900°C, leads to the stabilization of the ternary $\text{Nd}_2(\text{Fe,Ti})_{17}$, while annealing in the temperature interval of 950-1100°C stabilizes the $\text{Nd}_3(\text{Fe,Ti})_{29}$ phase. The desired tetragonal $\text{NdFe}_{11}\text{Ti}$ phase is stable only at high temperatures, between 1150 and 1200°C. The differentiation of these three ternary phases has shown to be

rather complex, since they share a common RECu_5 crystal structure frame, making the phase determination from the x-ray powder diffraction patterns is not straight forward. Complementary measurements are necessary for the exact identification of the existing phases in bulk samples. The study indicates that the best way of determining the present phases is through measurements of Curie temperature, since it is an intrinsic property and the different phases show distinct ferro to paramagnetic transition temperatures. The microstructural analysis studies of the 1:12 phase indicated the formation of twin boundaries with a reproducible misorientation angle of $57^\circ \pm 1^\circ$. To correlate this microstructural feature with the magnetic properties, Kerr analysis was carried out and, through the domain nucleation and motion, it was found that twin boundaries act as a nucleation center for reversal domains. This important finding could be one of the reasons to explain the low coercivity values of $\text{NdFe}_{11}\text{Ti}$ reported so far. It is true that the anisotropy field of the ternary compound is rather low, estimated to be around 1 T, and almost no coercivity is expected (Brown's Paradox). However, even in the corresponding nitrogenated compound, H_A reported to be around 8 T, the coercivity is far below than the expected one (between 20-30% of H_A). It is hypothesized that the twin boundaries would not be eliminated during the nitrogenation process, since these boundaries generally show low mobility, and because the temperature for the interstitial modification is relatively low, around 400°C . Taking into consideration that the twin boundaries would still be present in the $\text{NdFe}_{11}\text{TiN}_x$ compound, it will still cause a detrimental effect in the coercivity value despite the high anisotropy field, explaining the values achieved so far (below 0.6 T).

As a continuation on the path to explore promising RE-lean compounds, $\text{CeFe}_{11}\text{Ti}$ was studied in Publication B. Similar methodology successfully applied to Nd-Fe-Ti system (Publication A) was used. Annealing studies have shown that the highest fraction of Ce-1:12 was obtained after annealing at 850 and 950°C , depending on the Ce content used. At the optimized condition, a lower phase fraction of CeFe_2 Laves phase is observed (lower than 8% wt.). At higher temperatures, the formation of $\alpha\text{-Fe}$ was detected, while at lower temperatures the appearance of Fe_2Ti Laves phase was seen. The high purity $\text{CeFe}_{11}\text{Ti}$ phase sample was selected for further investigations and, similarly to what was obtained for $\text{NdFe}_{11}\text{Ti}$, twin boundaries with misorientation angle of $58^\circ \pm 2^\circ$ were noticed. The existence of twin boundaries in these two materials elucidate that this might be one important issue to develop coercivity in the ThMn_{12} -based materials, regardless the RE used. Even though Ce is an appealing RE element because of its high abundancy and lower price, when compared to Nd and Sm for example, the absence/small contribution of the $4f$ electron leads to a low anisotropy field, estimated to be around 2.5 T. Studies on interstitial modification by hydrogen and external isostatic pressure were carried out with the aim to change the Ce contribution to the magnetic properties. However, the results have shown no significant change in the intrinsic properties, in both saturation magnetization and anisotropy field. Considering the intrinsic limitation of $\text{CeFe}_{11}\text{Ti}$ and the Brown's paradox, it is unlikely that the ternary compound turns out to be an appealing material for future developments of permanent magnets. Nevertheless, studies to modify the magnetism of Ce using different stabilizing elements and/or methods would be beneficial, particularly in the direction to increase the intrinsic properties, especially H_A . Alternatively, Ce can also be used to partially substitute other RE elements in 1:12 compounds, as already demonstrated by Simon *et al.* in Sm-Ce-Fe-V-Ti [132].

The appearance and notable importance of twin boundaries on the development of ThMn₁₂-based magnets has been the main point of Publication C. To understand why this defect might be a microstructural weak link to obtain high coercivity values in the 1:12 material system, SmFe₁₁Ti was chosen as a prototypical compound, since it has H_A around 10 T. A direct comparison was drawn between the benchmark Nd₂Fe₁₄B (H_A of approximately 8 T) and SmFe₁₁Ti microcrystalline samples, in which was confirmed the formation of twins in the 1:12 sample while absent in the Nd-Fe-B one. High resolution microscopy investigations using a combination of STEM and APT revealed a zig-zag shaped twin boundary with chemical segregation across its thickness of 3 nm. It was observed an enrichment of Sm and depletion of Ti, leading to a stoichiometry that matches the Sm₃(Fe,Ti)₂₉ phase. The 3:29 phase possess different intrinsic magnetic properties than the 1:12, showing lower anisotropy constant (K_1). This information was used in micromagnetic simulations, adopting different models to match the experimental observations, to evaluate the impact on the coercivity. As expected, and observed experimentally, the simulations shows that twin boundary with 3:29 phase composition is deleterious to coercivity, acting as a nucleation center for reversal magnetic domains. Complimentary, molecular dynamics calculations were used to understand the possible reason for the formation of this defect. It was found that the internal stresses during solidification and phase formation, favors the formation of twin boundaries in the 1:12 grains larger than 1 μ m. These findings indicate that strategies, like grain refinement, should be adopted to avoid the appearance of twin boundaries in 1:12-type compounds. Considering the similarities in the REFe₁₁Ti twin structures, it is possible that the implications found in these works can be further expanded to other 1:12 compounds, regardless of the rare earth or the stabilizing element. This knowledge can serve as basis to further design strategies to overcome possible issues to improve the coercivity in the ThMn₁₂-type material systems. Other challenges involving the development of texture to obtain anisotropic magnets still remains, especially if the development of 1:12 magnets will be towards nanocrystalline materials. The difficulties to induce crystallographic texture during hot deformation in nanocrystalline 1:12 alloys were highlighted by Simon and Schönhöbel *et al* [90, 131, 132].

Moving from a RE-lean to a RE-free compound, the Publication D covered Mn-Al-C compound subjected to different processing routes to evaluate the microstructure differences and how this affects the extrinsic magnetic properties. As it was observed, techniques that involved melting and optimized annealing led to a microstructure of pure ferromagnetic τ -phase, showing a relative high magnetization but low coercivity, nearly zero. On the other hand, techniques that induce plastic deformation have shown to increase coercivity, reaching a value approximately 0.6 T for severe plastic deformed sample – among the highest values reported so far in bulk samples. Microstructural analysis revealed that the low coercivity samples are corresponding to the coarse grains combined with a high number of twins and low number of dislocations. In contrast, the samples with high coercivity show an increase of dislocations and a refined microstructure. These findings are supported by the literature, proving that twins are nucleation center for reversal domains, as observed for 1:12 compounds, while dislocations pin the domain wall motion. This shows that not all defects are deleterious to magnetic properties and studies about each defect and its effects on the functional properties are important. Despite the relatively high coercivity values achieved in

this work (maximum 0.58 T), there is still room for improvement, as shown by the values reported in thin film samples (around 1.2 T). This discrepancy means that further microstructural engineering is required to optimize processing routes to induce defects that promote coercivity while avoiding the deleterious ones. In addition, alloy design can also be explored to improve the stability of the τ -phase and to create a non-magnetic grain boundary phase that could possibly magnetic decouple adjacent grains, as successfully adopted for Nd-Fe-B magnets.

In summary, two types of prospective materials for permanent magnetic applications were investigated in this dissertation. A correlation between microstructure and extrinsic magnetic properties was made to understand the discrepancy in relation to the intrinsic properties. It was emphasized that microstructure and defects play a major role on the coercivity, but for each material system this relation needs to be investigated, since specific defects can be found and possibly have different impact on the magnetic properties. Additionally, it has also been shown that the use of multi scale characterization techniques, allied with different types of simulations, are powerful methods to give a better understanding of the overall aspects of phase formation, phase stability and to build the knowledge on the relation structure-processing-microstructure-magnetic properties. Through this evaluation and identification of microstructural weak links, insights about the coercivity mechanism can be gain to further create strategies to develop permanent magnet candidates, including Mn-Al and 1:12 material systems. The unfolding of such study is important to improve and create alternative magnets that can possibly reduce the dependency on critical raw materials, enabling possibilities for a more sustainable development of different technologies and applications.

Bibliography

- [1] O. Gutfleisch, M. A. Willard, E. Brück, C. H. Chen, S. G. Sankar, and J. P. Liu. Magnetic Materials and Devices for the 21st Century: Stronger, Lighter, and More Energy Efficient. *Advanced Materials*, 23(7):821–842, dec 2010. doi:[10.1002/adma.201002180](https://doi.org/10.1002/adma.201002180).
- [2] J. M. D. Coey. Permanent magnets: Plugging the gap. *Scripta Materialia*, 67(6):524–529, sep 2012. doi:[10.1016/j.scriptamat.2012.04.036](https://doi.org/10.1016/j.scriptamat.2012.04.036).
- [3] R. W. McCallum, L. Lewis, R. Skomski, M. J. Kramer, and I. E. Anderson. Practical Aspects of Modern and Future Permanent Magnets. *Annual Review of Materials Research*, 44(1):451–477, jul 2014. doi:[10.1146/annurev-matsci-070813-113457](https://doi.org/10.1146/annurev-matsci-070813-113457).
- [4] S. Bobba, S. Carrara, J. Huisman, F. Mathieux, and C. Pavel. Critical raw materials for strategic technologies and sectors in the EU A foresight study. Technical report, European Commission, 2020.
- [5] J. P. Sykes, J. P. Wright, and A. Trench. Discovery, supply and demand: From Metals of Antiquity to critical metals. *Applied Earth Science*, 125(1):3–20, jan 2016. doi:[10.1080/03717453.2015.1122274](https://doi.org/10.1080/03717453.2015.1122274).
- [6] A. Trench and J. P. Sykes. Rare Earth Permanent Magnets and Their Place in the Future Economy. *Engineering*, 6(2):115–118, feb 2020. doi:[10.1016/j.eng.2019.12.007](https://doi.org/10.1016/j.eng.2019.12.007).
- [7] S. M. Hayes and E. A. McCullough. Critical minerals: A review of elemental trends in comprehensive criticality studies. *Resources Policy*, 59:192–199, dec 2018. doi:[10.1016/j.resourpol.2018.06.015](https://doi.org/10.1016/j.resourpol.2018.06.015).
- [8] K.-H. Müller, S. Sawatzki, R. Gauß, and O. Gutfleisch. Permanent Magnet Materials. In *Handbook of Magnetism and Magnetic Materials*, pages 1–65. Springer International Publishing, 2021. doi:[10.1007/978-3-030-63101-7_29-1](https://doi.org/10.1007/978-3-030-63101-7_29-1).
- [9] J. M. D. Coey. Perspective and Prospects for Rare Earth Permanent Magnets. *Engineering*, 6(2): 119–131, feb 2020. doi:[10.1016/j.eng.2018.11.034](https://doi.org/10.1016/j.eng.2018.11.034).
- [10] K. P. Skokov and O. Gutfleisch. Heavy rare earth free, free rare earth and rare earth free magnets - Vision and reality. *Scripta Materialia*, 154:289–294, sep 2018. doi:[10.1016/j.scriptamat.2018.01.032](https://doi.org/10.1016/j.scriptamat.2018.01.032).
- [11] G. C. Hadjipanayis, A. M. Gabay, A. M. Schönhöbel, A. Martín-Cid, J. M. Barandiaran, and D. Niarchos. ThMn₁₂-Type Alloys for Permanent Magnets. *Engineering*, 6(2):141–147, feb 2020. doi:[10.1016/j.eng.2018.12.011](https://doi.org/10.1016/j.eng.2018.12.011).

-
- [12] J. Cui, M. Kramer, L. Zhou, F. Liu, A. Gabay, G. Hadjipanayis, B. Balasubramanian, and D. Sellmyer. Current progress and future challenges in rare-earth-free permanent magnets. *Acta Materialia*, 158: 118–137, oct 2018. doi:[10.1016/j.actamat.2018.07.049](https://doi.org/10.1016/j.actamat.2018.07.049).
- [13] K. H. J. Buschow, F. R. de Boer, Kurt H. J. Buschow, and F. R. Boer. *Physics of Magnetism and Magnetic Materials*. Springer US, 2003. ISBN 0306474212. URL https://www.ebook.de/de/product/3812431/k_h_j_buschow_f_r_de_boer_kurt_h_j_buschow_f_r_boer_physics_of_magnetism_and_magnetic_materials.html.
- [14] J. M. D. Coey. *Magnetism and Magnetic Materials*. Cambridge University Press, jan 2001. doi:[10.1017/cbo9780511845000](https://doi.org/10.1017/cbo9780511845000).
- [15] B. D. Cullity and C. D. Graham. *Introduction to Magnetic Materials*. John Wiley & Sons, Inc., nov 2008. doi:[10.1002/9780470386323](https://doi.org/10.1002/9780470386323).
- [16] J. Mohapatra and J. P. Liu. Rare-Earth-Free Permanent Magnets: The Past and Future. In *Handbook of Magnetic Materials*, pages 1–57. Elsevier, 2018. doi:[10.1016/bs.hmm.2018.08.001](https://doi.org/10.1016/bs.hmm.2018.08.001).
- [17] C. de J. Fernandez, C. Sangregorio, J. Figuera, B. Belec, D. Makovec, and A. Quesada. Topical Review: Progress and Prospects of Hard Hexaferrites for Permanent Magnet Applications. *Journal of Physics D: Applied Physics*, dec 2020. doi:[10.1088/1361-6463/abd272](https://doi.org/10.1088/1361-6463/abd272).
- [18] D. Givord, J. Laforest, H. S. Li, A. Liénard, R. Perrier de la Bâthie, and P. Tenaud. Rare Earth-Transition Metal Permanent Magnets. *Le Journal de Physique Colloques*, 46(C6):C6–213–C6–220, sep 1985. doi:[10.1051/jphyscol:1985637](https://doi.org/10.1051/jphyscol:1985637).
- [19] D. Givord. Rare Earth-Transition Metal Permanent Magnets. *Europhysics News*, 18(7-8):93–96, 1987. doi:[10.1051/epn/19871807093](https://doi.org/10.1051/epn/19871807093).
- [20] R. Skomski and D. J. Sellmyer. Anisotropy of rare-earth magnets. *Journal of Rare Earths*, 27(4): 675–679, aug 2009. doi:[10.1016/s1002-0721\(08\)60314-2](https://doi.org/10.1016/s1002-0721(08)60314-2).
- [21] M. E. McHenry, M. A. Willard, and D. E. Laughlin. Amorphous and nanocrystalline materials for applications as soft magnets. *Progress in Materials Science*, 44(4):291–433, oct 1999. doi:[10.1016/s0079-6425\(99\)00002-x](https://doi.org/10.1016/s0079-6425(99)00002-x).
- [22] P. Grünberg and D. E. Bürgler. Metallic Multilayers: Discovery of Interlayer Exchange Coupling and GMR. In *Handbook of Spintronics*, pages 1–16. Springer Netherlands, 2015. doi:[10.1007/978-94-007-7604-3_6-1](https://doi.org/10.1007/978-94-007-7604-3_6-1).
- [23] D. Jiles. *Introduction to Magnetism and Magnetic Materials*. Taylor & Francis Ltd., 2015. URL https://www.ebook.de/de/product/40462445/david_jiles_introduction_to_magnetism_and_magnetic_materials.html.
-

-
- [24] R. Hilzinger and W. Rodewald. *Magnetic Materials*. Publicis Kommunikationsag, 2012. ISBN 3895783528. URL https://www.ebook.de/de/product/13724329/rainer_hilzinger_werner_rodewald_magnetic_materials.html.
- [25] R. C. O’Handley. *Modern Magnetic Materials: Principles And Applications*. Wiley, 1999. ISBN 9780471155669. URL <https://books.google.de/books?id=RKV1QgAACAAJ>.
- [26] G. Bayreuther. Magnetic anisotropy. Lecture given at the European School on Magnetism, August 2011. URL <http://magnetism.eu/esm/2011/slides/bayreuther-slides.pdf>.
- [27] R. Skomski. *Simple Models of Magnetism*. Oxford University Press, jan 2008. doi:10.1093/acprof:oso/9780198570752.001.0001.
- [28] G. Laan. Microscopic origin of magnetocrystalline anisotropy in transition metal thin films. *Journal of Physics: Condensed Matter*, 10(14):3239–3253, apr 1998. doi:10.1088/0953-8984/10/14/012.
- [29] W. Suski. Magnetism of Uranium Intermetallics. *Acta Physica Polonica A*, 91(1):77–87, jan 1997. doi:10.12693/aphyspola.91.77.
- [30] J. Zhou and G. A. Fiete. Rare earths in a nutshell. *Physics Today*, 73(1):66–67, jan 2020. doi:10.1063/pt.3.4397.
- [31] T. Miyake and H. Akai. Quantum Theory of Rare-Earth Magnets. *Journal of the Physical Society of Japan*, 87(4):041009, apr 2018. doi:10.7566/jpsj.87.041009.
- [32] R. Skomski and J. M. D. Coey. Magnetic anisotropy - How much is enough for a permanent magnet? *Scripta Materialia*, 112:3–8, feb 2016. doi:10.1016/j.scriptamat.2015.09.021.
- [33] T. O. Helbig. *Demagnetizing and hardening mechanisms in Nd-Fe-B and Sr-hexaferrite permanent magnets*. PhD thesis, Technical University of Darmstadt, October 2018. URL <https://tuprints.ulb.tu-darmstadt.de/8199/>.
- [34] C. Kittel. Physical Theory of Ferromagnetic Domains. *Reviews of Modern Physics*, 21(4):541–583, oct 1949. doi:10.1103/revmodphys.21.541.
- [35] S. Sawatzki. *Der Korngrenzendiffusionsprozess in nanokristallinen Nd-Fe-B-Permanentmagneten - In German*. PhD thesis, Technische Universität Darmstadt, Darmstadt, October 2015. URL <http://tuprints.ulb.tu-darmstadt.de/5221/>.
- [36] M. Rossignol and J. P. Yonnet. *Magnetism: Materials and Applications*. Springer Nature, 2004. ISBN 0387230009. URL https://www.ebook.de/de/product/3231394/magnetism_materials_and_applications.html.
- [37] W. Fernengel, A. Lehnert, M. Katter, W. Rodewald, and B. Wall. Examination of the degree of alignment in sintered Nd-Fe-B magnets by measurements of the remanent polarizations. *Journal of*

-
- Magnetism and Magnetic Materials*, 157-158:19–20, may 1996. doi:[10.1016/0304-8853\(95\)01066-1](https://doi.org/10.1016/0304-8853(95)01066-1).
- [38] H. R. Kirchmayr. Permanent magnets and hard magnetic materials. *Journal of Physics D: Applied Physics*, 29(11):2763–2778, nov 1996. doi:[10.1088/0022-3727/29/11/007](https://doi.org/10.1088/0022-3727/29/11/007).
- [39] K. Hioki. High performance hot-deformed Nd-Fe-B magnets (Review). *Science and Technology of Advanced Materials*, 22(1):72–84, jan 2021. doi:[10.1080/14686996.2020.1868049](https://doi.org/10.1080/14686996.2020.1868049).
- [40] S. Sugimoto. Current status and recent topics of rare-earth permanent magnets. *Journal of Physics D: Applied Physics*, 44(6):064001, jan 2011. doi:[10.1088/0022-3727/44/6/064001](https://doi.org/10.1088/0022-3727/44/6/064001).
- [41] O. Gutfleisch, B. Gebel, M. Kubis, K. H. Müller, and L. Schultz. Modified HDDR procedures applied to NdFeB alloys. *IEEE Transactions on Magnetics*, 35(5):3250–3252, 1999. doi:[10.1109/20.800488](https://doi.org/10.1109/20.800488).
- [42] T. Ohtani, N. Kato, S. Kojima, K. Kojima, Y. Sakamoto, I. Konno, M. Tsukahara, and T. Kubo. Magnetic properties of Mn-Al-C permanent magnet alloys. *IEEE Transactions on Magnetics*, 13(5):1328–1330, sep 1977. doi:[10.1109/tmag.1977.1059574](https://doi.org/10.1109/tmag.1977.1059574).
- [43] D. Givord, M. F. Rossignol, and D. W. Taylor. Coercivity mechanisms in hard magnetic materials. *Journal of Physics IV*, 02(C3):C3–95–C3–104, dec 1992. doi:[10.1051/jp4:1992314](https://doi.org/10.1051/jp4:1992314).
- [44] J. Fliegans. *Coercivity of NdFeB-based sintered permanent magnets : experimental and numerical approaches*. Theses, Université Grenoble Alpes, December 2019. URL <https://tel.archives-ouvertes.fr/tel-02635105>.
- [45] Koichi Haneda, Choji Miyakawa, and Hiroshi Kojima. Preparation of High-Coercivity BaFe₁₂O₁₉. *Journal of the American Ceramic Society*, 57(8):354–357, aug 1974. doi:[10.1111/j.1151-2916.1974.tb10921.x](https://doi.org/10.1111/j.1151-2916.1974.tb10921.x).
- [46] C. D. Mee and J. C. Jeschke. Single-Domain Properties in Hexagonal Ferrites. *Journal of Applied Physics*, 34(4):1271–1272, apr 1963. doi:[10.1063/1.1729467](https://doi.org/10.1063/1.1729467).
- [47] H. Sepehri-Amin, H. Iwama, T. Ohkubo, T. Shima, and K. Hono. Microstructure and in-plane component of L1₀-FePt films deposited on MgO and MgAl₂O₄ substrates. *Scripta Materialia*, 130:247–251, mar 2017. doi:[10.1016/j.scriptamat.2016.12.018](https://doi.org/10.1016/j.scriptamat.2016.12.018).
- [48] H. Kronmüller. Theory of Nucleation Fields in Inhomogeneous Ferromagnets. *physica status solidi (b)*, 144(1):385–396, nov 1987. doi:[10.1002/pssb.2221440134](https://doi.org/10.1002/pssb.2221440134).
- [49] H. Kronmüller, K.-D. Durst, and M. Sagawa. Analysis of the magnetic hardening mechanism in RE-FeB permanent magnets. *Journal of Magnetism and Magnetic Materials*, 74(3):291–302, oct 1988. doi:[10.1016/0304-8853\(88\)90202-8](https://doi.org/10.1016/0304-8853(88)90202-8).
-

-
- [50] H. Sepehri-Amin, Y. Une, T. Ohkubo, K. Hono, and M. Sagawa. Microstructure of fine-grained Nd-Fe-B sintered magnets with high coercivity. *Scripta Materialia*, 65(5):396–399, sep 2011. doi:[10.1016/j.scriptamat.2011.05.006](https://doi.org/10.1016/j.scriptamat.2011.05.006).
- [51] K. Hono and H. Sepehri-Amin. Strategy for high-coercivity Nd-Fe-B magnets. *Scripta Materialia*, 67(6):530–535, sep 2012. doi:[10.1016/j.scriptamat.2012.06.038](https://doi.org/10.1016/j.scriptamat.2012.06.038).
- [52] T. G. Woodcock, Y. Zhang, G. Hrkac, G. Ciuta, N. M. Dempsey, T. Schrefl, O. Gutfleisch, and D. Givord. Understanding the microstructure and coercivity of high performance NdFeB-based magnets. *Scripta Materialia*, 67(6):536–541, sep 2012. doi:[10.1016/j.scriptamat.2012.05.038](https://doi.org/10.1016/j.scriptamat.2012.05.038).
- [53] J. Li, H. Sepehri-Amin, T. Sasaki, T. Ohkubo, and K. Hono. Most frequently asked questions about the coercivity of Nd-Fe-B permanent magnets. *Science and Technology of Advanced Materials*, 22(1):386–403, jun 2021. doi:[10.1080/14686996.2021.1916377](https://doi.org/10.1080/14686996.2021.1916377).
- [54] M. Duerrschnabel, M. Yi, K. Uestuener, M. Liesegang, M. Katter, H.-J. Kleebe, B. Xu, O. Gutfleisch, and L. Molina-Luna. Atomic structure and domain wall pinning in samarium-cobalt-based permanent magnets. *Nature Communications*, 8(1), jul 2017. doi:[10.1038/s41467-017-00059-9](https://doi.org/10.1038/s41467-017-00059-9).
- [55] J. P. Liu, E. Fullerton, O. Gutfleisch, and D. J. Sellmyer, editors. *Nanoscale Magnetic Materials and Applications*. Springer US, 2009. doi:[10.1007/978-0-387-85600-1](https://doi.org/10.1007/978-0-387-85600-1).
- [56] T. N. Lamichhane, M. T. Onyszczak, O. Palasyuk, S. Sharikadze, T.-H. Kim, Q. Lin, M. J. Kramer, R. W. McCallum, A. L. Wysocki, M. C. Nguyen, V. P. Antropov, T. Pandey, D. Parker, S. L. Bud'ko, P. C. Canfield, and A. Palasyuk. Single-Crystal Permanent Magnets: Extraordinary Magnetic Behavior in the Ta-, Cu-, and Fe-Substituted CeCo₅ Systems. *Physical Review Applied*, 11(1), jan 2019. doi:[10.1103/physrevapplied.11.014052](https://doi.org/10.1103/physrevapplied.11.014052).
- [57] K. Uestuener, M. Katter, and W. Rodewald. Dependence of the Mean Grain Size and Coercivity of Sintered Nd-Fe-B Magnets on the Initial Powder Particle Size. *IEEE Transactions on Magnetics*, 42(10):2897–2899, oct 2006. doi:[10.1109/tmag.2006.879889](https://doi.org/10.1109/tmag.2006.879889).
- [58] K. Kobayashi, R. Skomski, and J. M. D. Coey. Dependence of coercivity on particle size in Sm₂Fe₁₇N₃ powders. *Journal of Alloys and Compounds*, 222(1-2):1–7, may 1995. doi:[10.1016/0925-8388\(94\)04902-5](https://doi.org/10.1016/0925-8388(94)04902-5).
- [59] D. A. Porter and K. E. Easterling. *Phase Transformations in Metals and Alloys*. Springer US, 1992. doi:[10.1007/978-1-4899-3051-4](https://doi.org/10.1007/978-1-4899-3051-4).
- [60] S. Korte-Kerzel, T. Hickel, L. Huber, D. Raabe, S. Sandlöbes-Haut, M. Todorova, and J. Neugebauer. Defect phases - thermodynamics and impact on material properties. *International Materials Reviews*, pages 1–29, may 2021. doi:[10.1080/09506608.2021.1930734](https://doi.org/10.1080/09506608.2021.1930734).

-
- [61] J. Fischbacher, A. Kovacs, L. Exl, J. Kühnel, E. Mehofer, H. Sepehri-Amin, T. Ohkubo, K. Hono, and T. Schrefl. Searching the weakest link: Demagnetizing fields and magnetization reversal in permanent magnets. *Scripta Materialia*, 154:253–258, sep 2018. doi:[10.1016/j.scriptamat.2017.11.020](https://doi.org/10.1016/j.scriptamat.2017.11.020).
- [62] J. Fischbacher, A. Kovacs, M. Gusenbauer, H. Oezelt, L. Exl, S. Bance, and T. Schrefl. Micromagnetics of rare-earth efficient permanent magnets. *Journal of Physics D: Applied Physics*, 51(19):193002, apr 2018. doi:[10.1088/1361-6463/aab7d1](https://doi.org/10.1088/1361-6463/aab7d1).
- [63] T. G. Woodcock, F. Bittner, T. Mix, K.-H. Müller, S. Sawatzki, and O. Gutfleisch. On the reversible and fully repeatable increase in coercive field of sintered Nd-Fe-B magnets following post sinter annealing. *Journal of Magnetism and Magnetic Materials*, 360:157–164, jun 2014. doi:[10.1016/j.jmmm.2014.02.025](https://doi.org/10.1016/j.jmmm.2014.02.025).
- [64] K. Binnemans, P. T. Jones, T. Müller, and L. Yurramendi. Rare Earths and the Balance Problem: How to Deal with Changing Markets? *Journal of Sustainable Metallurgy*, 4(1):126–146, feb 2018. doi:[10.1007/s40831-018-0162-8](https://doi.org/10.1007/s40831-018-0162-8).
- [65] A. Lixandru, P. Venkatesan, C. Jönsson, I. Poenaru, B. Hall, Y. Yang, A. Walton, K. Güth, R. Gauß, and O. Gutfleisch. Identification and recovery of rare-earth permanent magnets from waste electrical and electronic equipment. *Waste Management*, 68:482–489, oct 2017. doi:[10.1016/j.wasman.2017.07.028](https://doi.org/10.1016/j.wasman.2017.07.028).
- [66] O. Diehl, M. Schönfeldt, E. Brouwer, A. Dirks, K. Rachut, J. Gassmann, K. Güth, A. Buckow, R. Gauß, R. Stauber, and O. Gutfleisch. Towards an Alloy Recycling of Nd-Fe-B Permanent Magnets in a Circular Economy. *Journal of Sustainable Metallurgy*, 4(2):163–175, mar 2018. doi:[10.1007/s40831-018-0171-7](https://doi.org/10.1007/s40831-018-0171-7).
- [67] S. Ali. Social and Environmental Impact of the Rare Earth Industries. *Resources*, 3(1):123–134, feb 2014. doi:[10.3390/resources3010123](https://doi.org/10.3390/resources3010123).
- [68] H. Sepehri-Amin, T. Ohkubo, and K. Hono. The mechanism of coercivity enhancement by the grain boundary diffusion process of Nd-Fe-B sintered magnets. *Acta Materialia*, 61(6):1982–1990, apr 2013. doi:[10.1016/j.actamat.2012.12.018](https://doi.org/10.1016/j.actamat.2012.12.018).
- [69] T.-H. Kim, S.-R. Lee, S. J. Yun, S. H. Lim, H.-J. Kim, M.-W. Lee, and T.-S. Jang. Anisotropic diffusion mechanism in grain boundary diffusion processed Nd-Fe-B sintered magnet. *Acta Materialia*, 112: 59–66, jun 2016. doi:[10.1016/j.actamat.2016.04.019](https://doi.org/10.1016/j.actamat.2016.04.019).
- [70] K. Loewe, D. Benke, C. Kübel, T. Lienig, K. P. Skokov, and O. Gutfleisch. Grain boundary diffusion of different rare earth elements in Nd-Fe-B sintered magnets by experiment and FEM simulation. *Acta Materialia*, 124:421–429, feb 2017. doi:[10.1016/j.actamat.2016.11.034](https://doi.org/10.1016/j.actamat.2016.11.034).

-
- [71] S. Sawatzki, C. Kübel, S. Ener, and O. Gutfleisch. Grain boundary diffusion in nanocrystalline Nd-Fe-B permanent magnets with low-melting eutectics. *Acta Materialia*, 115:354–363, aug 2016. doi:[10.1016/j.actamat.2016.05.048](https://doi.org/10.1016/j.actamat.2016.05.048).
- [72] K. Opelt, T. Ahmad, O. Diehl, M. Schönfeldt, E. Brouwer, I. Vogel, J. D. Rossa, J. Gassmann, S. Ener, and O. Gutfleisch. Upscaling the 2-Powder Method for the Manufacturing of Heavy Rare Earth-Lean Sintered didymium-based Magnets. *Advanced Engineering Materials*, aug 2021. doi:[10.1002/adem.202100459](https://doi.org/10.1002/adem.202100459).
- [73] I. Poenaru, A. Lixandru, S. Riegg, B. Fayyazi, A. Taubel, K. Güth, R. Gauß, and O. Gutfleisch. Ce and La as substitutes for Nd in Nd₂Fe₁₄B-based melt-spun alloys and hot-deformed magnets: a comparison of structural and magnetic properties. *Journal of Magnetism and Magnetic Materials*, 478:198–205, may 2019. doi:[10.1016/j.jmmm.2019.01.095](https://doi.org/10.1016/j.jmmm.2019.01.095).
- [74] I. Poenaru, A. Lixandru, K. Güth, A. Malfliet, S. Yoon, I. Škulj, and O. Gutfleisch. HDDR treatment of Ce-substituted Nd₂Fe₁₄B-based permanent magnet alloys - phase structure evolution, intergranular processes and magnetic property development. *Journal of Alloys and Compounds*, 814:152215, jan 2020. doi:[10.1016/j.jallcom.2019.152215](https://doi.org/10.1016/j.jallcom.2019.152215).
- [75] L. Zhao, C. Li, Z. Hao, X. Liu, X. Liao, J. Zhang, K. Su, L. Li, H. Yu, J.-M. Greneche, J. Jin, and Z. Liu. Influences of element segregation on the magnetic properties in nanocrystalline Nd-Ce-Fe-B alloys. *Materials Characterization*, 148:208–213, feb 2019. doi:[10.1016/j.matchar.2018.12.022](https://doi.org/10.1016/j.matchar.2018.12.022).
- [76] X. Liao, J. Zhang, W. Li, A. J. Khan, H. Yu, X. Zhong, and Z. Liu. Performance improvement and element segregation behavior in Y substituted nanocrystalline (La,Ce)-Fe-B permanent magnetic alloys without critical RE elements. *Journal of Alloys and Compounds*, 834:155226, sep 2020. doi:[10.1016/j.jallcom.2020.155226](https://doi.org/10.1016/j.jallcom.2020.155226).
- [77] H.-R. Cha, Y.-K. Baek, J.-G. Lee, and D.-H. Kim. Development Trend of Nd-Reduced Nd-Fe-B Permanent Magnets for Solving Rare-Earth Resources Problem. *Journal of the Korean Magnetics Society*, 29(3):98–107, jun 2019. doi:[10.4283/jkms.2019.29.3.098](https://doi.org/10.4283/jkms.2019.29.3.098).
- [78] B. Fayyazi, K. P. Skokov, T. Faske, D. Y. Karpenkov, W. Donner, and O. Gutfleisch. Bulk combinatorial analysis for searching new rare-earth free permanent magnets: Reactive crucible melting applied to the Fe-Sn binary system. *Acta Materialia*, 141:434–443, dec 2017. doi:[10.1016/j.actamat.2017.09.036](https://doi.org/10.1016/j.actamat.2017.09.036).
- [79] J. M. D. Coey, P. Stamenov, S. B. Porter, M. Venkatesan, Rui Zhang, and T. Iriyama. Sm-Fe-N revisited; remanence enhancement in melt-spun Nitroquench material. *Journal of Magnetism and Magnetic Materials*, 480:186–192, jun 2019. doi:[10.1016/j.jmmm.2019.02.076](https://doi.org/10.1016/j.jmmm.2019.02.076).
- [80] K. H. J. Buschow and A. M. van der Kraan. Magnetic ordering in ternary rare earth iron aluminium compounds (RFe₄Al₈). *Journal of Physics F: Metal Physics*, 8(5):921–932, may 1978. doi:[10.1088/0305-4608/8/5/021](https://doi.org/10.1088/0305-4608/8/5/021).
-

-
- [81] K. H. J. Buschow. Permanent magnet materials based on tetragonal rare earth compounds of the type $RFe_{12-x}M_x$. *Journal of Magnetism and Magnetic Materials*, 100(1-3):79–89, nov 1991. doi:[10.1016/0304-8853\(91\)90813-p](https://doi.org/10.1016/0304-8853(91)90813-p).
- [82] W. Suski. Chapter 149 : The $ThMn_{12}$ -type compounds of rare earths and actinides: Structure, magnetic and related properties. In *Handbook on the Physics and Chemistry of Rare Earths*, pages 143–294. Elsevier, 1996. doi:[10.1016/s0168-1273\(96\)22006-9](https://doi.org/10.1016/s0168-1273(96)22006-9).
- [83] K. Ohashi, T. Yokoyama, R. Osugi, and Y. Tawara. The magnetic and structural properties of R-Ti-Fe ternary compounds. *IEEE Transactions on Magnetics*, 23(5):3101–3103, sep 1987. doi:[10.1109/tmag.1987.1065256](https://doi.org/10.1109/tmag.1987.1065256).
- [84] K. H. J. Buschow, D. B. de Mooij, M. Brouha, H. H. Smit, and R. C. Thiel. Magnetic properties of ternary Fe-rich rare earth intermetallic compounds. *IEEE Transactions on Magnetics*, 24(2): 1611–1616, mar 1988. doi:[10.1109/20.11547](https://doi.org/10.1109/20.11547).
- [85] F. R. de Boer, Z. G. Zhao, and K. H. J. Buschow. 4f-3d interaction and magnetic anisotropy in $ThMn_{12}$ -type rare-earth transition-metal compounds. *Journal of Magnetism and Magnetic Materials*, 157-158:504–507, may 1996. doi:[10.1016/0304-8853\(95\)01270-2](https://doi.org/10.1016/0304-8853(95)01270-2).
- [86] W. Körner, G. Krugel, and C. Elsässer. Theoretical screening of intermetallic $ThMn_{12}$ -type phases for new hard-magnetic compounds with low rare earth content. *Scientific Reports*, 6(1), apr 2016. doi:[10.1038/srep24686](https://doi.org/10.1038/srep24686).
- [87] Y. Hirayama, Y. K. Takahashi, S. Hirosawa, and K. Hono. $NdFe_{12}N$ hard-magnetic compound with high magnetization and anisotropy field. *Scripta Materialia*, 95:70–72, jan 2015. doi:[10.1016/j.scriptamat.2014.10.016](https://doi.org/10.1016/j.scriptamat.2014.10.016).
- [88] Y. Hirayama, T. Miyake, and K. Hono. Rare-Earth Lean Hard Magnet Compound $NdFe_{12}N$. *JOM*, 67 (6):1344–1349, apr 2015. doi:[10.1007/s11837-015-1421-9](https://doi.org/10.1007/s11837-015-1421-9).
- [89] Y. Hirayama, Y. K. Takahashi, S. Hirosawa, and K. Hono. Intrinsic hard magnetic properties of $Sm(Fe_{1-x}Co_x)_{12}$ compound with the $ThMn_{12}$ structure. *Scripta Materialia*, 138:62–65, sep 2017. doi:[10.1016/j.scriptamat.2017.05.029](https://doi.org/10.1016/j.scriptamat.2017.05.029).
- [90] Yukiko Takahashi, Hossein Sepehri-Amin, and Tadakatsu Ohkubo. Recent advances in $SmFe_{12}$ -based permanent magnets. *Science and Technology of Advanced Materials*, 22(1):449–460, jun 2021. doi:[10.1080/14686996.2021.1913038](https://doi.org/10.1080/14686996.2021.1913038).
- [91] J. M. Cadogan, H.-S. Li, A. Margarian, J. B. Dunlop, D. H. Ryan, S. J. Collocott, and R. L. Davis. New rare-earth intermetallic phases $R_3(Fe,M)_{29}X_n$: (R=Ce, Pr, Nd, Sm, Gd; M=Ti, V, Cr, Mn; and X=H, N, C) (invited). *Journal of Applied Physics*, 76(10):6138–6143, nov 1994. doi:[10.1063/1.358333](https://doi.org/10.1063/1.358333).
- [92] H.-S. Li and J. M. D. Coey. Magnetic properties of ternary rare-earth transition-metal compounds. In *Handbook of Magnetic Materials*, pages 87–196. Elsevier, 2019. doi:[10.1016/bs.hmm.2019.10.001](https://doi.org/10.1016/bs.hmm.2019.10.001).
-

-
- [93] K. Kobayashi, S. Suzuki, T. Kuno, K. Urushibata, N. Sakuma, M. Yano, T. Shoji, A. Kato, and A. Manabe. The origin of high magnetic properties in $(R, Zr)(Fe, Co)_{11.0-11.5}Ti_{1.0-0.5}N_y$ ($y=1.0-1.4$ for $R=Nd$, $y=0$ for $R=Sm$) compounds. *Journal of Magnetism and Magnetic Materials*, 426:273–278, mar 2017. doi:[10.1016/j.jmmm.2016.11.070](https://doi.org/10.1016/j.jmmm.2016.11.070).
- [94] D. B. De Mooij and K. H. J. Buschow. Some novel ternary $ThMn_{12}$ -type compounds. *Journal of the Less Common Metals*, 136(2):207–215, jan 1988. doi:[10.1016/0022-5088\(88\)90424-9](https://doi.org/10.1016/0022-5088(88)90424-9).
- [95] S. Suzuki, T. Kuno, K. Urushibata, K. Kobayashi, N. Sakuma, K. Washio, H. Kishimoto, A. Kato, and A. Manabe. A $(Nd, Zr)(Fe, Co)_{11.5}Ti_{0.5}N_x$ compound as a permanent magnet material. *AIP Advances*, 4(11):117131, nov 2014. doi:[10.1063/1.4902176](https://doi.org/10.1063/1.4902176).
- [96] S. Suzuki, T. Kuno, K. Urushibata, K. Kobayashi, N. Sakuma, K. Washio, M. Yano, A. Kato, and A. Manabe. A new magnet material with $ThMn_{12}$ structure: $(Nd_{1-x}Zr_x)(Fe_{1-y}Co_y)_{11+z}Ti_{1-z}N_\alpha$ ($\alpha=0.6-1.3$). *Journal of Magnetism and Magnetic Materials*, 401:259–268, mar 2016. doi:[10.1016/j.jmmm.2015.10.042](https://doi.org/10.1016/j.jmmm.2015.10.042).
- [97] A. M. Gabay and G. C. Hadjipanayis. High-coercivity $ThMn_{12}$ -type monocrystalline Sm-Zr-Fe-Co-Ti particles by high-temperature reduction diffusion. *Scripta Materialia*, 196:113760, apr 2021. doi:[10.1016/j.scriptamat.2021.113760](https://doi.org/10.1016/j.scriptamat.2021.113760).
- [98] A. M. Gabay and G. C. Hadjipanayis. Recent developments in RFe_{12} -type compounds for permanent magnets. *Scripta Materialia*, 154:284–288, sep 2018. doi:[10.1016/j.scriptamat.2017.10.033](https://doi.org/10.1016/j.scriptamat.2017.10.033).
- [99] J. M. D. Coey. Comparison of the intrinsic magnetic properties of $R_2Fe_{14}B$ and $RFe_{11}Ti$; $R =$ rare earth. *Journal of Magnetism and Magnetic Materials*, 80(1):9–13, aug 1989. doi:[10.1016/0304-8853\(89\)90314-4](https://doi.org/10.1016/0304-8853(89)90314-4).
- [100] Y. Yang, X. Pei, H. Li, X. Zhang, L. Kong, Q. Pan, and M. Zhang. Theoretical explanations of magnetocrystalline anisotropy behaviors in $RTiFe_{11}N_x$ compounds. *Journal of Applied Physics*, 70(10):6574–6576, nov 1991. doi:[10.1063/1.349861](https://doi.org/10.1063/1.349861).
- [101] C. Piquer, F. Grandjean, O. Isnard, V. Pop, and G. J. Long. A magnetic and Mössbauer spectral study of the spin reorientation in $NdFe_{11}Ti$ and $NdFe_{11}TiH$. *Journal of Applied Physics*, 95(11):6308–6316, jun 2004. doi:[10.1063/1.1736333](https://doi.org/10.1063/1.1736333).
- [102] F. Maccari, L. Schäfer, I. Radulov, L. V. B. Diop, S. Ener, E. Bruder, K. Skokov, and O. Gutfleisch. Rapid solidification of $Nd_{1+x}Fe_{11}Ti$ compounds: Phase formation and magnetic properties. *Acta Materialia*, 180:15–23, nov 2019. doi:[10.1016/j.actamat.2019.08.057](https://doi.org/10.1016/j.actamat.2019.08.057).
- [103] D. Niarchos, M. Gjoka, A. M. Schönhöbel, A. Aubert, R. Madugundo, J. J. S. Garitaonandía, J. M. Barandiran, and G. Hadjipanayis. Intrinsic magnetic properties of $(Nd_{1-x}Sm_x)Fe_{11}Ti$. *Journal of Alloys and Compounds*, 864:158097, may 2021. doi:[10.1016/j.jallcom.2020.158097](https://doi.org/10.1016/j.jallcom.2020.158097).
-

-
- [104] A. Navarathna, H. Hegde, R. Rani, and F. J. Cadieu. High anisotropy Nd(Fe,T)₁₂N_x, T=Ti, Mo, films and disordered RE(Fe,Ti) phases before and after nitriding. *Journal of Applied Physics*, 73(10): 6242–6244, may 1993. doi:[10.1063/1.352711](https://doi.org/10.1063/1.352711).
- [105] L. V. B. Diop, M. D. Kuz'min, Y. Skourski, K. P. Skokov, I. A. Radulov, and O. Gutfleisch. Determination of the crystal field parameters in SmFe₁₁Ti. *Physical Review B*, 102(6), aug 2020. doi:[10.1103/physrevb.102.064423](https://doi.org/10.1103/physrevb.102.064423).
- [106] S. Ener, K. P. Skokov, D. Palanisamy, T. Devillers, J. Fischbacher, G. G. Eslava, F. Maccari, L. Schäfer, L. V. B. Diop, I. Radulov, B. Gault, G. Hrkac, N. M. Dempsey, T. Schrefl, D. Raabe, and O. Gutfleisch. Twins - A weak link in the magnetic hardening of ThMn₁₂-type permanent magnets. *Acta Materialia*, 214:116968, aug 2021. doi:[10.1016/j.actamat.2021.116968](https://doi.org/10.1016/j.actamat.2021.116968).
- [107] S. Hirosawa, M. Nishino, and S. Miyashita. Perspectives for high-performance permanent magnets: applications, coercivity, and new materials. *Advances in Natural Sciences: Nanoscience and Nanotechnology*, 8(1):013002, mar 2017. doi:[10.1088/2043-6254/aa597c](https://doi.org/10.1088/2043-6254/aa597c).
- [108] B.-P. Hu, H.-S. Li, J. P. Gavigan, and J. M. D. Coey. Intrinsic magnetic properties of the iron-rich ThMn₁₂-structure alloys RFe₁₁Ti; R=Y, Nd, Sm, Gd, Tb, Dy, Ho, Er, Tm and Lu. *Journal of Physics: Condensed Matter*, 1(4):755–770, jan 1989. doi:[10.1088/0953-8984/1/4/009](https://doi.org/10.1088/0953-8984/1/4/009).
- [109] N. Sakuma, S. Suzuki, T. Kuno, K. Urushibata, K. Kobayashi, M. Yano, A. Kato, and A. Manabe. Influence of Zr substitution on the stabilization of ThMn₁₂-type (Nd_{1-α}Zr_α)(Fe_{0.75}Co_{0.25})_{11.25}Ti_{0.75}N_{1.2-1.4} (α = 0-0.3) compounds. *AIP Advances*, 6(5):056023, may 2016. doi:[10.1063/1.4944521](https://doi.org/10.1063/1.4944521).
- [110] Y. Z. Wang and G. C. Hadjipanayis. Effect of nitrogen on the structural and magnetic properties of intermetallic compounds with the ThMn₁₂ structure. *Journal of Applied Physics*, 70(10):6009–6011, nov 1991. doi:[10.1063/1.350076](https://doi.org/10.1063/1.350076).
- [111] A. Aubert, I. Puente-Orench, J. M. Porro, S. Luca, J. S. Garitaonandia, J. M. Barandiaran, and G. C. Hadjipanayis. Denitrogenation process in ThMn₁₂ nitride by in situ neutron powder diffraction. *Physical Review Materials*, 5(1), jan 2021. doi:[10.1103/physrevmaterials.5.014415](https://doi.org/10.1103/physrevmaterials.5.014415).
- [112] S. L. Tang, C. H. Wu, X. M. Jin, B. W. Wang, G. S. Li, B. Z. Ding, and Y. C. Chuang. Phase formation and magnetic properties of annealed mechanical alloying Nd-Fe-V-Ti alloys and their nitrides. *Journal of Alloys and Compounds*, 264(1-2):240–243, jan 1998. doi:[10.1016/s0925-8388\(97\)00250-8](https://doi.org/10.1016/s0925-8388(97)00250-8).
- [113] A. Aubert, R. Madugundo, A. M. Schönhöbel, D. Salazar, J. S. Garitaonandia, J. M. Barandiaran, and G. Hadjipanayis. Structural and magnetic properties of Nd-Fe-Mo-(N) melt-spun ribbons with ThMn₁₂ structure. *Acta Materialia*, 195:519–526, aug 2020. doi:[10.1016/j.actamat.2020.05.045](https://doi.org/10.1016/j.actamat.2020.05.045).

-
- [114] H. M. Sánchez, G. Hadjipanayis, G. A. P. Alcázar, L. E. Z. Alfonso, and J. S. T. Hernández. Mechanochemical Synthesis and Nitrogenation of the Nd_{1.1}Fe₁₀CoTi Alloy for Permanent Magnet. *Molecules*, 26(13):3854, jun 2021. doi:[10.3390/molecules26133854](https://doi.org/10.3390/molecules26133854).
- [115] J. Yang, P. Oleinek, and K.-H. Müller. Hard magnetic properties of melt-spun R(Fe,M)₁₂ nitrides (R=Nd or Pr; M=Mo or V). *Journal of Applied Physics*, 88(2):988–992, jul 2000. doi:[10.1063/1.373766](https://doi.org/10.1063/1.373766).
- [116] J. Hu, T. Dragon, A. Forkl, and H. Kronmüller. Investigation of the Domain Structure of NdFe₁₁Ti and NdFe₁₁TiN_x. *Physica Status Solidi (a)*, 154(2):749–754, apr 1996. doi:[10.1002/pssa.2211540228](https://doi.org/10.1002/pssa.2211540228).
- [117] T. Tatsuki, H. Nakamura, S. Sugimoto, M. Okada, and M. Homma. Enhancement of the Magnetic Properties of Sm-Fe and Nd-Fe-N Alloys with ThMn₁₂ Structure by Utilizing HDDR Phenomena. *IEEE Transaction Journal on Magnetism in Japan*, 8(11):755–762, nov 1993. doi:[10.1109/tjmj.1993.4565741](https://doi.org/10.1109/tjmj.1993.4565741).
- [118] Bo-Ping Hu, P. A. P. Wendhausen, D. Eckert, W. Pitschke, A. Handstein, and K.-H. Muller. Development of coercivity on NdFe_{12-x}Mo_xN_{0.9} nitrides with low Mo concentration. *IEEE Transactions on Magnetism*, 30(2):645–647, mar 1994. doi:[10.1109/20.312363](https://doi.org/10.1109/20.312363).
- [119] M. Anagnostou, C. Christides, M. Pissas, and D. Niarchos. Preparation and characterization of the NdFe₁₀T₂N_x (T=Mo,V) compounds with the ThMn₁₂ tetragonal-type structure. *Journal of Applied Physics*, 70(10):6012–6014, nov 1991. doi:[10.1063/1.350077](https://doi.org/10.1063/1.350077).
- [120] N. Inoue and S. Suzuki. Influence of nitrogenating conditions on magnetic properties of NdFe₈Co₃TiN_x. *Journal of Alloys and Compounds*, 222(1-2):82–86, may 1995. doi:[10.1016/0925-8388\(94\)04922-x](https://doi.org/10.1016/0925-8388(94)04922-x).
- [121] S. L. Tang, J. H. Yin, Z. Q. Jin, J. R. Zhang, S. Y. Zhang, and Y. W. Du. Structure and magnetic properties of PrFe₁₀V_xMo_{2-x} compounds and their nitrides. *Journal of Applied Physics*, 85(8):4687–4689, apr 1999. doi:[10.1063/1.370448](https://doi.org/10.1063/1.370448).
- [122] T. S. Chin, S. H. Huang, and Y. S. Chen. Magnetic properties of Nd-Fe-Ti-B alloys with NdFe₁₁Ti and/or Nd₂Fe₁₄B phases. *Journal of Magnetism and Magnetic Materials*, 111(1-2):177–185, jun 1992. doi:[10.1016/0304-8853\(92\)91073-3](https://doi.org/10.1016/0304-8853(92)91073-3).
- [123] D. Nunes, R. Colaço, A. P. Gonçalves, L. C. J. Pereira, and P. A. Carvalho. Microstructures and magnetic domain configurations of NdFe₁₁Ti and Nd₂(Fe,Ti)₁₇ aggregates. *Applied Physics A*, 104(4):1053–1060, mar 2011. doi:[10.1007/s00339-011-6365-5](https://doi.org/10.1007/s00339-011-6365-5).
- [124] D. Nunes, A. P. Gonçalves, and P. A. Carvalho. Electron Diffraction of ThMn₁₂/Th₂Zn₁₇-Type Structures in the Nd-Fe-Ti System. *Microscopy and Microanalysis*, 19(5):1211–1215, jun 2013. doi:[10.1017/s1431927613001748](https://doi.org/10.1017/s1431927613001748).
-

-
- [125] D. Simon. *Development and Assessment of Rare Earth-lean $\text{Th}_1\text{Mn}_{12}$ -Phases for the Use in Permanent Magnets*. PhD thesis, Technische Universitaet, Darmstadt, 2019. URL <http://tuprints.ulb.tu-darmstadt.de/8964/>.
- [126] H. Sepehri-Amin, Y. Tamazawa, M. Kambayashi, G. Saito, Y. K. Takahashi, D. Ogawa, T. Ohkubo, S. Hirosawa, M. Doi, T. Shima, and K. Hono. Achievement of high coercivity in $\text{Sm}(\text{Fe}_{0.8}\text{Co}_{0.2})_{12}$ anisotropic magnetic thin film by boron doping. *Acta Materialia*, 194:337–342, aug 2020. doi:[10.1016/j.actamat.2020.05.026](https://doi.org/10.1016/j.actamat.2020.05.026).
- [127] T. Saito, F. Watanabe, and D. Nishio-Hamane. Magnetic properties of SmFe_{12} -based magnets produced by spark plasma sintering method. *Journal of Alloys and Compounds*, 773:1018–1022, jan 2019. doi:[10.1016/j.jallcom.2018.09.297](https://doi.org/10.1016/j.jallcom.2018.09.297).
- [128] T. Saito, F. Watanabe, and D. Nishio-Hamane. High-coercivity $\text{Sm}(\text{Fe},\text{V},\text{Ti})_{12}$ bulk magnets. *Materials Research Bulletin*, 133:111060, jan 2021. doi:[10.1016/j.materresbull.2020.111060](https://doi.org/10.1016/j.materresbull.2020.111060).
- [129] A. M. Schönhöbel, R. Madugundo, J. M. Barandiarán, G. C. Hadjipanayis, D. Palanisamy, T. Schwarz, B. Gault, D. Raabe, K. Skokov, O. Gutfleisch, J. Fischbacher, and T. Schrefl. Nanocrystalline Sm-based 1:12 magnets. *Acta Materialia*, 200:652–658, nov 2020. doi:[10.1016/j.actamat.2020.08.075](https://doi.org/10.1016/j.actamat.2020.08.075).
- [130] J. S. Zhang, Xin Tang, H. Sepehri-Amin, A. K. Srinithi, T. Ohkubo, and K. Hono. Origin of coercivity in an anisotropic $\text{Sm}(\text{Fe},\text{Ti},\text{V})_{12}$ -based sintered magnet. *Acta Materialia*, 217:117161, sep 2021. doi:[10.1016/j.actamat.2021.117161](https://doi.org/10.1016/j.actamat.2021.117161).
- [131] A. M. Schönhöbel, R. Madugundo, A. M. Gabay, J. M. Barandiarán, and G. C. Hadjipanayis. The Sm-Fe-V based 1:12 bulk magnets. *Journal of Alloys and Compounds*, 791:1122–1127, jun 2019. doi:[10.1016/j.jallcom.2019.03.249](https://doi.org/10.1016/j.jallcom.2019.03.249).
- [132] D. Simon, H. Wuest, S. Hinderberger, T. Koehler, A. Marusczyk, S. Sawatzki, L. V. B. Diop, K. Skokov, F. Maccari, A. Senyshyn, H. Ehrenberg, and O. Gutfleisch. Structural and magnetic properties of $\text{Ce}_{1-x}\text{Sm}_x\text{Fe}_{11-y}\text{Ti}_1\text{V}_y$. *Acta Materialia*, 172:131–138, jun 2019. doi:[10.1016/j.actamat.2019.04.006](https://doi.org/10.1016/j.actamat.2019.04.006).
- [133] A. K. Srinithi, H. Sepehri-Amin, Xin Tang, P. Tozman, J. Li, J. Zhang, S. Kobayashi, T. Ohkubo, T. Nakamura, and K. Hono. Phase relations and extrinsic magnetic properties of Sm-(Fe,Co)-Ti-(Ga)-based alloys for ThMn_{12} -type permanent magnets. *Journal of Magnetism and Magnetic Materials*, 529:167866, jul 2021. doi:[10.1016/j.jmmm.2021.167866](https://doi.org/10.1016/j.jmmm.2021.167866).
- [134] S. Pandian, V. Chandrasekaran, G. Markandeyulu, K. J. L. Iyer, and K. V. S. Rama Rao. Effect of Al, Cu, Ga, and Nb additions on the magnetic properties and microstructural features of sintered NdFeB. *Journal of Applied Physics*, 92(10):6082–6086, nov 2002. doi:[10.1063/1.1513879](https://doi.org/10.1063/1.1513879).
-

-
- [135] S. Sugimoto, T. Shimono, H. Nakamura, T. Kagotani, M. Okada, and M. Homma. Phase Relation of Sm-Fe-V Alloys around the Compound $\text{Sm}_3(\text{Fe,V})_{29}$. *Materials Transactions, JIM*, 37(3):494–498, 1996. doi:[10.2320/matertrans1989.37.494](https://doi.org/10.2320/matertrans1989.37.494).
- [136] A. C. Neiva, F. P. Missell, B. Grieb, E.-Th. Henig, and G. Petzow. Phase equilibria around $\text{SmFe}_{11}\text{Ti}$ at 1000°C. *Journal of the Less Common Metals*, 170(2):293–299, jun 1991. doi:[10.1016/0022-5088\(91\)90331-w](https://doi.org/10.1016/0022-5088(91)90331-w).
- [137] D. Palanisamy, S. Ener, F. Maccari, L. Schäfer, K. P. Skokov, O. Gutfleisch, D. Raabe, and B. Gault. Grain boundary segregation, phase formation, and their influence on the coercivity of rapidly solidified $\text{SmFe}_{11}\text{Ti}$ hard magnetic alloys. *Physical Review Materials*, 4(5), may 2020. doi:[10.1103/physrevmaterials.4.054404](https://doi.org/10.1103/physrevmaterials.4.054404).
- [138] H. I. Sözen. *Ab initio phase stabilities of Ce-based hard magnetic materials*. PhD thesis, Ruhr-Universitaet Bochum, 2019.
- [139] H. I. Sözen, S. Ener, F. Maccari, K. P. Skokov, O. Gutfleisch, F. Körmann, J. Neugebauer, and T. Hickel. Ab initio phase stabilities of Ce-based hard magnetic materials and comparison with experimental phase diagrams. *Physical Review Materials*, 3(8), aug 2019. doi:[10.1103/physrevmaterials.3.084407](https://doi.org/10.1103/physrevmaterials.3.084407).
- [140] J. Jin, Y. Zhang, G. Bai, Z. Qian, C. Wu, T. Ma, B. Shen, and M. Yan. Manipulating Ce Valence in $\text{RE}_2\text{Fe}_{14}\text{B}$ Tetragonal Compounds by La-Ce Co-doping: Resultant Crystallographic and Magnetic Anomaly. *Scientific Reports*, 6(1), jul 2016. doi:[10.1038/srep30194](https://doi.org/10.1038/srep30194).
- [141] C. Zhou, F. E. Pinkerton, and J. F. Herbst. Magnetic properties of $\text{CeFe}_{11-x}\text{Co}_x\text{Ti}$ with ThMn_{12} structure. *Journal of Applied Physics*, 115(17) : 17C716, may 2014. doi : [10.1063/1.4863382](https://doi.org/10.1063/1.4863382).
- [142] S. L. Tang, L. Y. Lui, Z. Q. Jin, J. R. Zhang, S. Y. Zhang, and Y. W. Du. Investigation of phase formation of $\text{RFe}_{11}\text{V}_{1-x}\text{Ti}_x$ (R = Pr, Ce) compounds. *Journal of Materials Science*, 35(9):2241–2244, 2000. doi:[10.1023/a:1004726926274](https://doi.org/10.1023/a:1004726926274).
- [143] O. Isnard, S. Miraglia, M. Guillot, and D. Fruchart. Hydrogen effects on the magnetic properties of RFe_{11}Ti compounds. *Journal of Alloys and Compounds*, 275-277:637–641, jul 1998. doi:[10.1016/s0925-8388\(98\)00409-5](https://doi.org/10.1016/s0925-8388(98)00409-5).
- [144] Q. Pan, Z.-X. Liu, and Y.-C. Yang. Structural and magnetic properties of $\text{Ce}(\text{Fe,M})_{12}\text{N}_x$ interstitial compounds, M=Ti, V, Cr, and Mo. *Journal of Applied Physics*, 76(10):6728–6730, nov 1994. doi:[10.1063/1.358184](https://doi.org/10.1063/1.358184).
- [145] A. M. Gabay and G. C. Hadjipanayis. ThMn_{12} -type structure and uniaxial magnetic anisotropy in $\text{ZrFe}_{10}\text{Si}_2$ and $\text{Zr}_{1-x}\text{Ce}_x\text{Fe}_{10}\text{Si}_2$ alloys. *Journal of Alloys and Compounds*, 657:133–137, feb 2016. doi:[10.1016/j.jallcom.2015.10.073](https://doi.org/10.1016/j.jallcom.2015.10.073).

-
- [146] A. Galler, S. Ener, F. Maccari, I. Dirba, K. P. Skokov, O. Gutfleisch, S. Biermann, and L. V. Pourovskii. Intrinsically weak magnetic anisotropy of cerium in potential hard-magnetic intermetallics. *npj Quantum Materials*, 6(1), jan 2021. doi:[10.1038/s41535-020-00301-6](https://doi.org/10.1038/s41535-020-00301-6).
- [147] M. Akayama, H. Fujii, K. Yamamoto, and K. Tatami. Physical properties of nitrogenated RFe₁₁Ti intermetallic compounds (R=Ce, Pr and Nd) with ThMn₁₂-type structure. *Journal of Magnetism and Magnetic Materials*, 130(1-3):99–107, feb 1994. doi:[10.1016/0304-8853\(94\)90662-9](https://doi.org/10.1016/0304-8853(94)90662-9).
- [148] F. Maccari, S. Ener, D. Koch, I. Dirba, K. P. Skokov, E. Bruder, L. Schäfer, and O. Gutfleisch. Correlating changes of the unit cell parameters and microstructure with magnetic properties in the CeFe₁₁Ti compound. *Journal of Alloys and Compounds*, 867:158805, jun 2021. doi:[10.1016/j.jallcom.2021.158805](https://doi.org/10.1016/j.jallcom.2021.158805).
- [149] C. Zhou, D. Haddad, R. S. Kukreja, F. E. Pinkerton, K. Sun, and M. J. Kramer. Magnetic Hardening of CeFe₁₁Ti and the Effect of TiC Addition. *IEEE Transactions on Magnetics*, 51(4):1–4, apr 2015. doi:[10.1109/tmag.2014.2361644](https://doi.org/10.1109/tmag.2014.2361644).
- [150] C. Zhou and F. E. Pinkerton. Magnetic properties of Ce-Nd-Fe-Mo alloys and their nitrides. *Journal of Magnetism and Magnetic Materials*, 369:127–131, nov 2014. doi:[10.1016/j.jmmm.2014.06.041](https://doi.org/10.1016/j.jmmm.2014.06.041).
- [151] V. Øygarden, J. Rial, A. Bollero, and S. Deledda. Phase-pure τ -MnAlC produced by mechanical alloying and a one-step annealing route. *Journal of Alloys and Compounds*, 779:776–783, mar 2019. doi:[10.1016/j.jallcom.2018.11.175](https://doi.org/10.1016/j.jallcom.2018.11.175).
- [152] J. Yang, W. Yang, Z. Shao, D. Liang, H. Zhao, Y. Xia, and Y. Yang. Mn-based permanent magnets. *Chinese Physics B*, 27(11):117503, nov 2018. doi:[10.1088/1674-1056/27/11/117503](https://doi.org/10.1088/1674-1056/27/11/117503).
- [153] S. Kontos, A. Ibrayeva, J. Leijon, G. Mörée, A. E. Frost, L. Schönström, K. Gunnarsson, P. Svedlindh, M. Leijon, and S. Eriksson. An Overview of MnAl Permanent Magnets with a Study on Their Potential in Electrical Machines. *Energies*, 13(21):5549, oct 2020. doi:[10.3390/en13215549](https://doi.org/10.3390/en13215549).
- [154] K. Patel, J. Zhang, and S. Ren. Rare-earth-free high energy product manganese-based magnetic materials. *Nanoscale*, 10(25):11701–11718, 2018. doi:[10.1039/c8nr01847b](https://doi.org/10.1039/c8nr01847b).
- [155] J. M. D. Coey. New permanent magnets; manganese compounds. *Journal of Physics: Condensed Matter*, 26(6):064211, jan 2014. doi:[10.1088/0953-8984/26/6/064211](https://doi.org/10.1088/0953-8984/26/6/064211).
- [156] T. Woodcock. Recent Progress in the Development of MnAl-C Magnets - Invited Talk. In *26th International Workshop on Rare-Earth and Future Permanent Magnets and their Applications (REPM2021) - Virtual Conference*, June 2021.
- [157] S. Zhao, Y. Wu, Z. Jiao, Y. Jia, Y. Xu, J. Wang, T. Zhang, and C. Jiang. Evolution of Intrinsic Magnetic Properties in L1₀ Mn-Al Alloys Doped with Substitutional Atoms and Correlated Mechanism: Experimental and Theoretical Studies. *Physical Review Applied*, 11(6), jun 2019. doi:[10.1103/physrevapplied.11.064008](https://doi.org/10.1103/physrevapplied.11.064008).
-

-
- [158] Q. Zeng, I. Baker, J. B. Cui, and Z. C. Yan. Structural and magnetic properties of nanostructured Mn-Al-C magnetic materials. *Journal of Magnetism and Magnetic Materials*, 308(2):214–226, jan 2007. doi:[10.1016/j.jmmm.2006.05.032](https://doi.org/10.1016/j.jmmm.2006.05.032).
- [159] J. Z. Wei, Z. G. Song, Y. B. Yang, S. Q. Liu, H. L. Du, J. Z. Han, D. Zhou, C. S. Wang, Y. C. Yang, A. Franz, D. Töbrens, and J. B. Yang. τ -MnAl with high coercivity and saturation magnetization. *AIP Advances*, 4(12):127113, dec 2014. doi:[10.1063/1.4903773](https://doi.org/10.1063/1.4903773).
- [160] R. Gavrea, R. Hirian, S. Mican, D. Benea, O. Isnard, M. Coldea, and V. Pop. Structural, electronic and magnetic properties of the $\text{Mn}_{54-x}\text{Al}_{46}\text{Ti}_x$ ($x=2; 4$) alloys. *Intermetallics*, 82:101–106, mar 2017. doi:[10.1016/j.intermet.2016.11.012](https://doi.org/10.1016/j.intermet.2016.11.012).
- [161] Z. Xiang, X. Wang, Y. Song, L. Yu, E. Cui, B. Deng, D. Batalu, and W. Lu. Effect of cooling rates on the microstructure and magnetic properties of MnAl permanent magnetic alloys. *Journal of Magnetism and Magnetic Materials*, 475:479–483, apr 2019. doi:[10.1016/j.jmmm.2018.12.003](https://doi.org/10.1016/j.jmmm.2018.12.003).
- [162] F. Bittner, L. Schultz, and T. G. Woodcock. The role of the interface distribution in the decomposition of metastable $\text{L1}_0\text{-Mn}_{54}\text{Al}_{46}$. *Journal of Alloys and Compounds*, 727:1095–1099, dec 2017. doi:[10.1016/j.jallcom.2017.08.197](https://doi.org/10.1016/j.jallcom.2017.08.197).
- [163] W. Lu, J. Niu, T. Wang, K. Xia, Z. Xiang, Y. Song, Z. Mi, W. Zhang, W. Tian, and Y. Yan. Phase transformation kinetics and microstructural evolution of MnAl permanent magnet alloys. *Journal of Alloys and Compounds*, 685:992–996, nov 2016. doi:[10.1016/j.jallcom.2016.06.285](https://doi.org/10.1016/j.jallcom.2016.06.285).
- [164] D. Palanisamy, D. Raabe, and B. Gault. On the compositional partitioning during phase transformation in a binary ferromagnetic MnAl alloy. *Acta Materialia*, 174:227–236, aug 2019. doi:[10.1016/j.actamat.2019.05.037](https://doi.org/10.1016/j.actamat.2019.05.037).
- [165] V. V. Popov, F. Maccari, I. A. Radulov, A. Kovalevsky, A. Katz-Demyanetz, and M. Bamberger. Microstructure and magnetic properties of Mn-Al-C permanent magnets produced by various techniques. *Manufacturing Review*, 8:10, 2021. doi:[10.1051/mfreview/2021008](https://doi.org/10.1051/mfreview/2021008).
- [166] P.-Z. Si, H.-D. Qian, C.-J. Choi, J. Park, S. Han, H.-L. Ge, and K. Shinde. In situ Observation of Phase Transformation in MnAl(C) Magnetic Materials. *Materials*, 10(9):1016, aug 2017. doi:[10.3390/ma10091016](https://doi.org/10.3390/ma10091016).
- [167] Jorg M. K. Wiezorek, Andreas K. Kulovits, Cagatay Yanar, and William A. Soffa. Grain Boundary Mediated Displacive-Diffusional Formation of τ -Phase MnAl. *Metallurgical and Materials Transactions A*, 42(3):594–604, may 2010. doi:[10.1007/s11661-010-0308-1](https://doi.org/10.1007/s11661-010-0308-1).
- [168] P. Müllner, B. E. Bürgler, H. Heinrich, A. S. Sologubenko, and G. Kostorz. Observation of the shear mode of the $\epsilon \rightarrow \tau$ phase transformation in a Mn-Al-C single crystal. *Philosophical Magazine Letters*, 82(2):71–79, feb 2002. doi:[10.1080/09500830110103225](https://doi.org/10.1080/09500830110103225).
-

-
- [169] C. Yanar, J. M. K. Wiezorek, W. A. Soffa, and V. Radmilovic. Massive transformation and the formation of the ferromagnetic $L1_0$ phase in manganese-aluminum-based alloys. *Metallurgical and Materials Transactions A*, 33(8):2413–2423, aug 2002. doi:[10.1007/s11661-002-0363-3](https://doi.org/10.1007/s11661-002-0363-3).
- [170] S. Zhao, Y. Wu, C. Zhang, J. Wang, Z. Fu, R. Zhang, and C. Jiang. Stabilization of τ -phase in carbon-doped MnAl magnetic alloys. *Journal of Alloys and Compounds*, 755:257–264, jul 2018. doi:[10.1016/j.jallcom.2018.04.318](https://doi.org/10.1016/j.jallcom.2018.04.318).
- [171] P. Zhao, L. Feng, K. Nielsch, and T. G. Woodcock. Microstructural defects in hot deformed and as-transformed τ -MnAl-C. *Journal of Alloys and Compounds*, 852:156998, jan 2021. doi:[10.1016/j.jallcom.2020.156998](https://doi.org/10.1016/j.jallcom.2020.156998).
- [172] Y. Jia, Y. Wu, S. Zhao, S. Zuo, K. P. Skokov, O. Gutfleisch, C. Jiang, and H. Xu. $L1_0$ rare-earth-free permanent magnets: The effects of twinning versus dislocations in Mn-Al magnets. *Physical Review Materials*, 4(9), sep 2020. doi:[10.1103/physrevmaterials.4.094402](https://doi.org/10.1103/physrevmaterials.4.094402).
- [173] S. Arapan, P. Nieves, S. Cuesta-López, M. Gusenbauer, H. Oezelt, T. Schrefl, E. K. Delczeg-Czirjak, H. C. Herper, and O. Eriksson. Influence of antiphase boundary of the MnAl τ -phase on the energy product. *Physical Review Materials*, 3(6), jun 2019. doi:[10.1103/physrevmaterials.3.064412](https://doi.org/10.1103/physrevmaterials.3.064412).
- [174] D. Palanisamy, A. Kovács, O. Hegde, R. E. Dunin-Borkowski, D. Raabe, T. Hickel, and B. Gault. Influence of crystalline defects on magnetic nanodomains in a rare-earth-free magnetocrystalline anisotropic alloy. *Physical Review Materials*, 5(6), jun 2021. doi:[10.1103/physrevmaterials.5.064403](https://doi.org/10.1103/physrevmaterials.5.064403).
- [175] J. Rial, P. Švec, P. Švec, A. Bollero, and S. Deledda. Coercivity development in MnAl ribbons by microstructural modifications achieved through cold-rolling process. *Journal of Magnetism and Magnetic Materials*, 529:167826, jul 2021. doi:[10.1016/j.jmmm.2021.167826](https://doi.org/10.1016/j.jmmm.2021.167826).
- [176] F. Bittner, J. Freudenberger, L. Schultz, and T. G. Woodcock. The impact of dislocations on coercivity in $L1_0$ -MnAl. *Journal of Alloys and Compounds*, 704:528–536, may 2017. doi:[10.1016/j.jallcom.2017.02.028](https://doi.org/10.1016/j.jallcom.2017.02.028).
- [177] H. Zijlstra and H. B. Haanstra. Evidence by Lorentz Microscopy for Magnetically Active Stacking Faults in MnAl Alloy. *Journal of Applied Physics*, 37(7):2853–2856, jun 1966. doi:[10.1063/1.1782138](https://doi.org/10.1063/1.1782138).
- [178] J. Landuyt, G. Tendeloo, J. J. Broek, H. Donkersloot, and H. Zijlstra. Defect structure and magnetic properties of MnAl permanent magnet materials. *IEEE Transactions on Magnetics*, 14(5):679–681, sep 1978. doi:[10.1109/tmag.1978.1059949](https://doi.org/10.1109/tmag.1978.1059949).
- [179] M. Gusenbauer, A. Kovacs, H. Oezelt, J. Fischbacher, P. Zhao, T. G. Woodcock, and T. Schrefl. Insights into MnAl-C nano-twin defects by micromagnetic characterization. *Journal of Applied Physics*, 129(9):093902, mar 2021. doi:[10.1063/5.0035387](https://doi.org/10.1063/5.0035387).
-

-
- [180] D. Palanisamy, D. Raabe, and B. Gault. Elemental segregation to twin boundaries in a MnAl ferromagnetic Heusler alloy. *Scripta Materialia*, 155:144–148, oct 2018. doi:[10.1016/j.scriptamat.2018.06.037](https://doi.org/10.1016/j.scriptamat.2018.06.037).
- [181] M. V. Gorshenkov, D. Y. Karpenkov, R. V. Sundeev, V. V. Cheverikin, and I. V. Shchetinin. Magnetic properties of Mn-Al alloy after HPT deformation. *Materials Letters*, 272:127864, aug 2020. doi:[10.1016/j.matlet.2020.127864](https://doi.org/10.1016/j.matlet.2020.127864).
- [182] P. Z. Si, J. T. Lim, J. Park, H. H. Lee, H. Ge, H. Lee, S. Han, H. S. Kim, and C. Jin Choi. High Coercivity in MnAl Disc Prepared by Severe Plastic Deformation. *physica status solidi (b)*, 257(3):1900356, sep 2019. doi:[10.1002/pssb.201900356](https://doi.org/10.1002/pssb.201900356).
- [183] J. Y. Law, J. Rial, M. Villanueva, N. López, J. Camarero, L. G. Marshall, J. S. Blázquez, J. M. Borrego, V. Franco, A. Conde, L. H. Lewis, and A. Bollero. Study of phases evolution in high-coercive MnAl powders obtained through short milling time of gas-atomized particles. *Journal of Alloys and Compounds*, 712:373–378, jul 2017. doi:[10.1016/j.jallcom.2017.04.038](https://doi.org/10.1016/j.jallcom.2017.04.038).
- [184] H. Jian, K. P. Skokov, and O. Gutfleisch. Microstructure and magnetic properties of Mn-Al-C alloy powders prepared by ball milling. *Journal of Alloys and Compounds*, 622:524–528, feb 2015. doi:[10.1016/j.jallcom.2014.10.138](https://doi.org/10.1016/j.jallcom.2014.10.138).
- [185] R. Madugundo, O. Koylu-Alkan, and G. C. Hadjipanayis. Bulk Mn-Al-C permanent magnets prepared by various techniques. *AIP Advances*, 6(5):056009, may 2016. doi:[10.1063/1.4943242](https://doi.org/10.1063/1.4943242).
- [186] H. Fang, S. Kontos, J. Ångström, J. Cedervall, P. Svedlindh, K. Gunnarsson, and M. Sahlberg. Directly obtained τ -phase MnAl, a high performance magnetic material for permanent magnets. *Journal of Solid State Chemistry*, 237:300–306, may 2016. doi:[10.1016/j.jssc.2016.02.031](https://doi.org/10.1016/j.jssc.2016.02.031).
- [187] P.-Z. Si, H.-D. Qian, C.-J. Choi, J. Park, and H.-L. Ge. A novel method for measuring the phase transformation temperature and enhanced coercivity in cold-rolled MnAlC_x (x=0-5) alloys. *Journal of Magnetism and Magnetic Materials*, 451:540–545, apr 2018. doi:[10.1016/j.jmmm.2017.11.094](https://doi.org/10.1016/j.jmmm.2017.11.094).
- [188] A. Chaturvedi, R. Yaqub, and I. Baker. Microstructure and Magnetic Properties of Bulk Nanocrystalline MnAl. *Metals*, 4(1):20–27, jan 2014. doi:[10.3390/met4010020](https://doi.org/10.3390/met4010020).
- [189] S. Bance, F. Bittner, T. G. Woodcock, L. Schultz, and T. Schrefl. Role of twin and anti-phase defects in MnAl permanent magnets. *Acta Materialia*, 131:48–56, jun 2017. doi:[10.1016/j.actamat.2017.04.004](https://doi.org/10.1016/j.actamat.2017.04.004).
- [190] L. Feng, J. Freudenberger, T. Mix, K. Nielsch, and T. G. Woodcock. Rare-earth-free MnAl-C-Ni permanent magnets produced by extrusion of powder milled from bulk. *Acta Materialia*, 199:155–168, oct 2020. doi:[10.1016/j.actamat.2020.08.031](https://doi.org/10.1016/j.actamat.2020.08.031).

-
- [191] Y. Jia, Y. Wu, S. Zhao, J. Wang, and C. Jiang. Relation between solidification microstructure and coercivity in MnAl permanent-magnet alloys. *Intermetallics*, 96:41–48, may 2018. doi:[10.1016/j.intermet.2018.02.011](https://doi.org/10.1016/j.intermet.2018.02.011).
- [192] R. McCurrie, J. Rickman, P. Dunk, and D. Hawkrigde. Dependence of the permanent magnet properties of Mn₅₅Al₄₅ on particle size. *IEEE Transactions on Magnetics*, 14(5):682–684, sep 1978. doi:[10.1109/tmag.1978.1059950](https://doi.org/10.1109/tmag.1978.1059950).
- [193] J. P. Jakubovics and T. W. Jolly. The effect of crystal defects on the domain structure of Mn-Al alloys. *Physica B+C*, 86-88:1357–1359, jan 1977. doi:[10.1016/0378-4363\(77\)90910-x](https://doi.org/10.1016/0378-4363(77)90910-x).
- [194] S. H. Nie, L. J. Zhu, J. Lu, D. Pan, H. L. Wang, X. Z. Yu, J. X. Xiao, and J. H. Zhao. Perpendicularly magnetized τ -MnAl (001) thin films epitaxied on GaAs. *Applied Physics Letters*, 102(15):152405, apr 2013. doi:[10.1063/1.4801932](https://doi.org/10.1063/1.4801932).
- [195] C. Zhang, T. Zhang, J. Wang, S. Zhao, Y. Wu, and C. Jiang. Anisotropic single-variant of (Mn₅₄Al₄₆)₉₇C₃. *Scripta Materialia*, 143:72–76, jan 2018. doi:[10.1016/j.scriptamat.2017.09.008](https://doi.org/10.1016/j.scriptamat.2017.09.008).
- [196] B. Gault, A. Chiamonti, O. Cojocar-Mirédin, P. Stender, R. Dubosq, C. Freysoldt, S. K. Makineni, T. Li, M. Moody, and J. M. Cairney. Atom probe tomography. *Nature Reviews Methods Primers*, 1(1), jul 2021. doi:[10.1038/s43586-021-00047-w](https://doi.org/10.1038/s43586-021-00047-w).
- [197] O. Gutfleisch. Hysteresis design of magnetic materials for efficient energy conversion. Online Planary Lecture of the European Magnetism Association, May 2021. URL <http://magnetism.eu/184-recordings-of-ema-plenary-lectures-2021.htm>.
- [198] L. M. Moreno-Ramírez, C. Romero-Muniz, J. Y. Law, V. Franco, A. Conde, I. A. Radulov, F. Maccari, K. P. Skokov, and O. Gutfleisch. The role of Ni in modifying the order of the phase transition of La(Fe,Ni,Si)₁₃. *Acta Materialia*, 160:137–146, nov 2018. doi:[10.1016/j.actamat.2018.08.054](https://doi.org/10.1016/j.actamat.2018.08.054).
- [199] A. Margarian, J. B. Dunlop, R. K. Day, and W. Kalceff. Phase equilibria in the Fe-rich corner of the Nd-Fe-Ti ternary alloy system at 1100°C. *Journal of Applied Physics*, 76(10):6153–6155, nov 1994. doi:[10.1063/1.358338](https://doi.org/10.1063/1.358338).
- [200] K. Skokov, A. Grushishev, A. Khokholkov, Yu Pastushenkov, N. Pankratov, T. Ivanova, and S. Nikitin. Magnetic properties of Gd₃Fe_xTi₃ (x=34, 33, ..., 24), TbFe₁₁Ti and TbFe₁₀Ti single crystals. *Journal of Magnetism and Magnetic Materials*, 272-276:374–375, may 2004. doi:[10.1016/j.jmmm.2003.11.147](https://doi.org/10.1016/j.jmmm.2003.11.147).
- [201] R. Martinez-Casado, A. Dasmahapatra, M. F. Sgroi, C. Romero-Muniz, Heike C. Herper, Olga Yu Vekilova, A. M. Ferrari, D. Pullini, J. Desmarais, and L. Maschio. The CeFe₁₁Ti permanent magnet: a closer look at the microstructure of the compound. *Journal of Physics: Condensed Matter*, 31(50): 505505, sep 2019. doi:[10.1088/1361-648x/ab4096](https://doi.org/10.1088/1361-648x/ab4096).

-
- [202] M. Hatherly F.J. Humphreys. *Recrystallization and Related Annealing Phenomena*. Elsevier, 2004. doi:[10.1016/b978-0-08-044164-1.x5000-2](https://doi.org/10.1016/b978-0-08-044164-1.x5000-2).
- [203] A. Zhilyaev and T. Langdon. Using high-pressure torsion for metal processing: Fundamentals and applications. *Progress in Materials Science*, 53(6):893–979, aug 2008. doi:[10.1016/j.pmatsci.2008.03.002](https://doi.org/10.1016/j.pmatsci.2008.03.002).
- [204] L. Allen, A. O’Connell, and V. Kiermer. How can we ensure visibility and diversity in research contributions? How the Contributor Role Taxonomy (CRediT) is helping the shift from authorship to contributorship. *Learned Publishing*, 32(1):71–74, jan 2019. doi:[10.1002/leap.1210](https://doi.org/10.1002/leap.1210).

5 Cumulative Part of the Thesis

In this chapter, the statement of personal contribution will be given for all authors of each of the four selected publications, followed by the reproduction of the full-text of these publications. The statement contribution will be based on the definitions used in the Contributor Roles Taxonomy (CRediT), as given in the Table 5.1 [204].

Table 5.1: Statement of personal contribution according to Contributor Roles Taxonomy (CRediT) [204].

Term	Definition
Conceptualization	Ideas; formulation or evolution of overarching research goals and aims
Methodology	Development or design of methodology; creation of models
Software	Programming, software development; implementation of the computer code and supporting algorithms
Formal analysis	Application of statistical, mathematical or other formal techniques to analyse data
Investigation	Conducting a research and investigation process, performing experiments
Writing - original draft	Preparation, creation and/or presentation of the published work, writing the initial draft
Writing - review and editing	Critical review, commentary or revision - including pre- or post-publication stages
Visualization	Preparation, creation and/or presentation specifically visualization/data presentation
Supervision	Oversight and leadership responsibility for the research plan and execution
Funding acquisition	Acquisition of the financial support for the project leading to this publication

5.1 Statement of Personal Contribution

Publication A: Rapid solidification of $\text{Nd}_{1+X}\text{Fe}_{11}\text{Ti}$ compounds: Phase formation and magnetic properties

Authors: **Fernando Maccari**, Lukas Schäfer, Iliya A. Radulov, Léopold V. B. Diop, Semih Ener, Enrico Bruder, Konstantin P. Skokov and Oliver Gutfleisch

Journal: *Acta Materialia*, 180(2019), p.15-23 - DOI: 10.1016/j.actamat.2019.08.057

F. Maccari: Methodology, Investigation, Formal analysis, Writing - Original Draft preparation, Visualization, Writing - Review & Editing; **L. Schäfer:** Investigation; **I. A. Radulov:** Writing - Review & Editing; **L. V. B. Diop:** Investigation, Writing - Review & Editing; **S. Ener:** Writing - Review & Editing; **E. Bruder:** Investigation, Writing - Review & Editing; **K. P. Skokov:** Methodology, Writing - Review & Editing; **O. Gutfleisch:** Writing - Review & Editing, Supervision, Funding acquisition.

Publication B: Correlating changes of the unit cell parameters and microstructure with magnetic properties in the CeFe₁₁Ti compound

Authors: **Fernando Maccari**, Semih Ener, David Koch, Imants Dirba, Konstantin P. Skokov, Enrico Bruder, Lukas Schäfer and Oliver Gutfleisch

Journal: *Journal of Alloys and Compounds*, vol. 867(2021) 158805 - DOI: 10.1016/j.jallcom.2021.158805

F. Maccari: Methodology, Investigation, Formal analysis, Writing - Review & Editing; **S. Ener:** Conceptualization, Investigation, Formal analysis, Writing - Original Draft preparation, Visualization; **D. Koch:** Investigation; **I. Dirba:** Methodology, Investigation, Writing - Review & Editing; **K.P. Skokov:** Investigation; **E. Bruder:** Investigation, Writing - Review & Editing; **L. Schäfer:** Investigation. **O. Gutfleisch:** Writing - Review & Editing, Supervision, Funding acquisition.

Publication C: Twins – A weak link in the magnetic hardening of ThMn₁₂-type permanent magnets

Authors: Semih Ener, Konstantin P. Skokov, Dhanalakshmi Palanisamy, Thibaut Devillers, Johann Fischbacher, Gabriel Gomez Eslava, **Fernando Maccari**, Lukas Schäfer, Léopold V. B. Diop, Iliya A. Radulov, Baptist Gault, Gino Hrkac, Nora M. Dempsey, Thomas Schrefl, Dierk Raabe and Oliver Gutfleisch

Journal: *Acta Materialia*, vol. 214(2021) 116968 - DOI: 10.1016/j.actamat.2021.116968

S. Ener: Methodology, Investigation, Formal analysis, Conceptualization, Writing - Original Draft preparation, Writing - Review & Editing; **K. P. Skokov:** Conceptualization, Writing - Original Draft preparation, Writing - Review & Editing; **D. Palanisamy:** Investigation, Visualization, Writing - Original Draft preparation, Writing - Review & Editing; **T. Devillers:** Investigation, Visualization, Writing - Original Draft preparation; **J. Fischbacher:** Software, Visualization, Writing - Original Draft preparation, Writing - Review & Editing; **G. G. Eslava:** Investigation, Writing - Original Draft preparation, Writing - Review & Editing; **F. Maccari:** Investigation, Formal analysis, Visualization, Writing - Original Draft preparation, Writing - Review & Editing; **L. Schäfer:** Investigation, Visualization; **L. V. B. Diop:** Investigation; **I. A. Radulov:** Investigation; **B. Gault:** Investigation, Supervision, Visualization, Writing - Review & Editing; **G. Hrkac:** Software, Writing - Review & Editing; **N. M. Dempsey:** Supervision, Writing - Original Draft preparation; **T. Schrefl:** Software, Writing - Original Draft preparation, Writing - Review & Editing; **D. Raabe:** Supervision, Writing - Original Draft preparation; **O. Gutfleisch:** Writing - Review & Editing, Supervision, Funding acquisition.

Publication D: Microstructure and magnetic properties of Mn-Al-C permanent magnets produced by various techniques

Authors: Vladimir V. Popov. Jr., **Fernando Maccari**, Iliya A. Radulov, Aleksey Kovalevsky, Alexander Katz-Demyanetz and Menahem Bamberger - Both V.V.Popov Jr. and F.Maccari equally contributed to this work.

Journal: *Manufacturing Review*, 8, 10 (2021) - DOI: 10.1051/mfreview/2021008

V. V. Popov Jr.: Methodology, Investigation, Conceptualization, Supervision, Writing - Original Draft preparation, Writing - Review & Editing; **F. Maccari:** Methodology, Investigation, Conceptualization, Visualization, Writing - Original Draft preparation, Writing - Review & Editing; **I. A. Radulov:** Investigation, Visualization, Writing - Original Draft preparation; **A. Kovalevsky:** Investigation, Visualization; **A. Katz-Demyanetz:** Investigation, Visualization; **M. Bamberger:** Investigation, Supervision, Funding acquisition.

5.2 Full-text of Selected Publications

In the following, the full-text of the selected publications will be given, including supplementary materials when it is applicable.

5.2.1 Full-text of Selected Publication A

Reproduced full text article with permission from Elsevier.

Copyright (2019), *Acta Materialia*.



Full length article

Rapid solidification of Nd_{1+x}Fe₁₁Ti compounds: Phase formation and magnetic properties



F. Maccari^{a,*}, L. Schäfer^a, I. Radulov^a, L.V.B. Diop^{a,b}, S. Ener^a, E. Bruder^c, K. Skokov^a, O. Gutfleisch^a

^a Functional Materials, Department of Material Science, Technische Universität Darmstadt, 64287, Darmstadt, Germany

^b Institut Jean Lamour, CNRS-Université de Lorraine, 2 allée André Guinier, BP 50840 54011 Nancy, France

^c Physical Metallurgy, Department of Material Science, Technische Universität Darmstadt, 64287, Darmstadt, Germany

ARTICLE INFO

Article history:

Received 1 April 2019

Received in revised form

15 August 2019

Accepted 28 August 2019

Available online 31 August 2019

Keywords:

ThMn₁₂ structure

NdFe₁₁Ti

Magnetic properties

Twin boundaries

ABSTRACT

The effects of compositional variations and different annealing regimes in Nd(Fe,Ti)₁₂ alloys were studied in terms of phase formation and magnetic properties analysis. Nd_xFe₁₁Ti (x = 1.05, 1.10, 1.15, 1.20) alloys were produced by rapid solidification through suction casting technique. The effect of Nd content and post annealing were investigated in the temperature range of 700–1200 °C. Single 1:12 phase samples were obtained at temperatures between 1150 and 1200 °C for compositions with Nd concentration of 1.15 and 1.20. Intrinsic magnetic properties and magnetization reversal were studied for 1:12 single phase samples, revealing uniaxial anisotropy with anisotropy field (H_A) of 1.08T and saturation magnetization of 137 Am²kg⁻¹ at room temperature. In addition, the demagnetization mechanism in bulk polycrystalline samples was analyzed by means of Kerr microscopy under applied magnetic fields. Magnetization reversal process starts at the twin boundary, which acts as a nucleation center for the reversal domain, and coupling between adjacent grains is also observed. These may be part of the reasons for the observed low coercivity in the NdFe₁₁Ti systems. The findings of the present study leads to a better understanding of the relation between magnetic properties and microstructure, and can open new strategies to obtain coercivity in this 1:12 phase system and, possibly, in the corresponding nitride.

© 2019 Acta Materialia Inc. Published by Elsevier Ltd. All rights reserved.

1. Introduction

The development of magnetic materials and their processing are essential and indispensable for improving the efficiency of devices in electric power generation, air conditioning, conversion, transportation, and other energy-use sectors of economy [1]. Many of these applications requires high performance magnets, like (Nd,Dy)-Fe-B and Sm-Co alloys, which are based on strategic and critical elements [2,3].

The criticality issue of Co and rare-earth (RE) elements, such as Nd and Dy, in combination with the increasing demand for high performance permanent magnets on the world market, triggered intensive worldwide research activities [4]. The main goal is to find new hard magnetic materials possessing comparable performance to Nd₂Fe₁₄B but employing significantly reduced Nd and Dy. The reduction of the RE content relative to the Fe content with respect

to the benchmark Nd₂Fe₁₄B permanent magnet would be important steps forward in terms of cost reduction and supply reliability [4–6]. Most recently, intermetallic compounds based on the tetragonal ThMn₁₂ prototype crystal structure have attracted renewed interest in the field of permanent magnets because of the favorable composition ratio RE:Fe = 1:12, their relatively high Curie temperature, saturation magnetization and magnetocrystalline anisotropy [5,7].

Recent work of Y. Hirayama et al. [8], shows the possibility to achieve better intrinsic magnetic properties in NdFe₁₂N_x systems (in ThMn₁₂-type structure) in thin films. Unfortunately, it is not possible to obtain the binary system in bulk form, raising the necessity to substitute part of the iron atoms by other transition metal (e.g. Ti, V, Cr, Mo, W and Si) for this purpose.

Different alloys on the REFe_{12-x}M_x system have been studied, regarding different rare-earths (RE) and the nonmagnetic element (M) used to stabilize the phase, which can be found elsewhere [9–15]. Among the Fe-based 1:12 systems already reported, the ones focusing on Nd and Ti are very promising based on the

* Corresponding author.

E-mail address: maccari@fm.tu-darmstadt.de (F. Maccari).

intrinsic magnetic properties of the corresponding nitrides, which can reach Curie temperature (T_C) values above 700 K and anisotropy field (H_A) up to 8T at room temperature [16–18]. Despite the very attractive intrinsic properties, no reasonable coercivity was obtained for these compounds, even though different approaches having been employed for the precursor synthesis, like melt spinning, mechanical alloying, conventional melting (induction and arc melting) among different annealing and nitrogenation conditions [16–23]. Since the $NdFe_{11}Ti$ phase is described to be stable in a broad temperature range (from 800 to 1200 °C), understanding the formation of the 1:12 structure and the existence of competing phases is imperative to obtain high purity precursor for accurate magnetic properties determination and further strategies for improvement, including nitrogenation [12,24,25]. Besides the phase purity, the relation between microstructure and the extrinsic magnetic properties are an important factor for the development of this compound as a permanent magnet candidate [7].

In the present work, we focus on the phase stability of the $Nd_xFe_{11}Ti$ precursor, synthesized by rapid solidification, through a systematic investigation on the ratio of the RE content and annealing temperature. The formation of the desired 1:12 phase in relation to the competing $Nd_2(Fe,Ti)_{17}$ and $Nd_3(Fe,Ti)_{29}$ phases (hereafter 2:17 and 3:29, respectively) is evaluated and discussed. Microstructural, structural and magnetic properties are investigated. Magnetization reversal mechanism of $NdFe_{11}Ti$ system is discussed by using Kerr microscopy and the possible reasons for the observed low coercivity are proposed. We believe that the phase formation mechanisms and microstructure peculiarities, disclosed in this work, are of interest not only for this particular Nd-Fe-Ti system, but the knowledge gained here may be useful for understanding and generalizing the hysteresis phenomena in other related systems, such as Sm-Fe-Ti, Pr-Fe-Ti and Ce-Fe-Ti.

2. Experimental procedure

$Nd_xFe_{11}Ti$ ($x = 1.05, 1.10, 1.15$ and 1.20) alloys were prepared by melting high-purity starting elements in an induction furnace under a purified argon gas atmosphere. The resulting ingots were suction-casted (arc melting/suction casting setup MAM-1 Edmund Bühler GmbH) from melt into bulk rectangular ingots of thickness 0.5 mm, to ensure fast solidification/cooling. The samples were wrapped in Mo foil, sealed in quartz ampules under argon atmosphere and annealed at 12 different temperatures. Within the temperature range, from 700 to 950 °C (see Table 2), 12 h annealing was employed and for the temperature range, 1000–1200 °C, 2 h of dwelling was done. Since the sample annealed at 1200 °C was partially molten and reacted with the foil, one additional annealing was made at 1175 °C. All samples were quenched in water after annealing to prevent any possible decomposition and to retain the phases which are present at the annealing temperature.

To investigate the phase formation and microstructure, the samples were analyzed using scanning electron microscope (SEM - Tescan VEGA 3 and FEG-SEM JEOL JSM-7600F) with backscattered electrons (BSE) detector. In addition, energy-dispersive X-ray

Table 1
Chemical composition obtained by EDS analysis for the three major phases in $Nd_{1.15}Fe_{11}Ti$. Ten points were measured for each phase and for calculation of standard deviation.

Phase	Composition (at.%)		
	Nd	Fe	Ti
$Nd(Fe,Ti)_{12}$	8.1 ± 0.1	balance	7.7 ± 0.1
$Nd_2(Fe,Ti)_{17}$	10.9 ± 0.1	balance	3.7 ± 0.1
$Nd_3(Fe,Ti)_{29}$	9.8 ± 0.1	balance	5.0 ± 0.2

Table 2

Present phases in different annealing conditions for the $Nd_{1.15}Fe_{11}Ti$ composition.

Condition	Phases Identified
Suction casted	1:12, α -Fe, Nd-rich
700 °C-12 h	1:12, 2:17, α -Fe, Nd-rich
750 °C -12 h	1:12, 2:17, α -Fe, Nd-rich
800 °C -12 h	1:12, Nd-rich ^a , α -Fe ^a
850 °C -12 h	1:12, 2:17, α -Fe, Nd-rich ^a
900 °C -12 h	1:12, 2:17, α -Fe
950 °C-12 h	1:12, 3:29, α -Fe
1000 °C-2h	1:12, 3:29, α -Fe
1050 °C-2 h	1:12, 3:29, α -Fe
1100 °C-2 h	1:12, 3:29, Nd-rich ^a
1150 °C-2 h	1:12, Nd-rich
1175 °C-2 h	1:12, Nd-rich
1200 °C-2 h ^b	1:12, Nd-rich

^a Residual.

^b Partially molten.

spectroscopy (EDS) measurements were performed to quantify chemical composition of the present phases, for this purpose, different regions of the sample were used. This was done in order to exclude any composition gradient and/or microstructure changes because of possible differences in the cooling rate within the suction casted plate.

Electron backscatter diffraction (EBSD) was used in a FEG-SEM (Tescan Mira3) to analyze selected samples and determine the misorientation angle in twinned grains.

The crystallographic structures were characterized by X-ray powder diffraction (XRD). The measurements were carried out on a Stoe Stadi P diffractometer with $Mo K_{\alpha 1}$ radiation, in transmission mode and an angular 2θ range from 5° to 40°. Phase matching and unit-cell refinements were performed using FullProf/WinPLOTR suite software [26,27].

Thermomagnetic measurements were carried out on bulk suction casted samples, using Lake Shore 7410 Vibrating Sample Magnetometer (VSM). The magnetization was measured upon heating the samples from 350 to 700 K, with heating rate of 5 $Kmin^{-1}$ under constant applied magnetic field of 1T.

Isothermal magnetization measurements were performed on aligned powder samples using PPMS-VSM (Quantum Design PPMS-14), at room temperature, under applied magnetic field up to 3T. The powder consists of particles, assumed to be monocrystalline, with size less than 80 μm . The particles were mixed with paraffin-wax and encapsulated in metallic pan. Afterwards, the pan was heated above the melting point of the wax and an external magnetic field of 1.3T was applied for texturing.

The magnetic domain structures were observed by magneto-optical Kerr effect (MOKE) microscopy (Zeiss Axio Imager.D2m evico magnetics GmbH). To analyze the domain wall motion, the electromagnet option of MOKE microscope was used to apply magnetic fields up to 380 mT. The image contrast was enhanced by subtracting the non-magnetic background image from the collected average image using KerrLab software.

3. Results and discussion

3.1. Effect of synthesis route on the phase formation

The microstructure and the present phases were evaluated through SEM-EDS analysis. For the main observed ternary phases, 1:12, 2:17 and 3:29, the identification was done by taken into account the ratio between the concentration of Nd and Ti, according to the mean values shown in Table 1. These values are in agreement with those reported in the literature by Margarian et al. for all three phases [28].

As shown in Fig. 1a, the initial microstructure of the induction melted $\text{Nd}_{1.15}\text{Fe}_{11}\text{Ti}$ sample consists of a coarse distribution of α -Fe(Ti) solid solution (dark areas), 1:12 (dark grey), a mixture of 2:17 and 3:29 (light grey) and Nd-rich phase spots (bright contrast). Comparatively, the microstructure of suction casted plate (Fig. 1b) consists of α -Fe(Ti) precipitates, Nd-rich phase in the grain boundaries and a majority fraction of fine grains of the desired 1:12 phase. 3:29 and 2:17 phases were not observed, within the resolution limits of the instrument. The cooling rate in the suction casting process is dependent of the chemical composition, shape and dimension of the mold. According to the work of Chen et al. [29] and Koziel et al. [30], it is possible to infer that the cooling rates in the present study are in the range of 10^3 K s^{-1} .

It is worth mentioning that the rapid cooling within the suction casted plate lead to homogenous microstructure, which is suitable for shortening annealing times, because favors the formation of the thermodynamic stable phases as compared to coarser microstructures. Similar features have already been shown for other alloys and for different processing techniques, such as strip casting and melt spinning [31–33]. This effect is commonly related to a combination of: lower path of atomic diffusion and higher number of heterogeneous sites for isothermal nucleation [34,35]. Consequently, suction casting was selected as a method to produce bulk samples for further studies related to annealing and chemical composition optimization.

3.2. Effect of composition and annealing temperature on the phase formation

3.2.1. Microstructure and chemical analysis

After suction casting and annealing, the $\text{Nd}_x\text{Fe}_{11}\text{Ti}$ samples with $x = 1.05$ and $x = 1.10$ were investigated. A mixture of different

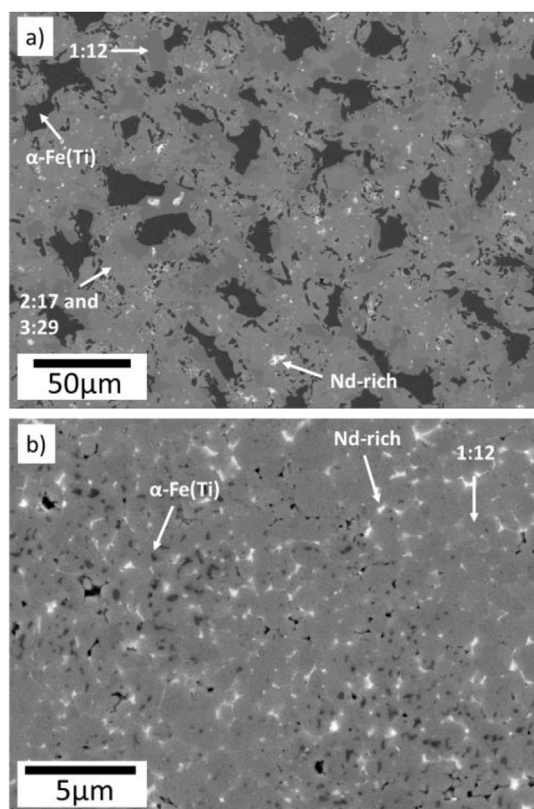


Fig. 1. Initial microstructure of $\text{Nd}_{1.15}\text{Fe}_{11}\text{Ti}$ induction melted (a) and middle part of the suction casted plate (b) using BSE contrast.

phases was observed in all samples in the evaluated temperature range and no single 1:12 phase state was obtained in these samples.

By increasing the rare-earth content to 1.15, the desired 1:12 single-phase samples were obtained after annealing at temperatures above 1150°C . In addition, at this temperature, Nd-rich phase is seen at the triple grain boundary junctions (Fig. 2c). At lower temperatures, e.g. 1100°C , it is observed partial decomposition of 1:12 and appearance of 3:29 phase (Fig. 2b), which is consistent to the results reported by Margarian et al. [28]. After annealing at lower temperatures, down to 950°C , the 3:29 and 1:12 phases are still present with α -Fe(Ti) precipitates.

As represented in Fig. 2a for the sample annealed at 800°C , we observe partial decomposition of 1:12 and the formation of 2:17 around α -Fe(Ti) precipitates in the temperatures range between 700 and 900°C . It is worth to notice that the 3:29 phase is absent in this temperature range. A summary of the observed phases for

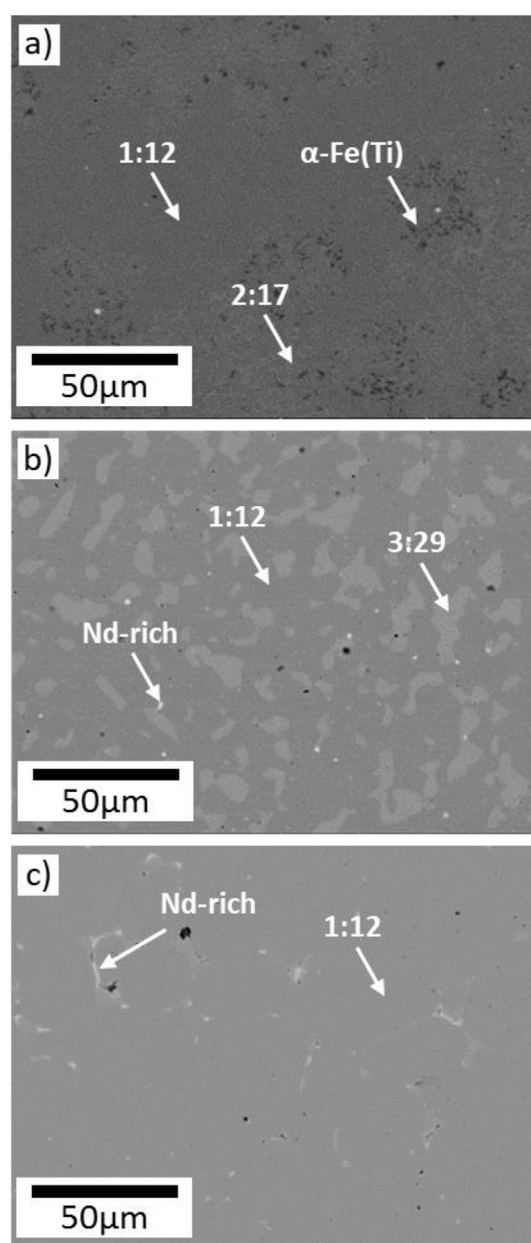


Fig. 2. SEM-BSE contrast micrography of $\text{Nd}_{1.15}\text{Fe}_{11}\text{Ti}$ annealed at 800°C (a), 1100°C (b) and 1175°C (c).

Nd_{1.15}Fe₁₁Ti samples is given in Table 2.

For the samples with highest Nd content, $x = 1.20$, no significant change was seen in the microstructure compared to $x = 1.15$, except for the higher amount of Nd-rich phase. For this reason, and taken into consideration the RE-lean concept of this class of materials, samples with lower content of rare-earth ($x = 1.15$) were selected for further characterization.

Based on these results, we propose that the 1:12 in single-phase state in the Nd-Fe-Ti hyper-stoichiometric system is stable only in a very narrow window, between 1150 and 1200 °C. As was expected, the microstructure in this temperature range is similar, except for the increase of the mean grain size with increasing the annealing temperature.

3.2.2. Structural analysis

In an attempt to confirm the present phases and to quantify the phase fraction and unit cell parameters, room temperature XRD was performed in the Nd_{1.15}Fe₁₁Ti samples. The patterns are displayed in Fig. 3 for three different annealing conditions: 800, 1100 and 1175 °C (Fig. 3a) with the correspondent simulated patterns for 1:12, 2:17 and 3:29 phases (Fig. 3b).

The pattern of annealed sample at 1175 °C was indexed with the ThMn₁₂ tetragonal structure. Rietveld refinement was performed with good agreement ($\chi^2 = 1.3$), as shown by the difference of observed and calculated pattern (Fig. 3a). The unit cell parameters are $a=b=8.591$ Å and $c=4.796$ Å, which is in good agreement with previous reports [17].

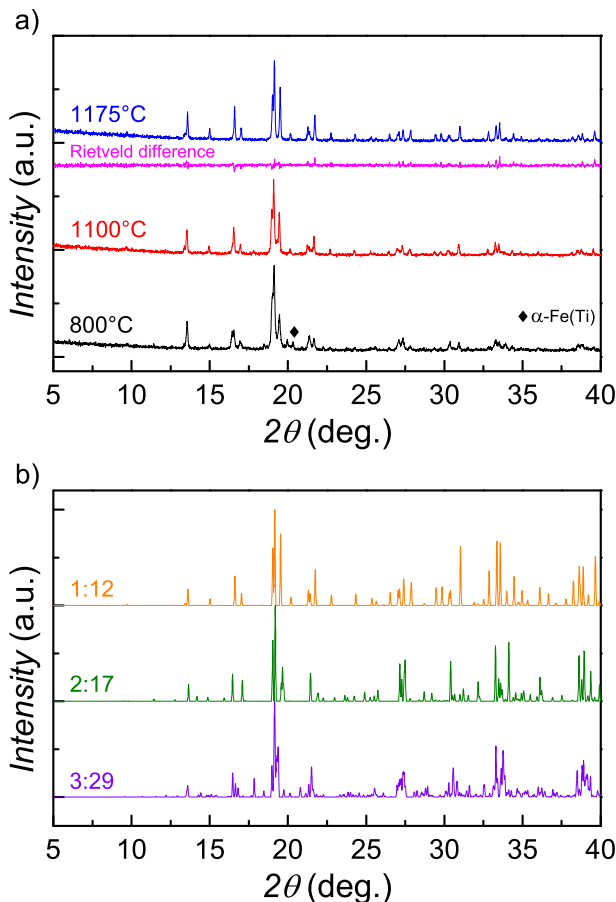


Fig. 3. XRD patterns of the three selected samples (a) and the calculated patterns of 1:12, 2:17 and 3:29 phases (b). It is also shown the results of Rietveld refinement (difference between the observed and calculated pattern-Rietveld difference) of the sample annealed at 1175 °C (see text).

Regarding the samples annealed at 1100 and 800 °C, similar patterns to 1:12 are seen, even though SEM-EDS analysis shows clearly different phases present with the tetragonal phase, as described previously in section 3.2.1. The 2:17 (rhombohedral) and 3:29 (monoclinic) phases have also similar simulated patterns to the tetragonal 1:12 structure (Fig. 3b), since they are based on a common frame founded in the RECo₅ compounds (CaCu₅ structure), as already reported by Cadogan [36–39].

For this specific materials system, XRD analysis can be only used as a first approximation in the interpretation of the present phases, including the determination of single-phase state. Thus, the peak overlapping between these three structures inhibits the precise quantification of the phase fraction of mixed phase state, as the Rietveld refinement leads to high errors by means of the phase ratios.

3.2.3. Thermomagnetic measurements

In the literature, the determination of the phases in this material system is often done by only using the XRD analysis. As we presented in our studies, this method alone may mislead interpretation as a result of similarities between the crystal structures of the observed 1:12, 2:17 and 3:29 phases (Fig. 3). One alternative way to tackle this problem is to use SEM-EDS analysis to distinguish the phases from their chemical compositions. This gives stronger separation between the 1:12 and 2:17/3:29 phases but the distinction of 3:29 and 2:17 can be overlooked (see Table 1). Due to this reason, one needs a complimentary technique to distinguish these three phases from each other. The use of thermomagnetic measurements for phase determination in similar material systems have shown to be a reliable method for this purpose [40–44].

To confirm the results obtained by SEM-EDS, thermomagnetic analysis was employed to evaluate qualitatively and systematically the present phases in the Nd_{1.15}Fe₁₁Ti samples.

In order to ensure the difference between the Curie temperature of the competing phases (2:17 and 3:29), a new sample was produced with composition Nd_{1.35}Fe₁₁Ti_{0.6} and annealed at 1100 °C for 2 h. This composition and annealing regime led to a microstructure which both competing phases coexist without any traces of 1:12 phase. The microstructure can be seen in Fig. 4c, where SEM-EDS analysis shown both phases with chemical composition within the range presented in Table 1.

The thermomagnetic measurement ($M(T)$) result and the derivative curve ($dM(T)/dT$) are shown in Fig. 4a and b, respectively. It is known that if the $M(T)$ dependencies are measured in an external field surpassing the demagnetization field of the sample, then the position of $dM(T)/dT$ minima is slightly higher than the actual value of T_C of the compound. At the same time, if all $M(T)$ dependencies are measured in the same field (e.g. 1T) and all samples have similar shape, the specific temperatures at which $dM(T)/dT$ minima occur allow us to unequivocally detect and identify the transition temperature of different phases. The dashed areas in Fig. 4 correspond to T_C values reported in the literature for the different phases. The use of $dM(T)/dT$ curve to evaluate the local/global minima and correlate with the T_C values was found to be a direct approach to identify this intrinsic property, since the relatively high applied field during the measurement (1T) can lead to overlap in the $M(T)$ curves in a mix phase state sample, as presented in Fig. 4a and b.

As can be seen in Fig. 4a and b, the T_C values found in the literature for both phases are in good agreement with the ones found in this work, where for 2:17 is in between 390 and 401 K [45,46] and for 3:29 lies in the range of 413–440 K [47,48]. No changes in the magnetization value was observed in the temperature range where the T_C of 1:12 phase is expected, confirming the absence of this phase in this sample.

After confirming the differences in the T_C values of 2:17 and

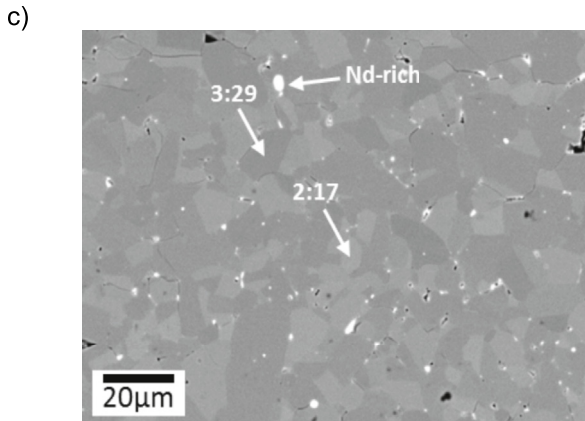
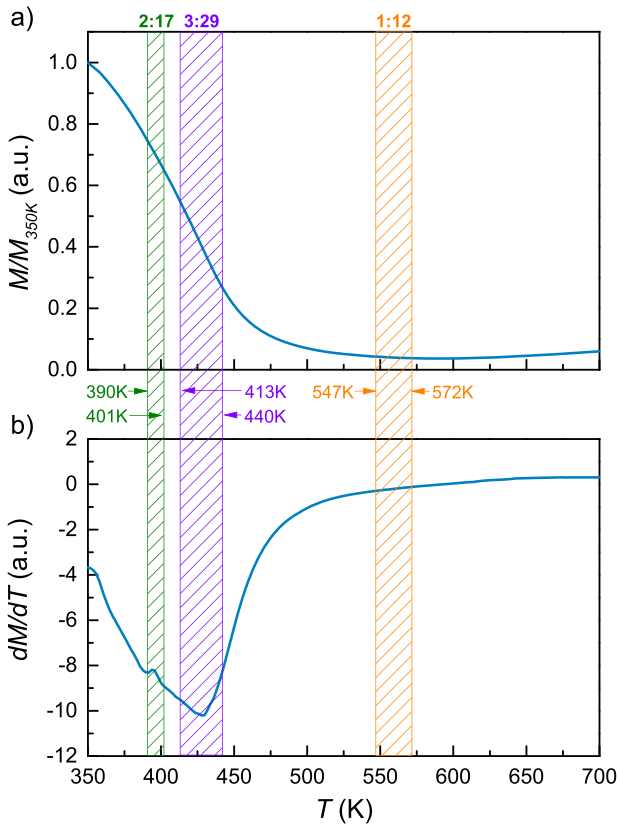


Fig. 4. Thermomagnetic measurements of $\text{Nd}_{1.15}\text{Fe}_{11}\text{Ti}_{0.6}$ sample (a) and the derivative curve (b). The dashed areas are the minimum and maximum T_C value found in the literature for 2:17, 3:29 and 1:12 phases. The applied field of 1T and heating rate of 5 Kmin^{-1} was used and the magnetization values were normalized in respect to 350 K. The SEM-BSE image (c) shows 2:17, 3:29 and Nd-rich phases in the microstructure.

3:29, the thermomagnetic analysis was employed in the $\text{Nd}_{1.15}\text{Fe}_{11}\text{Ti}$ samples annealed under different regimes. For better visualization of the observed trend, the results are shown in two figures to evaluate the differences between two different annealing ranges, below and above 900°C (Figs. 5a and 6a respectively). In addition, the derivative curves from these samples are also shown in Figs. 5b and 6b. The sample in the as suction casted state is included for comparison.

In the initial condition (suction casted state), the main drop in the magnetization, and the global minimum in the derivative curve, occurs around 550 K, which is a similar value reported by Hu et al. [45] for the T_C of 1:12 phase in this compound. The magnetization value is non zero above 550 K, which is due to the presence of α -

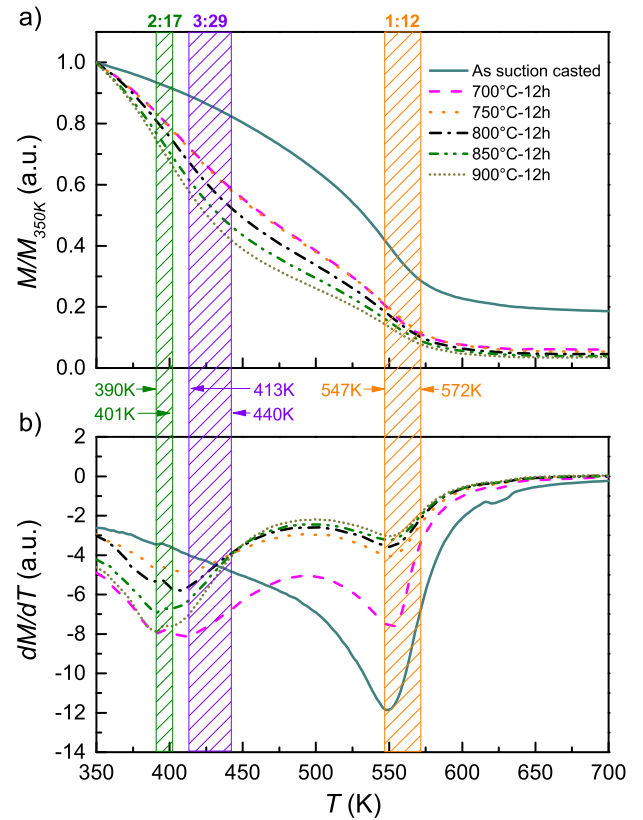


Fig. 5. Thermomagnetic measurements of $\text{Nd}_{1.15}\text{Fe}_{11}\text{Ti}$ samples in annealed between 700 and 900°C (a) and the derivative curves (b). The dashed areas are the minimum and maximum T_C value found in the literature for 2:17, 3:29 and 1:12 phases. The applied field of 1T and heating rate of 5 Kmin^{-1} was used and the magnetization values were normalized in respect to 350 K.

$\text{Fe}(\text{Ti})$ which was already identified in the SEM-EDS analysis (Fig. 1b).

Annealing $\text{Nd}_{1.15}\text{Fe}_{11}\text{Ti}$ suction casted plates between 700 and 900°C leads to partial decomposition of the initial 1:12 and nucleation of a phase with lower T_C . From the Curie temperature range reported in the literature (390–401 K), it can be conclude that these samples consist of a mixture of $\text{Nd}_2(\text{Fe,Ti})_{17}$ and $\text{Nd}(\text{Fe,Ti})_{12}$ phases [46,47]. This is as also shown by the local minima in the derivative curve (see Fig. 4b) around 390 K (2:17 phase) and at 550 K (1:12 phase), confirming the results obtained previously by EDS-SEM. It is worth mentioning that the drop in magnetization becomes more pronounced with increasing annealing temperature, indicating higher fraction of 2:17 phase is forming while 1:12 is decomposing in these conditions.

Similar results have been obtained upon increasing the annealing temperature up to 950°C (Fig. 6), indicating a similar behavior regarding 1:12 phase decomposition. However, the shift in the thermomagnetic curve is not pronounced as shown by the samples annealed at lower temperatures, as can be observed in Fig. 6b between samples annealed at 900 and 950°C . At higher temperatures, up to 1100°C , the shift of the thermomagnetic curves goes to higher temperatures which, combined to the shift in the local minima (from 390 to 425 K), indicates a partial decomposition of the 1:12 to 3:29 phase. The T_C value of the 3:29 phase found in this work ($T_C = 425 \text{ K}$) is consistent with the values reported in the literature, that is between $T_C = 413$ [48] and $T_C = 440 \text{ K}$ [49].

For the sample annealed at 1175°C , as can be seen from the heating curve, the decrease in magnetization shows only a single

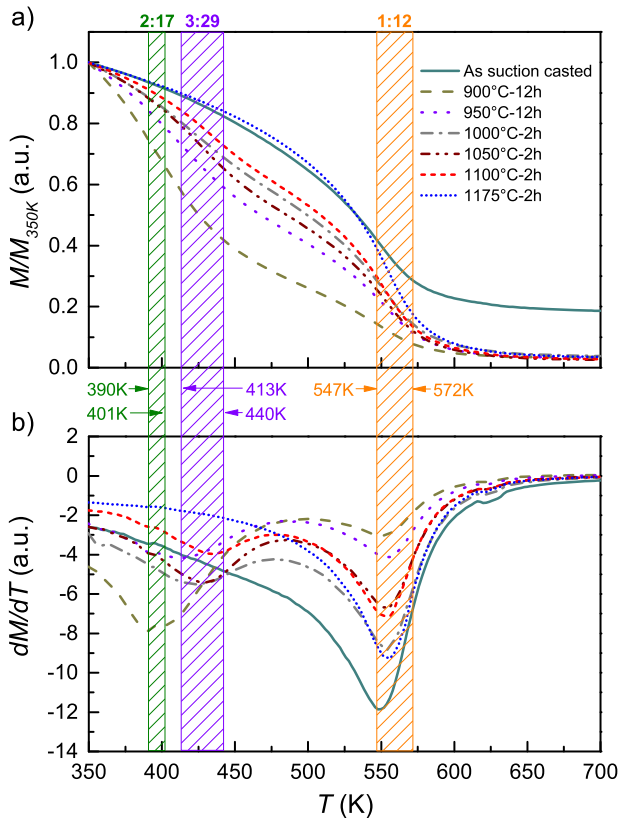


Fig. 6. Thermomagnetic measurements of $\text{Nd}_{1.15}\text{Fe}_{11}\text{Ti}$ samples in annealed between 900 and 1175 °C (a) and the derivative curves (b). The dashed areas are the minimum and maximum T_C value found in the literature for 2:17, 3:29 and 1:12 phases. The applied field of 1T and heating rate of 5 Kmin^{-1} was used and the magnetization values were normalized in respect to 350 K.

inflection (global minima) around 560 K, related to the Curie temperature of the $\text{NdFe}_{11}\text{Ti}$ compound. This result is similar to the one reported by Suzuki et al. [17], in which similar measurement conditions were used.

As the Curie temperature is well separated between these phases, one can easily distinguish each other by using the $dM(T)/dT$ plots, as shown in Figs. 4b, 5b and 6b. Using this method, it was possible to identify the present phases in the evaluated temperature range. In summary, annealing between 700 °C and 900 °C leads to decomposition of 1:12 and nucleation of 2:17; annealing in the range of 950 °C and 1100 °C, 3:29 nucleate at expenses of 1:12; single 1:12 phase samples were obtained after annealing at temperatures above 1150 °C.

3.3. Magnetic properties

3.3.1. Isothermal magnetization measurements

Magnetization isotherms were performed using textured powder of the 1:12 single-phase sample ($\text{Nd}_{1.15}\text{Fe}_{11}\text{Ti}$ annealed at 1175 °C) in the easy and hard directions, as displayed in Fig. 7. The saturation magnetization (M_{sat}) amounts of $137 \text{ Am}^2\text{kg}^{-1}$ was obtained. An estimation of the anisotropy field (H_A) was taken from the point at which the magnetization curve in the parallel and perpendicular direction merges. This method yields an anisotropy field of around 1.5T. The anisotropy field was also determined by plotting the magnetization in the perpendicular direction as a function of $(\mu_0 H_{\text{appl}})^{-2}$, as described by Durst et al. [50]. From the kink point (Fig. 7-inset graph), an anisotropy field of 1.08T has been obtained, which is similar to the value reported by Buschow [5].

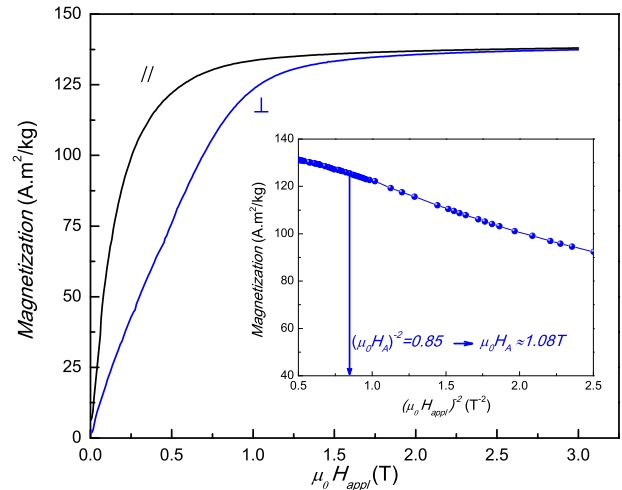


Fig. 7. Isothermal magnetization curve from 1:12 single-phase sample oriented powder in the parallel and perpendicular directions. The inset shows a plot of magnetization in the perpendicular direction as a function of $(\mu_0 H_{\text{appl}})^{-2}$ to determine the anisotropy field ($H_A = 1.08\text{T}$).

3.3.2. Magnetic domain observations

The analysis of the $\text{Nd}_{1.15}\text{Fe}_{11}\text{Ti}$ sample (1:12 phase) by means of magneto-optical Kerr microscopy in Fig. 8 reveals the typical uniaxial anisotropy domain type in this compound. It is also seen the existence of twin boundaries (indicated by arrows), as has been previously shown by Skokov et al. [51] in Gd-Fe-Ti alloy with 1:12 structure. The specific orientation (mirror image) which exists in the twin pair leads to opposite polar magnetization, explaining the inverse contrast between these grains [52]. In addition, on Fig. 8, three grains are numbered with different domain change along the twin boundary. The grains labeled 1 and 2 have a transition from stripe to branch like domains. The third grain shows a more complex arrangement with three twins, creating a triple point, where a transition between two stripe domain regions and branch like domain take place.

To evaluate the relation of the existing twin boundaries, EBSD was used to analyze the grain orientation, as show in the in the inverse pole figure (Fig. 9b). The misorientation between grains with twins (marked with arrows in Fig. 9b) was found to be a constant value of $57^\circ \pm 1^\circ$. The consistency of this angle is a strong indication that a lower energy of the twin boundaries is achieved in this configuration for this system [34].

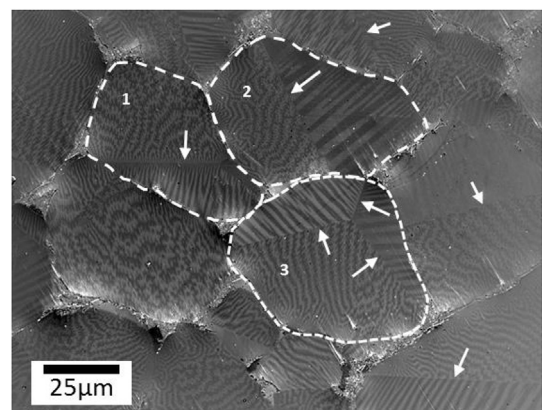


Fig. 8. Kerr micrograph of $\text{Nd}_{1.15}\text{Fe}_{11}\text{Ti}$ sample annealed at 1175 °C. Three grains are emphasized with different types of domain change along the twin boundary. The arrows shows the observed twin boundaries.

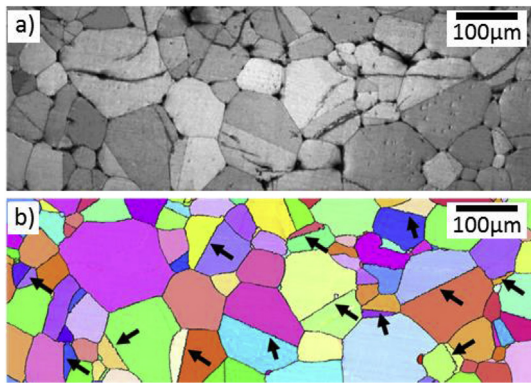


Fig. 9. EBSD analysis from isotropic $\text{Nd}_{1.15}\text{Fe}_{11}\text{Ti}$ annealed at 1175°C for 2 h. BSE contrast (a) and inverse polar figure (b) with arrows showing some of the existing twin boundaries.

The existence of twin boundaries has been typically observed in alloys with low stacking fault energy and is commonly related to deformation caused by internal or external stresses [53]. In the case of 1:12 phase formation, since no external stresses were applied, one can assume that thermal stresses during annealing can play a role in the twin formation. Another possibility for internal stresses can be related to the interfacial strain, which may exist between the adjacent phases during nucleation and growth. This arises because of mismatch between unit cell parameters of different phases with similar structure, the case of 1:12, 2:17 and 3:29, which can lead to incoherent or semi-coherent interface and strain associated to it [34].

Similar behavior was also reported by Courtois et al., [54] in the $\text{Y}_3(\text{Fe},\text{V})_{29}$ compound. In their work, the single-crystal of 3:29 was grown from a 2:17 crystal, in which twins were observed with a misorientation of 60° . These similarities between the twinning angles, found in 3:29 and the one reported here for 1:12, can be a result of the correlation of these structures.

Further detailed investigation needs to be done to understand the formation of the twin boundaries, since they can play a major role in the demagnetization mechanism as will be shown in the following section.

3.3.3. Nucleation of reversal domains in twinned grains

In order to investigate the weak links within the microstructure, where the reversal domains nucleate, Kerr analysis using in plane magnetic field were performed in an isotropic suction casted sample annealed at 1175°C (single 1:12 phase). Fig. 10 shows the selected grain with in-plane magnetization (low demagnetization factor), surrounded by other grains, where the magnetization makes a significant angle with the surface (high demagnetization factor). When the sample is saturated in an external magnetic field of 380 mT, and then the field is decreased, first branched magnetic domains appear in the grains with out-of-plane magnetization, and in lower fields, the stripe magnetic domains nucleate and grow in the selected grain. The sequence of Kerr micrographs (Fig. 10a–d) shows, in detail, a grain that is divided in two equal parts by a twin boundary. For this reason, half of the grain presents dark contrast and the other half bright contrast in saturated state when a magnetic field of 380 mT is applied (Fig. 10a). By decreasing the applied magnetic field to 150 mT (Fig. 10b), it was possible to observe the nucleation of reversal domains starting from the twin boundary (highlighted by the arrow) growing towards the grain boundary with further decreasing of the applied field.

As shown in the sequence of micrographs, it is possible to notice clearly the nucleation and growth of reversal domains without the presence of pinning centers.

Additionally, when the magnetic field is decrease to 50 mT (Fig. 10c), the reversal domains from the twinned grain directly affect the adjacent grain, shown by the dashed arrow, indicating a strong coupling between neighboring grains.

The impact of twin boundaries was reported for Fe-Pd [55] and Mn-Al [56] ferromagnets and, in summary, was identified to be deleterious for the coercivity and it can be directly related to the

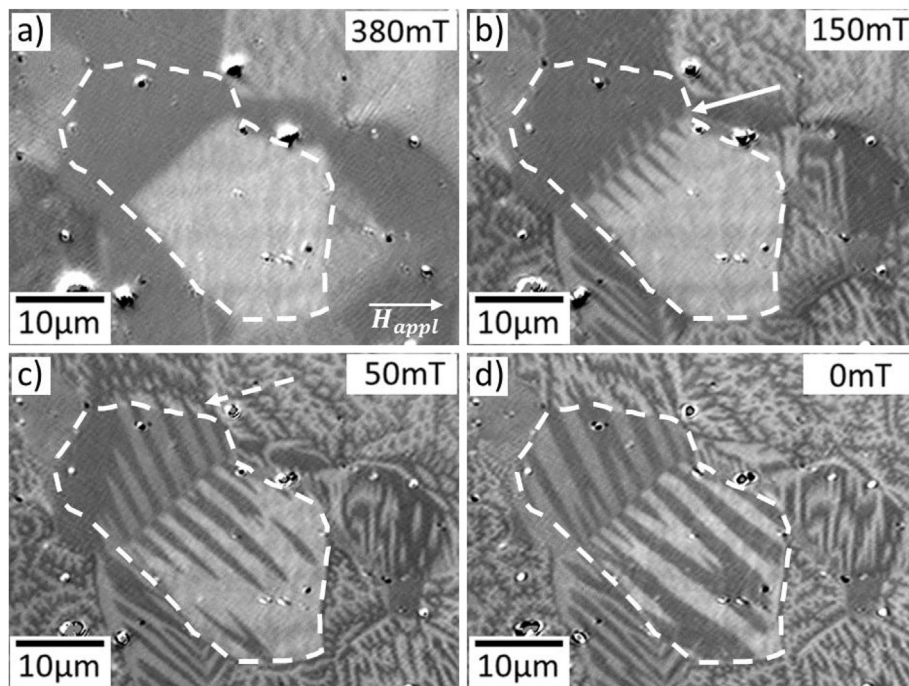


Fig. 10. MOKE analysis from 380 mT (a) applied magnetic field (grains with twin boundary saturated) down to 0 mT (d-demagnetized state). The arrow showing the nucleation at the twin boundary with applied field of 150 mT (b) and the coupling between adjacent grains at 50 mT (c-dashed arrow).

density of this defect within the microstructure. It was also evaluated, by micromagnetic simulations, the possible effect as a pinning center in the Mn-Al alloys, but it was found that the effect as nucleation center for reversal domains is more pronounced in this system [56]. These characteristics are very similar to the ones found and observed in this work. For this reason, this type of defect seems to be prejudicial for the magnetic properties.

Another important feature that can be also determinant for low magnetic properties in the 1:12 compound is the fact that the grains appear to be magnetically coupled, as mentioned previously. It is a very determinant factor to obtain high coercivity values in Nd-Fe-B sintered magnets, in which an Nd-rich layer is covering the grain boundaries, decoupling the grains and decreasing the interaction between them [57–59]. Even though, in the 1:12 microstructure of Nd_{1.15}Fe₁₁Ti, the Nd-rich layer is present, it is mainly agglomerated in the triple junctions and in less amount compared to the commercially Nd-Fe-B sintered magnets. For this reason, this has to be taken into account to prevent the magnetic coupling between grains in bulk magnets and, therefore, improve the magnetic properties.

The obtained magnetic properties on textured NdFe₁₁Ti samples show that enhancement of the magnetic properties are necessary to use these systems in applications. The literature shows the possibility of improving the anisotropy of the NdFe₁₁Ti system from 1T to 8T by nitrogenation [21] along with an improvement of the Curie temperature [17]. Even though the intrinsic properties are enhanced, the reported extrinsic properties of NdFe₁₁TiN_x are far below from the expected values. One reason for this low extrinsic properties might be the existence of twins in the starting material, as previously shown. As the nitrogenation processes are carried out under relative low treatment temperature (between 400 °C and 500 °C), it is not expected to have any modification of the twins as at these temperatures low atomic diffusion and low mobility is expected. This might lead to the observed limitations in the extrinsic properties as twins might be acting as a nucleation center for reversal domains even in the NdFe₁₁TiN_x compound, preventing the high coercivity values expected based on the anisotropy field of this material system.

4. Summary

Polycrystalline Nd_xFe₁₁Ti ($x = 1.05, 1.10, 1.15, 1.20$) alloys were produced by using a rapid solidification method (suction casting). Different annealing treatments were applied to the resulting samples and structural, microstructural and magnetic characterizations of these samples were done. The results indicate that the fast solidification, which is obtained by the suction casting, is necessary to achieve the single phase materials, after short annealing, with the desired ThMn₁₂-type structure. Samples annealed at temperatures in between 700 and 900 °C show coexistence of ThMn₁₂-type and Th₂Zn₁₇-type structure. The annealing temperatures between 950 and 1100 °C leads to the mixture of ThMn₁₂-type and Nd₃(Fe,Ti)₂₉-type structures. Single phase ThMn₁₂-type samples can be obtained for the annealing temperatures in the range of 1150–1200 °C.

Off-stoichiometric Nd-rich composition was found to be necessary to obtain phase-pure materials. Nd_{1.15}Fe₁₁Ti and Nd_{1.20}Fe₁₁Ti compositions lead to the formation of ThMn₁₂-type after getting annealed in the temperature range of 1150–1200 °C. For Nd-lean compositions ($x < 1.15$ compositions) secondary phases are observed.

By using complementary methods, we managed to distinguish different competing Nd(Fe, Ti)₁₂, Nd₂(Fe,Ti)₁₇ and Nd₃(Fe,Ti)₂₉ phases. Considering the methods used in this study, determination of chemical composition, via EDS analysis, and thermomagnetic analysis gives the most accurate determination of the phase purity.

The magnetic measurements done on the textured polycrystalline single phase NdFe₁₁Ti sample show a spontaneous magnetization of 137 Am²kg⁻¹ and anisotropy field of 1.08T at room temperature. In addition, the link between microstructure and extrinsic magnetic properties was studied. The microstructural analysis (EBSD) and Kerr measurement results indicate the formation of “twin like” structures which have a specific misorientation of 57° ± 1°. The analysis of magnetic domains under external magnetic field, revealed that the twins are nucleation center for reversal domains, as already observed for other compounds like Mn-Al and Fe-Pd. This could be one of the reasons for the low coercivity achieved so far, even in the nitrogenated compound, which has a high H_A of 8T. In addition to the twins, magnetic domain analysis revealed coupling between the grains, which is also has to be reduced or eliminated for coercivity development. To obtain reasonable coercivity from Nd-based ThMn₁₂-type systems one need to find a way to eliminate the formation of twins and engineer a proper grain boundary phase to magnetically isolate the individual grains from each other.

Acknowledgements

F.M. acknowledges the funding provided by the Deutsche Forschungsgemeinschaft (DFG, German Research Foundation) under the Priority Programme SPP1959. K.S. and O.G. acknowledge support from NOVAMAG project, under Grant Agreement No. 686056, EU Horizon 2020 Framework Programme and the Hessen LOEWE Response Programme. S.E., K.S. and O.G. gratefully acknowledge the financial support of the Technology Research Association of Magnetic Materials for High-Efficiency Motors (MagHEM) program commissioned by the New Energy and Industrial Technology Development Organization (NEDO).

References

- [1] O. Gutfleisch, M.A. Willard, E. Brück, C.H. Chen, S.G. Sankar, J.P. Liu, Magnetic materials and devices for the 21st century: stronger, lighter, and more energy efficient, *Adv. Mater.* 23 (7) (2010) 821–842, <https://doi.org/10.1002/adma.201002180>.
- [2] K. Hono, H. Sepehri-Amin, Strategy for high-coercivity Nd-Fe-B magnets, *Scr. Mater.* 67 (6) (2012) 530–535, <https://doi.org/10.1016/j.scriptamat.2012.06.038>.
- [3] D. Brown, B.-M. Ma, Z. Chen, Developments in the processing and properties of NdFeB-type permanent magnets, *J. Magn. Magn. Mater.* 248 (3) (2002) 432–440, [https://doi.org/10.1016/S0304-8853\(02\)00334-7](https://doi.org/10.1016/S0304-8853(02)00334-7).
- [4] K.P. Skokov, O. Gutfleisch, Heavy rare earth free, free rare earth and rare earth free magnets - vision and reality, *Scr. Mater.* 154 (2018) 289–294, <https://doi.org/10.1016/j.scriptamat.2018.01.032>.
- [5] K.H.J. Buschow, Permanent magnet materials based on tetragonal rare earth compounds of the type RFe_{12-x}M_x, *J. Magn. Magn. Mater.* 100 (1–3) (1991) 79–89, [https://doi.org/10.1016/0304-8853\(91\)90813-p](https://doi.org/10.1016/0304-8853(91)90813-p).
- [6] W. Körner, G. Krugel, C. Elsässer, Theoretical screening of intermetallic ThMn₁₂-type phases for new hard-magnetic compounds with low rare earth content, *Sci. Rep.* 6 (1), doi:10.1038/srep24686.
- [7] A.M. Gabay, G.C. Hadjipanayis, Recent developments in RFe₁₂-type compounds for permanent magnets, *Scr. Mater.* 154 (2018) 284–288, <https://doi.org/10.1016/j.scriptamat.2017.10.033>.
- [8] Y. Hirayama, Y.K. Takahashi, S. Hirotsawa, K. Hono, NdFe₁₂N hard-magnetic compound with high magnetization and anisotropy field, *Scr. Mater.* 95 (2015) 70–72, <https://doi.org/10.1016/j.scriptamat.2014.10.016>.
- [9] A.M. Gabay, A. Martín-Cid, J.M. Barandiaran, D. Salazar, G.C. Hadjipanayis, Low-cost Ce_{1-x}Sm_x(Fe,Co,Ti)₁₂ alloys for permanent magnets, *AIP Adv.* 6 (5) (2016) 056015, doi:10.1063/1.4944066.
- [10] C. Zhou, F.E. Pinkerton, J.F. Herbst, High Curie temperature of Ce-Fe-Si compounds with ThMn₁₂ structure, *J. Alloy. Comp.* 583 (2014) 345–350, <https://doi.org/10.1016/j.jallcom.2013.08.175>.
- [11] C. Zhou, F.E. Pinkerton, Magnetic hardening of CeFe_{12-x}Mo_x and the effect of nitrogenation, *J. Alloy. Comp.* 95 (2014) 345–350, <https://doi.org/10.1016/j.scriptamat.2014.10.006>.
- [12] K. Kobayashi, S. Suzuki, T. Kuno, K. Urushibata, N. Sakuma, M. Yano, T. Shoji, A. Kato, A. Manabe, The origin of high magnetic properties in (R,Zr)(Fe,Co)_{11.0-11.5}Ti_{1.0-0.5}N_y (y=1.0-1.4 for R=Nd, y=0 for R=Sm) compounds, *J. Magn. Magn. Mater.* 426 (2017) 273–278, <https://doi.org/10.1016/j.jmmm.2016.11.070>.

- [13] M. Endoh, K. Nakamura, H. Mikami, Nd(Fe,Mo)₁₂N_x compounds and magnets, IEEE Trans. Magn. 28 (5) (1992) 2560–2562, <https://doi.org/10.1109/20.179556>.
- [14] Z.X. Tang, E.W. Singleton, G.C. Hadjipanayis, Hard magnetic properties of melt-spun Nd(Fe,M)₁₂ nitrides and carbides, J. Appl. Phys. 73 (10) (1993) 6254–6256, <https://doi.org/10.1063/1.352662>.
- [15] J. Yang, O. Mao, Z. Altounian, Structure and magnetic properties of mechanically alloyed Nd(Fe,V)₁₂N_x compounds, J. Appl. Phys. 79 (8) (1996) 5519, <https://doi.org/10.1063/1.362296>.
- [16] N. Sakuma, S. Suzuki, T. Kuno, K. Urushibata, K. Kobayashi, M. Yano, A. Kato, A. Manabe, Influence of Zr substitution on the stabilization of ThMn₁₂-type (Nd_{1-x}Zr_x)(Fe_{0.75}Co_{0.25})_{11.25}Ti_{0.75}N_{1.2-1.4} (α = 0 - 0.3) compounds, AIP Adv. 6 (5) (2016) 056023, <https://doi.org/10.1063/1.4944521>.
- [17] S. Suzuki, T. Kuno, K. Urushibata, K. Kobayashi, N. Sakuma, K. Washio, M. Yano, A. Kato, A. Manabe, A new magnet material with ThMn₁₂ structure: (Nd_{1-x}Zr_x)(Fe_{1-y}Co_y)_{11+z}Ti_{1-z}N_z (α=0.6 - 1.3), J. Magn. Magn. Mater. 401 (2016) 259–268, <https://doi.org/10.1016/j.jmmm.2015.10.042>.
- [18] N. Inoue, S. Suzuki, Influence of nitrogenating conditions on magnetic properties of NdFe₈Co₃TiN_x, J. Alloy. Comp. 222 (1–2) (1995) 82–86, [https://doi.org/10.1016/0925-8388\(94\)04922-x](https://doi.org/10.1016/0925-8388(94)04922-x).
- [19] T. Saito, W.Q. Wang, Y. Kamagata, Structures and magnetic properties of Nd-Fe-Ti alloys produced by melt-spinning technique, J. Alloy. Comp. 402 (1–2) (2005) 242–245, <https://doi.org/10.1016/j.jallcom.2005.03.091>.
- [20] Z.-Q. Jin, W. Tang, J.-R. Zhang, H.-X. Qin, Y.-W. Du, Effective magnetocrystalline anisotropy of nanocrystalline Nd-Fe-Ti-N hard magnetic alloys, Eur. Phys. J. B 3 (1) (1998) 41–44, <https://doi.org/10.1007/s100510050282>.
- [21] Y. Yang, X. Zhang, L. Kong, Q. Pan, S. Lin Ge, Magnetocrystalline anisotropies of RTiFe₁₁N_x compounds, Appl. Phys. Lett. 58 (18) (1991) 2042–2044, <https://doi.org/10.1063/1.105007>.
- [22] G.C. Hadjipanayis, Y.Z. Wang, E.W. Singleton, W.B. Yelon, Rare-earth nitrides and carbides: a new class of permanent magnet materials, J. Mater. Eng. Perform. 1 (2) (1992) 193–203, <https://doi.org/10.1007/bf02648617>.
- [23] S. Suzuki, N. Inoue, T. Miura, Magnetic properties of RFe_{11-x}Co_xTiN_y (R:Nd,Pr) compounds with ThMn₁₂ type structure, IEEE Trans. Magn. 28 (5) (1992) 2005–2009, <https://doi.org/10.1109/20.179659>.
- [24] Y.Z. Wang, G.C. Hadjipanayis, Effect of nitrogen on the structural and magnetic properties of intermetallic compounds with the ThMn₁₂ structure, J. Appl. Phys. 70 (10) (1991) 6009–6011, <https://doi.org/10.1063/1.350076>.
- [25] M. Akayama, H. Fujii, K. Yamamoto, K. Tatami, Physical properties of nitrogenated RFe₁₁Ti intermetallic compounds (R=Ce, Pr and Nd) with ThMn₁₂-type structure, J. Magn. Magn. Mater. 130 (1–3) (1994) 99–107, [https://doi.org/10.1016/0304-8853\(94\)90662-9](https://doi.org/10.1016/0304-8853(94)90662-9).
- [26] J. Rodríguez-Carvajal, Recent advances in magnetic structure determination by neutron powder diffraction, Phys. B Condens. Matter 192 (1–2) (1993) 55–69, [https://doi.org/10.1016/0921-4526\(93\)90108-i](https://doi.org/10.1016/0921-4526(93)90108-i).
- [27] T. Roisnel, J. Rodríguez-Carvajal, WinPLOTR: a windows tool for powder diffraction pattern analysis, Mater. Sci. Forum 378–381 (2001) 118–123, <https://doi.org/10.4028/www.scientific.net/msf378-381.118>.
- [28] A. Margarian, J.B. Dunlop, R.K. Day, W. Kalceff, Phase equilibria in the Fe-rich corner of the Nd-Fe-Ti ternary alloy system at 1100°C, J. Appl. Phys. 76 (10) (1994) 6153–6155, <https://doi.org/10.1063/1.358338>.
- [29] Z. Chen, H. Zhang, Y. Lei, Secondary solidification behaviour of AA8006 alloy prepared by suction casting, J. Mater. Sci. Technol. 27 (9) (2011) 769–775, [https://doi.org/10.1016/s1005-0302\(11\)60141-2](https://doi.org/10.1016/s1005-0302(11)60141-2).
- [30] T. Koziel, Estimation of cooling rates in suction casting and copper mould casting processes, Arch. Metall. Mater. 60 (2) (2015) 767–771, <https://doi.org/10.1515/amm-2015-0204>.
- [31] A. Yan, K.-H. Müller, O. Gutfleisch, Magnetocaloric effect in LaFe_{11.8-x}Co_xSi_{1.2} melt-spun ribbons, J. Alloy. Comp. 450 (1–2) (2008) 18–21, <https://doi.org/10.1016/j.jallcom.2006.10.093>.
- [32] M. Krautz, J. Hosko, K. Skokov, P. Svec, M. Stoica, L. Schultz, J. Eckert, O. Gutfleisch, A. Waske, Pathways for novel magnetocaloric materials: a processing prospect, Phys. Status Solidi 11 (5–6) (2014) 1039–1042, <https://doi.org/10.1002/pssc.201300637>.
- [33] G. Tan, W. Liu, S. Wang, Y. Yan, H. Li, X. Tang, C. Uher, Rapid preparation of CeFe₄Sb₁₂ skutterudite by melt spinning: rich nanostructures and high thermoelectric performance, J. Mater. Chem. 1 (40) (2013) 12657, <https://doi.org/10.1039/c3ta13024j>.
- [34] D.A. Porter, K.E. Easterling, Phase Transformations in Metals and Alloys, Springer US, 1992, <https://doi.org/10.1007/978-1-4899-3051-4>.
- [35] L.M. Moreno-Ramírez, C. Romero-Muniz, J.Y. Law, V. Franco, A. Conde, I.A. Radulov, F. Maccari, K.P. Skokov, O. Gutfleisch, The role of Ni in modifying the order of the phase transition of La(Fe,Ni,Si)₁₃, Acta Mater. 160 (2018) 137–146, <https://doi.org/10.1016/j.actamat.2018.08.054>.
- [36] NdFe₁₁Ti (NdTiFe₁₁) Crystal Structure: Datasheet from “PAULING FILE Multinaries Edition-2012” in Copyright 2016, Springer-Verlag Berlin Heidelberg & Material Phases Data System (MPDS), Switzerland & National Institute for Materials Science (NIMS), Japan, 2012. https://materials.springer.com/isp/crystallographic/docs/sd_0312099.
- [37] Nd₂(Fe,Ti)₁₇ (Nd₂TiFe₁₆) Crystal Structure: Datasheet from “PAULING FILE Multinaries Edition-2012” Copyright 2016, Springer-Verlag Berlin Heidelberg & Material Phases Data System (MPDS), Switzerland & National Institute for Materials Science (NIMS), Japan, 2012. https://materials.springer.com/isp/crystallographic/docs/sd_0380612.
- [38] Nd₃Fe_{27.76}Ti_{1.24} (Nd₃Ti_{14.5}Fe_{14.5}) Crystal Structure: Datasheet from “PAULING FILE Multinaries Edition-2012” Copyright 2016, Springer-Verlag Berlin Heidelberg & Material Phases Data System (MPDS), Switzerland & National Institute for Materials Science (NIMS), Japan, 2012. https://materials.springer.com/isp/crystallographic/docs/sd_0311082.
- [39] J.M. Cadogan, H.-S. Li, A. Margarian, J.B. Dunlop, D.H. Ryan, S.J. Collocott, R.L. Davis, New rare-earth intermetallic phases R₃(Fe,M)₂₉X_n: (R=Ce, Pr, Nd, Sm, Gd; M=Ti, V, Cr, Mn; and X=H, N, C) (invited), J. Appl. Phys. 76 (10) (1994) 6138–6143, <https://doi.org/10.1063/1.358333>.
- [40] O. Kalogirou, V. Psycharis, L. Saettas, D. Niarchos, “Existence range, structural and magnetic properties of Nd₃Fe_{27.5}Ti_{1.5-y}Mo_y and Nd₃Fe_{27.5}Ti_{1.5-y}Mo_yN_x (0.0 ≤ y ≤ 1.5), J. Magn. Magn. Mater. 146 (3) (May 1995) 335–345.
- [41] G.V. Ivanova, G.M. Makarova, Y.V. Shcherbakova, Y.V. Belozero, A.S. Yermolenko, Peculiarities of the R₃(Fe,Si)₂₉ phase formation in the Sm-Fe-Si system, J. Alloy. Comp. 260 (1–2) (Sep. 1997) 139–142.
- [42] V. Psycharis, M. Gjoka, O. Kalogirou, E. Devlin, D. Niarchos, Structural and magnetic properties of a novel compound with Y₃(Fe, V)₂₉ stoichiometry and disordered CaCu₅-type structure, J. Alloy. Comp. 270 (1–2) (May 1998) 21–27.
- [43] K. Sirisha, Q. Chen, B.M. Ma, M.-Q. Huang, M.E. McHenry, Effect of refractory metals addition on the structural and magnetic properties of Pr₃(Fe, Co, Ti)₂₉ system, J. Magn. Magn. Mater. 321 (15) (Aug. 2009) 2359–2364.
- [44] T. Saito, H. Miyoshi, D. Nishio-Hamane, Magnetic properties of Sm-Fe-Ti nanocomposite magnets with a ThMn₁₂ structure, J. Alloy. Comp. 519 (Apr. 2012) 144–148.
- [45] J. Hu, T. Wang, S. Zhang, Y. Wang, Z. Wang, Structure and magnetic properties of RTi₁₁Fe_{10.9}, J. Magn. Magn. Mater. 74 (1) (1988) 22–26, [https://doi.org/10.1016/0304-8853\(88\)90144-8](https://doi.org/10.1016/0304-8853(88)90144-8).
- [46] M. Ellouze, P. l’Héritier, A. Cheikh-Rouhou, J.C. Joubert, New method of insertion of hydrogen in R₂Fe₁₆Ti alloys with R=Y and Nd, J. Alloy. Comp. 322 (1–2) (2001) 211–213, [https://doi.org/10.1016/s0925-8388\(00\)01501-2](https://doi.org/10.1016/s0925-8388(00)01501-2).
- [47] X.F. Liu, D.F. Chen, Y.M. Hao, J.Y. Lv, S.B. Han, Y.J. Xue, J.H. Li, Z.B. Hu, Investigations on the structural and magnetic properties of doubly substituted Nd₂Fe_{17-x-y}Ti_xGa_y compounds (0 ≤ x ≤ 1.0, 0 ≤ y ≤ 3), J. Alloy. Comp. 407 (1–2) (2006) 58–64, <https://doi.org/10.1016/j.jallcom.2005.06.042>.
- [48] L. Morellon, L. Pareti, P.A. Algarabel, F. Albertini, M.R. Ibarra, Anisotropy and magnetic ordering in the new phase Nd₃(FeTi)₂₉, J. Phys. Condens. Matter 6 (27) (1994) L379–L384, <https://doi.org/10.1088/0953-8984/6/27/004>.
- [49] M. Gjoka, O. Kalogirou, V. Psycharis, D. Niarchos, F. Leccabue, B.E. Watts, G. Bocelli, Synthesis of melt-spun rare-earth transition-metal intermetallics with Nd₃(Fe,Ti)₂₉-type structure, J. Alloy. Comp. 290 (1–2) (1999) 1–5, [https://doi.org/10.1016/s0925-8388\(99\)00197-8](https://doi.org/10.1016/s0925-8388(99)00197-8).
- [50] K.-D. Durst, H. Kronmüller, Determination of intrinsic magnetic material parameters of Nd₂Fe₁₄B from magnetic measurements of sintered Nd₁₅Fe₇₇B₈ magnets, J. Magn. Magn. Mater. 59 (1–2) (1986) 86–94, [https://doi.org/10.1016/0304-8853\(86\)90014-4](https://doi.org/10.1016/0304-8853(86)90014-4).
- [51] K. Skokov, A. Grushishev, A. Khokhlov, Y. Pastushenkov, N. Pankratov, T. Ivanova, S. Nikitin, Magnetic properties of Gd₃Fe₂Ti₃ (x=34, 33, ..., 24), TbFe₁₁Ti and TbFe₁₀Ti single crystals, J. Magn. Magn. Mater. 272–276 (2004) 374–375, <https://doi.org/10.1016/j.jmmm.2003.11.147>.
- [52] A. Hubert, R. Schäfer, Magnetic Domains: The Analysis of Magnetic Microstructures, Springer Science & Business Media, 2008.
- [53] F.J. Humphreys, M. Hatherly, Recrystallization and Related Annealing Phenomena, Elsevier, 2012.
- [54] D. Courtois, D. Givord, B. Lambert-Andron, E. Bourgeat-Lami, Y. Amako, H.-S. Li, J.M. Cadogan, X-ray and magnetic single-crystal analysis of the crystallographic structure of the Y₃(Fe_{0.933}V_{0.067})₂₉ compound, J. Magn. Magn. Mater. 189 (2) (1998) 173–182, [https://doi.org/10.1016/s0304-8853\(98\)00175-9](https://doi.org/10.1016/s0304-8853(98)00175-9).
- [55] T. Klemmer, D. Hoydick, H. Okumura, B. Zhang, W.A. Soffa, Magnetic hardening and coercivity mechanisms in L1₀ ordered FePd ferromagnets, Scr. Metall. Mater. 33 (10–11) (1995) 1793–1805, [https://doi.org/10.1016/0956-716x\(95\)00413-p](https://doi.org/10.1016/0956-716x(95)00413-p).
- [56] S. Bance, F. Bittner, T.G. Woodcock, L. Schultz, T. Schrefl, Role of twin and anti-phase defects in MnAl permanent magnets, Acta Mater. 131 (2017) 48–56, <https://doi.org/10.1016/j.actamat.2017.04.004>.
- [57] M. Soderznic, H. Seprehri-Amin, T.T. Sasaki, T. Ohkubo, Y. Takada, T. Sato, Y. Kaneko, A. Kato, T. Schrefl, K. Hono, Magnetization reversal of exchange-coupled and exchange-decoupled Nd-Fe-B magnets observed by magneto-optical Kerr effect microscopy, Acta Mater. 135 (2017) 68–76, <https://doi.org/10.1016/j.actamat.2017.05.006>.
- [58] T.G. Woodcock, Y. Zhang, G. Hrkac, G. Ciuta, N.M. Dempsey, T. Schrefl, O. Gutfleisch, D. Givord, Understanding the microstructure and coercivity of high performance NdFeB-based magnets, Scr. Mater. 67 (6) (2012) 536–541, <https://doi.org/10.1016/j.scriptamat.2012.05.038>.
- [59] T.G. Woodcock, O. Gutfleisch, Multi-phase EBSD mapping and local texture analysis in NdFeB sintered magnets, Acta Mater. 59 (3) (2011) 1026–1036, <https://doi.org/10.1016/j.actamat.2010.10.033>.



5.2.2 Full-text of Selected Publication B

Reproduced full text article with permission from Elsevier.

Copyright (2021), *Journal of Alloys and Compounds*.



Correlating changes of the unit cell parameters and microstructure with magnetic properties in the CeFe₁₁Ti compound



F. Maccari^{a,1}, S. Ener^{a,*,1}, D. Koch^b, I. Dirba^a, K.P. Skokov^a, E. Bruder^c, L. Schäfer^a, O. Gutfleisch^a

^a Functional Materials, Department of Material Science, Technische Universität Darmstadt, 64287 Darmstadt, Germany

^b Structural Research, Department of Material Science, Technische Universität Darmstadt, 64287 Darmstadt, Germany

^c Physical Metallurgy, Department of Material Science, Technische Universität Darmstadt, 64287 Darmstadt, Germany

ARTICLE INFO

Article history:

Received 22 October 2020

Received in revised form 14 January 2021

Accepted 17 January 2021

Available online 2 February 2021

2010 MSC:

2.02 - 7.01

Keywords:

Magnetostriction

CeFe₁₁Ti

Magneto-crystalline anisotropy

Hard magnetic materials

ABSTRACT

The criticality of rare-earth elements and its impact on the permanent magnet market have initiated a search for alternative material systems, either to fill the magnetic performance gap between ferrites and Nd-Fe-B magnets or to even replace the existing benchmark systems. Ce-based systems are attractive due to the abundance of cerium, however the formation of secondary phases leads to challenges for Ce-based compounds. We investigated the formation and magnetic properties of ThMn₁₂-type Ce_{1+x}Fe₁₁Ti samples for $x = 0.15$ and 0.20 compositions. Microstructural investigations reveal the formation of twin boundaries in the ThMn₁₂ grains with a misorientation angle of $58^\circ \pm 2^\circ$. By varying the chemical composition and lowering the annealing temperatures, a grain refinement and reduction in twin boundary density was achieved. In addition, the magnetostrictive characteristic of CeFe₁₁Ti-phase was investigated. Around the Curie temperature, an M^2 behaviour is noted, in contrast to an M^3 behaviour at lower temperatures. To probe the effect of unit cell compression and expansion on the magnetic properties, magnetic characterizations were carried out under hydrostatic pressure and after hydrogenation. A slight reduction is observed for the measured anisotropy field under 0.45 GPa hydrostatic pressure in the temperature interval of 10–300 K, which is consistent with the small increase detected for the hydrogenated compound.

© 2021 Elsevier B.V. All rights reserved.

1. Introduction

Hard magnetic materials have received increasing attention during the last years due to the new developments in renewable energies and electric motors [1,2]. The current permanent magnet market is mainly shared between the high energy product Nd₂Fe₁₄B-type magnets and low energy product hard ferrites. Due to the lack of proper gap magnets between these two systems, in some applications (e.g. sensor applications) the Nd₂Fe₁₄B-type magnets are in use which are performing way under their limits. To minimize the use of critical elements it is essential to find alternative gap magnet materials which can perform in the mid-energy product region.

The REFe_{12-x}M_x alloys (RE-rare-earth and M-stabilizing 3d metal element), which form the ThMn₁₂-type ($I4/mmm$) structure, are promising hard magnetic material candidates due to their low rare-

earth content and potentially high intrinsic magnetic properties [3–9]. Among the other rare-earth elements, cerium is an interesting candidate for the hard magnetic ThMn₁₂-type materials due to its relatively high abundance. However, the ThMn₁₂-type binary RE-Fe systems are not stable in bulk form, and additional stabilization elements must be introduced for increased stability in bulk state [10–15]. Among these stabilization elements, Ti stands out as it has the smallest atomic concentration for stabilizing the ThMn₁₂-type structure, leading to a higher Fe content and, consequently, higher magnetization [3]. In literature, different modifications for the improvement of the hard magnetic properties of the CeFe₁₁Ti compound have been proposed, including: partial substitution of iron by cobalt [16–21], different stabilization elements [22,23] and interstitial incorporation of hydrogen and nitrogen [17,24–28].

Akayama et al. reported a reduced magneto-crystalline anisotropy for the nitrogenated CeFe₁₁Ti samples [4]. A small increase of the magneto-crystalline anisotropy has been reported by Isnard et al. on CeFe₁₁TiH compound [27]. Even though the magneto-crystalline anisotropy behaves differently for interstitial H and N, both interstitial

* Corresponding author.

E-mail address: semih.ener@tu-darmstadt.de (S. Ener).

¹ Both F.M. and S.E. equally contributed to this work.

atoms lead to an increase of the Curie temperature related to the unit cell expansion and the increase of Fe-Fe exchange interaction [24,27].

Apart from these investigations, there are no comprehensive studies on the phase formation in correlation with magnetic properties of ThMn₁₂-type CeFe₁₁Ti system.

In the present work, we report on the microstructural, structural and magnetic properties of ThMn₁₂-type Ce_{1+x}Fe₁₁Ti alloys. Detailed microstructural observations are compared with the magnetic domain structure, in which the formation of twin boundaries in 1:12 grains are observed. Additionally, lattice thermal expansion is investigated and correlated to the magnetic properties of Ce_{1.20}Fe₁₁Ti sample. The effect of compressive strain, by applying hydrostatic pressure, and also expansive strain, by interstitial hydrogen, on the anisotropy field of CeFe₁₁Ti compound is reported.

2. Experimental details

The off-stoichiometric Ce_{1+x}Fe₁₁Ti ($x = 0.15$ and 0.20) alloys were prepared by melting high-purity starting elements (purity above 99.8%) in an induction furnace under a purified argon atmosphere. The off-stoichiometric compositions were used to suppress the formation of the undesired α -Fe phase. The resulting bulk ingots were suction-casted by using a commercial arc melting & suction casting setup (MAM-1 Edmund Bühler GmbH). To ensure rapid solidification a rectangular cavity with 0.5 mm edge length was used. The suction casted plates were wrapped in Mo foil and sealed in quartz ampoules under argon atmosphere for annealing. Annealing was carried out for 12 h at 10 different temperatures: ranging from 700 up to 1150 °C in 50 °C steps. To prevent possible decomposition reactions and to retain the phases which are present at the annealing temperature, all samples were water-quenched to room temperature.

Part of the suction-casted plates were ground into powders <63 μ m to carry out the hydrogenation. All handling steps were done in an Ar filled glovebox to avoid surface oxidation. A custom-built pressure reactor equipped with a vertical tube furnace for temperature control was used. The hydrogenation experiments on the CeFe₁₁Ti powders were carried out under 20 bar H₂ pressure at 150 °C for 20 h.

Room temperature microstructural analysis and phase determination of the investigated samples were carried out using scanning electron microscope (SEM - Tescan VEGA 3) equipped with backscattered electrons (BSE) and energy dispersive x-ray (EDX) detectors. Chemical compositions of the observed phases were determined by averaging 5 different measurements from different parts of the sample to ensure the minimization of statistical errors.

Electron backscatter diffraction (EBSD) was performed in a FEG-SEM (Tescan Mira3) to analyze selected samples and determine the grain orientations and calculate the misorientation angle for twinned grains. For the determination of misorientation angle, different twinned grains were measured and the obtained results were averaged to minimize errors.

For the observation of magnetic domain structures, magneto-optical Kerr effect (MOKE) microscopy measurements were carried out by using a Zeiss Axio Imager.D2m light microscope equipped with polarization options (from evico magnetics GmbH). The image contrast was enhanced by subtracting the non-magnetic averaged background image from the collected average image using KerrLab software.

The structural properties were investigated by refining the x-ray powder diffraction (XRD) patterns. XRD measurements were carried out on powders ground below 60 μ m by using a custom build diffractometer with a Mythen2 R 1 K detector (Dectris Ltd.) using Mo K α radiation in transmission geometry. For controlling the temperature, a closed cycle He-cryostat (SHI Cryogenics Group) was used. The measurements were taken in the temperature range between 140 K and 700 K with a cooling/heating rate of 2 K/min and a 10 min dwell time for temperature stabilization before collecting the data. To correct the

geometrical errors, the sample was mixed with NIST 640d standard silicon powder and glued on a graphite foil with high temperature varnish. Crystal structure determination and unit cell parameter refinements were done using the FullProf software [29].

Thermomagnetic measurements were carried out using a vibrating sample magnetometer (LakeShore 7410). The measurements were done in the temperature range between 350 K $\leq T \leq$ 700 K with a heating rate of 5 K/min under an applied field of 1 T. Isothermal magnetic measurements were performed using a physical properties measurement system (Quantum Design PPMS14) in the temperature range between 10 and 300 K. Prior to the isothermal measurements the samples were ground to powder below 20 μ m and mixed with paraffin wax and encapsulated in an aluminium pan. Afterwards, the pan was heated above the melting point of the wax and an external magnetic field of 1.3 T was applied for texturing the CeFe₁₁Ti powder. The magnetization measurements were performed in the parallel and perpendicular direction of the alignment direction for anisotropy field determination. Additionally, the effect of isostatic pressure was investigated by using a high pressure sample cell setup, in which a 0.45 GPa pressure was applied to the sample during the measurement.

3. Results and discussion

The microstructure and phase analysis of the Ce_{1.15}Fe₁₁Ti (see Supplementary materials Fig. S1 and S2) and Ce_{1.20}Fe₁₁Ti samples were evaluated from the combination of BSE-SEM images and EDX analysis. The BSE contrast images of the Ce_{1.20}Fe₁₁Ti samples are shown in Fig. 1 in the suction-cast state and after annealing at different temperatures for 12 h. All the images consist of a white and 2 different grey contrasts. The white contrast is related to the CeFe₂-Laves phase, while the dark grey corresponds to a mixture of α -Fe(Ti) and Fe₂Ti-Laves phase and the light-grey which corresponds to the CeFe₁₁Ti. The chemical compositions of these phases are determined from the EDX measurements and listed with their corresponding error range in Table 1. More detailed information about microstructure and micrographs are presented in Supplementary materials.

In addition to the chemical compositional analysis, room temperature XRD measurements of these samples were carried out (see Supplementary materials Fig. S3 and S4) and the obtained results agree with the findings of the BSE-SEM. The corresponding Rietveld refinements confirm the formation of four phases; i) Fe₂Ti-Laves phase with the space group of $P6_3/mmc$ (#194), ii) CeFe₂-Laves phase with the space group of $Fd-3m$ (#227), iii) ThMn₁₂-type CeFe₁₁Ti with the space group of $I4/mmm$ (#139) and α -Fe with the space group of $Im-3m$ (#229).

The microstructure in the suction-cast state Ce_{1.20}Fe₁₁Ti consists of very fine and homogeneously distributed Laves- (Fe₂Ti and CeFe₂), and CeFe₁₁Ti phases - a corresponding image with higher magnification is given in Supplementary materials (Fig. S2). This homogeneous microstructure has been proved to be suitable to reduce the annealing time in comparison to coarser microstructure [12]. As can be seen from Fig. 1, the optimum annealing temperature for the highest ThMn₁₂-type phase fraction is achieved at 850 °C, with a small fraction of CeFe₂ (less than 8 wt%), and complete absence of the soft magnetic α -Fe phase. A further increase of the annealing temperature leads to the formation of undesired Fe₂Ti and α -Fe phases combined with CeFe₁₁Ti grain coarsening. Based on these results, we selected the Ce_{1.20}Fe₁₁Ti sample which was suction-cast and annealed at 850 °C for 12 h for further analysis. Similar annealing studies were carried out for Ce_{1.15}Fe₁₁Ti samples and the results show that the highest phase ratio of ThMn₁₂ is obtained for the sample annealed at 950 °C. The ThMn₁₂ grains are coarser in comparison to the Ce_{1.20}Fe₁₁Ti sample annealed at 850 °C (all data not

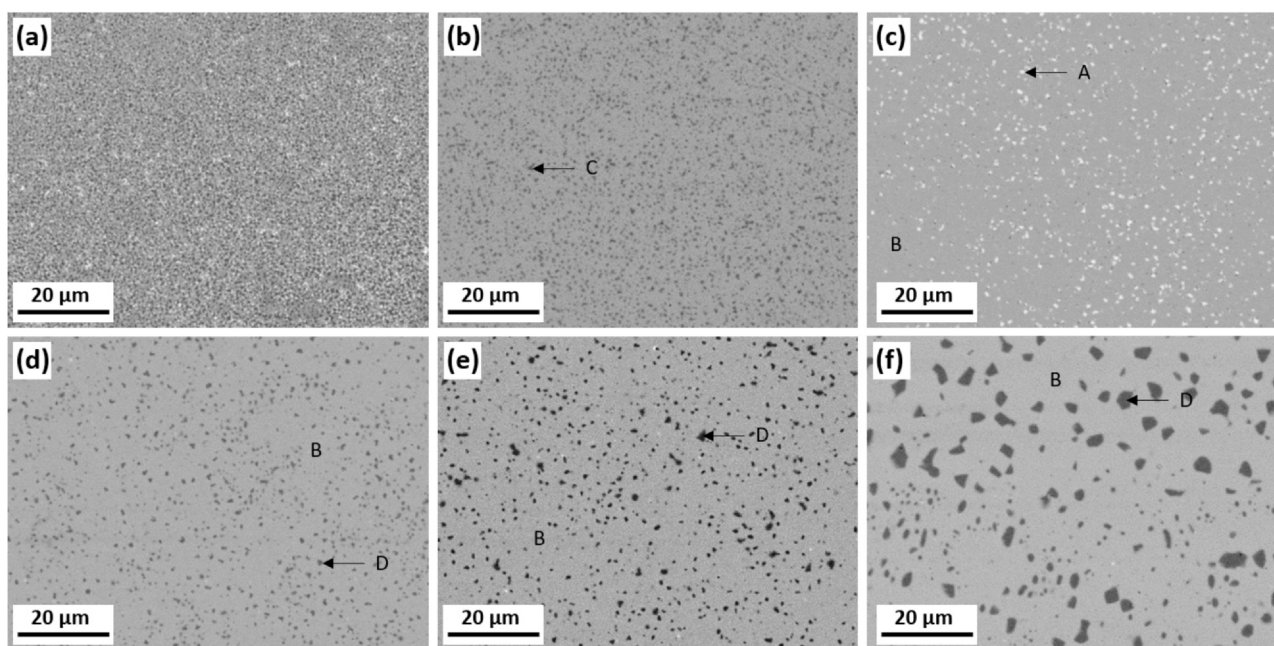


Fig. 1. BSE contrast SEM images of the $Ce_{1.20}Fe_{11}Ti$ samples in (a) the suction-cast state and after annealing at (b) 700 °C, (c) 850 °C, (d) 900 °C, (e) 1000 °C and (f) 1100 °C for 12 h. Corresponding compositions of the phases labeled with letters can be found in Table 1.

Table 1

Chemical composition analysis of the occurring corresponding phases. Corresponding labels are also indicated in Fig. 1 and Fig. S2 in Supplementary materials.

Label	Composition	Phase
A	$Ce_{32.90 \pm 0.27}Fe_{66.59 \pm 0.28}Ti_{0.50 \pm 0.03}$	CeFe ₂ -Laves
B	$Ce_{8.23 \pm 0.16}Fe_{84.53 \pm 0.12}Ti_{7.24 \pm 0.11}$	Ce(Fe,Ti) ₁₂
C	$Ce_{1.65 \pm 0.28}Fe_{72.60 \pm 0.56}Ti_{25.75 \pm 0.84}$	Fe ₂ Ti-Laves
D	$Ce_{0.83 \pm 0.13}Fe_{93.26 \pm 0.25}Ti_{5.91 \pm 0.13}$	α -Fe(Ti)

*Comparison of the phases are shown in detail in Supplementary materials.

shown here), as expected from the higher annealing temperature, as exemplified on Fig. 2a and 2b.

The magneto-optical Kerr effect (MOKE) microscopy images of the $Ce_{1+x}Fe_{11}Ti$ samples are shown in Fig. 2c and 2d in comparison with the corresponding room temperature BSE images (Fig. 2a and 2b). The microstructure of the $Ce_{1.15}Fe_{11}Ti$ sample annealed at 950 °C show grains with an average size between 20 and 30 μm. The corresponding magneto-optical Kerr effect (MOKE) image shows star- and maze-like domain structures which are correlated to the uniaxial anisotropy of ThMn₁₂-type Ce(Fe,Ti)₁₂ system.

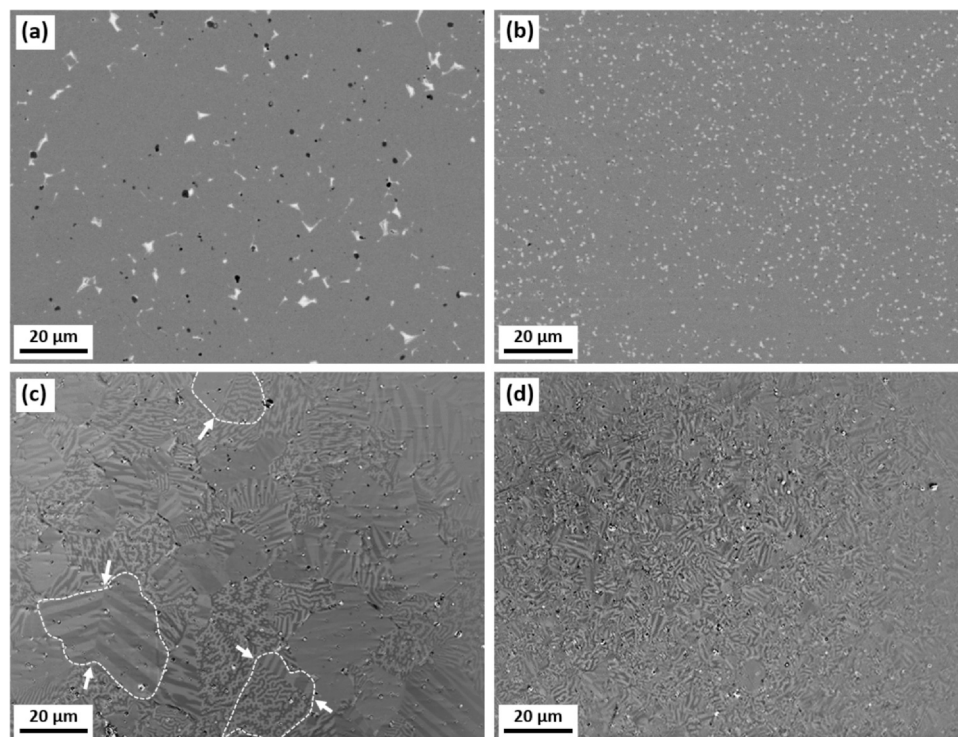


Fig. 2. Room temperature BSE contrast images of (a) $Ce_{1.15}Fe_{11}Ti$ (annealed at 950 °C) and (b) $Ce_{1.20}Fe_{11}Ti$ (annealed at 850 °C) samples and (c,d) corresponding MOKE images.

Some of the CeFe₁₁Ti grains of the Ce_{1.15}Fe₁₁Ti sample show the appearance of twin boundaries, which were already reported for Gd- and Nd-based 1:12 that can act as a nucleation center for reversal domains, decreasing the coercivity of such compounds [12,30]. MOKE microscopy is a very useful tool as different twin variants show different domain patterns which are originated from the alternating crystal orientations. Even though the BSE contrast image show no significant contrast changes in the grains, the MOKE image exhibit some changes of the domain pattern within the grain which indicates the formation of twins. Similar SEM and Kerr images obtained for the Ce_{1.20}Fe₁₁Ti sample, annealed at 850 °C, indicate that the grains of the ThMn₁₂-type phase have average size around 7 μm (calculated from the EBSD analysis). The domain structure of the Ce_{1.20}Fe₁₁Ti sample also shows features of high magneto-crystalline anisotropy coming from the ThMn₁₂-type phase but twins were not observable from the MOKE images.

To evaluate the microstructure further and confirm the formation of twins also for the Ce_{1.20}Fe₁₁Ti sample, EBSD was used and the results of the analysis are shown in Fig. 3. For a better visualization, the twins are marked with arrows both in the image quality (IQ) and inverse pole figure (IPF) maps. The misorientation angle between the two variants of the twin was found to be 58° ± 2° (see Fig. 3c). Similar angle were reported also for different ThMn₁₂-type structures with different rare-earth elements [12]. The twin formation has been reported for material systems with low stacking fault energy and is commonly related to internal or external stresses. As there was no external stress applied to the Ce_{1.20}Fe₁₁Ti, one can rule out the external stress but it is possible that internal stresses which were existing during the rapid solidification and annealing may play a role for the formation of twins. Additionally, the starting off-stoichiometric composition may play a role for the formation of twins as the compositional space of ThMn₁₂-type is quite limited and excessive cerium during the solidification may create an internal stress.

In addition to the microstructural analysis, temperature-dependent XRD was carried out. Fig. 4 shows the temperature dependence of the unit cell parameters *a* and *c* and the unit cell volume *V* for the ThMn₁₂-type phase of the Ce_{1.20}Fe₁₁Ti sample. The symbols correspond to the unit cell parameters obtained from the Rietveld refinement of each corresponding temperature. Solid black lines indicate the linear fit of 3 different temperature intervals where linear-like behaviours are observed and the dashed line corresponds to the Curie temperature (*T_c*)-as will be presented later. Above the Curie temperature, the observed linear thermal expansion only show the phonon contribution. One can extrapolate this high temperature (above *T_c*) linear fit to lower temperatures to extract the effect of magnetism to the linear thermal expansion. In the paramagnetic region of the Ce_{1.20}Fe₁₁Ti, the thermal expansion is almost isotropic showing a similar linear thermal expansion coefficient for both *a*- and *c*-axis (see Fig. 5). Well below the Curie temperature, where the Ce_{1.20}Fe₁₁Ti is ferromagnetic with uniaxial anisotropy, the linear thermal expansion coefficients α_a and α_c clearly differ from each other, which indicates an anisotropic effect of magnetism to the thermal expansion. Additionally, around the Curie temperature both unit cell parameters and the unit cell volume show an anomaly which is an Invar-type anomaly. This kind of Invar-type anomaly is due to the large magnetostrictive deformation of the magnetically ordered lattice originating from the magnetic anisotropy and magnetic exchange interactions of the rare-earth elements and 3d transition metals. For the rare-earth transition-metal alloys, the magnetostriction depends slightly on the rare-earth element and is mainly caused by the Fe-Fe exchange interaction. Similar Invar-like anomalies have been reported for different rare-earth transition-metal systems like RE(Fe,Nb)₁₂ [31], RE₂Fe₁₇ [32] and Y₂(Fe_{1-x}Co_x)₁₄B [33]. Both a unit cell parameter and the volume presented in the Fig. 4 show a small dip around 240 K region, which corresponds to the Curie temperature of the CeFe₂-Laves phase. As previously

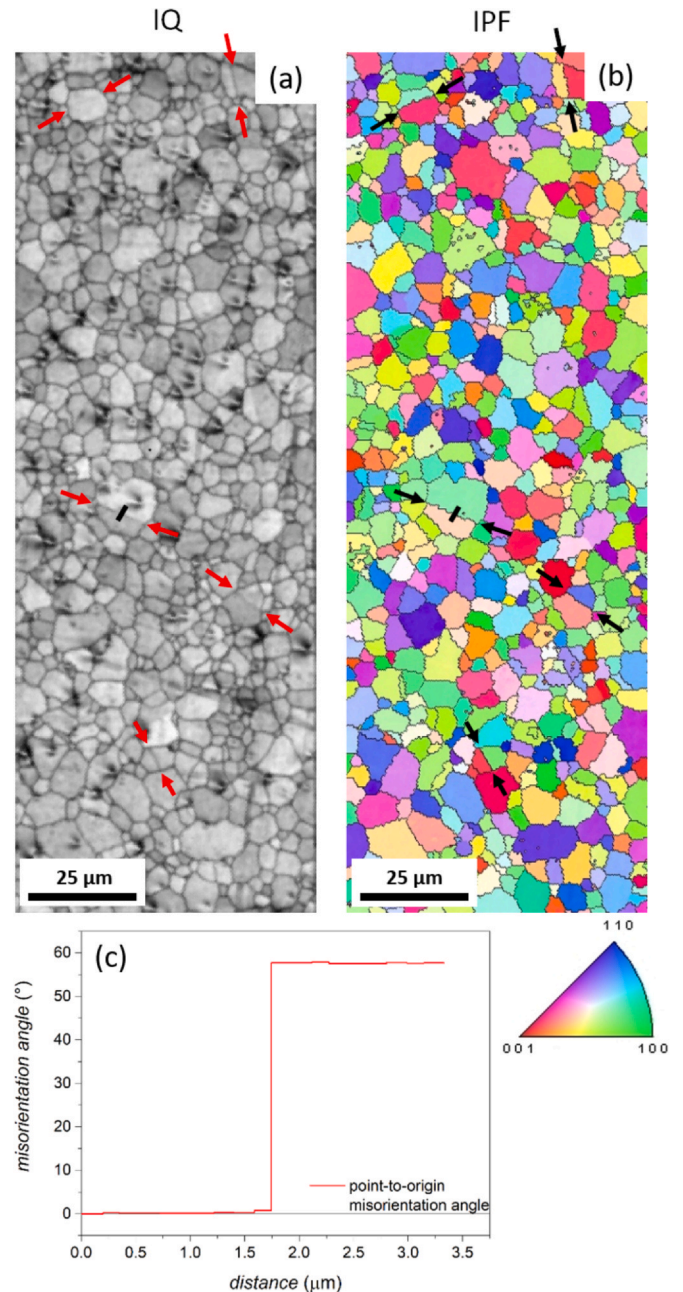


Fig. 3. Room temperature microstructural analysis of the Ce_{1.20}Fe₁₁Ti annealed at 850 °C samples with (a) the image quality (IQ) contrast image, (b) corresponding inverse pole figure (IPF) images. Observed twins are highlighted with arrows. (c) Point-to-origin misorientation angle measurement through the twin boundary where the measurement line is indicated in IQ and IPF images with black line.

mentioned, this sample show 8 wt% of secondary CeFe₂-Laves phase and, as presented in Fig. S6 in Supplementary materials, an Invar type anomaly is also observed for this phase. Considering the co-existence of the matrix ThMn₁₂-type phase along with the secondary Laves phase, this observed small dip around 240 K can be related to the magnetostriction of the CeFe₂-Laves phase [34,35].

The linear thermal expansion coefficients of the ThMn₁₂-type structure are calculated for the both *a*- and *c*-axis and also for the unit cell volume *V* and the results are shown in Fig. 5. For the determination of linear thermal expansion coefficients of unit cell parameters (α_a and α_c) the following equations are used;

$$\alpha_a = \frac{1}{a_{140K}} \frac{\delta a}{\delta T} \quad \text{and} \quad \alpha_c = \frac{1}{c_{140K}} \frac{\delta c}{\delta T} \quad (1)$$

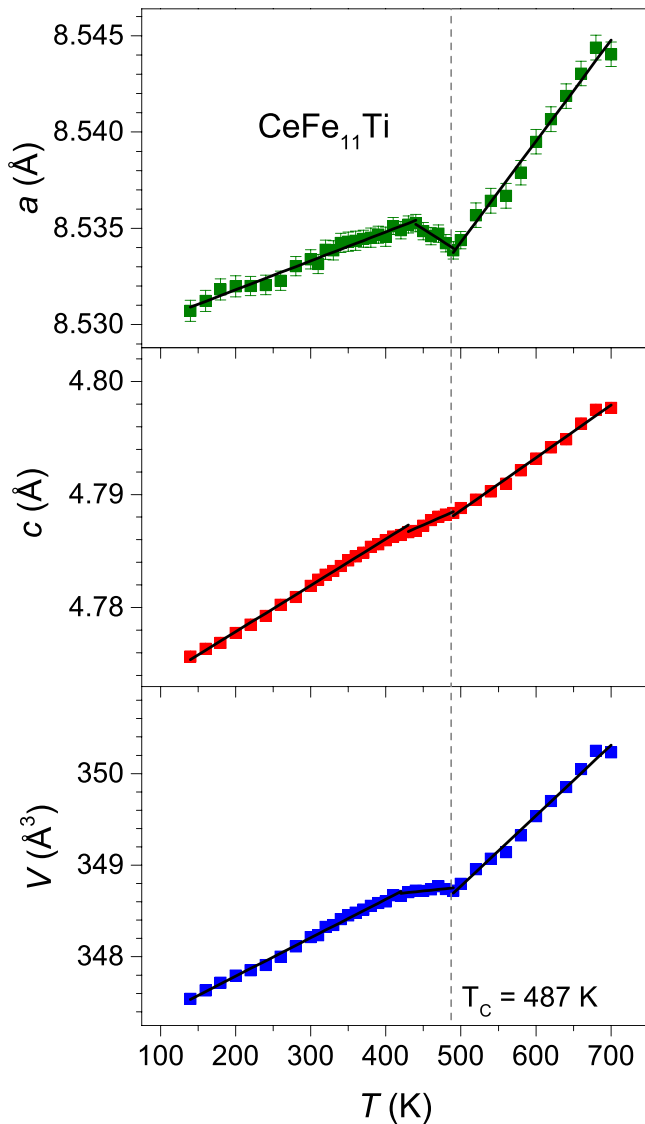


Fig. 4. Temperature dependence of the unit cell parameters (a , c) and unit cell volume (V) of ThMn₁₂-type phase of Ce_{1.20}Fe₁₁Ti sample. The error bars are also shown in the figures. For the unit cell parameter c and the volume V the estimated errors are smaller than the symbol size.

where, a_{140K} and c_{140K} corresponds to the unit cell parameters of a and c at lowest measured temperature of 140 K and T is temperature. Similarly, the linear thermal expansion parameter (α_V) was obtained by using the calculated volume value of each temperature. Both the α_a and α_V show quite different averaged thermal expansion coefficient values above and below the T_C . In contrast, for the whole measured temperature range, the α_c show no significant change. Both α_a and α_V show negative values of thermal expansion at the T_C which indicates the effect of uniaxial magneto-crystalline anisotropy and contraction in the $a - b$ basal plane.

In order to determine the magnetic properties of the Ce_{1.20}Fe₁₁Ti sample, thermomagnetic and isothermal magnetization measurements were carried out and the results are shown in Fig. 6. For the estimation of the T_C the first derivative of the thermomagnetic measurement is used and the data is shown in Fig. 6 inset. As the thermomagnetic measurements were carried out under 1 T external magnetic field the measured T_C is expected to be higher than the actual value. The Curie temperature estimated from the first derivative of the $M(T)$ measurement is 487 K. Additionally, the paramagnetic Curie temperature is calculated from the Curie-Weiss law.

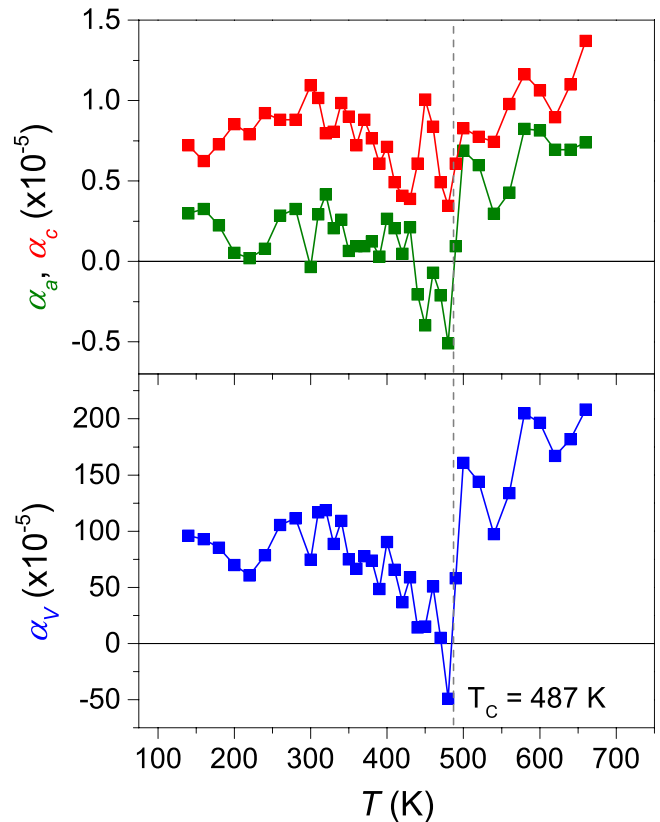


Fig. 5. Linear thermal expansion coefficients of the unit cell parameters (a , c) and the unit cell volume (V) of ThMn₁₂-type phase of Ce_{1.20}Fe₁₁Ti sample.

The temperature dependence of the paramagnetic susceptibility follows the Curie-Weiss law $\chi = C/(T - \Theta)$ with paramagnetic Curie temperature $\Theta = 482$ K which is slightly lower than the T_C obtained from the $\delta M/\delta T$. At high temperatures (above 600 K) a slight increase in the magnetization is observed due to formation of α -Fe during the measurement.

For direct correlation of the thermal expansion, the deviation of the c unit cell parameter (Δc) from the Debye model is plotted together with the temperature dependence of the magnetization square and magnetization cube and shown in Fig. 7. For calculating the Δc , the high temperature linear thermal expansion of the unit cell parameter c is extrapolated from the high temperature region (see Fig. 4) and the difference between the data and the extrapolated region gives the Δc value. Direct comparison of the Δc to the magnetization follows an M^2 behaviour around the Curie temperature and an M^3 behaviour for low temperatures. The inset in Fig. 7 shows a direct comparison of different power laws of magnetization versus the Δc . The M^2 behaviour around the Curie temperature and M^3 behaviour at lower temperatures were observed which are shown in blue and red colors in Fig. 7, respectively. These observed M^2 and M^3 behaviours agree well with established theoretical models of magnetostriction [36–38]. For a similar material system with ThMn₁₂-type structure Salazar et al. reported an M^3 behaviour for the whole temperature region and relate this M^3 behaviour to single-ion contribution to the magnetostriction [39].

Isothermal magnetization measurements of the Ce_{1.20}Fe₁₁Ti were performed on textured powder at room temperature. Magnetic measurements were done along two different directions, parallel and perpendicular to the texture direction for the estimation of the anisotropy field. In Fig. 6b, a direct observation of the anisotropy field is not straightforward from these textured powder measurements. For a more precise determination of the anisotropy field, the method established by Durst and Kronmüller is used which is widely

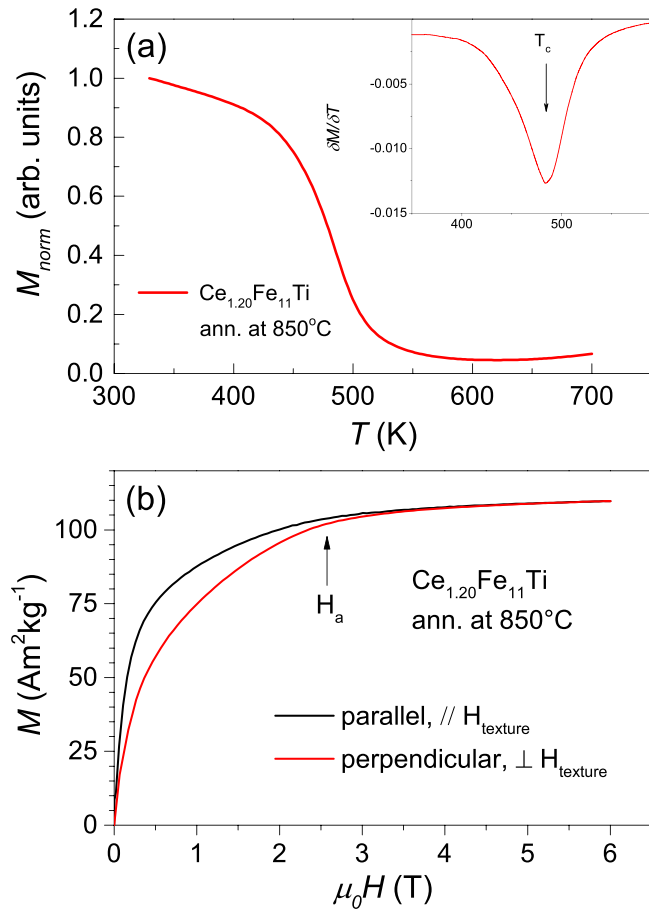


Fig. 6. (a) Thermomagnetic measurement of $\text{Ce}_{1.20}\text{Fe}_{11}\text{Ti}$ sample under 1 T external magnetic field and the inset shows the first order temperature derivative of the magnetisation data for the determination of Curie temperature. (b) Room temperature isothermal magnetization measurements of textured $\text{Ce}_{1.20}\text{Fe}_{11}\text{Ti}$ along and perpendicular to the alignment direction. A comparison with the sample $\text{Ce}_{1.15}\text{Fe}_{11}\text{Ti}$ is given in Supplementary materials-Fig. S7. (For interpretation of the references to colour in this figure, the reader is referred to the web version of this article.)

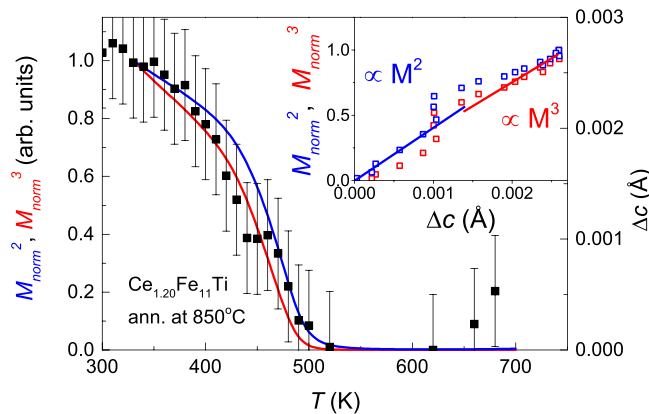


Fig. 7. Direct comparison of the change of deviation of the c unit cell parameter from Debye model and the temperature dependences of M^2 and M^3 . The inset shows the linear regions of the Δc and magnetization powers. (For interpretation of the references to colour in this figure, the reader is referred to the web version of this article.)

used for hard magnetic polycrystalline systems [40]. In this method, the anisotropy field is estimated from the $M(T^{-2})$ curves using the minimum which is obtained from the first derivative of the $M(T^{-2})$ plot. The value estimated by the Durst and Kronmüller method gives the value of $H_a = 2.57$ T. For the confirmation of this method we also estimate the anisotropy field value by using the Sucksmith-

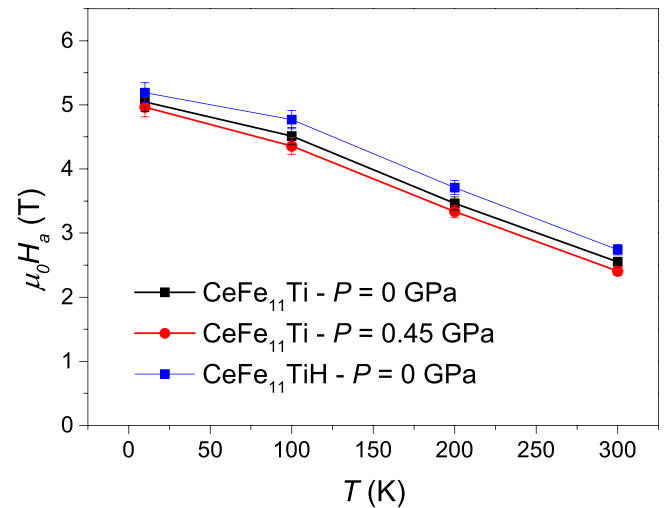


Fig. 8. The anisotropy fields calculated from the Durst and Kronmüller method both for $\text{CeFe}_{11}\text{Ti}$ sample under 0 GPa and 0.45 GPa external hydrostatic pressure together with hydrogenated $\text{CeFe}_{11}\text{Ti}$ sample.

Thompson method [41] which agrees with the Durst and Kronmüller method. Additionally, due to the formation of twins in the micro-structure of the ThMn_{12} -type phase, it is not possible to achieve a good texture. As a result of it, the perpendicular direction measurements deviate from ideal hard direction measurements (red curve in Fig. 6b).

The literature shows a significant reduction of the anisotropy fields with nitrogenation of $\text{CeFe}_{11}\text{Ti}$ [4,42]. In contrary, as shown in Fig. 8, the hydrogenation slightly increases the anisotropy of the $\text{CeFe}_{11}\text{Ti}$ system which is in good agreement with the literature [27]. As these hydrogen and nitrogen atoms occupy the interstitial positions in the unit cell, they cause a lattice expansion that leads to an increase of Curie temperature. After nitrogenation, the Curie temperature of $\text{CeFe}_{11}\text{Ti}$ increases from 487 to 765 K, approximately. Similar increase is observed for the hydrogenated $\text{CeFe}_{11}\text{TiH}_x$ sample where the Curie temperature of approx. 540 K is observed. The anomalous behaviour of the anisotropy field of the $\text{CeFe}_{11}\text{TiH}_x$ is attributed to the Kondo screening [42] which is not the case for $\text{CeFe}_{11}\text{TiH}_x$. The room temperature XRD patterns of the $\text{CeFe}_{11}\text{Ti}$ and $\text{CeFe}_{11}\text{TiH}_x$ samples are given in Fig. S5 in the supplementary materials. Prior to hydrogenation, the Rietveld analysis results in the unit cell parameters of $a = 8.5333 \pm 0.0005$ Å and $c = 4.7881 \pm 0.0003$ Å for the ThMn_{12} -type phase. After hydrogenation, the unit cell parameters obtained from the Rietveld analysis for $\text{CeFe}_{11}\text{TiH}_x$ phase changed to $a = 8.5704 \pm 0.0006$ Å and $c = 4.8069 \pm 0.0003$ Å. As expected from the interstitial hydrogen modification, an expansion of the unit cell parameters is observed. The tetragonality (c/a) does not change significantly after hydrogenation. For a better comparison, the structural parameters and the measured anisotropy field values are compared in Table 2. The anisotropy field values can not be directly correlated to the tetragonality of the unit cell. Observed lattice expansion is lower for hydrogen in comparison to nitrogen but leads to a higher anisotropy field. These results indicate that the lattice expansion and tetragonality do not have a monotonous relation with the anisotropy field values. Literature reports the effect of Kondo screening of the Ce-4f electrons in the nitrogenated samples. Further theoretical calculations are necessary to understand the effect of hydrogen on the Kondo screening behaviour.

The effect of external hydrostatic pressure on the anisotropy field values of $\text{Ce}_{1.20}\text{Fe}_{11}\text{Ti}$ sample is given in Fig. 8. A hydrostatic pressure of 0.45 GPa leads to a small reduction of the anisotropy field. The anisotropy field at room temperature (300 K) is reduced by 5.5%

Table 2

Comparison of the structural properties (a , c , c/a) of CeFe₁₁Ti, CeFe₁₁TiH_x and CeFe₁₁TiN_x samples with corresponding room temperature anisotropy field (H_a) values.

Sample	a (Å)	c (Å)	c/a	H_a (T)
CeFe ₁₁ Ti	8.5333	4.7881	0.5611	2.5
CeFe ₁₁ TiH _x	8.5704	4.8069	0.5609	2.74
CeFe ₁₁ TiN _x ¹	8.62	4.84	0.561	2.0

¹ Values from Ref. [4].

whereas the reduction at 10 K is only 1.6%. These results indicate that both chemical expansion of the unit cell by nitrogeneration and compression of the unit cell by external hydrostatic pressure reduces the anisotropy field values whereas the hydrogenation is working in the opposing direction. Additionally, the expansion of the unit cell leads to an increase of the Curie temperature and the compression of the lattice should reduce the T_C , which can be one of the reasons for the observed results.

4. Summary and conclusions

Polycrystalline Ce_{1.20}Fe₁₁Ti and Ce_{1.15}Fe₁₁Ti samples were produced by using a rapid solidification method (suction casting). Different annealing treatments were applied to the suction-cast samples and microstructural, structural and magnetic characterizations were carried out. Results of different annealing temperatures indicate that the optimum annealing temperature for Ce_{1.20}Fe₁₁Ti sample is 850 °C for 12 h. Detailed MOKE microscopy and EBSD analysis indicate the formation of twin boundaries, which have been also reported for other ThMn₁₂-type structures with different rare-earth elements. The misorientation angle between the twin variants is measured to be $58^\circ \pm 2^\circ$ from the EBSD measurements. The formation of twins in the microstructure makes these materials not suitable for proper texturing but with a proper control of the microstructure the formation of the twins can be suppressed.

The temperature dependence of the unit cell parameters and unit cell volume shows an anomaly at the Curie temperature which is related to the Invar-type behaviour. This Invar-type anomaly is due to the large magnetostrictive deformation of the lattice originating from the exchange interaction and magneto-crystalline anisotropy of the ThMn₁₂-type structure. Around the Curie temperature an M^2 behaviour of the magnetostriction is observed whereas an M^3 behaviour is observed for low temperatures both behaviours agreeing well with the theoretical models of the magnetostriction.

Isothermal magnetization measurements of CeFe₁₁Ti compound under hydrostatic pressure have shown a slight decrease in the anisotropy field values in the investigated temperature range. The reduction of the spontaneous magnetization is attributed to the expected reduction of the Curie temperature under 0.45 GPa hydrostatic pressure. The anisotropy field values estimated for the CeFe₁₁TiH sample show a slight increase in agreement with the literature which show a different behaviour than the CeFe₁₁TiN sample.

CRedit authorship contribution statement

F. Maccari: Methodology, Investigation, Formal analysis, Writing - Review & Editing. **S. Ener:** Conceptualization, Investigation, Formal analysis, Writing - Original Draft preparation, Visualization. **D. Koch:** Investigation. **I. Dirba:** Methodology, Investigation, Writing - Review & Editing. **K.P. Skokov:** Investigation. **E. Bruder:** Investigation, Writing - Review & Editing. **L. Schäfer:** Investigation. **O. Gutfleisch:** Writing - Review & Editing, Supervision, Funding acquisition.

Declaration of Competing Interest

The authors declare that they have no known competing financial interests or personal relationships that could have appeared to influence the work reported in this paper.

Acknowledgements

Authors gratefully acknowledge the funding provided by the Deutsche Forschungsgemeinschaft (DFG, German Research Foundation) on the project "Rare-earth based alloys for hard-magnetic applications: temperature and pressure dependent phase stabilities (RE-MAP)" with the project number 316912154. This work was also supported by the Deutsche Forschungsgemeinschaft (DFG, German Research Foundation), Project ID No. 405553726, TRR 270 and the future pioneering program development of magnetic material technology for high-efficiency motors (MagHEM) commissioned by the New Energy and Industrial Technology Development Organization (NEDO).

Appendix A. Supporting information

Supplementary data associated with this article can be found in the online version at doi:10.1016/j.jallcom.2021.158805.

References

- [1] O. Gutfleisch, M.A. Willard, E. Brück, C.H. Chen, S.G. Sankar, J.P. Liu, Magnetic materials and devices for the 21st century: stronger, lighter, and more energy efficient, *Adv. Mater.* 23 (7) (2011) 821–842, <https://doi.org/10.1002/adma.201002180>
- [2] K.P. Skokov, O. Gutfleisch, Heavy rare earth free, free rare earth and rare earth free magnets - Vision and reality, *Scr. Mater.* 154 (2018) 289–294, <https://doi.org/10.1016/j.scriptamat.2018.01.032>
- [3] A. Müller, Magnetic material R₂Fe₁₄Mo₂(Co) with ThMn₁₂ structure, *J. Appl. Phys.* 64 (1) (1988) 249–251, <https://doi.org/10.1063/1.341473>
- [4] M. Akayama, H. Fujii, K. Yamamoto, K. Tatami, Physical properties of nitrogenated RFe₁₁Ti intermetallic compounds (R=Ce, Pr and Nd) with ThMn₁₂-type structure, *J. Magn. Magn. Mater.* 130 (1) (1994) 99–107, [https://doi.org/10.1016/0304-8853\(94\)90662-9](https://doi.org/10.1016/0304-8853(94)90662-9)
- [5] P. Qi, Z. Xiao-dong, Z. Ming-hou, Y. Ying-chang, Magnetic properties of new series R-Mo-Fe nitrides with the ThMn₁₂-type structure at a lower Mo content, *Acta Phys. Sin.* 3 (6) (1994) 460–469, <https://doi.org/10.1088/1004-423x/3/6/009>
- [6] W. Suski, The ThMn₁₂-Type compounds of rare earths and actinides: Structure, magnetic and related properties, *Handbook on the Physics and Chemistry of Rare Earths*, vol. 22, Elsevier, 1996, pp. 143–294, [https://doi.org/10.1016/S0168-1273\(96\)22006-9](https://doi.org/10.1016/S0168-1273(96)22006-9) Chapter 149.
- [7] A.M. Gabay, G.C. Hadjipanayis, Mechanochemical synthesis of magnetically hard anisotropic RFe₁₀Si₂ powders with R representing combinations of Sm, Ce and Zr, *J. Magn. Magn. Mater.* 422 (2017) 43–48, <https://doi.org/10.1016/j.jmmm.2016.08.064>
- [8] G.C. Hadjipanayis, A.M. Gabay, A.M. Schönhöbel, A. Martín-Cid, J.M. Barandiaran, D. Niarchos, ThMn₁₂-type alloys for permanent magnets, *Engineering* 6 (2) (2020) 141–147, <https://doi.org/10.1016/j.eng.2018.12.011>
- [9] A. Aubert, R. Madugundo, A. Schoenhoebe, D. Salazar, J. Garitaonandia, J. Barandiaran, G. Hadjipanayis, Structural and magnetic properties of Nd-Fe-Mo-(N) melt-spun ribbons with ThMn₁₂ structure, *Acta Mater.* 195 (2020) 519–526, <https://doi.org/10.1016/j.actamat.2020.05.045>
- [10] Y. Hirayama, T. Miyake, K. Hono, Rare-earth lean hard magnet compound NdFe₁₂N, *JOM* 67 (2015) 1344–1349, <https://doi.org/10.1007/s11837-015-1421-9>
- [11] Y. Hirayama, Y.K. Takahashi, S. Hirose, K. Hono, Intrinsic hard magnetic properties of Sm(Fe_{1-x}Co_x)₁₂ compound with the ThMn₁₂ structure, *Scr. Mater.* 138 (2017) 62–65, <https://doi.org/10.1016/j.scriptamat.2017.05.029>
- [12] F. Maccari, L. Schäfer, I. Radulov, L.V.B. Diop, S. Ener, E. Bruder, K. Skokov, O. Gutfleisch, Rapid solidification of Nd_{1-x}Fe₁₁Ti compounds: phase formation and magnetic properties, *Acta Mater.* 180 (2019) 15–23, <https://doi.org/10.1016/j.actamat.2019.08.057>
- [13] I. Dirba, J. Li, H. Sepehri-Amin, T. Ohkubo, T. Schrefl, K. Hono, Anisotropic, single-crystalline SmFe₁₂-based microparticles with high roundness fabricated by jet-milling, *J. Alloy. Compd.* 804 (2019) 155–162, <https://doi.org/10.1016/j.jallcom.2019.06.365>
- [14] I. Dirba, Y. Harashima, H. Sepehri-Amin, T. Ohkubo, T. Miyake, S. Hirose, K. Hono, Thermal decomposition of ThMn₁₂-type phase and its optimum stabilizing elements in SmFe₁₂-based alloys, *J. Alloy. Compd.* 813 (2020) 152224, <https://doi.org/10.1016/j.jallcom.2019.152224>
- [15] D. Palanisamy, S. Ener, F. Maccari, L. Schäfer, K.P. Skokov, O. Gutfleisch, D. Raabe, B. Gault, Grain boundary segregation, phase formation, and their influence on the coercivity of rapidly solidified SmFe₁₁Ti hard magnetic alloys, *Phys. Rev. Mater.* 4 (2020) 054404, <https://doi.org/10.1103/PhysRevMaterials.4.054404>

- [16] B.S. Conner, M.A. McGuire, M.A. Susner, B.C. Sales, Phase relationships in the $\text{CeFe}_8\text{Co}_3\text{Ti}_{1-y}\text{Si}_y$ system, *J. Alloy. Compd.* 712 (2017) 30–35, <https://doi.org/10.1016/j.jallcom.2017.04.048>
- [17] L. Ke, D.D. Johnson, Intrinsic magnetic properties in $\text{R}(\text{Fe}_{1-x}\text{Co}_x)_{11}\text{TiZ}$ ($\text{R} = \text{Y}$ and Ce ; $\text{Z} = \text{H}, \text{C}$ and N), *Phys. Rev. B* 94 (2016) 024423, <https://doi.org/10.1103/PhysRevB.94.024423>
- [18] A. Martín-Cid, A.M. Gabay, D. Salazar, J.M. Barandiaran, G.C. Hadjipanayis, Tetragonal Ce-based Ce-Sm(Fe,Co,Ti)₁₂ alloys for permanent magnets, *Phys. Status Solidi C* 13 (10–12) (2016) 962–964, <https://doi.org/10.1002/pssc.201600102>
- [19] C. Piquer, F. Grandjean, O. Isnard, G.J. Long, An analysis of the hyperfine parameters of the RFe_{11}Ti and $\text{RFe}_{11}\text{TiH}$ compounds, where R is a rare-earth element, *J. Phys. Condens. Matter* 18 (1) (2005) 205–219, <https://doi.org/10.1088/0953-8984/18/1/015>
- [20] H. Wuest, L. Bommer, A.M. Huber, D. Goll, T. Weissgaerber, B. Kieback, Preparation of nanocrystalline $\text{Ce}_{1-x}\text{Sm}_x(\text{Fe,Co})_{11}\text{Ti}$ by melt spinning and mechanical alloying, *J. Magn. Magn. Mater.* 428 (2017) 194–197, <https://doi.org/10.1016/j.jmmm.2016.12.036>
- [21] C. Zhou, F.E. Pinkerton, J.F. Herbst, Magnetic properties of $\text{CeFe}_{11-x}\text{Co}_x\text{Ti}$ with ThMn_{12} structure, *J. Appl. Phys.* 115 (17) (2014) 17C716, <https://doi.org/10.1063/1.4863382>
- [22] Q. Pan, Z.-X. Liu, Y.-C. Yang, Structural and magnetic properties of $\text{Ce}(\text{Fe,M})_{12}\text{N}_x$ interstitial compounds, $\text{M}=\text{Ti}, \text{V}, \text{Cr}$, and Mo , *J. Appl. Phys.* 76 (10) (1994) 6728–6730, <https://doi.org/10.1063/1.358184>
- [23] D. Simon, H. Wuest, S. Hinderberger, T. Koehler, A. Maruszczyk, S. Sawatzki, L.V.B. Diop, K. Skokov, F. Maccari, A. Senyshyn, H. Ehrenberg, O. Gutfleisch, Structural and magnetic properties of $\text{Ce}_{1-x}\text{Sm}_x\text{Fe}_{11-y}\text{Ti}_1\text{V}_y$, *Acta Mater.* 172 (2019) 131–138, <https://doi.org/10.1016/j.actamat.2019.04.006>
- [24] L. Bozukov, A. Apostolov, M. Stoytchev, A change in magnetic and structural properties of the $\text{CeFe}_{11}\text{Ti}$ intermetallic compound upon hydrogen absorption, *J. Magn. Magn. Mater.* 101 (1) (1991) 355–356, [https://doi.org/10.1016/0304-8853\(91\)90777-8](https://doi.org/10.1016/0304-8853(91)90777-8)
- [25] J. Chaboy, A. Marcelli, L. Bozukov, F. Baudelet, E. Dartyge, A. Fontaine, S. Pizzini, Effect of hydrogen absorption on the cerium electronic state in $\text{CeFe}_{11}\text{Ti}$: an x-ray-absorption and circular-magnetic-dichroism investigation, *Phys. Rev. B* 51 (1995) 9005–9014, <https://doi.org/10.1103/PhysRevB.51.9005>
- [26] O. Isnard, Influence of hydrogen insertion on the magnetic properties of the RFe_{11}Ti phases, *J. Alloy. Compd.* 356–357 (2003) 17–21, [https://doi.org/10.1016/S0925-8388\(02\)01213-6](https://doi.org/10.1016/S0925-8388(02)01213-6)
- [27] O. Isnard, S. Miraglia, M. Guillot, D. Fruchart, Hydrogen effects on the magnetic properties of RFe_{11}Ti compounds, *J. Alloy. Compd.* 275–277 (1998) 637–641, [https://doi.org/10.1016/S0925-8388\(98\)00409-5](https://doi.org/10.1016/S0925-8388(98)00409-5)
- [28] G.J. Long, D. Hautot, F. Grandjean, O. Isnard, S. Miraglia, A. Mössbauer, spectral study of $\text{CeFe}_{11}\text{Ti}$ and $\text{CeFe}_{11}\text{TiH}$, *J. Magn. Magn. Mater.* 202 (1) (1999) 100–106, [https://doi.org/10.1016/S0304-8853\(98\)01070-1](https://doi.org/10.1016/S0304-8853(98)01070-1)
- [29] J. Rodríguez-Carvajal, Recent advances in magnetic structure determination by neutron powder diffraction, *Phys. B Condens. Matter* 192 (1–2) (1993) 55–69, [https://doi.org/10.1016/0921-4526\(93\)90108-i](https://doi.org/10.1016/0921-4526(93)90108-i)
- [30] K. Skokov, A. Grushishev, A. Khokhlov, Y. Pastushenkov, N. Pankratov, T. Ivanova, S. Nikitin, Magnetic properties of $\text{Gd}_3\text{Fe}_x\text{Ti}_3$ ($x=34, 33, \dots, 24$), $\text{TbFe}_{11}\text{Ti}$ and $\text{TbFe}_{10}\text{Ti}$ single crystals, *J. Magn. Magn. Mater.* 272–276 (2004) 374–375, <https://doi.org/10.1016/j.jmmm.2003.11.147>
- [31] J.L. Wang, C. Marquina, B. Garcia-Landa, M.R. Ibarra, F.M. Yang, G.H. Wu, Magnetovolume effect in ThMn_{12} -type Fe-rich $\text{R}(\text{Fe,Nb})_{12}$ -based compounds, *Phys. B Condens. Matter* 319 (1) (2002) 73–77, [https://doi.org/10.1016/S0921-4526\(02\)01109-2](https://doi.org/10.1016/S0921-4526(02)01109-2)
- [32] D. Givord, R. Lemaire, Magnetic transition and anomalous thermal expansion in R_2Fe_{17} compounds, *IEEE Trans. Magn.* 10 (2) (1974) 109–113, <https://doi.org/10.1109/TMAG.1974.1058311>
- [33] A. Andreev, M. Bartashevich, Spontaneous magnetostriction of the $\text{Y}_2(\text{Fe}_{1-x}\text{Co}_x)_{14}\text{B}$ intermetallic compounds, *J. Less Common Metals* 162 (1) (1990) 33–37, [https://doi.org/10.1016/0022-5088\(90\)90456-T](https://doi.org/10.1016/0022-5088(90)90456-T)
- [34] Y. Muraoka, M. Shiga, Y. Nakamura, Thermal expansion of TFe_2 ($\text{T}=\text{Zr}, \text{Hf}, \text{Ti}, \text{Sc}$ and Ce) laves phase intermetallic compounds, *J. Phys. Soc. Jpn.* 40 (3) (1976) 905–906, <https://doi.org/10.1143/JPSJ.40.905>
- [35] D. Melville, K.M. Al-Rawi, W.I. Khan, Magnetostriction and magnetisation of CeFe_2 , *Phys. Status Solidi A* 66 (1) (1981) 133–137, <https://doi.org/10.1002/pssa.2210660114>
- [36] R.H. Fowler, P. Kapitza, Magnetostriction and the phenomena of the Curie point, *Proc. Math. Phys. Eng. Sci.* 124 (793) (1929) 1–15, <https://doi.org/10.1098/rspa.1929.0095>
- [37] R.C. O'Handley, Magnetostriction of transition-metal-metalloid glasses: temperature dependence, *Phys. Rev. B* 18 (1978) 930–938, <https://doi.org/10.1103/PhysRevB.18.930>
- [38] G. Engdahl, Physics of giant magnetostriction, in: G. Engdahl (Ed.), *Handbook of Giant Magnetostrictive Materials*, Electromagnetism, Academic Press, San Diego, 2000, pp. 1–125, <https://doi.org/10.1016/B978-012238640-4/50017-6> Chapter 1.
- [39] D. Salazar, A. Martín-Cid, J.S. Garitaonandia, T.C. Hansen, J.M. Barandiaran, G.C. Hadjipanayis, Role of Ce substitution in the magneto-crystalline anisotropy of tetragonal $\text{ZrFe}_{10}\text{Si}_2$, *J. Alloy. Compd.* 766 (2018) 291–296, <https://doi.org/10.1016/j.jallcom.2018.06.225>
- [40] K.-D. Durst, H. Kronmüller, Determination of intrinsic magnetic material parameters of $\text{Nd}_2\text{Fe}_{14}\text{B}$ from magnetic measurements of sintered $\text{Nd}_{15}\text{Fe}_{77}\text{B}_8$ magnets, *J. Magn. Magn. Mater.* 59 (1) (1986) 86–94, [https://doi.org/10.1016/0304-8853\(86\)90014-4](https://doi.org/10.1016/0304-8853(86)90014-4)
- [41] W. Sucksmith, J.E. Thompson, The magnetic anisotropy of cobalt, *Proc. Math. Phys. Eng. Sci.* 225 (1954) 362, <https://doi.org/10.1098/rspa.1954.0209>
- [42] A. Galler, S. Ener, F. Maccari, I. Dirba, K.P. Skokov, O. Gutfleisch, S. Biermann, L.V. Pourovskii, Intrinsically weak magnetic anisotropy of cerium in potential hard-magnetic intermetallics, *npj Quantum Mater.* 6 (2021) 2, <https://doi.org/10.1038/s41535-020-00301-6>

– Supplementary Materials –
Correlating changes of microstructure and unit cell
parameters with magnetic properties in the CeFe₁₁Ti
compound

F. Maccari^{a,1}, S. Ener^{a,1,*}, D. Koch^b, I. Dirba^a, K. P. Skokov^a, E. Bruder^c, L.
Schäfer^a, O. Gutfleisch^a

^a*Functional Materials, Department of Material Science, Technische Universität Darmstadt,
64287, Darmstadt, Germany*

^b*Structural Research, Department of Material Science, Technische Universität Darmstadt,
64287, Darmstadt, Germany*

^c*Physical Metallurgy, Department of Material Science, Technische Universität Darmstadt,
64287, Darmstadt, Germany*

1. Supplementary materials

As a comparison to the microstructure shown in the manuscript for the Ce_{1.20}Fe₁₁Ti, Fig. S1 shows the microstructure of Ce_{1.15}Fe₁₁Ti samples in different conditions, including as suction casted state and after annealing at different temperatures. It worth mentioning that during the annealing at 1150°C the sample was molten and lost its shape, which can be also denoted by the coarse microstructure and large grains of α -Fe(Ti). The different phases shown in Fig. S1 were also evaluated by SEM-EDS. The chemical composition of the different phases lies in the range shown for Ce_{1.20}Fe₁₁Ti in Table 1 from the manuscript.

*Corresponding author

Email address: semih.ener@tu-darmstadt.de (S. Ener)

¹Both F.M. and S.E. equally contributed to this work.

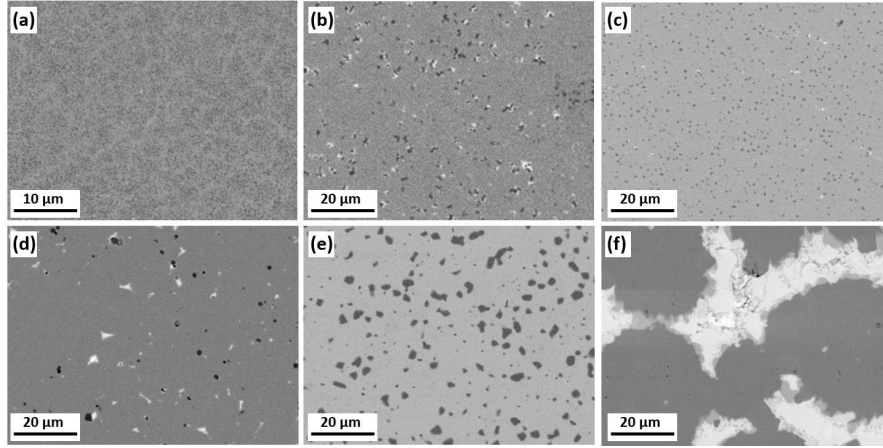


Fig. S1. BSE contrast SEM images of for $\text{Ce}_{1.15}\text{Fe}_{11}\text{Ti}$ samples in (a) the suction-cast state and after annealing at (b) 750°C , (c) 800°C , (d) 950°C , (e) 1100°C and (f) 1150°C for 12 hours.

High-resolution scanning electron microscopy images of $\text{Ce}_{1.20}\text{Fe}_{11}\text{Ti}$ samples in the as-cast and after annealing at 850°C are shown in Fig. S2. High resolution images confirm the formation of CeFe_2 - (labelled with "A"), Fe_2Ti -Laves (labelled with "C") and $\text{Ce}(\text{Fe},\text{Ti})_{12}$ (labelled with "B") phases in the as-cast state. Additionally, a small amount of $\text{Ce}_2(\text{Fe},\text{Ti})_{17}$ -type phase is observed (shown with dashed lines). After annealing at 850°C main phase of $\text{Ce}(\text{Fe},\text{Ti})_{12}$ (labelled with "B") with a small amount of CeFe_2 - (labelled with "A") are observed.

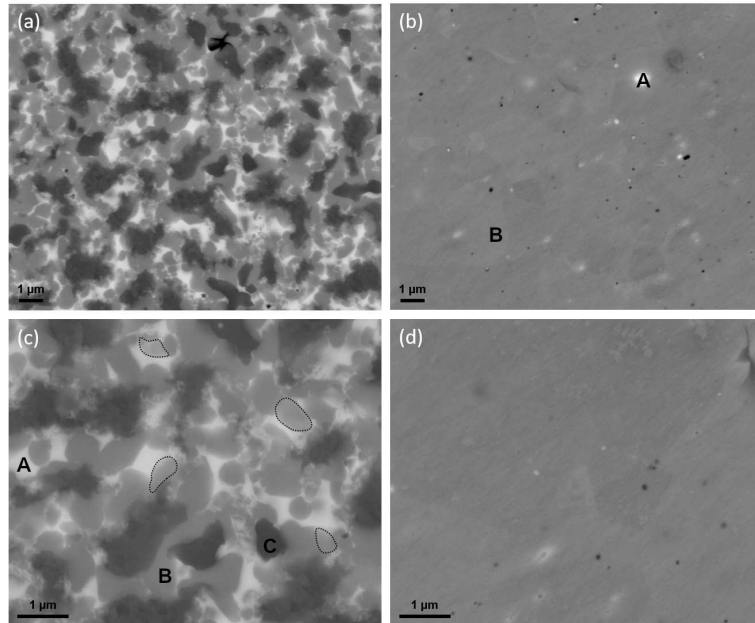


Fig. S2. BSE contrast SEM images of for $\text{Ce}_{1.20}\text{Fe}_{11}\text{Ti}$ samples in (a,c) the suction-cast state and (b,d) after annealing at 850°C for low (a,b) and high (c,d) magnifications.

Fig. S3 show the phase ratios (in weight percent) after annealing at different temperatures for $\text{Ce}_{1.20}\text{Fe}_{11}\text{Ti}$ sample series. Additionally, Fig. S4 shows the unit cell parameters for the observed phases after annealing, in which is possible to notice that there are no significant changes in these parameters.

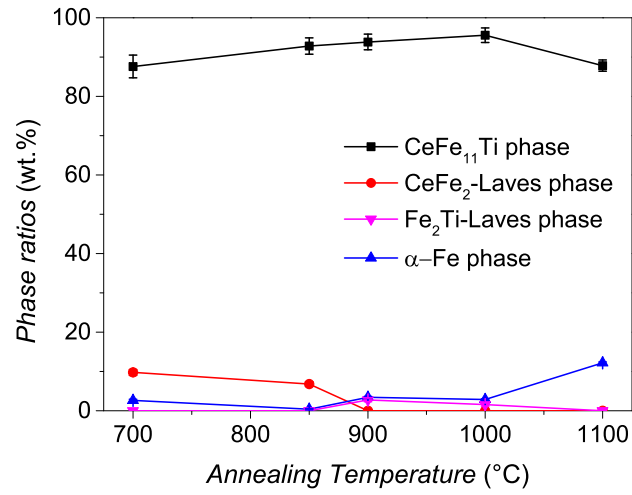


Fig. S3. Crystallographic phase ratios of the annealed $\text{Ce}_{1.20}\text{Fe}_{11}\text{Ti}$ samples obtained from the Rietveld refinement of the room temperature XRD patterns.

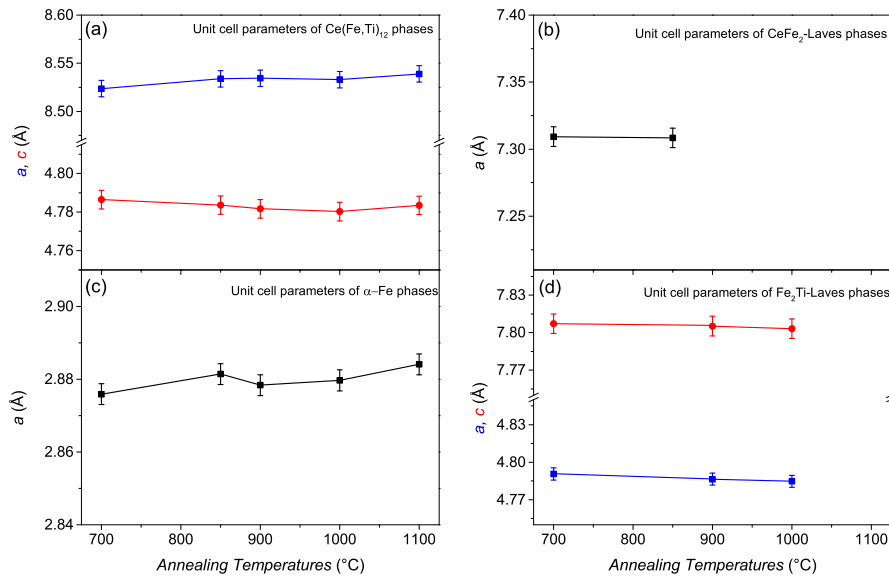


Fig. S4. Unit cell parameters of the phases observed from the analysis of the XRD patterns of annealed $\text{Ce}_{1.20}\text{Fe}_{11}\text{Ti}$ samples.

The room temperature XRD patterns of the $\text{CeFe}_{11}\text{Ti}$ and $\text{CeFe}_{11}\text{TiH}_x$ samples are shown in Fig. S5. Both of the measured patterns show the ThMn_{12} -type structure as the main phase. In the case of $\text{CeFe}_{11}\text{Ti}$ a small amount (less than 8 wt.%) of secondary phase of CeFe_2 -Laves phase is observed. Corresponding high intensity Laves peaks are indicated with * symbol in the diffraction patterns. The inset highlights the peak position shift related to the unit cell expansion after hydrogenation.

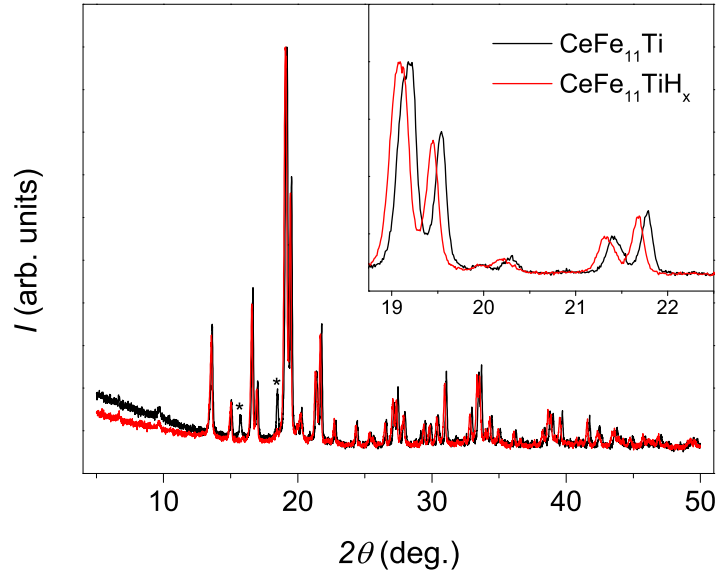


Fig. S5. Room temperature XRD patterns of $\text{CeFe}_{11}\text{Ti}$ and $\text{CeFe}_{11}\text{TiH}_x$ samples. The inset shows the high intensity Bragg reflections region of the diffraction pattern.

The temperature dependence of the unit cell parameters of the CeFe_2 -Laves phase is shown in Fig. S6. The secondary CeFe_2 -Laves phase crystallizes cubic C15 crystal structure. The dashed lines show the reported Curie temperatures of the CeFe_2 -Laves phase [1–4].

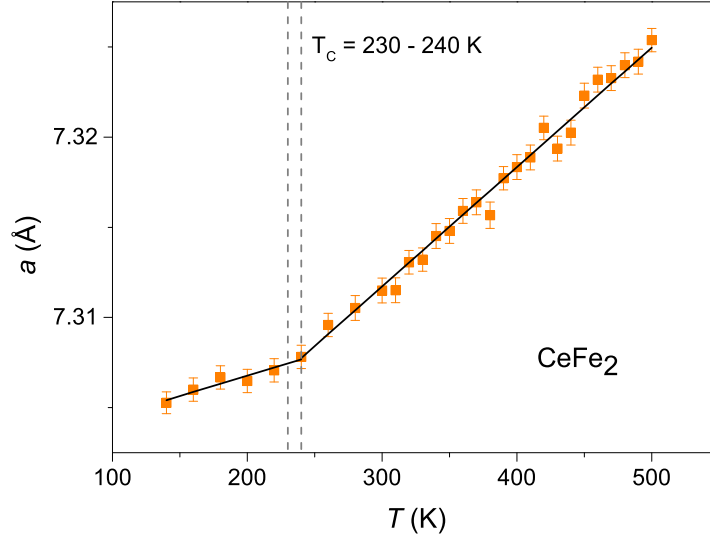


Fig. S6. Temperature dependence of the unit cell parameters of CeFe_2 -Laves secondary phase. The dashed lines are indicating the reported Curie temperatures in the literature.

The room temperature hysteresis measurements of $\text{Ce}_{1+x}\text{Fe}_{11}\text{Ti}$ samples were carried out on the textured samples and the results are shown in Fig. S7. As it can be seen from the hysteresis measurements of the textured samples (where the particle size is below $20\ \mu\text{m}$) the samples show low remanent magnetization and coercivity values. These observed low values can be attributed to the decremental effects of twin boundaries on the extrinsic magnetic properties. A detailed microstructure engineering is necessary to get the maximum energy product out of these material system by controlling the formation of twins and proper grain boundary phases.

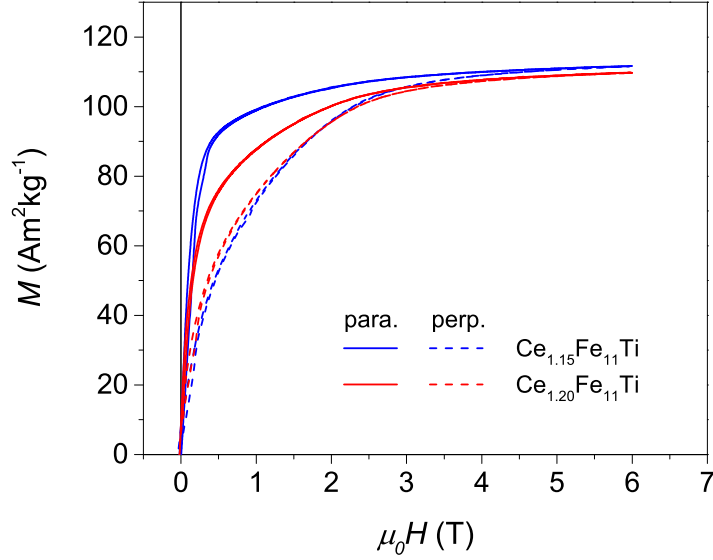


Fig. S7. Room temperature hysteresis measurements of $\text{Ce}_{1+x}\text{Fe}_{11}\text{Ti}$ samples on textured samples.

References

- [1] H. Okada, K. Koyama, M. Yamada, T. Goto, Y. Makihara, H. Fujii, K. Watanabe, Magnetic properties of $\text{Ce}(\text{Fe}_{1-x}\text{Co}_x)_2$ under high pressure, *J. Alloys Compd.* 408-412 (2006) 144–146. doi:10.1016/j.jallcom.2005.04.057.
- [2] C. S. Garde, J. Ray, G. Chandra, Hysteresis behavior in transport measurements in CeFe_2 and its alloys with Co, Al, and Ru substitutions, *Phys. Rev. B* 42 (1990) 8643–8646. doi:10.1103/PhysRevB.42.8643.
- [3] E. T. Miskinis, K. S. V. L. Narasimhan, W. E. Wallace, R. S. Craig, Magnetic properties of $\text{Gd}_{1-x}\text{Th}_x\text{Fe}_2$ and $\text{Gd}_{1-x}\text{Ce}_x\text{Fe}_2$, *J. Solid State Chem.* 13 (4) (1975) 311–314. doi:10.1016/0022-4596(75)90144-9.
- [4] A. Slebarski, M. Matlak, M. Hafez, Structural study of CeM_2 ($M = \text{Fe}, \text{Co}$),

Ni), *J. Alloys Compd.* 203 (1994) 35–44. doi:[https://doi.org/10.1016/0925-8388\(94\)90711-0](https://doi.org/10.1016/0925-8388(94)90711-0).

5.2.3 Full-text of Selected Publication C

Reproduced full text article with permission from Elsevier.

Copyright (2021), *Acta Materialia*.



Full length article

Twins – A weak link in the magnetic hardening of ThMn₁₂-type permanent magnets

Semih Ener^{a,*}, Konstantin P. Skokov^a, Dhanalakshmi Palanisamy^b, Thibaut Devillers^c, Johann Fischbacher^d, Gabriel Gomez Eslava^c, Fernando Maccari^a, Lukas Schäfer^a, Léopold V.B. Diop^a, Iliya Radulov^a, Baptiste Gault^{b,e}, Gino Hrkac^f, Nora M. Dempsey^c, Thomas Schrefl^d, Dierk Raabe^b, Oliver Gutfleisch^a

^a Functional Materials, Department of Material Science, Technical University of Darmstadt, Darmstadt, 64287, Germany

^b Max-Planck-Institute für Eisenforschung GmbH, Düsseldorf, 40237 Germany

^c Univ. Grenoble Alpes, CNRS, Institut NEEL, Grenoble, 38000 France

^d Department for Integrated Sensor Systems, Danube University Krems, Krems 3500, Austria

^e Department of Materials, Royal School of Mines, Imperial College London, London, SW7 2AZ, United Kingdom

^f College of Engineering, Mathematics and Physical Sciences, University of Exeter, North Park Road, Exeter EX4 4QF, United Kingdom



ARTICLE INFO

Article history:

Received 16 November 2020

Revised 10 April 2021

Accepted 3 May 2021

Available online 20 May 2021

Keywords:

Magnets

ThMn₁₂-type compounds

Coercivity

Twin boundaries

Microstructure

ABSTRACT

Nd₂Fe₁₄B-type materials exhibit the highest energy product around room temperature and hence dominate the high-performance permanent magnet market. Intensive research efforts aim at alternative material systems containing less critical elements with similar or better magnetic properties. Nd- and Sm-based compounds with a ThMn₁₂-type structure exhibit intrinsic properties comparable or even superior to Nd₂Fe₁₄B. However, it has not been possible to achieve technically relevant coercivity and remanent magnetization in ThMn₁₂-based bulk sintered magnets. Using SmFe₁₁Ti as a prototypical representative, we demonstrate that one important reason for the poor performance is the formation of twins inside micro-crystalline grains. The nature of the twins in SmFe₁₁Ti was investigated in twinned “single crystals” and both bulk and thin film poly-crystalline samples, using advanced electron microscopy and atom probe tomography as well as simulations and compared with benchmark Nd₂Fe₁₄B. Both micro-twins and nano-twins show a twin orientation of 57±2° and an enrichment in Sm, which could affect domain wall motion in this material. Micromagnetic simulations indicate that twins act as nucleation centers, representing the magnetically weakest link in the microstructure. The relation between twin formation energies and geometrical features are briefly discussed using molecular dynamic simulations.

© 2021 Acta Materialia Inc. Published by Elsevier Ltd. All rights reserved.

1. Introduction

Nd₂Fe₁₄B-type magnets are key components in electro-mobility, wind turbines, robotics and automatization with expected strong increases in demand in all sectors. The rare-earth (RE) supply crisis of ten years ago led to a drastic increase in prices and revealed the dependency on critical RE elements [1] for the production of high performance permanent magnets. Significant efforts are ongoing to find alternative material systems which present magnetic properties similar or superior to those the Nd₂Fe₁₄B benchmark, but which contain less critical elements [2].

RE-lean Nd- and Sm-based alloys with ThMn₁₂-type structures (tetragonal *I4/mmm* #139) have been known for more than 30 years. More recently, in 2015, Hirayama et al. reported the intrinsic magnetic properties of NdFe₁₂N_x thin films (saturation magnetization $\mu_0 M_s \sim 1.66$ T, anisotropy field $\mu_0 H_a \sim 8$ T and Curie temperature $T_c \sim 550$ °C) to be superior to those of Nd₂Fe₁₄B [3,4]. However, the ThMn₁₂-type structure was preserved only in thin-films with thicknesses up to 360 nm. A major drawback of the NdFe₁₂N_x system is the necessity of interstitial modification by nitrogen to obtain high saturation magnetization, anisotropy field and T_c . Decomposition of the nitride starting from around 570 °C prevents conventional densification via sintering or hot pressing. Nonetheless, investigations of materials with the Nd(Fe,X)₁₂-composition show the possibility to stabilize ThMn₁₂ structure in the bulk state by addition of doping elements, such as Cr, V, Ti, Mo, W or Si [5,6],

* Corresponding author.

E-mail address: semih.ener@tu-darmstadt.de (S. Ener).

that substitute Fe atoms. Among these elements, Ti is very effective and stabilizes the structure with minimal doping (approx. 7.7 at.%) [7].

The sign of the Stevens factor α_J of Sm^{3+} is opposite to that of Nd^{3+} , and as a consequence $\text{Sm}(\text{Fe},\text{Ti})_{12}$ exhibits a high anisotropy field ($\mu_0 H_A \sim 10$ T at room temperature [8]) without any interstitial modification, which makes it a promising material for the production of anisotropic bulk and fully dense permanent magnets. In 2017, Hirayama et al. reported that the intrinsic magnetic properties of cobalt doped $\text{Sm}(\text{Fe}_{1-x}\text{Co}_x)_{12}$ thin films are superior to those of $\text{Nd}_2\text{Fe}_{14}\text{B}$ [9]. Other studies showed that the addition of Zr reduces the Ti concentration required to stabilize the ThMn_{12} -type structure in Sm-based bulk samples [10,11]. Zr substitution also leads to an increase in the saturation magnetization, but the anisotropy field decreases.

Even though the intrinsic magnetic properties of both Nd and Sm based ThMn_{12} -type thin films are reported to be superior to those of $\text{Nd}_2\text{Fe}_{14}\text{B}$, the production of bulk ThMn_{12} -type structures remains challenging [12–20]. The hardness parameter, defined as:

$$\kappa = \sqrt{\frac{K_1}{\mu_0 M_s^2}} \quad (1)$$

quantitatively determines the probability of resisting self-demagnetization when hard magnetic materials are fabricated in any possible shape. An empirical rule of thumb to select materials as potential candidates for application as permanent magnet [21] is that κ must be significantly greater than one. For $\text{Nd}_2\text{Fe}_{14}\text{B}$ the κ value is 1.5, while it rises to a value of 2.1 for $\text{SmFe}_{11}\text{Ti}$ [22]. The excellent intrinsic magnetic properties measured on single crystalline samples (K_1 , M_s) and the high value of the hardness parameter κ cannot guarantee the direct use of the material for permanent magnet production. Indeed, each class of hard magnetic material requires its own special micro- and nanostructure, which needs to be controlled by utilizing peculiarities of the phase diagram and solid-state phase transformations. More importantly, in the context of this work, defects resulting from phase formation under specific processing regimes can serve as centers where reverse magnetic domains nucleate and propagate even in weak magnetic fields, thereby drastically reducing the coercivity of the sample. Due to the above mentioned promising intrinsic properties, the $\text{SmFe}_{11}\text{Ti}$ material is selected as a prototypical representative for ThMn_{12} -type materials.

Fig. 1 compares coercivity values from literature of benchmark $\text{Nd}_2\text{Fe}_{14}\text{B}$ -based materials [23–46] and $\text{Sm}(\text{Fe},\text{X})_{12}$ -based materials [20,47–61], as a function of grain size. For the $\text{Nd}_2\text{Fe}_{14}\text{B}$ system coercivity values up to 2.95 T have been reported for thin films, while coercivity around 1.95 T have been achieved for sintered bulk samples. Even though the Sm-based ThMn_{12} -systems show similar anisotropy field, the reported coercivity values do not surpass 1.1 T in melt-spun ribbons. The highest coercivity reported for the ThMn_{12} -type bulk system is 1.07 T for $\text{Sm}_8\text{Fe}_{75.5}\text{Ga}_{0.5}\text{Ti}_8\text{V}_8$. Recently, coercivities of 1.2 T and 1.26 T has been reported for $\text{Sm}(\text{Fe}_{0.8}\text{Co}_{0.2})_{12}\text{B}_{0.5}$ thin films and $\text{Sm}_{0.815}\text{Zr}_{0.185}(\text{Fe}_{0.81}\text{Co}_{0.19})_{11.19}\text{Ti}_{0.81}$ mechanochemically synthesized oriented particles, respectively, as indicated by the dashed line in Fig. 1. For Sm-Fe-Ti ternary compositions the reported coercivity values do not surpass 0.51 T, as indicated by a dotted line in Fig. 1.

A possible explanation for the low coercivity of $\text{SmFe}_{11}\text{Ti}$ -based magnets may be the absence of a non-magnetic grain boundary phase which magnetically decouples adjacent grains, as found in classical $\text{Nd}_2\text{Fe}_{14}\text{B}$ -type sintered magnets [63]. Another reason might be the presence of macroscopic twin boundaries and microscopic slip-bands, which were previously reported in ThMn_{12} -type structures [50,64,65]. Although the twins have been observed in

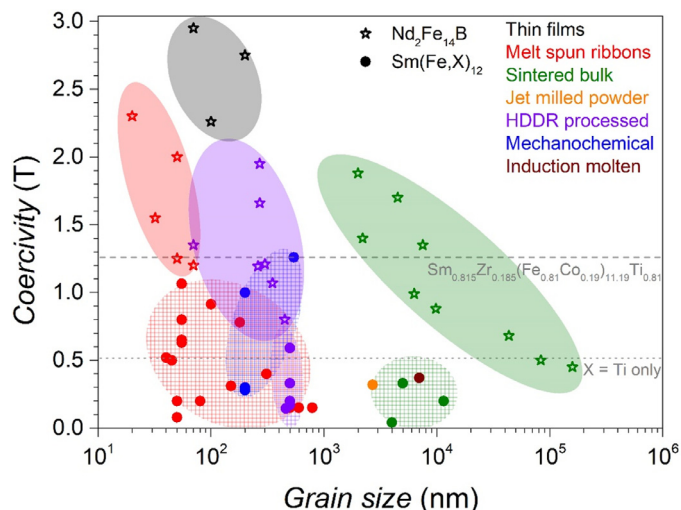


Fig. 1. Comparison of reported coercivity values as a function of grain size. Open symbols and full symbols correspond to $\text{Nd}_2\text{Fe}_{14}\text{B}$ and $\text{Sm}(\text{Fe},\text{X})_{12}$ systems, respectively. Different colors correspond to different sample production methods and shaded areas are guides to the eye. The highest reported coercivity of a ThMn_{12} -type structure is shown by the dashed line [62]. The highest reported coercivity for a ternary $\text{Sm}(\text{FeTi})_{12}$ sample is shown by the dotted line [55].

different ThMn_{12} -type material systems before, up to now, their influence on the physical properties were not investigated in detail. It is important to state that there are no reports on twins in high performance magnets based on $\text{Nd}_2\text{Fe}_{14}\text{B}$ -, SmCo_5 -, $\text{Sm}_2\text{Co}_{17}$ - and $\text{Sm}_2\text{Fe}_{17}\text{N}_x$ -type rare earth transition metal phases. In contrast and equally important, a mixture of stacking faults, anti-phase boundaries and abundant twins have been shown to occur in rare earth free L1_0 -type hard magnetic phases. For the Fe-Pd, Fe-Pt and Co-Pt systems twins conjugate along $\{110\}$ -planes, while for MnAl systems twins conjugate along $\{111\}$ -planes. These twins can form during a diffusional transformation or recrystallization [66–74]. In 2001, Attané et al., reported that micro-twins observed in FePt films act as pinning centers that increase coercivity [75]. Microscopic twins and stacking faults observed in Co-based high-density magnetic recording media materials such as CoCr and CoCrPt were also credited with increasing coercivity [76,77]. On the other hand, twins in Mn-Al have been reported to be deleterious for coercivity, by decreasing locally the energy necessary to nucleate reversed magnetic domains [78]. The bivalent role that twins appear to play in different hard magnetic material systems highlights the importance of a deeper understanding of the link between microstructure and magnetic properties in such technologically important materials.

To date, no detailed investigation has been reported on the nature of twins in $\text{SmFe}_{11}\text{Ti}$ -based compounds and their effect on the hard-magnetic properties. In this study, we address this issue by comprehensively investigating twins at different length-scales in (1) twinned bulk crystals, (2) poly-crystalline bulk samples and (3) poly-crystalline thin films. At various stages we also refer to the benchmark $\text{Nd}_2\text{Fe}_{14}\text{B}$ to elucidate commonalities and disparities. We reveal changes in atomic ordering across twin-like structures and a change in composition at the twin boundaries with respect to the adjacent lattice, using advanced electron microscopy and atom probe tomography. Micromagnetic modeling support our experimental results and elucidate how twins influence local and global magnetization reversal and ultimately macroscopic hysteresis properties in the $\text{SmFe}_{11}\text{Ti}$ system. We also consider how twin formation is associated with the accumulation of internal stresses during solidification and grain growth during thermal treatments, as a consequence the energy of the twin formation is becoming

more favoured in comparison to the formation of specific grain boundaries. Molecular dynamics shows that there is a fine balance between twin formation and certain grain boundary phases. In this work, we study in detail on all length scales how twins act as a weak link in the magnetic hardening of ThMn₁₂-type permanent magnets.

2. Experimental and simulation details

Poly-crystalline and single-crystalline sample preparation and characterization: Polycrystalline Sm_{1.25}Fe₁₁Ti ingots were prepared by melting high-purity (>99.99%) starting elements in an induction furnace under a purified argon atmosphere. Using an arc-melting setup, the ingot was suction-cast into a rectangular slab of 0.5 mm thickness, to ensure fast solidification/cooling (approx. 10³ K.s⁻¹). The suction-cast slabs were wrapped in Mo foil, sealed in quartz ampules under Ar atmosphere and annealed at 1175 °C for 30 min to stabilize the Sm(Fe,Ti)₁₂ phase and then quenched in room temperature water. It is worth mentioning that an off-stoichiometric (higher Sm concentration) composition was used to compensate for evaporation losses during the melting and annealing procedures.

Structural characterization and phase determination of the annealed samples were done using room temperature x-ray powder diffraction (XRD). The measurements were carried out on a Stoe Stadi P diffractometer with Mo K α_1 radiation, in transmission mode and an angular 2 θ range from 5° to 50°. Phase matching and structural refinements were performed using FullProf software [79]. Microstructural analysis was carried out using a Tescan VEGA3 scanning electron microscope (SEM) with secondary electron (SE) and backscattered electron (BSE) detectors. The chemical composition of the observed phases was determined by energy-dispersive X-ray spectroscopy (EDS) measurements.

Magneto-optical Kerr effect (MOKE) measurements were performed on a Zeiss Axio Imager.D2m microscope with polarized light function equipped with an electromagnet (evico magnetics GmbH). The MOKE measurements were done using polar contrast mode to ensure highest contrast between the magnetic domains pointing in opposite directions. To enhance the magnetic contrast of the images, the non-magnetic background image was subtracted from the measurement images by using the KerrLab software.

SmFe₁₁Ti single crystals were produced by re-melting Sm_{1.25}Fe₁₁Ti polycrystalline samples and then slowly cooling them at a rate of 1 °C/h. Re-melting was carried out in a ZrO₂ crucible in a sealed quartz tube under a protective Ar atmosphere. The obtained particles, of typical size 500–1000 μ m, were mechanically separated from each other and they are referred as twinned crystals. Selected crystals were oriented using back-scattering Laue x-ray diffraction and mounted for magnetic characterization along three different directions: [100], [110] and [001]. Magnetic measurements were performed at room temperature using a PPMS-VSM (Quantum Design PPMS-14) under external applied magnetic fields of up to 14 T. For investigation of magnetic domain structures by the MOKE technique, two twinned single crystals were used. The observation surface of one crystal was polished perpendicular to the [100] direction (in-plane magnetization) and that of the other perpendicular to the [001] direction (out-of-plane magnetization).

Thin film sample preparation and characterization: Sm-based 1:12-type films of thickness 1.5 μ m were deposited by triode sputtering onto thermally oxidized Si wafers at 700 °C. 50 nm Ta buffer layers were used to prevent chemical reaction between the wafer and the magnetic layer and 10 nm Ta capping layers were added to prevent oxidation. We present results from two samples with composition Sm_{0.7}Fe_{11.3}Ti_{0.9} and Sm_{0.7}Zr_{0.2}Fe_{11.4}Ti_{0.7}, as estimated by EDS, referred to as the Sm(Fe,Ti)₁₂ film and the

(Sm,Zr)(Fe,Ti)₁₂ film, respectively. Atomic structure and diffraction analysis of the films were carried out using transmission electron diffraction (TEM) microscopy. TEM samples were prepared in cross-sectional configuration by mechanical polishing (down to 25 μ m) followed by ion milling with a Gatan PIPS II (Precision Ion Polishing System). Ion milling of the TEM samples was performed at 3 kV for several hours until an electron transparent hole appears, followed by 5 min of cleaning at 0.5 kV.

High resolution microscopy on polycrystalline samples: To locate grains with twin boundaries, electron backscatter diffraction (EBSD) analysis was performed on the polycrystalline samples using a Jeol JSM-6500F SEM operated at 15 kV. EBSD acquisition was performed using the TSL OIM EBSD system equipped with a Digiview IV EBSD detector with a step size of 0.1 μ m. Correlative electron microscopy and atom probe tomography (APT) investigations were carried out using a JEOL 2200FS aberration-corrected electron microscope (Thermo-Fischer TITAN) in scanning-transmission (STEM) mode and a local-electrode-atom-probe (LEAP 5000 XR, Cameca) instrument equipped with reflection lens, respectively. For APT, needle-shaped specimens were prepared from the twin boundary regions using a dual beam SEM/focused-ion-beam (FIB) instrument (FEI Helios Nanolab 600i) with an in-situ-lift-out procedure detailed in references [66,80,81]. The prepared lamella, containing the twin boundary region, was positioned and Pt-welded using the in-situ gas-injection system on the electro-polished posts of a halved TEM Mo-grid. The Mo-grid with the attached specimen was held in a special correlative holder designed in-house, as described in reference [82]. The welded regions on the Mo-posts were sharpened by Ga ions accelerated at 30 kV with currents ranging from 80 pA to 0.78 nA. The sharpened specimens were checked by TEM to get the exact location of the twin boundary and further Ga-ion milling was performed such that the boundary is within 150 ~ 200 nm from the apex of the specimen. Before APT analysis, the specimens were cleaned by 5 kV with 8 pA current to remove regions of the specimen severely damaged by the implantation of high-energy Ga-ions.

Near-atomic-scale compositional analysis was performed using a LEAP 5000 XR instrument operated in laser pulsing mode with a pulse repetition of 200 kHz and a pulse energy of 40 pJ. The specimen was kept at a base temperature of 60 K with a target detection rate of 5 ions detected per 1000 pulses. The APT reconstruction and analysis were performed using IVAS 3.8.2 software.

Micromagnetic simulations: Magnetization reversal in a single twinned grain was computed by micromagnetic simulations. The shape of the grain was generated with the Neper software [83]. The twin boundary was defined with the computer aided design software Salome [84]. The geometric model is meshed with tetrahedral finite elements using MeshGems [85]. In order to treat the magnetostatic open boundary problem [86], the finite element mesh for the magnetostatic scalar potential is extended outside the magnetic grains. The mesh size at the grain surfaces and twin boundaries was 1.5 nm. We computed the demagnetization curve by minimization of the Gibbs free energy for a decreasing external field. To solve for the next local minimum, we used a preconditioned conjugate gradient method [87]. Plots of the demagnetization curves were created using matplotlib [88].

Molecular dynamics simulations: The molecular dynamics calculations were carried out by using modified Morse potentials on supercell structures with the crystallographic interface orientation and composition taken from experiments. The different surface energies of the 1:12 phase were calculated. The twin formation was incorporated as an additional interface energy contribution. After the total energy with and without twin formation has been derived, we saw that once the grain reaches a certain size, twin formation is deemed preferential. This result underpins the findings in the experiments.

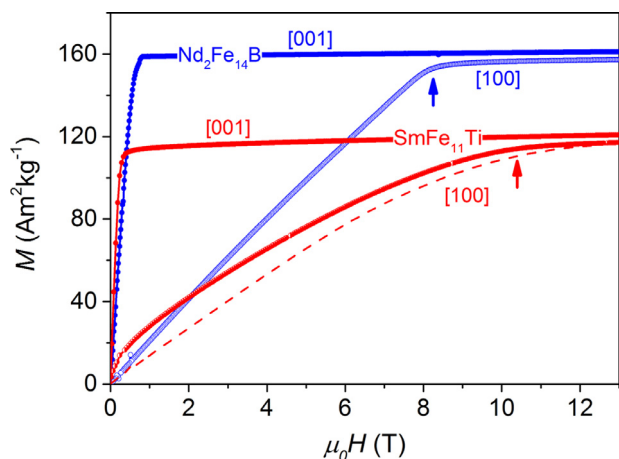


Fig. 2. Comparison of room temperature magnetic measurements of $\text{Nd}_2\text{Fe}_{14}\text{B}$ (blue) and $\text{SmFe}_{11}\text{Ti}$ (red) twinned “single-crystals” along easy and hard magnetization directions. The dashed red line indicates the magnetization behavior of a twin-free single crystal along the [100] direction [95].

3. Results and discussion

3.1. Single crystals and intrinsic magnetic properties

Magnetic anisotropy is the key requisite for achieving a large coercivity, and in the ideal case of uniform rotation of the magnetic moments in single domain particles, the coercivity H_c is given by $H_c = H_a = 2K_1/\mu_0M_s$ (H_a is anisotropy field, K_1 is anisotropy constant, μ_0 is the permeability of free space, M_s is the spontaneous magnetization). In reality, prediction of H_c from K_1 and M_s , using the Stoner Wohlfarth model [89], leads to a large overestimation. This is known as Brown’s paradox [2,90,91], and it is attributed to local magnetic softening caused by crystallographic defects, strain, secondary phases, magnetic and chemical inhomogeneities which reduce H_c to about αH_a (α is the “Kronmüller factor”, which is related to nano-structural imperfections). As-cast materials often exhibit $\alpha = 0.01$, and via sophisticated processing methods, e.g. melt spinning, jet milling, or die upsetting, α can reach to 0.25 of the theoretical limit in laboratory-made Nd-Fe-B and Sm-Co-based magnets.

We start by reporting in Fig. 2 the room temperature magnetization curves of a $\text{SmFe}_{11}\text{Ti}$ twinned crystal, with the magnetic field applied along the [100] and [001] directions. The typical behavior of easy-axis magnetocrystalline anisotropy is observed; the data measured along the 4-fold symmetry axis [001] clearly identifies this as the easy magnetization direction, leading to a $\mu_0M_s = 1.17$ T (calculated by converting the mass magnetization to volume magnetization considering the x-ray density of the $\text{SmFe}_{11}\text{Ti}$). At room temperature, curves recorded along the [100] and [110] directions are practically identical (the [110] curve is not shown), reflecting a weak magnetic anisotropy within the basal plane of this system at room temperature (see supplementary materials for details of the crystal structure). The anisotropy field, μ_0H_a , estimated from the slope change in the magnetic hard [100]-axis curve (identified by an arrow in Fig. 2), amounts to 10.5 T at 300 K. The value of K_1 is estimated to be 627 J/kg (approx. 4.8 MJ/m³, considering the theoretical x-ray density). The hard-axis magnetization curve does not reach the same maximum value as the easy-axis curve above μ_0H_a , due to anisotropy of the magnetic moment. This observed difference of the easy and hard axes magnetization values above the anisotropy field indicates a possible anisotropy of the magnetization, as has been reported for different rare-earth transition-metal systems [92–94]. Additionally, the low field region of the hard axis measurements shows non-linear

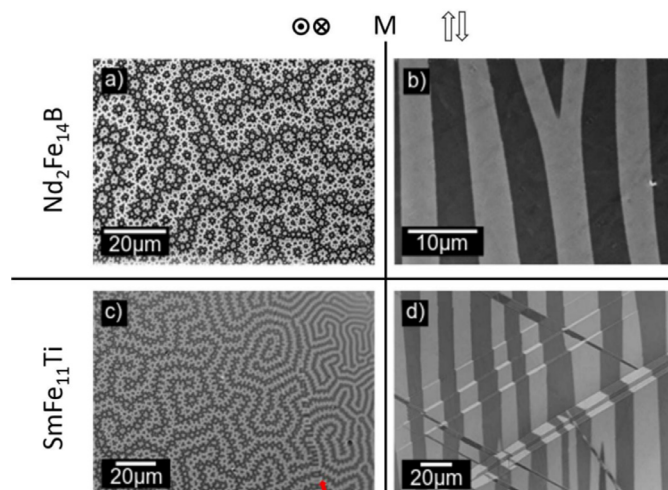


Fig. 3. Comparison of room temperature Kerr microscopy images of (a,b) $\text{Nd}_2\text{Fe}_{14}\text{B}$ and (c,d) $\text{SmFe}_{11}\text{Ti}$ twinned single-crystals along easy and hard directions.

behavior which is due to the formation of twins in the “single-crystals”. The dashed red line corresponds to the hard axis measurement of a twin-free $\text{SmFe}_{11}\text{Ti}$ single crystal, as reported in [95].

For comparison, Fig. 2 shows the magnetization curves of a $\text{Nd}_2\text{Fe}_{14}\text{B}$ single crystal, measured along [001] and [100], corresponding to the easy and hard magnetization directions, respectively. One can see that the spontaneous magnetization of the $\text{Nd}_2\text{Fe}_{14}\text{B}$ single crystal is significantly higher than that of the $\text{SmFe}_{11}\text{Ti}$ single crystal. On the other hand, the anisotropy field of $\text{SmFe}_{11}\text{Ti}$ is larger than that of $\text{Nd}_2\text{Fe}_{14}\text{B}$.

Next it is instructive to compare the magnetic domain structures imaged by Kerr microscopy of 0.5–1 mm-sized single crystals of $\text{Nd}_2\text{Fe}_{14}\text{B}$ (Fig. 3a,b) and $\text{SmFe}_{11}\text{Ti}$ (Fig. 3c,d). One can see that for the $\text{Nd}_2\text{Fe}_{14}\text{B}$ single crystal, the branched domain pattern on the basal plane (Fig. 3a, the c axis and magnetization are perpendicular to the crystal surface) and stripe-like domains on the prismatic plane (Fig. 3b, the c axis and magnetization lie in the plane of the image) are rather periodic and without significant distortions. In contrast, the domain structures of the $\text{SmFe}_{11}\text{Ti}$ twinned crystal (Fig. 3c) are locally distorted (highlighted by the arrow), and this is more pronounced when the magnetization lies in the plane of the image (Fig. 3d). Such step-like features observed on stripe magnetic domains are a signature of the presence of a crystallographic twinning structure, and this phenomenon was well-studied in other materials, such as magnetic shape memory materials [96,97], and materials showing giant magnetostriction [98,99].

In contrast to the $\text{Nd}_2\text{Fe}_{14}\text{B}$ single crystal, the microstructure of the $\text{SmFe}_{11}\text{Ti}$ crystal comprises a significant number of crystallographic twins, which leads to the appearance of micrometer-sized blocks of changing orientation. As a result, the magnetization curve measured in the hard direction of the $\text{SmFe}_{11}\text{Ti}$ crystal (Fig. 2) is not linear but exhibits a kink at low fields – i.e. a “soft-magnetic like” curvature, which is not observable in the $\text{Nd}_2\text{Fe}_{14}\text{B}$ single crystal.

3.2. Polycrystalline samples

Fig. 4 shows the magnetic domain structures of Nd-Fe-B and Sm-Fe-Ti polycrystalline bulk samples. The domain patterns were observed on arbitrarily oriented polished surfaces of isotropic samples. In $\text{Nd}_2\text{Fe}_{14}\text{B}$ grains, Fig. 4a, the domain structure is rather uniform and the domain pattern changes only across grain boundaries, i.e. due to the different crystallographic orientation of adjacent grains. In contrast, the domain structure of the $\text{SmFe}_{11}\text{Ti}$

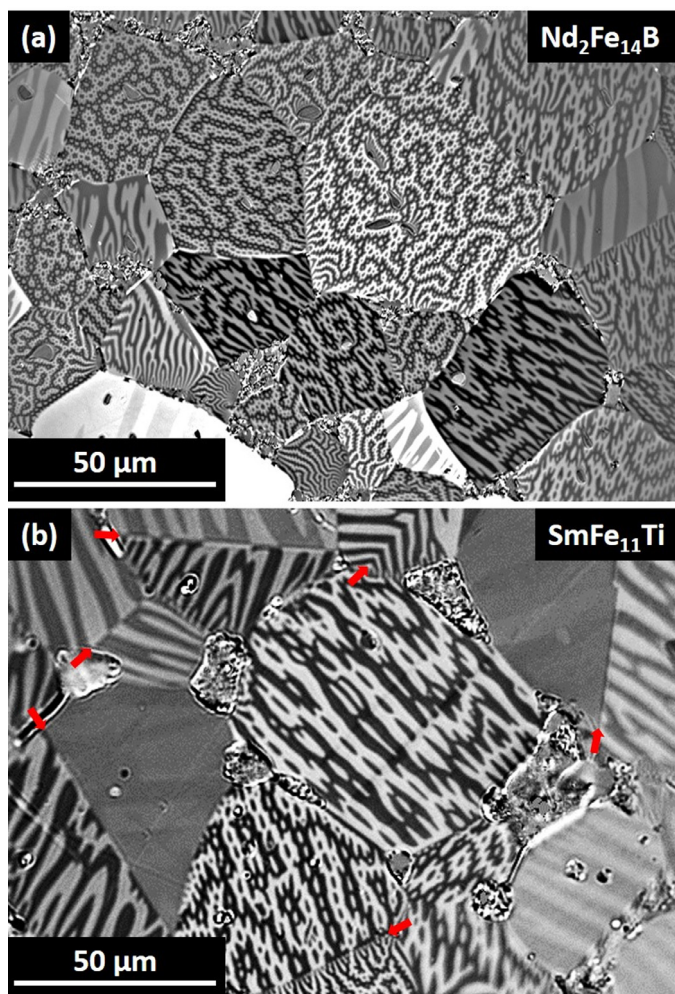


Fig. 4. Comparison of room temperature Kerr microscopy images of polycrystalline (a) $\text{Nd}_2\text{Fe}_{14}\text{B}$ and (b) $\text{SmFe}_{11}\text{Ti}$ bulk samples. Red arrows indicate some of the twins observed in the $\text{SmFe}_{11}\text{Ti}$ sample.

grains, Fig. 4b, is often divided in two (or more) well distinguishable patterns by a twin boundary, some of which are marked by red arrows.

Fig. 5a shows an electron back scattered diffraction (EBSD) map of the $\text{SmFe}_{11}\text{Ti}$ polycrystalline bulk sample evidencing grains with different orientations. The EBSD map was indexed as $\text{Sm}(\text{Fe},\text{Ti})_{12}$ (1:12 phase) matrix phase having a tetragonal crystal structure (space group $I4/mmm$) with lattice parameters $a = b = 0.8589$ nm and $c = 0.4807$ nm. Some grains contain unique boundaries corresponding to twins, such as the region within the black-dashed rectangle in Fig. 5a. The twin orientation relation between the twin variants is approximately 57° , as shown Fig. 5b. We also show a schematic view of the orientation with respect to the shared twin boundary, and found that the twinning boundary plane corresponds to $\{011\}$ -type planes in the unit cell of the $\text{Sm}(\text{Fe},\text{Ti})_{12}$ phase. Fig. 5c shows a back scattered electron (BSE) micrograph for a similar twinned region with a twin boundary inside a grain.

We confirmed the crystallographic relationship of two variants of a twin by using electron diffraction analysis and the results can be found in Supplementary Materials.

We prepared an atom probe tomography (APT) specimen specifically from the location marked by the dashed red outline in Fig. 5c. Fig. 6a is a low magnification high-angle dark-field (HAADF) image of the specimen with the twin boundary. HAADF provides Z-contrast, i.e. heavier atoms appear brighter. Fig. 6b is

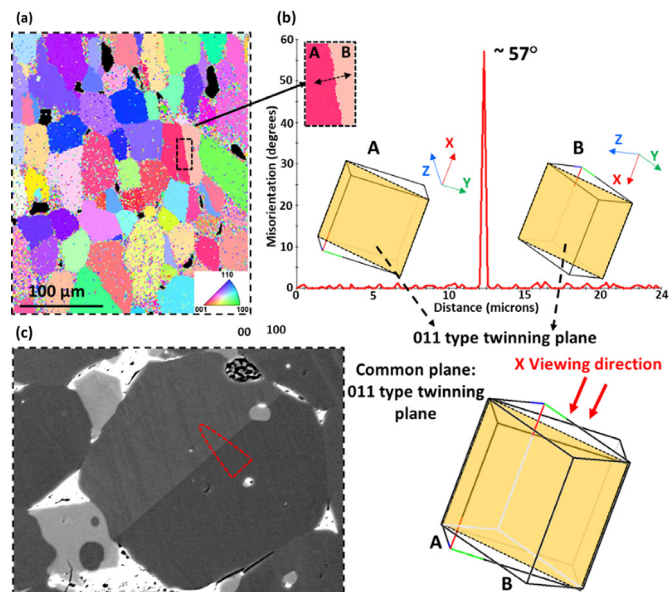


Fig. 5. (a) Inverse pole figure image of the investigated polycrystalline $\text{SmFe}_{11}\text{Ti}$ bulk sample derived from EBSD SEM data. (b) Measured angle between two neighboring twin variants and corresponding schematic representation of the unit cells. (c) A BSE SEM image of a twinned grain with the location of the APT specimen identified by a red triangle.

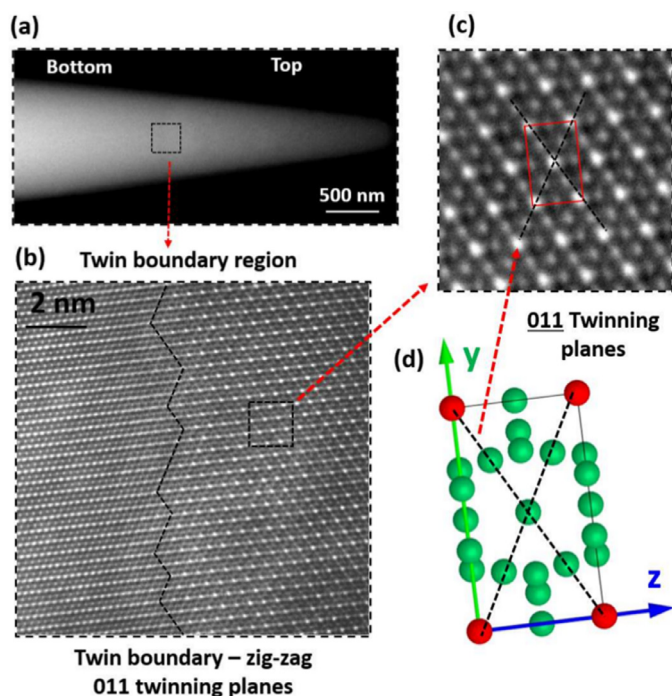


Fig. 6. (a) Low magnification HAADF image of $\text{SmFe}_{11}\text{Ti}$ at the twin boundary region. (b) High-resolution HAADF image of the interface region of the twin along the $[100]$ zone axis. (c) High magnification of the twin boundary region and (d) schematic representation of the 011 twinning planes.

a high-resolution (HR) HAADF image taken along the $[100]$ zone axis from the location marked by a black-dashed square in Fig. 6a. Fig. 6c is a close-up on the unit cell viewed along the $[100]$ zone axis, which can be compared with the simulated unit cell shown in Fig. 6d with Sm in red and Fe/Ti in green. As expected, atomic columns containing Sm appear bright. We can also clearly see the (011) planes, marked at black dashed lines, which exactly resem-

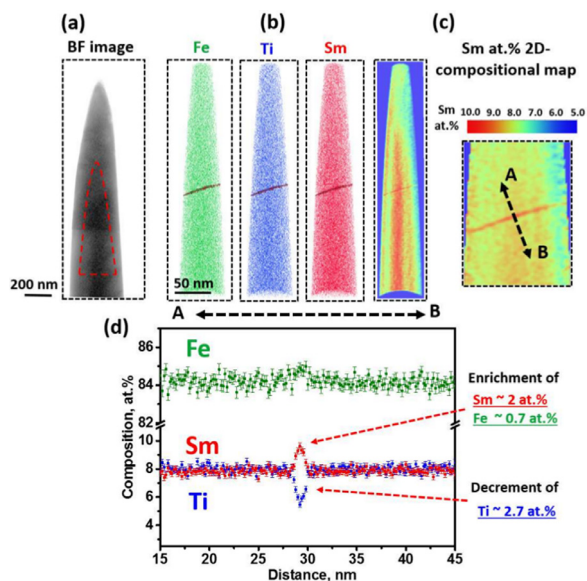


Fig. 7. (a) Bright-field image of one of the investigated APT specimens. (b) Atom probe tomography reconstruction of the elemental distribution of Sm, Fe and Ti. (c) 2D compositional map of Sm and (d) chemical composition distribution at the twin boundary region.

ble the zig-zag twin boundary, schematically shown with a black dashed line in Fig. 6b.

Fig. 7 details the results from the APT analysis of the same specimen. Fig. 7a is the bright-field electron micrograph of the specimen and Fig. 7b shows the corresponding APT reconstruction with the distribution of Fe, Ti, Sm atoms and a Sm 9 at.% iso-composition surface highlighting the location of the twin boundary. Fig. 7c shows a 2D Sm compositional map evidencing a local increase in the Sm content at the twin boundary. The measured matrix composition was found to be $\text{Sm}_{7.7}\text{Fe}_{84.3}\text{Ti}_{7.9}$, matching the 1:12 stoichiometry. The composition profile taken across the boundary, Fig. 7d, shows a Sm enrichment by approx. 2 at.% and a depletion of Ti by approx. 2.7 at.% with respect to the matrix phase. A slight enrichment of Fe, by approx. 0.7 at.%, is also observed. The composition at the twin boundary is close to the stoichiometry of the 3:29-phase i.e. $\text{Sm}_3(\text{Fe,Ti})_{29}$ phase. The electron diffraction measurements (see Figure S2) show no additional spots corresponding to the 3:29-phase, most probably due to the early nucleation stage of the twin boundary phase.

To complement the above reported studies of twins in bulk Sm-Fe-Ti samples, we also studied twins in polycrystalline Sm-Fe-Ti and Sm-Fe-Ti-Zr sputtered films (the latter were studied to probe the eventual influence of Zr additions in films). Both films contain a first layer of isotropically oriented equiaxed grains of maximum diameter 200 nm, at the interface with the Ta buffer, and elongated grains of width \sim 200 nm that traverse the rest of the film thickness. The elongated grains, with lattice parameters corresponding to the $\text{Sm}(\text{Fe,Ti})_{12}$ structure, are highly textured, with a dominant $\{101\}$ texture. Multiple planar defects oriented parallel to the growth direction, which are attributed to twins in the $\text{Sm}(\text{Fe,Ti})_{12}$ structure, were identified in the elongated grains of both films. A high-resolution micrograph (see Supplementary Materials) shows that along the particular zone axis, the atomic crystal structure on both sides of the twinning boundaries look identical, because they are probably seen under a similar zone axis (e.g. $[\bar{1}01]$ and $[\bar{1}0\bar{1}]$ with 59.8° angle between planes). High-resolution TEM micrographs confirm the formation of twins in polycrystalline film samples, as in their bulk counterparts. For further details and

crystallographic phase analysis of the investigated polycrystalline sample please see the Supplementary Materials.

3.3. Micromagnetic simulations and molecular dynamics calculations

In an isotropic granular magnet, a grain may be oriented at various directions with respect to the applied external field. For a single domain grain with uniaxial anisotropy and no defect, the demagnetization curves may be very close to the Stoner-Wohlfarth prediction, depending on the direction of the external field. The curve with the minimum switching field will occur when the applied field is oriented at 45° with respect to the anisotropy axis [89]. In this case the switching field will be half of the anisotropy field. Before irreversible switching, the magnetization will rotate reversibly out of the anisotropy axis. In micromagnetic simulations we expect a slight reduction of those switching fields, owing to the self-demagnetizing field of the grain.

We calculated the switching fields of a single twinned $\text{SmFe}_{11}\text{Ti}$ grain as a function of the orientation of the applied external field and compared the results to those of a single uniaxial $\text{Nd}_2\text{Fe}_{14}\text{B}$ grain of the same geometric shape. In the ideal microstructure of a permanent magnet, the grains are separated by a paramagnetic grain boundary phase. Thus, by comparing the single grain behavior of $\text{SmFe}_{11}\text{Ti}$ and $\text{Nd}_2\text{Fe}_{14}\text{B}$, we can derive the upper limits of coercivity for both systems.

The shape of the model is shown as an inset of Fig. 8a. The volume of the grain was equal to that of a cube with 295 nm sides. For $\text{Nd}_2\text{Fe}_{14}\text{B}$ calculations we assumed a magnetocrystalline easy-axis parallel to the z direction of the global coordinate system. The intrinsic magnetic properties used were: anisotropy constant $K_1 = 4.9 \text{ MJ/m}^3$, magnetization $\mu_0 M_s = 1.61 \text{ T}$, and exchange constant $A = 8 \text{ pJ/m}$ (page 401 of [100]). The anisotropy field of this phase is $\mu_0 H_a = 7.65 \text{ T}$. To model the effect of a twin in a $\text{SmFe}_{11}\text{Ti}$ grain, we introduced a 6 nm thick twin boundary (2.4 percent of the total volume) parallel to the xz -plane which separates the twin variants of the grain into two equally sized halves. The orientation of the two easy-axes of the two variants of the twin are shown as white double-headed arrows and are parallel to the yz -plane. The easy-axes enclose an angle of $180 - 58 = 122^\circ$, which is consistent with results from EBSD measurements and was checked with the Twiny software [101] which gives 121.5° for (011) twin planes of $\text{SmFe}_{11}\text{Ti}$. In this model we ignored the experimentally found zig-zag shape of the twin boundary. Test calculations revealed that due to the low amplitude (1–2 nm) of the pattern, which is smaller than the domain wall width, the zig-zag shape had no effect on our micromagnetic simulations. We used the following intrinsic magnetic properties for $\text{SmFe}_{11}\text{Ti}$: $K_1 = 4.8 \text{ MJ/m}^3$ and $\mu_0 M_s = 1.17 \text{ T}$ which are both equal to the measured values for single crystals shown above. This yields an anisotropy field of $\mu_0 H_a = 10.31 \text{ T}$. For the exchange constant we assumed $A = 10 \text{ pJ/m}$. For the twin boundary phase, as in agreement with the APT results, we assume a monoclinic ordered $\text{Sm}_3(\text{Fe,Ti})_{29}$ phase. For a monoclinic system the magneto-crystalline anisotropy energy density $K_1 \sin^2 \theta + K_2 \sin^2 \theta \cos 2\phi$ depends not only on the polar angle θ , but also on the azimuthal angle ϕ . For $\text{Sm}_3(\text{Fe,Ti})_{29}$ the anisotropy constants are $K_1 = 1.8 \text{ MJ/m}^3$, $K_2 = 0.4 \text{ MJ/m}^3$ and the magnetization is $\mu_0 M_s = 1.13 \text{ T}$ [102]. For our simulations we ignored the contribution of K_2 and assumed that the $\text{Sm}_3(\text{Fe,Ti})_{29}$ easy-axis is aligned with one of the easy-axes of two variants of the main phase [102–105].

The orientation of the external field is given in spherical coordinates (θ, φ) where θ is the polar angle ($z \rightarrow x$) and φ is the azimuthal angle ($x \rightarrow y$). The angle between the applied field and the magnetocrystalline easy-axis is given by α_i where i refers to one of the two variants of the $\text{SmFe}_{11}\text{Ti}$ phase. α is the average angle given by $\alpha = (\alpha_1 + \alpha_2)/2$. The anisotropy energy density is given

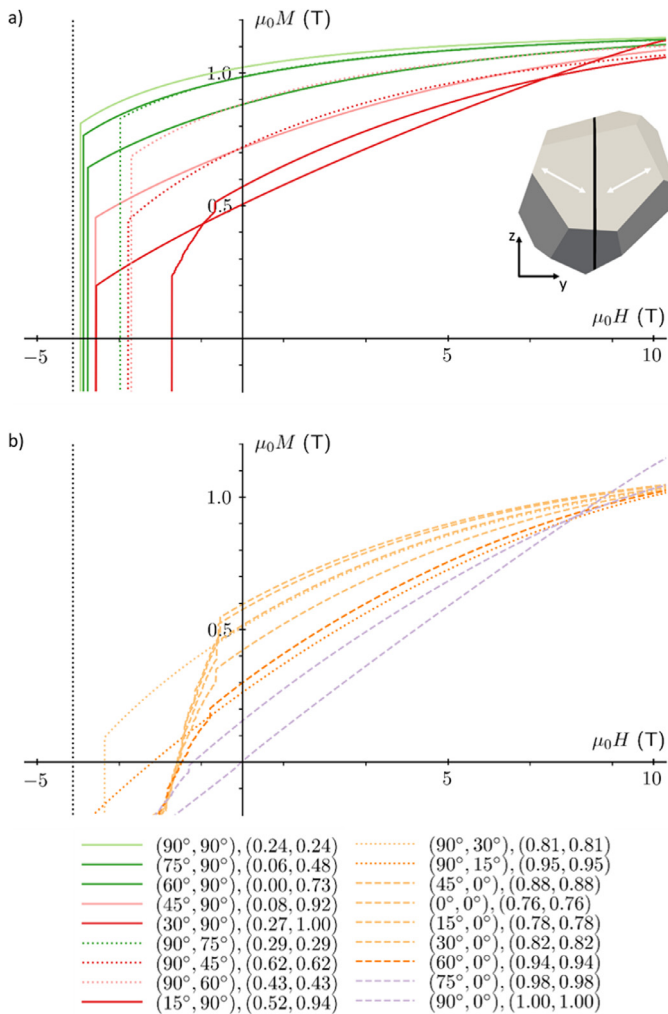


Fig. 8. Demagnetization curves as a function of the direction of the external field computed for a single twinned $\text{SmFe}_{11}\text{Ti}$ grain where a 6 nm thick $\text{Sm}_3(\text{Fe,Ti})_{29}$ twin boundary separates the two variants of the main phase. The inset in (a) shows the model setup. The twin boundary is parallel to the xz -plane. The two easy-axes of the two variants are shown as white double-headed arrows and are parallel to the yz -plane. The angle between the two easy-axes is 122° . The direction of the external field is given in the first bracket of the legend entries by spherical coordinates (θ, φ) where θ is the polar angle ($z \rightarrow x$) and φ is the azimuthal angle ($x \rightarrow y$). The second bracket gives $\sin^2 \alpha_i$ where α_i is the angle enclosed by the external field direction and one of the two easy-axes of the twin variants. $\sin^2 \alpha_i$ is proportional to the magnetocrystalline anisotropy energy density. Color changes from green to purple in 10° steps of the average α . Solid, dashed and dotted lines group similar rotation directions of the external field from z to y , z to x , and x to y , respectively. Entries in the legend are sorted by coercive field. a) shows the easy-axis-like demagnetization curves where average $\alpha < 61^\circ$, b) shows the hard-axis-like curves with average $\alpha \geq 61^\circ$. The dotted black line on the left-hand side marks 40 percent of the anisotropy field of $\text{SmFe}_{11}\text{Ti}$.

by $E_a = K_1 \sin^2 \alpha_i$. The switching field is defined as the first kink in the demagnetization curve when the behavior changes from reversible rotation to irreversible nucleation of reversed domains.

The micromagnetic simulations for a $\text{Nd}_2\text{Fe}_{14}\text{B}$ grain without a defect (graphs not shown) give switching field ($\mu_0 H_{sw}$) values that vary between -5.42 T for $\theta = 1^\circ$ and -3.23 T for $\theta = 45^\circ$. This corresponds to 71 percent or 42 percent of the anisotropy field of $\text{Nd}_2\text{Fe}_{14}\text{B}$, respectively. The switching field of all other computed orientations of the external field were between those values, consistent with Stoner-Wohlfarth results mentioned above, and also considering self-demagnetizing effects.

In contrast, despite the higher anisotropy field of the $\text{SmFe}_{11}\text{Ti}$ phase, much lower switching fields were found for $\text{SmFe}_{11}\text{Ti}$, due

to the twin defect. Fig. 8 shows demagnetization curves for various orientations of the external field computed for a twinned $\text{SmFe}_{11}\text{Ti}$ grain split by a single 6 nm thick $\text{Sm}_3(\text{Fe,Ti})_{29}$ twin boundary. Irreversible switching always starts at fields below 40 percent of the anisotropy field of $\text{SmFe}_{11}\text{Ti}$. Switching fields of between -3.94 T and -0.55 T were found for external field directions of $(90^\circ, 90^\circ)$ and $(0^\circ, 0^\circ)$, respectively. This corresponds to 38 percent and 5 percent of the anisotropy field of $\text{SmFe}_{11}\text{Ti}$, respectively. Please note that the curvature seen in the hard axis loop of Fig. 2 of the single crystal measurements could not be reproduced by our model, see $(90^\circ, 0^\circ)$ in Fig. 8. Similarly, we did not observe any curvature in the hard axis loop for a reference calculation with zero magnetocrystalline anisotropy ($K_1 = 0$) in the twin boundary phase. The contribution of the twin boundary phase to the total magnetization is negligible as its volume fraction is only 2.4 percent of the total volume. A possible reason for the curvature might be canting between the Fe and the Sm sublattices. The switching field strongly depends on the field angle. The magnetocrystalline anisotropy energy density is proportional to $K_1 \sin^2 \alpha$. The lowest switching fields are found if the average α is greater than 61° .

Due to the small thickness of the $\text{Sm}_3(\text{Fe,Ti})_{29}$ phase at the twin boundary, it is not clear if the assumption of a uniaxial magnetocrystalline anisotropy is valid. Thus, we also considered the twin boundary phase to be a soft defect with $K_1 = 0$. The switching fields were then in the range of -3.56 T to -1.3 T. In this case, the spread of the switching field values with field angle was reduced from 35 percent to 13 percent of the anisotropy field of $\text{SmFe}_{11}\text{Ti}$.

If we reuse the geometric model of the twin and change the setup of the $\text{Nd}_2\text{Fe}_{14}\text{B}$ single grain simulations to consider a 6 nm wide $\text{Nd}_{20}\text{Fe}_{80}$ ferromagnetic grain boundary phase ($K_1 = 0$, $\mu_0 M_s = 0.93$ T, $A = 9.99$ pJ/m [106]) but keep the easy-axes of both grains next to the boundary parallel to z , the switching field is also reduced to a range of 35 percent to 26 percent of the $\text{Nd}_2\text{Fe}_{14}\text{B}$ anisotropy field. As mentioned before, in $\text{Nd}_2\text{Fe}_{14}\text{B}$ permanent magnets, Nd-rich grain boundary phases with low or no magnetization are believed to magnetically decouple grains and, therefore, increase coercivity in an isotropic granular bulk magnet. Even if a similar grain boundary phase was found for $\text{SmFe}_{11}\text{Ti}$, the defect due to twinning within the grains remains, and will act as a weak spot for nucleation of reversed domains. The computation of the magnetization distribution at the saddle point for thermal switching identified the twin boundary region as the location where the nucleus of reversed magnetization forms.

Summarizing at this point, even if a similar grain boundary phase was found for $\text{SmFe}_{11}\text{Ti}$, the defect due to twinning within the grains remains, and will act as a weak spot for nucleation of reversed domains. The computation of the magnetization distribution at the saddle point for thermal switching identified the twin boundary region as the location where the nucleus of reversed magnetization forms for the geometry shown in Fig. 8. It is well known that ferromagnetic exchange coupling between crystallites with different orientations of the easy axes reduces the coercive field [107]. This holds for misoriented, exchange coupled grains as well as for twinned grains with a well-defined orientation relationship between the easy axes of two variants of the twinned grains. From a micromagnetic point of view, in both cases the formation of a partial domain wall causes the nucleation of reversed domains. Table 1 summarizes the micromagnetic simulations giving the hard magnetic phase, the model setup, and the range of the switching field due to the orientation of the external field.

Ab initio informed molecular dynamics calculations indicate that the twin formation energies are low and in the coherent regime. The competition between the formation energies of a twin boundary and a grain boundary are strongly dependent on the grain size and geometry. The molecular dynamics calculations predict that the twin formation is more energetically favourable for

Table 1

Range of the switching field due to the orientation of the external field for different geometries obtained by micromagnetic simulations. The columns refer to the main hard magnetic phase, the micromagnetic model setup and the coercivity range relative to the anisotropy field of the hard magnetic phases. The volume of the polyhedral grain was equal to that of a cube with an edge length of 295 nm.

Material	Model setup	Switching field range (relative to the H_a)
SmFe ₁₁ Ti	Twinned grain with 6 nm Sm ₃ (Fe,Ti) ₂₉ twin boundary	0.05 to 0.38
	Twinned grain with 6 nm twin boundary with $K_f = 0$	0.13 to 0.35
Nd ₂ Fe ₁₄ B	Single grain without defect	0.42 to 0.71
	Two aligned grains separated by a 6 nm ferromagnetic Nd ₂₀ Fe ₈₀ grain boundary phase (same model geometry as used for single grain simulation)	0.26 to 0.35

the grains of size above 1 micrometer. Additionally, the molecular dynamics calculations indicate that the interface energies play a significant role in twin formation.

4. Summary & conclusions

We carried out detailed structural characterization of twins in “single crystal” and polycrystalline bulk samples of composition SmFe₁₁Ti as well as ternary Sm(Fe,Ti)₁₂ and Zr-substituted (Sm,Zr)(Fe,Ti)₁₂ thin films. Twins were observed at micro- and nano-length scales, and it was found that the twin orientation in all sample types is approximately $57 \pm 2^\circ$. Thus twins appear to be a generic feature of the Sm(Fe,Ti)₁₂-system. The twin boundary plane corresponds to a {011}-plane family in the unit cell of Sm(Fe,Ti)₁₂. The significantly higher density of twins in the thin films compared to the bulk samples may be due to substrate mediated stress. High resolution electron microscopy studies on polycrystalline bulk samples show an enrichment of Sm and a depletion of Ti at the twin boundary. The composition of the twin boundary is determined to be Sm_{9.6}Fe_{84.9}Ti_{5.5}, matching the composition of the Sm₃(Fe,Ti)₂₉ phase, which has a lower anisotropy field. Modification of the intrinsic magnetic properties of the Sm₃(Fe,Ti)₂₉ phase may lead to an enhancement of the coercivity of the Sm(Fe,Ti)₁₂-systems.

Micromagnetic simulations were carried out with a microstructure reproducing that of bulk samples, and the results show that the formation of twins reduces the estimated coercivity values to 38% of the expected switching field. The simulation results account for the observation of low coercivity values in twinned SmFe₁₁Ti systems which confirms the detrimental effect of twins. Additionally, the fixed angle between neighboring twin variants would hinder obtaining perfect texture which also would reduce the remanent magnetization significantly.

Formation of twin boundaries in grains larger than 1 micrometer can be attributed to the accumulation of internal stresses during solidification, where twin formation is favoured over the formation of specific grain boundaries. The specific size, morphology and interface energy dependency and the resulting detailed model of the proposed mechanism will be an object of a further study/publication.

However, tuning hard magnetic alloys with the intent to render them less prone to twin formation is challenging. Three approaches, having different probabilities of a successful outcome, are conceivable in that context. The first one lies in substitutional compositional modification of the alloy with the aim to increase the twin formation energy which in turn would reduce the tendency for twin formation. However, most of the known reported compositional variants of these materials show twins, irrespective of substitutional variations. Also, twin interface energies are generally so low compared to those of less coherent grain boundaries (i.e. about a factor of 10 smaller) that such effects do not sufficiently alter this relation to reduce their frequency.

The second option lies in exposing the material to heat treatment under stress. This measure bears the risk though that imposing stresses on systems that are already prone to twin formation could lead to more rather than less twins. However, deformation driven twinning is typically reduced at elevated temperatures, where energy dissipation by dislocation activity is often promoted over twin formation, so that this option might be worth exploring.

A third and rather promising pathway is grain size reduction as this change of volume-to-surface energy ratio decreases the need for stress relief via twin formation. For this reason, high coercivities can possibly be achieved in nanocrystalline systems like hot-pressed and die-upset ThMn₁₂-type bulk permanent magnets but are unlikely to be observed in their sintered microcrystalline counterparts.

Declaration of Competing Interest

The authors declare that they have no known competing financial interests or personal relationships that could have appeared to influence the work reported in this paper.

Acknowledgments

This work is partly based on results obtained within the future pioneering program *Development of magnetic material technology for high-efficiency motors* (MagHEM) commissioned by the New Energy and Industrial Technology Development Organization (NEDO) of Japan. This work was also supported by the Deutsche Forschungsgemeinschaft (DFG, German Research Foundation) – Project-ID 405553726 – TRR 270.

Supplementary materials

Supplementary material associated with this article can be found, in the online version, at doi:[10.1016/j.actamat.2021.116968](https://doi.org/10.1016/j.actamat.2021.116968).

References

- [1] O. Gutfleisch, M.A. Willard, E. Brück, C.H. Chen, S.G. Sankar, J.P. Liu, Magnetic materials and devices for the 21st century: stronger, lighter, and more energy efficient, *Adv. Mater.* 23 (7) (2011) 821–842, doi:[10.1002/adma.201002180](https://doi.org/10.1002/adma.201002180).
- [2] K.P. Skokov, O. Gutfleisch, Heavy rare earth free, free rare earth and rare earth free magnets - vision and reality, *Scr. Mater.* 154 (2018) 289–294, doi:[10.1016/j.scriptamat.2018.01.032](https://doi.org/10.1016/j.scriptamat.2018.01.032).
- [3] Y. Hirayama, Y.K. Takahashi, S. Hirose, K. Hono, NdFe₁₂Nx hard-magnetic compound with high magnetization and anisotropy field, *Scr. Mater.* 95 (2015) 70–72, doi:[10.1016/j.scriptamat.2014.10.016](https://doi.org/10.1016/j.scriptamat.2014.10.016).
- [4] Y. Hirayama, T. Miyake, K. Hono, Rare-earth lean hard magnet compound NdFe₁₂N, *JOM* 67 (6) (2015) 1344–1349, doi:[10.1007/s11837-015-1421-9](https://doi.org/10.1007/s11837-015-1421-9).
- [5] K.H.J. Buschow, Structure and properties of some novel ternary Fe-rich rare-earth intermetallics (invited), *J. Appl. Phys.* 63 (8) (1988) 3130–3135, doi:[10.1063/1.340865](https://doi.org/10.1063/1.340865).
- [6] D.B. De Mooij, K.H.J. Buschow, Some novel ternary ThMn₁₂-type compounds, *J. Less Common Metals* 136 (2) (1988) 207–215, doi:[10.1016/0022-5088\(88\)90424-9](https://doi.org/10.1016/0022-5088(88)90424-9).
- [7] J.M.D. Coey, Comparison of the intrinsic magnetic properties of R₂Fe₁₄B and R(Fe₁₁Ti); R = rare earth, *J. Magn. Magn. Mater.* 80 (1) (1989) 9–13, doi:[10.1016/0304-8853\(89\)90314-4](https://doi.org/10.1016/0304-8853(89)90314-4).

- [8] B.-P. Hu, H.-S. Li, J.P. Gavigan, J.M.D. Coey, Intrinsic magnetic properties of the iron-rich ThMn₁₂-structure alloys R(Fe₁₁Ti); R=Y, Nd, Sm, Gd, Tb, Dy, Ho, Er, Tm and Lu, *J. Phys.* 1 (4) (1989) 755–770, doi:[10.1088/0953-8984/1/4/009](https://doi.org/10.1088/0953-8984/1/4/009).
- [9] Y. Hirayama, Y.K. Takahashi, S. Hirose, K. Hono, Intrinsic hard magnetic properties of Sm(Fe_{1-x}Cox)₁₂ compound with the ThMn₁₂ structure, *Scr. Mater.* 138 (2017) 62–65, doi:[10.1016/j.scriptamat.2017.05.029](https://doi.org/10.1016/j.scriptamat.2017.05.029).
- [10] T. Kuno, S. Suzuki, K. Urushibata, K. Kobayashi, N. Sakuma, M. Yano, A. Kato, A. Manabe, (Sm,Zr)(Fe,Co)_{11.0-11.5}Ti_{1.0-0.5} compounds as new permanent magnet materials, *AIP Adv.* 6 (2) (2016) 025221, doi:[10.1063/1.4943051](https://doi.org/10.1063/1.4943051).
- [11] M. Hagiwara, N. Sanada, S. Sakurada, Structural and magnetic properties of rapidly quenched (Sm,R)(Fe,Co)_{11.4}Ti_{0.6} (R = Y, Zr) with ThMn₁₂ structure, *AIP Adv.* 9 (3) (2019) 035036, doi:[10.1063/1.5079949](https://doi.org/10.1063/1.5079949).
- [12] N. Inoue, S. Suzuki, Influence of nitrogenating conditions on magnetic properties of NdFe₈Co₃TiN_x, *J. Alloys Compd.* 222 (1) (1995) 82–86, doi:[10.1016/0925-8388\(94\)04922-X](https://doi.org/10.1016/0925-8388(94)04922-X).
- [13] J. Yang, O. Mao, Z. Altoumian, Structure and magnetic properties of mechanically alloyed Nd(Fe,V)₁₂N_x compounds, *J. Appl. Phys.* 79 (8) (1996) 5519–5521, doi:[10.1063/1.362296](https://doi.org/10.1063/1.362296).
- [14] J. Yang, W. Mao, B. Cheng, Y. Yang, H. Xu, B. Han, S. Ge, W. Ku, Magnetic properties and magnetic domain structures of NdFe_{10.5}Mo_{1.5} and NdFe_{10.5}Mo_{1.5}N_x, *Appl. Phys. Lett.* 71 (22) (1997) 3290–3292, doi:[10.1063/1.120315](https://doi.org/10.1063/1.120315).
- [15] J. Yang, B. Cui, W. Mao, B. Cheng, J. Yang, B. Hu, Y. Yang, S. Ge, Effect of interstitial nitrogen on the structural and magnetic properties of NdFe_{10.5}V_{1.5}N_x, *J. Appl. Phys.* 83 (5) (1998) 2700–2704, doi:[10.1063/1.366991](https://doi.org/10.1063/1.366991).
- [16] H. Wuest, L. Bommer, A.M. Huber, D. Goll, T. Weissgaerber, B. Kieback, Preparation of nanocrystalline Ce_{1-x}Sm_x(Fe,Co)₁₁Ti by melt spinning and mechanical alloying, *J. Magn. Magn. Mater.* 428 (2017) 194–197, doi:[10.1016/j.jmmm.2016.12.036](https://doi.org/10.1016/j.jmmm.2016.12.036).
- [17] P. Tozman, H. Sepehri-Amin, Y.K. Takahashi, S. Hirose, K. Hono, Intrinsic magnetic properties of Sm(Fe_{1-x}Cox)₁₁Ti and Zr-substituted Sm_{1-y}Zr_y(Fe_{0.8}Co_{0.2})_{11.5}Ti_{0.5} compounds with ThMn₁₂ structure toward the development of permanent magnets, *Acta Mater.* 153 (2018) 354–363, doi:[10.1016/j.actamat.2018.05.008](https://doi.org/10.1016/j.actamat.2018.05.008).
- [18] T. Saito, F. Watanabe, D. Nishio-Hamane, Magnetic properties of SmFe₁₂-based magnets produced by spark plasma sintering method, *J. Alloys Compd.* 773 (2019) 1018–1022, doi:[10.1016/j.jallcom.2018.09.297](https://doi.org/10.1016/j.jallcom.2018.09.297).
- [19] D.S. Neznakhin, S.V. Andreev, M.A. Semkin, N.V. Selezneva, M.N. Volochaev, A.S. Bolyachkin, N.V. Kudrevatykh, A.S. Volegov, Structure and magnetic properties of (Sm_{0.9}Zr_{0.1})Fe₁₁Ti alloys with ThMn₁₂-type structure, *J. Magn. Magn. Mater.* 484 (2019) 212–217, doi:[10.1016/j.jmmm.2019.04.030](https://doi.org/10.1016/j.jmmm.2019.04.030).
- [20] I. Dirba, H. Sepehri-Amin, T. Ohkubo, K. Hono, Development of ultra-fine grain sized SmFe₁₂-based powders using hydrogenation disproportionation desorption recombination process, *Acta Mater.* 165 (2019) 373–380, doi:[10.1016/j.actamat.2018.11.065](https://doi.org/10.1016/j.actamat.2018.11.065).
- [21] R. Skomski, J.M.D. Coey, Magnetic anisotropy – How much is enough for a permanent magnet? *Scr. Mater.* 112 (2016) 3–8, doi:[10.1016/j.scriptamat.2015.09.021](https://doi.org/10.1016/j.scriptamat.2015.09.021).
- [22] S. Hirose, M. Nishino, S. Miyashita, Perspectives for high-performance permanent magnets: applications, coercivity, and new materials, *Adv. Natural Sci.* 8 (1) (2017) 013002, doi:[10.1088/2043-6254/aa597c](https://doi.org/10.1088/2043-6254/aa597c).
- [23] Y. Kawashita, N. Waki, T. Tayu, T. Sugiyama, H. Ono, H. Koyama, H. Kanno, T. Uchida, Microstructures and magnetic properties of hydrogenation disproportionation desorption recombination-processed Nd–Fe–B materials with different Nd content of 11.0 and 12.6 at.%, *J. Alloys Compd.* 360 (1) (2003) 322–329, doi:[10.1016/S0925-8388\(03\)00504-8](https://doi.org/10.1016/S0925-8388(03)00504-8).
- [24] Y. Kawashita, N. Waki, T. Tayu, T. Sugiyama, H. Ono, H. Koyama, H. Kanno, T. Uchida, Magnetic properties of Nd–Fe–B system anisotropic HDDR powder made from segregated master ingots, *J. Magn. Magn. Mater.* 269 (3) (2004) 293–301, doi:[10.1016/S0304-8853\(03\)00595-X](https://doi.org/10.1016/S0304-8853(03)00595-X).
- [25] H. Sepehri-Amin, W.F. Li, T. Ohkubo, T. Nishiuchi, S. Hirose, K. Hono, Effect of Ga addition on the microstructure and magnetic properties of hydrogenation–disproportionation–desorption–recombination processed Nd–Fe–B powder, *Acta Mater.* 58 (4) (2010) 1309–1316, doi:[10.1016/j.actamat.2009.10.035](https://doi.org/10.1016/j.actamat.2009.10.035).
- [26] R. Nakayama, T. Takeshita, M. Itakura, N. Kuwano, K. Oki, Microstructures and crystallographic orientation of crystalline grains in anisotropic Nd–Fe–Co–B (Ga or Zr) magnet powders produced by the hydrogenation–decomposition–desorption–recombination process, *J. Appl. Phys.* 76 (1) (1994) 412–417, doi:[10.1063/1.357091](https://doi.org/10.1063/1.357091).
- [27] H. Sepehri-Amin, T. Ohkubo, T. Nishiuchi, S. Hirose, K. Hono, Coercivity enhancement of hydrogenation–disproportionation–desorption–recombination processed Nd–Fe–B powders by the diffusion of Nd–Cu eutectic alloys, *Scr. Mater.* 63 (11) (2010) 1124–1127, doi:[10.1016/j.scriptamat.2010.08.021](https://doi.org/10.1016/j.scriptamat.2010.08.021).
- [28] K. Güth, J. Lyubina, B. Gebel, L. Schultz, O. Gutfleisch, Ultra-fine grained Nd–Fe–B by high pressure reactive milling and desorption, *J. Magn. Magn. Mater.* 324 (18) (2012) 2731–2735, doi:[10.1016/j.jmmm.2012.03.059](https://doi.org/10.1016/j.jmmm.2012.03.059).
- [29] O. Gutfleisch, B. Gebel, M. Kubis, K.H. Müller, L. Schultz, Modified HDDR procedures applied to NdFeB alloys, *IEEE Trans. Magn.* 35 (5) (1999) 3250–3252, doi:[10.1109/20.800488](https://doi.org/10.1109/20.800488).
- [30] A. Hütten, G. Thomas, Microstructural parameters of melt-spun Nd₁₅Fe₇₇B₈ ribbons, *Ultramicroscopy* 47 (4) (1992) 447–454, doi:[10.1016/0304-3991\(92\)90176-K](https://doi.org/10.1016/0304-3991(92)90176-K).
- [31] C.L. Harland, H.A. Davies, Magnetic properties of melt-spun Nd-rich NdFeB alloys with Dy and Ga substitutions, *J. Alloys Compd.* 281 (1) (1998) 37–40, doi:[10.1016/S0925-8388\(98\)00767-1](https://doi.org/10.1016/S0925-8388(98)00767-1).
- [32] J.H. Vincent, M.J.P.D. Wyborn, Production of Nd–Fe–B magnets by the rapid solidification processing route, *Mater. Des.* 11 (4) (1990) 207–212, doi:[10.1016/0261-3069\(90\)90156-E](https://doi.org/10.1016/0261-3069(90)90156-E).
- [33] H.C. Hua, G.Y. Wang, C.H. Zheng, G.X. Huang, Q.Z. Xu, L.H. Wu, S.Y. Shi, Microstructure of melt-spun NdFeB magnet, *Mater. Lett.* 7 (1) (1988) 65–67, doi:[10.1016/0167-577X\(88\)90085-7](https://doi.org/10.1016/0167-577X(88)90085-7).
- [34] R. Ramesh, G. Thomas, B.M. Ma, Magnetization reversal in nucleation controlled magnets. II. Effect of grain size and size distribution on intrinsic coercivity of Fe–Nd–B magnets, *J. Appl. Phys.* 64 (11) (1988) 6416–6423, doi:[10.1063/1.342055](https://doi.org/10.1063/1.342055).
- [35] W.F. Li, T. Ohkubo, K. Hono, M. Sagawa, The origin of coercivity decrease in fine grained Nd–Fe–B sintered magnets, *J. Magn. Magn. Mater.* 321 (8) (2009) 1100–1105, doi:[10.1016/j.jmmm.2008.10.032](https://doi.org/10.1016/j.jmmm.2008.10.032).
- [36] R. Goto, M. Matsuura, S. Sugimoto, N. Tezuka, Y. Une, M. Sagawa, Microstructure evaluation for Dy-free Nd–Fe–B sintered magnets with high coercivity, *J. Appl. Phys.* 111 (7) (2012) 07A739, doi:[10.1063/1.3680190](https://doi.org/10.1063/1.3680190).
- [37] W.B. Cui, Y.K. Takahashi, K. Hono, Microstructure optimization to achieve high coercivity in anisotropic Nd–Fe–B thin films, *Acta Mater.* 59 (20) (2011) 7768–7775, doi:[10.1016/j.actamat.2011.09.006](https://doi.org/10.1016/j.actamat.2011.09.006).
- [38] N.G. Akdogan, N.M. Dempsey, D. Givord, A. Manabe, T. Shoji, M. Yano, A. Kato, Influence of Nd and Cu content on the microstructural and magnetic properties of NdFeB thick films, *J. Appl. Phys.* 115 (17) (2014) 17A722, doi:[10.1063/1.4865462](https://doi.org/10.1063/1.4865462).
- [39] Y. Xie, Y. Yang, T. Zhang, Y. Fu, Q. Jiang, S. Ma, Z. Zhong, W. Cui, Q. Wang, Microstructure evolution and coercivity enhancement in Nd–Fe–B thin films diffusion-processed by R–Al alloys (R=Nd, Pr), *AIP Adv.* 8 (5) (2018) 056202, doi:[10.1063/1.5006110](https://doi.org/10.1063/1.5006110).
- [40] K. Khlopkov, O. Gutfleisch, D. Eckert, D. Hinz, B. Wall, W. Rodewald, K.H. Müller, L. Schultz, Local texture in Nd–Fe–B sintered magnets with maximised energy density, *J. Alloys Compd.* 365 (1) (2004) 259–265, doi:[10.1016/S0925-8388\(03\)00636-4](https://doi.org/10.1016/S0925-8388(03)00636-4).
- [41] K. Khlopkov, O. Gutfleisch, D. Hinz, K.-H. Müller, L. Schultz, Evolution of interaction domains in textured fine-grained Nd₂Fe₁₄B magnets, *J. Appl. Phys.* 102 (2) (2007) 023912, doi:[10.1063/1.2751092](https://doi.org/10.1063/1.2751092).
- [42] A. Walther, K. Khlopkov, O. Gutfleisch, D. Givord, N.M. Dempsey, Evolution of magnetic and microstructural properties of thick sputtered NdFeB films with processing temperature, *J. Magn. Magn. Mater.* 316 (2) (2007) 174–176, doi:[10.1016/j.jmmm.2007.02.047](https://doi.org/10.1016/j.jmmm.2007.02.047).
- [43] O. Gutfleisch, K. Khlopkov, A. Teresiak, K. Müller, G. Drazic, C. Mishima, Y. Honkura, Memory of texture during HDDR Processing of NdFeB, *IEEE Trans. Magn.* 39 (5) (2003) 2926–2931, doi:[10.1109/TMAG.2003.815749](https://doi.org/10.1109/TMAG.2003.815749).
- [44] A. Bollero, A. Kirchner, O. Gutfleisch, K. Müller, L. Schultz, Highly coercive milled and melt-spun (Pr,Nd)Fe₂-type magnets and their hot workability, *IEEE Trans. Magn.* 37 (4) (2001) 2483–2485, doi:[10.1109/20.951210](https://doi.org/10.1109/20.951210).
- [45] A. Kirchner, W. Grünberger, O. Gutfleisch, V. Neu, K.H. Müller, L. Schultz, A comparison of the magnetic properties and deformation behaviour of Nd–Fe–B magnets made from melt-spun, mechanically alloyed and HDDR powders, *J. Phys. D Appl. Phys.* 31 (14) (1998) 1660–1666, doi:[10.1088/0022-3727/31/14/008](https://doi.org/10.1088/0022-3727/31/14/008).
- [46] O. Gutfleisch, D. Eckert, R. Schäfer, K.H. Müller, V. Panchanathan, Magnetization processes in two different types of anisotropic, fully dense NdFeB hydrogenation, disproportionation, desorption, and recombination magnets, *J. Appl. Phys.* 87 (9) (2000) 6119–6121, doi:[10.1063/1.372628](https://doi.org/10.1063/1.372628).
- [47] K. Ohashi, Y. Tawara, R. Osugi, M. Shimao, Magnetic properties of Fe-rich rare-earth intermetallic compounds with a ThMn₁₂ structure, *J. Appl. Phys.* 64 (10) (1988) 5714–5716, doi:[10.1063/1.342235](https://doi.org/10.1063/1.342235).
- [48] T. Tsuchi, H. Nakamura, S. Sugimoto, M. Okada, M. Homma, Enhancement of the magnetic properties of Sm–Fe and Nd–Fe–N Alloys with ThMn₁₂ structure by utilizing HDDR phenomena, *IEEE Trans. J. Magnetic. Japan* 8 (11) (1993) 755–762, doi:[10.1109/TJM.1993.4565741](https://doi.org/10.1109/TJM.1993.4565741).
- [49] S. Sugimoto, T. Shimono, H. Nakamura, T. Kagotani, M. Okada, M. Homma, Magnetic properties and microstructures of the (SmFe₁₀V₂)_{1-x}(Sm₂Fe₁₇)_x cast alloys, *Mater. Chem. Phys.* 42 (4) (1995) 298–301, doi:[10.1016/0254-0584\(96\)80018-6](https://doi.org/10.1016/0254-0584(96)80018-6).
- [50] I. Dirba, J. Li, H. Sepehri-Amin, T. Ohkubo, T. Schrefl, K. Hono, Anisotropic, single-crystalline SmFe₁₂-based microparticles with high roundness fabricated by jet-milling, *J. Alloys Compd.* 804 (2019) 155–162, doi:[10.1016/j.jallcom.2019.06.365](https://doi.org/10.1016/j.jallcom.2019.06.365).
- [51] A.M. Gabay, G.C. Hadjipanayis, Mechanochemical synthesis of magnetically hard anisotropic RFe₁₀Si₂ powders with R representing combinations of Sm, Ce and Zr, *J. Magn. Magn. Mater.* 422 (2017) 43–48, doi:[10.1016/j.jmmm.2016.08.064](https://doi.org/10.1016/j.jmmm.2016.08.064).
- [52] E.W. Singleton, J. Strzeszewski, G.C. Hadjipanayis, D.J. Sellmyer, Magnetic and structural properties of melt-spun rare-earth transition-metal intermetallics with ThMn₁₂ structure, *J. Appl. Phys.* 64 (10) (1988) 5717–5719, doi:[10.1063/1.342236](https://doi.org/10.1063/1.342236).
- [53] J. Strzeszewski, Y.Z. Wang, E.W. Singleton, G.C. Hadjipanayis, High coercivity in Sm(FeTi)₂ type magnets, *IEEE Trans. Magn.* 25 (5) (1989) 3309–3311, doi:[10.1109/20.42287](https://doi.org/10.1109/20.42287).
- [54] M. Okada, K. Yamagishi, M. Homma, High Coercivity in Melt-Spun SmFe₁₀(TiV)₂ Ribbons, *Mater. Trans. JIM* 30 (5) (1989) 374–377, doi:[10.2320/matertrans1989.30.374](https://doi.org/10.2320/matertrans1989.30.374).
- [55] S. Sugimoto, A. Kojima, M. Okada, M. Homma, Enhancement of Magnetic Properties of Sm(Fe,Co,Ti)₁₂ Melt-Spun Ribbons by Refining Crystallized Grains, *Mater. Trans.* 32 (12) (1991) 1180–1183 JIM, doi:[10.2320/matertrans1989.32.1180](https://doi.org/10.2320/matertrans1989.32.1180).

- [56] F.E. Pinkerton, D.J.V. Wingerden, Magnetic hardening of SmFe10V2 by melt-spinning, *IEEE Trans. Magn.* 25 (5) (1989) 3306–3308, doi:10.1109/20.42285.
- [57] Y. Wang, G.C. Hadjipanayis, A. Kim, N.C. Liu, D.J. Sellmyer, Magnetic and structural studies in Sm-Fe-Ti magnets, *J. Appl. Phys.* 67 (9) (1990) 4954–4956, doi:10.1063/1.344745.
- [58] T. Saito, H. Miyoshi, D. Nishio-Hamane, Magnetic properties of Sm-Fe-Ti nanocomposite magnets with a ThMn12 structure, *J. Alloys Compd.* 519 (2012) 144–148, doi:10.1016/j.jallcom.2011.12.156.
- [59] J.E. Shield, C.P. Li, D.J. Branagan, Microstructures and phase formation in rapidly solidified Sm-Fe and Sm-Fe-Ti-C alloys, *J. Magn. Mater.* 188 (3) (1998) 353–360, doi:10.1016/S0304-8853(98)00208-X.
- [60] G.C. Hadjipanayis, A.M. Gabay, A.M. Schönhöbel, A. Martín-Cid, J.M. Barandiaran, D. Niarchos, ThMn₁₂-Type Alloys for Permanent Magnets, *Engineering* (2019) In Press, doi:10.1016/j.eng.2018.12.011.
- [61] H. Sepehri-Amin, Y. Tamazawa, M. Kambayashi, G. Saito, Y.K. Takahashi, D. Ogawa, T. Ohkubo, S. Hirotsawa, M. Doi, T. Shima, K. Hono, Achievement of high coercivity in Sm(Fe_{0.8}Co_{0.2})₁₂ anisotropic magnetic thin film by boron doping, *Acta Mater.* 194 (2020) 337–342, doi:10.1016/j.actamat.2020.05.026.
- [62] A.M. Gabay, G.C. Hadjipanayis, High-coercivity ThMn₁₂-type monocrystalline Sm-Zr-Fe-Co-Ti particles by high-temperature reduction diffusion, *Scr. Mater.* 196 (2021) 113760, doi:10.1016/j.scriptamat.2021.113760.
- [63] D. Palanisamy, S. Ener, F. Maccari, L. Schäfer, K.P. Skokov, O. Gutfleisch, D. Raabe, B. Gault, Grain boundary segregation, phase formation, and their influence on the coercivity of rapidly solidified SmFe₁₁Ti hard magnetic alloys, *Phys. Rev. Mater.* 4 (5) (2020) 054404, doi:10.1103/PhysRevMaterials.4.054404.
- [64] K. Skokov, A. Grushishev, A. Khokhlov, Y. Pastushenkov, N. Pankratov, T. Ivanova, S. Nikitin, Magnetic properties of Gd₃Fe_xTi₃ (x=34, 33, ..., 24), TbFe₁₁Ti and TbFe₁₀Ti single crystals, *J. Magn. Mater.* 272–276 (2004) 374–375, doi:10.1016/j.jmmm.2003.11.147.
- [65] F. Maccari, L. Schäfer, I. Radulov, L.V.B. Diop, S. Ener, E. Bruder, K. Skokov, O. Gutfleisch, Rapid solidification of Nd_{1+x}Fe₁₁Ti compounds: phase formation and magnetic properties, *Acta Mater.* 180 (2019) 15–23, doi:10.1016/j.actamat.2019.08.057.
- [66] D. Palanisamy, D. Raabe, B. Gault, Elemental segregation to twin boundaries in a MnAl ferromagnetic Heusler alloy, *Scr. Mater.* 155 (2018) 144–148, doi:10.1016/j.scriptamat.2018.06.037.
- [67] C. Yanar, V. Radmilovic, W.A. Soffa, J.M.K. Wiezorek, Evolution of microstructure and defect structure in L1₀-ordered manganese aluminide permanent magnet alloys, *Intermetallics* 9 (10) (2001) 949–954, doi:10.1016/S0966-9795(01)00095-4.
- [68] J. Landuyt, G. Tendeloo, J.J. Broek, H. Donkersloot, H. Zijlstra, Defect structure and magnetic properties of MnAl permanent magnet materials, *IEEE Trans. Magn.* 14 (5) (1978) 679–681, doi:10.1109/TMAG.1978.1059949.
- [69] J.P. Jakubovics, T.W. Jolly, The effect of crystal defects on the domain structure of Mn-Al alloys, *Physica B+C* 86–88 (1977) 1357–1359, doi:10.1016/0378-4363(77)90910-X.
- [70] S. Bance, F. Bittner, T.G. Woodcock, L. Schultz, T. Schrefl, Role of twin and anti-phase defects in MnAl permanent magnets, *Acta Mater.* 131 (2017) 48–56, doi:10.1016/j.actamat.2017.04.004.
- [71] T. Klemmer, D. Hoydick, H. Okumura, B. Zhang, W.A. Soffa, Magnetic hardening and coercivity mechanisms in L1₀ ordered FePd ferromagnets, *Scripta Metallurgica et Materialia* 33 (10) (1995) 1793–1805, doi:10.1016/0956-716X(95)00413-P.
- [72] T. Shima, K. Takanashi, *Hard magnetic films*, in: *Handbook of Magnetism and Advanced Magnetic Materials*, H.K.a.S. Parkin, Editor, John Wiley & Sons, Ltd., 2007, pp. 1–19.
- [73] J.S. Gau, R.K. Mishra, T. Graule, Electron microscopy of Mn-Al-C magnets, in: *Magnetics*, IEEE Transactions on, 19, 1983, pp. 2256–2260, doi:10.1109/TMAG.1983.1062798.
- [74] B. Zhang, W.A. Soffa, Magnetic domains and coercivity in polytwinned ferromagnets, *Phys. Status Solidi (a)* 131 (2) (1992) 707–725, doi:10.1002/pssa.2211310239.
- [75] J.P. Attané, Y. Samson, A. Marty, D. Halley, C. Beigné, Domain wall pinning on strain relaxation defects in FePt(001)/Pt thin films, *Appl. Phys. Lett.* 79 (6) (2001) 794–796, doi:10.1063/1.1390321.
- [76] P. Glijer, K. Sin, J.M. Sivertsen, J.H. Judy, Correlation of structural defects and magnetic properties in CoCrPt/Cr and CoCrTaPt/Cr thin films for ultra high density magnetic recording media, *Scripta Metallurgica et Materialia* 33 (10) (1995) 1585–1592, doi:10.1016/0956-716X(95)00403-1.
- [77] B.G. Demczyk, D.E. Laughlin, Growth characteristics of Co-Cr thin films for magnetic recording, *MRS Proc.* 119 (1988) 159, doi:10.1557/PROC-119-159.
- [78] Y. Jia, Y. Wu, S. Zhao, S. Zuo, K.P. Skokov, O. Gutfleisch, C. Jiang, H. Xu, L1₀ rare-earth-free permanent magnets: the effects of twinning versus dislocations in Mn-Al magnets, *Phys. Rev. Mater.* 4 (9) (2020) 094402, doi:10.1103/PhysRevMaterials.4.094402.
- [79] J. Rodríguez-Carvajal, Recent advances in magnetic structure determination by neutron powder diffraction, *Physica B: Condensed Matter* 192 (1) (1993) 55–69, doi:10.1016/0921-4526(93)90108-1.
- [80] P.J. Felfel, T. Alam, S.P. Ringer, J.M. Cairney, A reproducible method for damage-free site-specific preparation of atom probe tips from interfaces, *Microw. Res. Tech.* 75 (4) (2012) 484–491, doi:10.1002/jemt.21081.
- [81] S.K. Mäkinen, M. Lenz, P. Kontis, Z. Li, A. Kumar, P.J. Felfel, S. Neumeier, M. Herbig, E. Spiecker, D. Raabe, B. Gault, Correlative microscopy—novel methods and their applications to explore 3D chemistry and structure of nanoscale lattice defects: a case study in Superalloys, *JOM* 70 (9) (2018) 1736–1743, doi:10.1007/s11837-018-2802-7.
- [82] M. Herbig, P. Choi, D. Raabe, Combining structural and chemical information at the nanometer scale by correlative transmission electron microscopy and atom probe tomography, *Ultramicroscopy* 153 (2015) 32–39, doi:10.1016/j.ultramicro.2015.02.003.
- [83] R. Quey, P.R. Dawson, F. Barbe, Large-scale 3D random polycrystals for the finite element method: generation, meshing and remeshing, *Comput. Methods Appl. Mech. Eng.* 200 (17) (2011) 1729–1745, doi:10.1016/j.cma.2011.01.002.
- [84] A. Ribes, C. Caremoli, *Salomé platform component model for numerical simulation*, 31st Annual International Computer Software and Applications Conference (COMPSAC 2007), 2007.
- [85] MeshGems, Distene's MeshGem Software. <http://www.meshgems.com/>, 2016.
- [86] C. Qiushi, A. Konrad, A review of finite element open boundary techniques for static and quasi-static electromagnetic field problems, *IEEE Trans. Magn.* 33 (1) (1997) 663–676, doi:10.1109/20.560095.
- [87] L. Exl, J. Fischbacher, A. Kovacs, H. Oezelt, M. Gusenbauer, T. Schrefl, Pre-conditioned nonlinear conjugate gradient method for micromagnetic energy minimization, *Comput. Phys. Commun.* 235 (2019) 179–186, doi:10.1016/j.cpc.2018.09.004.
- [88] J.D. Hunter, Matplotlib: a 2D graphics environment, *Comput. Sci. Eng.* 9 (3) (2007) 90–95, doi:10.1109/MCSE.2007.55.
- [89] E.C. Stoner, E.P. Wohlfarth, A mechanism of magnetic hysteresis in heterogeneous alloys, *Philos. Trans. R. Soc. Lond. Ser. A, Math. Phys. Sci.* 240 (826) (1948) 599–642, doi:10.1098/rsta.1948.0007.
- [90] H. Kronmüller, K.D. Durst, M. Sagawa, Analysis of the magnetic hardening mechanism in RE-FeB permanent magnets, *J. Magn. Mater.* 74 (3) (1988) 291–302, doi:10.1016/0304-8853(88)90202-8.
- [91] W.F. Brown, Virtues and weaknesses of the domain concept, *Rev. Mod. Phys.* 17 (1) (1945) 15–19, doi:10.1103/RevModPhys.17.15.
- [92] D.Y. Karpenkov, K.P. Skokov, M.B. Lyakhova, I.A. Radulov, T. Fasje, Y. Skourski, O. Gutfleisch, Intrinsic magnetic properties of hydrided and non-hydrided Nd₅Fe₁₇ single crystals, *J. Alloys Compd.* 741 (2018) 1012–1020, doi:10.1016/j.jallcom.2018.01.239.
- [93] A.S. Bolyachkin, D.S. Neznakhin, T.V. Garaeva, A.V. Andreev, M.I. Bartashevich, Magnetic anisotropy of YFe₃ compound, *J. Magn. Mater.* 426 (2017) 740–743, doi:10.1016/j.jmmm.2016.10.133.
- [94] M.D. Kuz'min, K.P. Skokov, I. Radulov, C.A. Schwöbel, S. Foro, W. Donner, M. Werwiński, J. Ruz, E. Delczeg-Czirjak, O. Gutfleisch, Magnetic anisotropy of La₂Co₇, *J. Appl. Phys.* 118 (5) (2015) 053905, doi:10.1063/1.4927849.
- [95] L.V.B. Diop, M.D. Kuz'min, Y. Skourski, K.P. Skokov, I.A. Radulov, O. Gutfleisch, Determination of the crystal field parameters in SmFe₁₁Ti, *Phys. Rev. B* 102 (6) (2020) 064423, doi:10.1103/PhysRevB.102.064423.
- [96] S.P. Venkateswaran, N.T. Nuhfer, M. De Graef, Magnetic domain memory in multiferroic Ni₂MnGa, *Acta Mater.* 55 (16) (2007) 5419–5427, doi:10.1016/j.actamat.2007.05.055.
- [97] Y. Ge, O. Heczko, O. Söderberg, S.-P. Hannula, Direct optical observation of magnetic domains in Ni-Mn-Ga martensite, *Appl. Phys. Lett.* 89 (8) (2006) 082502, doi:10.1063/1.2335811.
- [98] D.G. Lord, A.P. Holden, P.J. Grundy, Magnetic force microscopy of Terfenol-D fracture surfaces, *J. Appl. Phys.* 81 (8) (1997) 5728–5730, doi:10.1063/1.364650.
- [99] J. Dooley, M.D. Graef, M.E. McHenry, Induction mapping of magnetostrictive materials, *J. Appl. Phys.* 83 (11) (1998) 6837–6839, doi:10.1063/1.367817.
- [100] J.M.D. Coey, *Magnetism and Magnetic Materials*, Cambridge University Press, Cambridge, 2010.
- [101] M. Nespolo, C. Iordache, Twiny: from morphology to twin element and vice versa, *J. Appl. Crystallogr.* 46 (3) (2013) 801–803, doi:10.1107/S0021889813009746.
- [102] S.W.M. Wirth, K.H. Müller, A Margarian, Determination of anisotropy constants for monoclinic ferromagnetic compounds, 9. international symposium on magnetic anisotropy and coercivity in rare-earth transition metal alloys and 14. international workshop on rare-earth magnets and their applications, 1996.
- [103] H.A. Sobh, S.H. Aly, S. Yehia, Calculation of magnetization curves and probability distribution for monoclinic and uniaxial systems, *J. Magn. Mater.* 331 (2013) 174–182, doi:10.1016/j.jmmm.2012.11.017.
- [104] N. Tang, X.C. Kou, F.R.d. Boer, K.H.J. Buschow, J.L. Wang, F. Yang, Magnetocrystalline anisotropy of novel R₃(Fe,M)₂₉ compounds, *J. Phys.* 11 (27) (1999) 5313–5320, doi:10.1088/0953-8984/11/27/307.
- [105] D. Negri, A. Paoluzi, L. Pareti, Magnetic anisotropy and magnetisation processes in 3:29, 1:12 and 2:17 type Nd:(Fe, Co, Ti) related compounds, *J. Magn. Mater.* 269 (3) (2004) 302–310, doi:10.1016/S0304-8853(03)00618-8.
- [106] A. Sakuma, T. Suzuki, T. Furuuchi, T. Shima, K. Hono, Magnetism of Nd-Fe films as a model of grain boundary phase in Nd-Fe-B permanent magnets, *Appl. Phys. Express* 9 (1) (2015) 013002, doi:10.7567/apex.9.013002.
- [107] T. Schrefl, H.F. Schmidts, J. Fidler, H. Kronmüller, The role of exchange and dipolar coupling at grain boundaries in hard magnetic materials, *J. Magn. Mater.* 124 (3) (1993) 251–261, doi:10.1016/0304-8853(93)90123-J.

Supplementary Materials

Twins – A weak link in the magnetic hardening of ThMn₁₂-type permanent magnets

Semih Ener ^{1,*}, Konstantin P. Skokov ¹, Dhanalakshmi Palanisamy ², Thibaut Devillers ³, Johann Fischbacher ⁴, Gabriel Gomez Eslava ³, Fernando Maccari ¹, Lukas Schäfer ¹, Léopold V. B. Diop ¹, Iliya Radulov ¹, Baptiste Gault ^{2,5}, Gino Hrkac ⁶, Nora M. Dempsey ³, Thomas Schrefl ⁴, Dierk Raabe ² and Oliver Gutfleisch ¹

¹ *Functional Materials, Department of Material Science, Technical University of Darmstadt, Darmstadt, 64287, Germany*

² *Max-Planck-Institute für Eisenforschung GmbH, Düsseldorf, 40237 Germany*

³ *Univ. Grenoble Alpes, CNRS, Institut NEEL, Grenoble, 38000 France*

⁴ *Department for Integrated Sensor Systems, Danube University Krems, Krems 3500, Austria*

⁵ *Department of Materials, Royal School of Mines, Imperial College London, London, SW7 2AZ, United Kingdom*

⁶ *College of Engineering, Mathematics and Physical Sciences, University of Exeter, North Park Road, Exeter EX4 4QF, United Kingdom*

ThMn₁₂-type crystal structure of SmFe₁₁Ti composition is shown in **Figure S1**. Sm(Fe,Ti)₁₂ phase having a tetragonal crystal structure (space group *I4/mmm*) with lattice parameters $a = b = 0.8589$ nm and $c = 0.4807$ nm. Rare-earth atoms (shown in pink in Figure S1) occupy the $2a$ Wyckoff site, iron atoms (shown in gold in Figure S1) fully occupy the $8f$ and $8j$ sites and the $8i$ site is shared between the iron and titanium (shown in light blue in Figure S1) atoms. The magnetic easy axis is along the c -axis of the crystal structure.

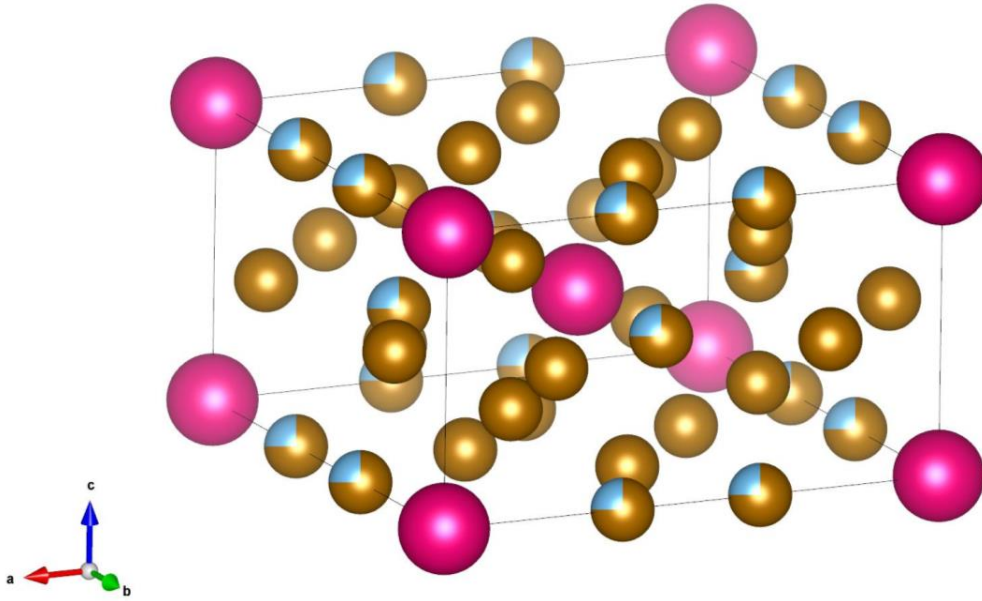


Figure S1. ThMn₁₂-type crystal structure of SmFe₁₁Ti which was displayed with Vesta [1].

Figure S2a shows a TEM bright-field micrograph of the APT specimen containing the twin boundary oriented along the [111] zone axis. Figure S2b shows the diffraction patterns (DPs) obtained from grains on either side of the twin boundary. The indexed simulated pattern (Figure S2c) confirms the tetragonal Sm(Fe,Ti)₁₂ matrix phase. In the same orientation of the specimen, the DP from the region below the twin boundary, shown in Figure S2d, indicates the same pattern, however, with a twinned orientation. This is more clearly evidenced in the DP taken from the twin boundary region, shown in Figure S2e, which shows that the two regions are twinned with a common twinning plane of (011)-type. This is similar to what we observe in the EBSD data shown in Figure 5 of the article. We also show that the dark-field micrographs taken from 110 spots clearly distinguishes the two twinned regions by reflections from the corresponding regions.

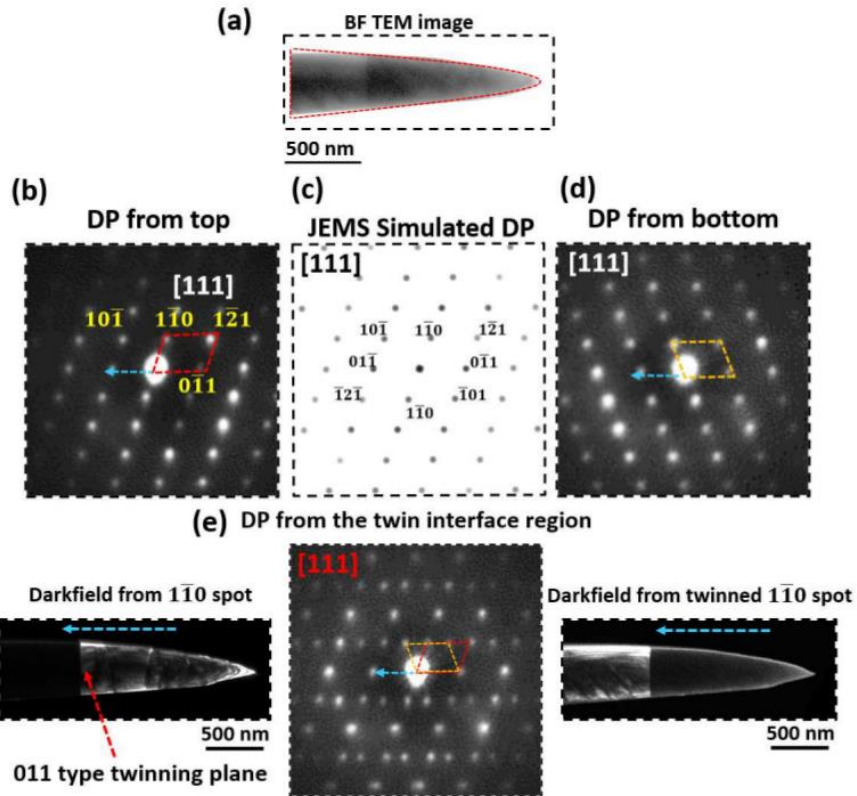


Figure S2. (a) TEM bright field image of the SmFe₁₁Ti sample at the twin boundary. Electron diffraction patterns of (b) the top part of the twin boundary, (c) corresponding simulated pattern and (d) the bottom part of the twin boundary. (e) The electron diffraction pattern at the interface region of the twin boundary.

To complement the studies of twins in bulk Sm-Fe-Ti samples, we also studied twins in Sm-Fe-Ti sputtered films. Films with and without addition of Zr were investigated, to evaluate the eventual impact of Zr substitution on the films' microstructure. Both the Sm(Fe,Ti)₁₂ and (Sm,Zr)(Fe,Ti)₁₂ films contain a first layer of isotropically oriented equiaxed grains of maximum diameter 200 nm, at the interface with the Ta buffer, and elongated grains of width ~200 nm that traverse the rest of the film thickness. The elongated grains, with lattice parameters corresponding to the Sm(Fe,Ti)₁₂ structure, are highly textured, with a dominant {101} or {200} texture. It is difficult to distinguish between these using 2θ x-ray or TEM diffraction analysis, since there is only a 2% difference

between the 101 and 200 inter-planar spacing. However, a comparison of the in-plane and out-of-plane hysteresis loops (data not shown here) reveals that both films show a pronounced easy axis out-of-plane magnetic anisotropy. Knowing that $\text{Sm}(\text{Fe,Ti})_{12}$ is characterized by uniaxial anisotropy [2-4], we can rule out the {200} texture, as this would induce in-plane magnetic anisotropy. Therefore, we will consider in the following a {101} texture, meaning that the [020] direction lies in the plane of the sample.

Multiple planar defects oriented parallel to the growth direction, which are attributed to twins in the $\text{Sm}(\text{Fe,Ti})_{12}$ structure, were identified in the elongated grains of both films. In **Figure S3a** we present a bright field electron micrograph of the $(\text{Sm,Zr})(\text{Fe,Ti})_{12}$ film, observed in a [101] zone axis. The twin boundaries are parallel to the (010) planes. A higher resolution micrograph (Figure S3b) shows that along this particular zone axis, the atomic crystal structure on both sides of the twinning boundaries looks identical, because they are probably seen under a similar zone axis (*e.g.* $[\bar{1}01]$ and $[\bar{1}0\bar{1}]$). This is confirmed in Figure S3c by selected-area electron diffraction (SAED) from a region containing multiple twin boundaries, which can be indexed as a single diffraction pattern (as if it was the diffraction from a single crystal). Because of the already discussed out-of-plane magnetic anisotropy, we assume that the (020) planes are preserved on both sides of the twinning boundaries, and that the twins can be seen as rotation twins with a $\pi/3$ rotation around the [010] direction (the actual angle between (101) and $(\bar{1}01)$ planes is 59.8°). Therefore, the diffraction peak noted as (P1) in Figure S3c can be attributed to (101) of a crystal or $(10\bar{1})$ of its twin. The faint lines observed on the SAED pattern, which are perpendicular to the growth axis, correspond to diffuse diffraction by the regular planar defects.

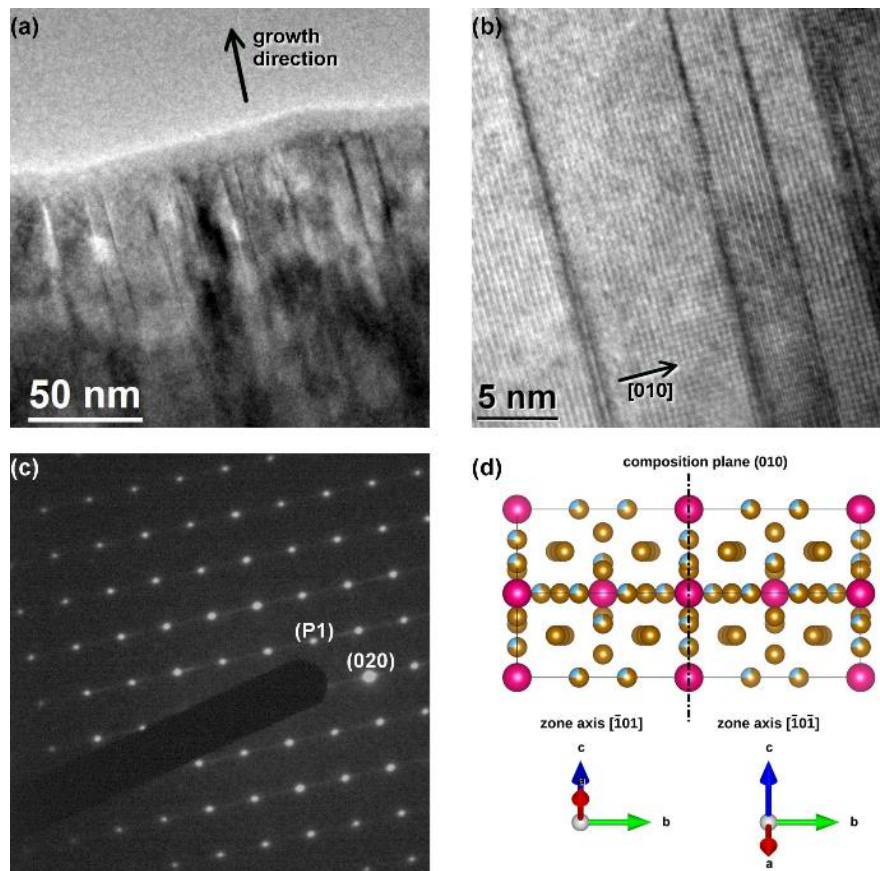


Figure S3. Transmission electron micrographs of the $(\text{Sm,Zr})(\text{Fe,Ti})_{12}$ film observed in cross-section. (a) Bright field image acquired along a $[101]$ zone axis, (b) High resolution TEM of a stack of twins and (c) corresponding Selected Area Electron Diffraction, (d) sketch of two $\text{Sm}(\text{Fe,Ti})_{12}$ unit cells, one of which is rotated by 59.8° around the $[010]$ direction with respect to the other one, in order to match the $[101]$ of the left crystal with the $[\bar{1}01]$ of the right crystal. Observed along these zone axes ($[\bar{1}01]$ and $[\bar{1}0\bar{1}]$), respectively), these crystals are indistinguishable. The crystal structure was displayed with Vesta [1].

In **Figure S4** we report on electron diffraction of the $\text{Sm}(\text{Fe,Ti})_{12}$ film in the $[111]$ zone axis. This electron diffraction pattern cannot be fully indexed from single crystal data and we need at least two variants to index the most intense peaks which are overlaid in red and blue on top of the original data (Figure S4a,b). The two-colored theoretical diffraction patterns both correspond to the

diffraction of $\text{SmFe}_{11}\text{Ti}$ observed under the $[111]$ zone axis but with a relative rotation of 41.3° around the $[111]$ direction. This can actually be seen as a rotation of 60° around the $[010]$ axis, as shown in Figure S4d. This result is in agreement with the data presented in Figure S3. Some additional faint diffraction peaks are not indexed in Figure S4b. They can all be indexed either as double diffraction through two twinned crystals, or by a third variant of the twin in the same grain. In films, the TEM data are coherent with high density twins, with (011) twinning plane and 60° rotation around the $[010]$ direction.

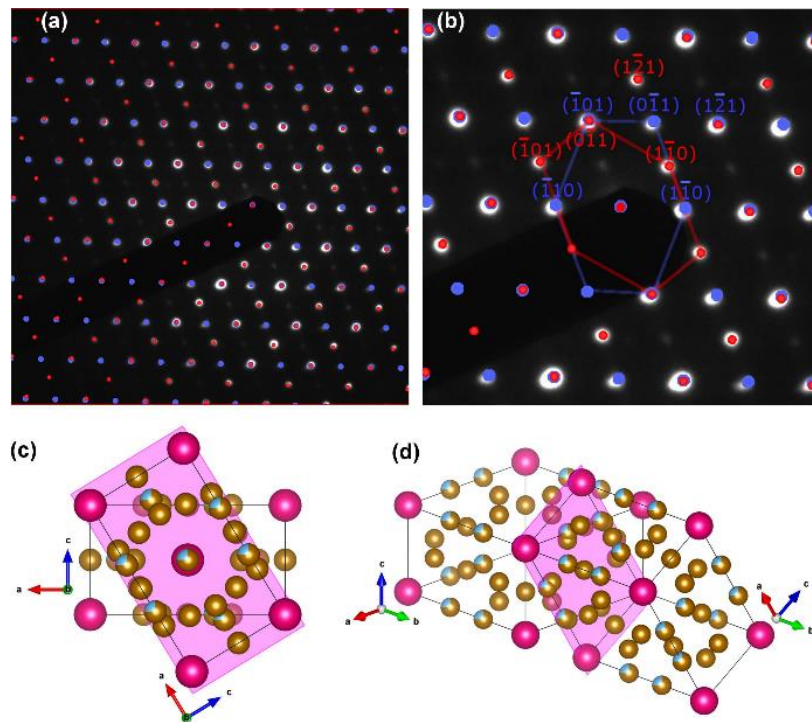


Figure S4. Transmission electron diffraction of the $\text{Sm}(\text{Fe},\text{Ti})_{12}$ film in cross section: (a) SAED pattern along a $[111]$ zone axis overlaid with two theoretical diffraction patterns (red and blue) of $\text{SmFe}_{11}\text{Ti}$ single crystals rotated by 41.3° with respect to each other around the zone axis. (b) Close up with indexation of both the blue and red diffraction patterns. (c) Schematic of the twinned crystal observed along the $[010]$ and (d) $[111]$ zone axis. The magenta plane corresponds to the (010) composition plane. Observed under the particular $[111]$ zone axis, a rotation of the crystal by 60°

around [010] axis is equivalent to a 41.3° rotation around the [111] axis, thus matching the experimental SAED data.

The room temperature x-ray powder diffraction pattern of the $\text{SmFe}_{11}\text{Ti}$ polycrystalline sample is shown in **Figure S5**. The Rietveld refinement agreement factors (R-factors) are given in the figure. The refinement results indicate the formation of ThMn_{12} -type (space group: $I4/mmm$) for the polycrystalline $\text{SmFe}_{11}\text{Ti}$ sample with the phase ratio of 96 ± 1 wt.%. A small amount of secondary phase of SmFe_2 -Laves phase is fitted to the pattern, which corresponds to a weight fraction of 4 ± 1 wt.%.

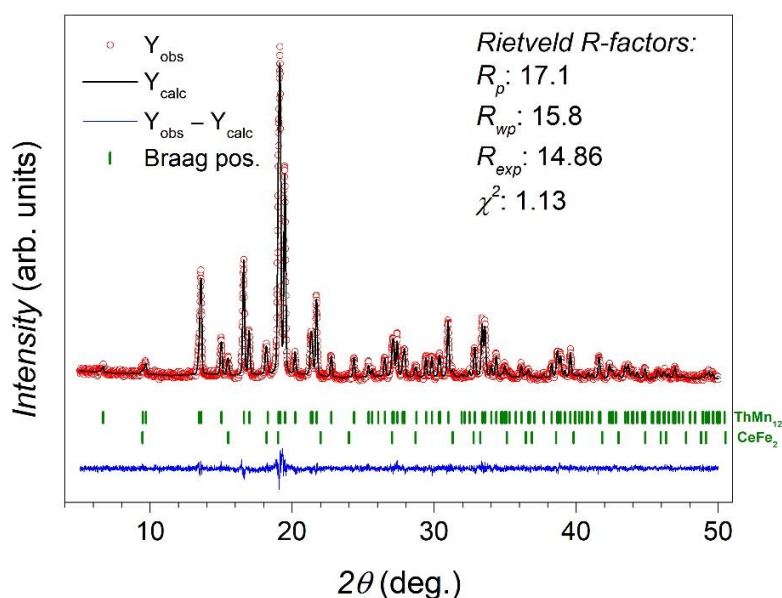


Figure S5. Room temperature x-ray powder diffraction pattern and corresponding Rietveld fit of polycrystalline $\text{SmFe}_{11}\text{Ti}$ sample.

References

1. Momma, K. and F. Izumi, *VESTA 3 for three-dimensional visualization of crystal, volumetric and morphology data*. Journal of Applied Crystallography, 2011. **44**(6): p. 1272-1276 DOI: doi:10.1107/S0021889811038970.

2. Bodriakov, V.Y., T.I. Ivanova, S.A. Nikitin, and I.S. Tereshina, *Magnetic anisotropy and magnetoelastic properties of SmFe₁₁Ti*. Journal of Alloys and Compounds, 1997. **259**(1): p. 265-269 DOI: [https://doi.org/10.1016/S0925-8388\(97\)00099-6](https://doi.org/10.1016/S0925-8388(97)00099-6).
3. Cadieu, F.J., H. Hegde, A. Navarathna, R. Rani, and K. Chen, *High-energy product ThMn₁₂ Sm-Fe-T and Sm-Fe permanent magnets synthesized as oriented sputtered films*. Applied Physics Letters, 1991. **59**(7): p. 875-877 DOI: 10.1063/1.105265.
4. Kou, X.C., T.S. Zhao, R. Grössinger, H.R. Kirchmayr, X. Li, and F.R. de Boer, *Magnetic phase transitions, magnetocrystalline anisotropy, and crystal-field interactions in the RFe₁₁Ti series (where R=Y, Pr, Nd, Sm, Gd, Tb, Dy, Ho, Er, or Tm)*. Physical Review B, 1993. **47**(6): p. 3231-3242 DOI: 10.1103/PhysRevB.47.3231.

5.2.4 Full-text of Selected Publication D

Reproduced full text article with permission from EDP Sciences.

Copyright (2021), *Manufacturing Review*.

Microstructure and magnetic properties of Mn-Al-C permanent magnets produced by various techniques

Vladimir V. Popov Jr.^{1,*,**}, Fernando Maccari^{2,**}, Iliya A. Radulov², Aleksey Kovalevsky¹, Alexander Katz-Demyanetz¹, and Menahem Bamberger³

¹ Israel Institute of Metals, Technion R&D Foundation, Technion City, Haifa 3200003, Israel

² Technical University Darmstadt, Alarich-Weiss-Street 16, Darmstadt 64287, Germany

³ Department of Materials Science and Engineering, Technion Israel Institute of Technology, Technion City, Haifa 3200003, Israel

Received: 7 February 2021 / Accepted: 14 March 2021

Abstract. Bulk $\text{Mn}_{52}\text{Al}_{46}\text{C}_2$ in τ -phase was prepared by vacuum induction melting and used as precursor for the production bulk permanent magnets by suction casting and hot-extrusion. Part of the precursor alloy was mechanically milled into a τ -phase powder and used as precursor for production of samples by electron beam melting, hot-compaction and high pressure torsion processes. The microstructure and magnetic properties of all samples were investigated and correlated. It was found that the mechanical deformation enhances coercivity, up to 0.58 T, while the absence of this strain is beneficial for magnetization. Among the observed techniques, hot extrusion and high pressure torsion have shown promising possibilities to further develop Mn-Al-C as permanent magnets. However, it should be taken into account the challenges related to design a proper processing window for hot extrusion and the limitation of HPT regarding the absence of texture.

Keywords: Manufacturing methods / permanent magnets / rare earth free magnets / Mn-Al-C alloys

1 Introduction

Mn-Al alloys belong to the well-known material systems, which have been intensively studied since the late 60's as perspective candidates for use as permanent magnets (PM) [1,2], but then faded into oblivion after the discovery of the Nd-Fe-B magnets in the 80's [3]. The abrupt increase of the rare earth elements price in 2011, along with the growing demand on permanent magnets, triggered the renewed interest in this material system in the past years [3,4]. This combination of circumstances has motivated many scientists to not only search for novel materials, but also to re-investigate already known materials systems like MnAl and work further on the development of new fabrication techniques, involving novel routes of powder metallurgy [5–7], hot deformation [8–12] and additive manufacturing [13–16] which can provide hard magnetic properties for these non-rare-earth relatively cheap permanent magnets [4].

The MnAl material system is characterized by the use of non-critical elements, low cost and reasonable magnetic properties [2,3,17]. These characteristics are

pointed as crucial to use and develop this material system as “gap magnets” [18,19]. This terminology is adopted to show that this material system has the intrinsic magnetic properties suitable to fill the magnetic performance gap (in the meaning of energy product – BH_{max}) between the cheap but low performance ferrites ($BH_{max} \approx 40 \text{ kJ/m}^3$) and the expensive, rare-earth based high performance magnets (N45 grade Nd-Fe-B- $BH_{max} \approx 450 \text{ kJ/m}^3$) [20]. The intrinsic properties of the Mn-Al compound show a high anisotropy constant (K_1 of 1.7 MJ/m^3), relatively high anisotropy field (H_A between 4.0 and 5.5 T), moderate saturation magnetization (M_S of 0.75 T) which yields in the theoretical value of $BH_{max} \approx 95 \text{ kJ/m}^3$ [20,21].

The magnetic properties of Mn-Al are related to the solely ferromagnetic metastable phase in this material system, the tetragonal τ -phase (Ll_0 type structure). As a general rule, the processing window has to be designed in a way to produce pure ferromagnetic phase in the Mn-Al system in order to maximize magnetization. This can be achieved by two common methods: (i) quenching from the melt or from high temperatures (around 1100°C) to stabilize the parent ε -phase (hexagonal structure-HCP) followed by annealing at moderate temperatures (around 500°C); (ii) high temperature annealing followed by controlled cooling, which results in τ -phase nucleation and

* e-mail: vvp@technion.ac.il

** Both V.V.P. and F.M. equally contributed to this work.

growth during this last step. As mentioned, the ferromagnetic phase is metastable, which means that long annealing times or high temperatures can lead to decomposition of the τ -phase and nucleation of the non-magnetic stable γ_2 and β -phases [20,22,23]. The formation of the ordered $L1_0$ τ -phase, from the parent chemically disordered HCP ε -phase, is reported to happen through two main mechanisms: massive and displacive. The first one is associated with diffusional nucleation at the ε -phase grain boundaries followed by growth via interphase boundary motion [24]. The latter is related to the shear of HCP atomic planes with short-range diffusion [25]. It can also be the case that these two mechanisms happen simultaneously, as observed by *in situ* experiments at temperatures around 500 °C or above [26]. The growth of the τ -phase develops lattice/microstructural defects which affects substantially the magnetic performance, as will be discussed later [24].

To increase the stability of the ferromagnetic phase, carbon is often added as interstitial dopant to the τ -phase compositional range, $Mn_{50+x}Al_{50-x}$ ($51 \leq x \leq 58$), at the expenses of decreasing the Curie temperature (T_C) from 630 to 570 K [20,22]. But only phase purity is not a guarantee for optimized magnetic properties, since different manufacturing processes affect the microstructure and, consequently, the extrinsic magnetic properties.

Different studies have shown the complex relation between the several types of microstructural defects of τ -MnAl phase and the magnetic properties, in terms of remanence, coercivity and, consequently, the BH_{max} value [10,21,27–32]. Among the possible defects in this material system, the existence of twin boundaries is often related to one of the major difficulties to obtain highly textured samples and improved remanence in Mn-Al magnets [31]. This is linked to the high density of twin variants created during the τ -phase formation, which will prevent the achievement high degree of texture along the easy magnetization axis since randomly multi-variant grains will be formed. Moreover, in addition to twin boundaries, other defects and metallurgical variables which were reported, namely: stacking faults, antiphase boundaries, dislocations, grain size and lattice strain; are related and affect coercivity, as reported in the literature [10,21,31,32]. The effect of each specific defect on the magnetic properties is still under investigation, as different characterization techniques are necessary to obtain qualitatively and/or quantitatively data about the density and distribution of these defects. Furthermore, these microstructural features are very often reported to coexist, which increase the challenge to understand the coercivity mechanism in τ -Mn-Al-based compounds.

Based on these factors, a complete understand of the processing route on the phase stability, microstructure and magnetic properties are indispensable to optimize the Mn-Al material system to be suitable for permanent magnet applications. Therefore, this present work is focused on the use of five different processing techniques for production of Mn-Al-C bulk samples and the correlation between microstructure and magnetic properties for each of these processes.

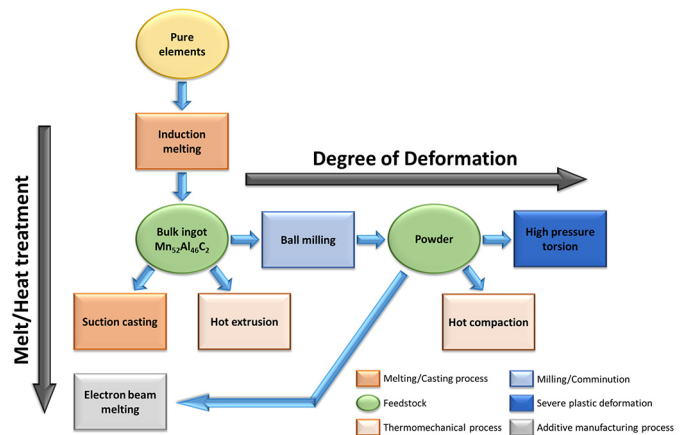


Fig. 1. Overview of the methods used to prepare Mn-Al-C based permanent magnets.

2 Sample synthesis and characterization

In the following subsections will be given experimental details of the different processing routes discussed in this work, according to the schematic presented in Figure 1. The master alloy composition, $Mn_{52}Al_{46}C_2$, chosen to perform these processes was based on the low ratio between Mn and Al atoms, to avoid decrease in magnetization from the Mn-Mn antiferromagnetic interaction, and interstitial C doping to prevent decomposition of the metastable hard magnetic $L1_0$ τ -phase.

2.1 Synthesis of the bulk precursor alloy

2.1.1 Vacuum induction melting

Vacuum induction melting (VIM) followed by casting into graphite crucible is a well-known fabrication technique, especially for Mn-Al production [2]. $Mn_{52}Al_{46}C_2$ alloy was prepared by melting pure elements (purity above 99 wt. %) using a single chamber vacuum induction melting furnace (Consarc Corp.). Before melting, the chamber purged with argon 5 times in order to reduce the oxygen content to a minimum level. The melting occurred under protective atmosphere of Ar (purity of 99.999%) and the alloy was kept in a molten state for 2 h for homogenization before casting into a graphite crucible. The so obtained bulk alloy was further characterized and used as a precursor in all subsequent processing routes, as shown in Figure 1, ensuring the same chemical composition for a direct comparison between the processes.

2.1.2 Suction casting

Part of the VIM Mn-Al-C bulk sample was subject to arc melting and, when in molten state, the alloy was rapidly “sucked” into a cylindrical cooled copper mold of 10 mm diameter. This is a method of casting that ensure high 95 cooling rates, in the order of 10^3 Ks⁻¹, and allows to obtain microstructural refinement and non-equilibrium phases. This technique has been reported for different intermetallic

rare-earth based compounds [33–35]. However, there are no reports of the use of suction casting for Mn-Al, to the best of authors knowledge. The suction cast samples were subjected to the following heat treatment procedure: annealing for 72 h at 1100 °C, followed by water quenching and subsequently annealing for 30 min at 550 °C.

2.1.3 Hot deformation/hot extrusion

The effect of hot extrusion was investigated by Matsushita Electrical Industrial company in 1977, it was reported values of $H_C = 0.30$ T, $(BH)_{max} \approx 56$ kJ/m³ for Mn-Al-C compound [36]. Texture along the hot extrusion direction was observed from the anisotropy behavior in the magnetic measurements. This result still remains as state of the art in terms of magnetic performance and difficulties on reproducing it were reported in literature (references). Only recently Feng et al. reported similar values $(BH)_{max} \approx 46$ kJ/m³ [37]. In this comprehensive study, it was highlighted the role of Ni-doping on the improving the plasticity of Mn-Al-C, which is imperative for the hot extrusion process.

A press (Beckwood corp.), with tools heated up to 550 °C, was used for the extrusion process. The diameter of the die used was 25 mm while the initial diameter of the samples was 50 mm, resulting in a ratio of the starting and final cross section area of 4. Prior extrusion the precursor alloy was heated up to 500 °C and kept at this temperature for ca. 20 min. Afterwards the preheated alloy was placed into the press and pressure of up to 225 MPa was applied. However, due to the rigid behaviour of the intermetallic phase at this temperature, the applied pressure was not sufficient to successfully complete the extrusion process.

Even though a small volume of the sample was extruded, a section of this volume was used for further characterization.

2.2 Synthesis of the powder precursor alloy

Various techniques have been previously applied to prepare Mn-Al based powder precursor for permanent magnets, including mechanical alloying, gas atomization and mechanical milling etc. [5–7,17,38,39]. Among this methods, mechanical milling (MM) seems to be the most cost-effective and efficient approach for preparation of powder with enhanced coercivity. Therefore, powder was produced by mechanical milling of the VIM obtained Mn-Al-C alloy, by using a planetary ball mill Fritsch-Pulverisette 6. The milling was done in protective gas atmosphere, for 2 h at rotation speed of 250 RPM, using 10:1 ball to powder mass ratio, and 10 mm hardened steel balls.

2.2.1 Hot compaction

After milling, the randomly shaped powder and flake like particles, with $D_{90} \leq 100$ μm was obtained. The powder was sieved and separated in fraction by particles sizes. The fraction with particle size below 100 μm was used for hot compaction. The hot compaction has been performed using a standard hydraulic hot press machine and closed die with

inner diameter of 300 mm and height (after compaction) of 800 mm. The compaction was done at pressure of 150 MPa and die temperature of 450 °C under protective argon atmosphere with holding time of 20 min.

2.2.2 High pressure torsion

The influence of plastic deformation as well as of crystal defects related to crystals plasticity on the formation magnetic properties of Mn-Al based alloys was intensively studied through recent years [30,31,40,41]. The high pressure torsion (HPT – Walter Klements GmbH) process was used to compact and deform τ -phase Mn-Al-C powder (particle size below 80 μm) into disc shaped samples of 10 mm diameter and 1 mm height. The pressure used was 4 GPa and 50 revolutions were applied with 1 RPM. The process was performed at room temperature and the tools were kept below 50 °C during the process.

During the HPT process, the strain generated within the sample is proportional to the radius, which means that the edges of the disc will be higher deformed than the center, leading to an inhomogeneous microstructure and, in this case, a magnetic properties gradient [42]. For this reason, we evaluated three regions of the sample: center (R_0), half radius ($R_{0.5}$) and on the edge (R_1).

2.2.3 Additive manufacturing

An Arcam EBM A2 machine (Arcam EBM, Sweden) was used for the additive manufacturing process. The EBM system has reduced working volume, optimized for the experiments with small powder batches e.g., for testing new alloys [43]. Processing parameters used: layer thickness 100 μm; line offset 100 μm; maximum beam current (EB) 30 mA and average chamber temperature of 830 °C. More details about the processing and optimization can be found in [15].

2.3 Characterisation techniques

2.3.1 SEM/Kerr microscopy

To investigate the present phases and microstructure, the samples were analyzed using scanning electron microscope (SEM – Tescan VEGA 3 and FEG-SEM JEOL JSM-7600F) with backscattered electrons (BSE) detector. Energy-dispersive X-ray spectroscopy (EDS) measurements were performed to quantify chemical composition of the present phases. In addition, EDS measurements were taken in larger portions of the sample (area scans) to ensure the Mn/Al ratio was preserved after each processing technique. In all cases, the overall error/deviation from the initial aimed stoichiometry was around 1 at%, within the limits of the EDS detector. The carbon content was evaluated qualitatively by comparing the different samples, since the quantitative determination through EDS is challenging and can be influenced by different measurements artifacts (specimen surface or SEM chamber contamination).

The magnetic domain structures were observed by magneto optical Kerr effect (MOKE) microscopy (Zeiss Axio Imager.D2m evico magnetics GmbH).

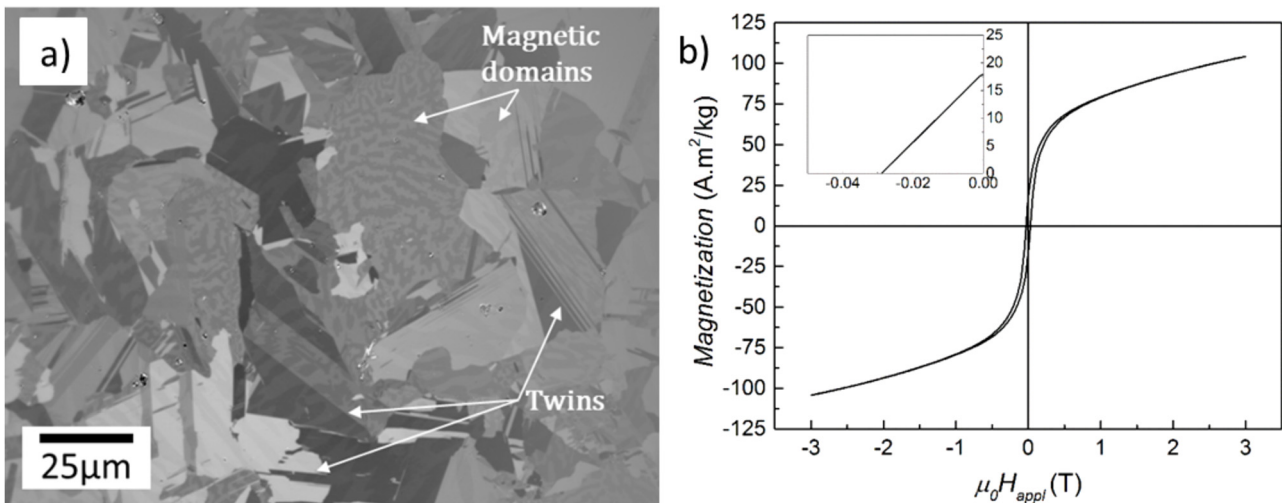


Fig. 2. Kerr micrograph (a) and magnetization measurement (b) of the VIM casted Mn-Al-C sample. The microstructure shows pure τ -phase with twin boundaries and the magnetic domain structure.

2.3.2 Magnetisation measurements

Isothermal magnetization measurements were performed using PPMS-VSM (Quantum Design PPMS-14), at room temperature, under applied magnetic field up to 3 T. No corrections regarding demagnetizing factor were made.

2.3.3 Transmission electron microscopy-TEM

Prior to TEM analysis, lamellas were prepared using plasma FIB (TescanS9000X) from samples in the VIM, powder and HPT states. The TEM TitanThemis G2 60-300 (FEI/Thermo Fisher) with aberration correction and rapid camera with 4K resolution was used to analyze the lamellas.

3 Results and discussion

3.1 Vacuum induction melting (VIM)

The sample after VIM shows ferromagnetic behavior, as presented in Figure 2b with relatively high magnetization at 3 T applied field (M_{3T}) of $100 \text{ A} \cdot \text{m}^2/\text{kg}$, in agreement with the microstructure shown in Figure 2a, in which only τ -phase is observed. It is important to notice the small value of coercivity ($H_C < 0.03 \text{ T}$), which is directly related with the coarse microstructure with high density of twin boundaries and the absence of defects which pin the domain wall motion, as similarly reported by [9,31]. The resultant phase/microstructure arises from the casting process, where the cooling is not fast enough to stabilize the high temperature ϵ -phase and not slow to promote the stable γ_2 - and β -phases. Since an intermediate cooling rate is achieved during VIM, the nucleation and growth of the τ -phase was achieved, leading to a single-phase sample.

3.2 Powder preparation – ball milling

$\text{Mn}_{52}\text{Al}_{46}\text{C}_2$ powder was prepared from the VIM bulk precursor, through ball milling, for further processing routes. As can be seen from the SEM-BSE image on Figure 3a, the powder consists of particles smaller than $100 \mu\text{m}$ of different shapes, including spherical and flake like morphology. The corresponding magnetization measurement is shown in Figure 3b, in which can be seen a M_{3T} of $90 \text{ A} \cdot \text{m}^2/\text{kg}$ and H_C of 0.12 T. This shows a substantial increase in coercivity from the VIM bulk precursor, $H_C < 0.03 \text{ T}$, and a slight decrease in the M_{3T} . This behavior is commonly attributed to the plastic deformation and strain of the produced powder during the mechanical milling, which is more evident in longer milling procedure, as reported by [7]. It worth mentioning that longer and more intensive milling can be used to produce powder that shows even higher coercivity, reaching values around 0.50 T, but this comes with a decrease in magnetization and even a decomposition of the τ -phase, as reported by Law et al. [39].

3.3 Suction casting

Through suction casting technique is expected to have a higher cooling rate compared to VIM method. Indeed, as shown in Figure 4a, the microstructure differs from the VIM sample where is observed the presence of three distinct phases: τ -, γ_2 - and ϵ -phases. The ϵ -phase arises from the higher cooling compared to VIM, which is also in agreement with the refinement of the τ -phase. The high fraction of γ_2 -phase present in the sample indicate that further annealing needs to be done to further homogenize and maximize the τ -phase fraction. After annealing at 1100°C , temperature region of ϵ -phase stability, for 72 h with subsequently quenching into water, leads to a change in the microstructure, as can be observed in Figure 4b. In the outer shell of the cylindrical sample is observed the

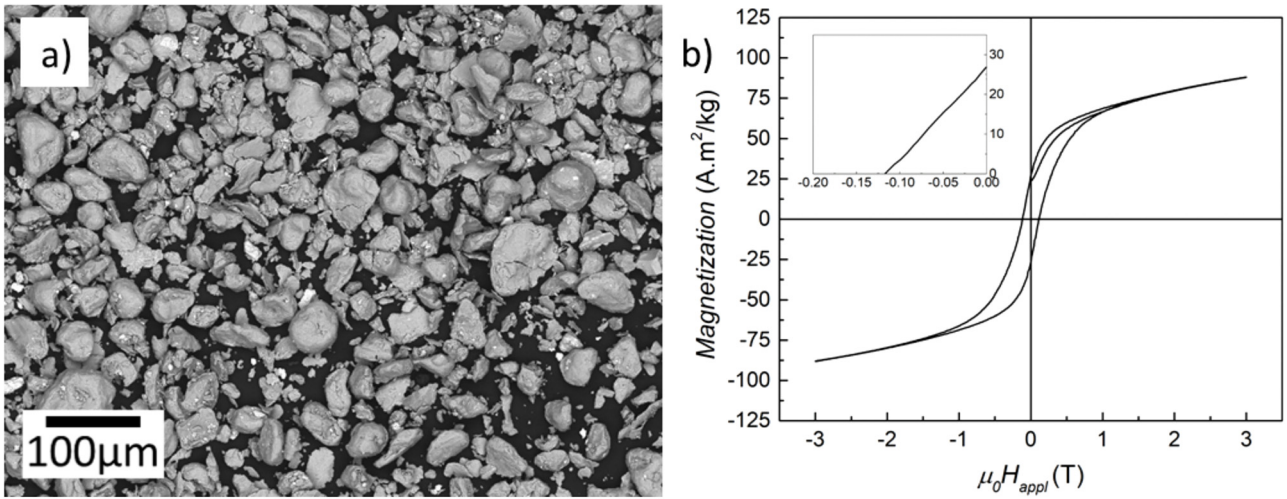


Fig. 3. SEM-BSE image of the produced Mn-Al-C powder (a) and the corresponding magnetization measurements (b).

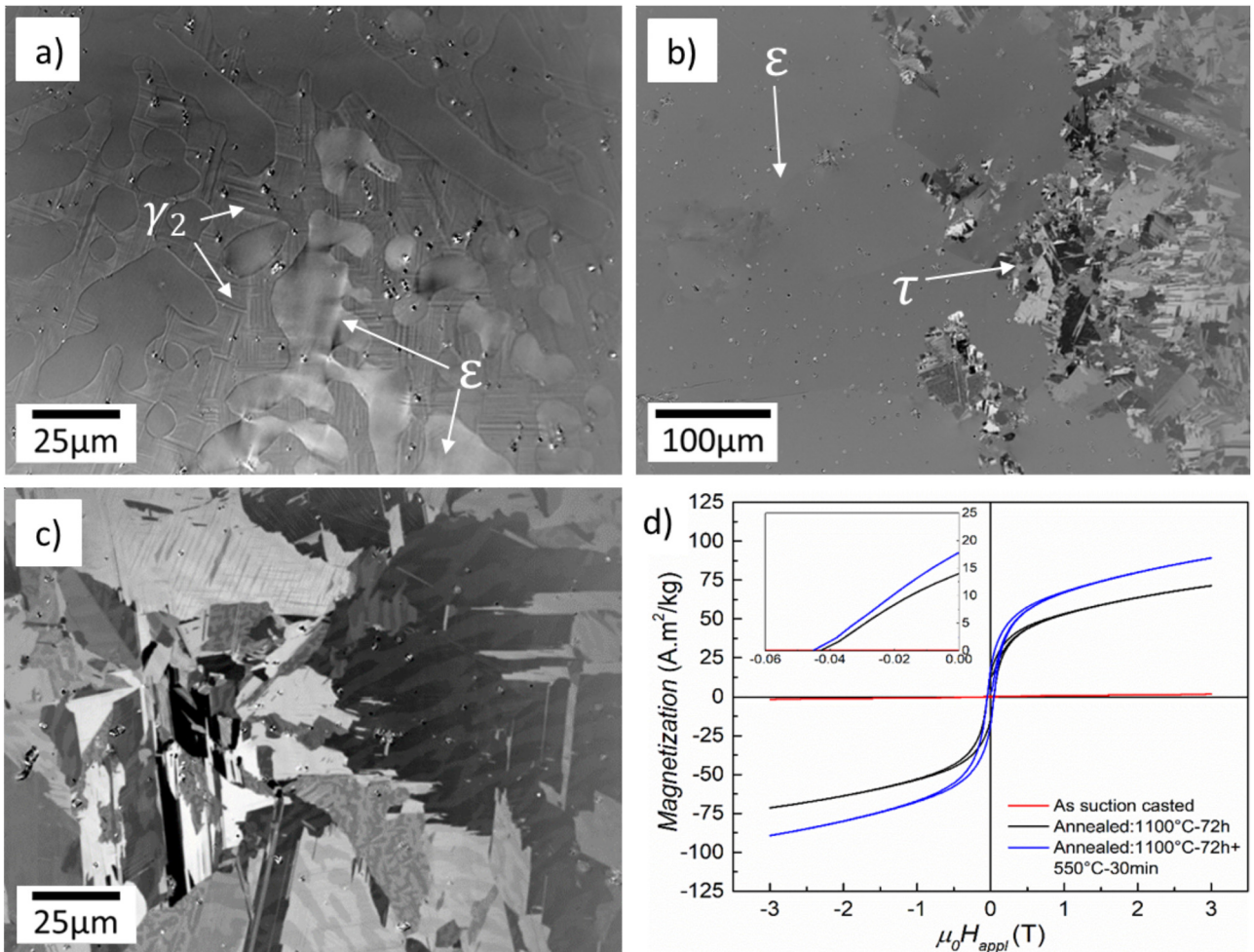


Fig. 4. Kerr images illustrating the microstructure of suction-casted sample in the as cast state (a), after annealing at 1100 °C for 72 h (b) and after annealing at 1100 °C for 72 h and 550 °C for 30 min and the corresponding magnetization measurements (d). The EDS of γ₂-phase has shown Mn₅₀Al₅₀ composition.

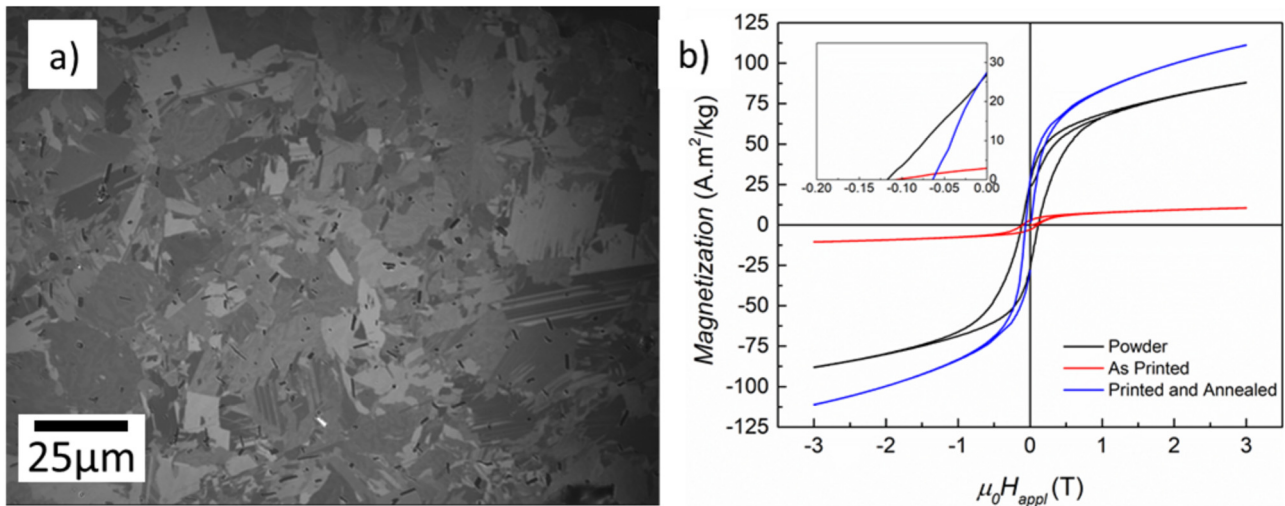


Fig. 5. Mn-Al-C sample produced by EBM (a) Kerr image preprocessed sample, showing the τ phase is predominantly present and (b) magnetization measurement of the initial powder, the EBM samples and the EBM samples after post-processing.

presence of ε -phase because of the higher quenching rate on the edges of the sample, while in the interior we observe the τ -phase. To further maximize the ferromagnetic phase fraction, an additional annealing step at 550 °C for 30 min was adopted, which led to a microstructure of pure τ -phase, as can be seen in the Figure 4c and from the magnetization values in Figure 4d. Similar to the VIM sample, features like twin boundaries and micro twins are observed in the microstructure.

Accordingly, the magnetization measurements shown in Figure 4d agrees well with the microstructure observation. In the as suction casted state, small fraction of τ -phase, the low magnetization represents the non-magnetic γ_2 - and ε -phases, which are in large fraction in this state. By annealing at 1100 °C, there is an increasing the τ -phase fraction and the change on the curve shape to a ferromagnetic behavior with coercivity around 0.04 T and M_{3T} of 70 A · m²/kg. After annealing at 550 °C, we promote the $\varepsilon \rightarrow \tau$ transformation, leading to a higher ferromagnetic phase fraction resulting in a higher magnetization (M_{3T} of 90 A · m²/kg) with similar coercivity. It is worth to mention that only a slight increase in the coercivity value was observed from the suction casted sample when compared to the VIM sample, from below 0.03 T to around 0.04 T.

3.4 Beam-based powder bed additive manufacturing

The part of the current work devoted on the Additive Manufacturing of MnAl-C magnets by Beam-based Powder Bed technology is a continuation of the work published previously [14] and [15], where ball milled binary Mn-Al alloy was used as a precursor. The samples were printed using a modified ArcamA2 EBM machine and ball-milled Mn-Al-C alloy with particles size of 50–60 μm (see Fig. 1). As already discussed above, the use of C doped powder was expected to improve the phase stability and enhance the magnetic properties of the printed magnets. The experiment has shown that contrary to the induction

melting process, after electron beam melting the magnetic τ -phase is not predominant. This can be due to the use of not optimal process parameter settings like scanning rate, hatching distance, process temperature, etc. Therefore, further investigation of the influence of process parameter settings on the microstructure forming aspects responsible for formation of proper magnetic properties should be done. On another hand, the amount of τ -phase in the printed samples can be increased by post processing. Magnetization measurements confirmed (Fig. 5) that the properties of the printed magnets can be fully recovered by two step annealing at 1100 and 500 °C. However, the properties cannot be further improved.

3.5 Hot extrusion/deformation and hot pressing

Figure 6a and b presents the microstructure and magnetic properties of the hot deformed (slightly extruded) Mn-Al-C sample, respectively. It can be observed that the hot deformation has caused dynamic recrystallization, which explains the microstructure refinement while preserving the τ -phase which can be also observed by the high M_{3T} value of 97 A · m²/kg. The coercivity value has substantially increase when compared to the previous processing routes, going from 0.03 to 0.12 T. This shows that the combination of grain refinement and the induced defects during plastic deformation, such as dislocation, can improve coercivity without affecting the magnetization, which is in agreement to results reported by Thielsch et al. [9] and Feng et al. [37].

As it was mentioned above, because of the brittle nature of this compound, the sample has been deformed and only slightly extruded at the beginning of the extrusion die. This show that the extrusion temperature of 500 °C was not enough to induce plasticity for deformation process, but, as mentioned previously, higher temperatures could lead to decomposition of the metastable ferromagnetic phase. For this reason, a further detailed study on the influence of

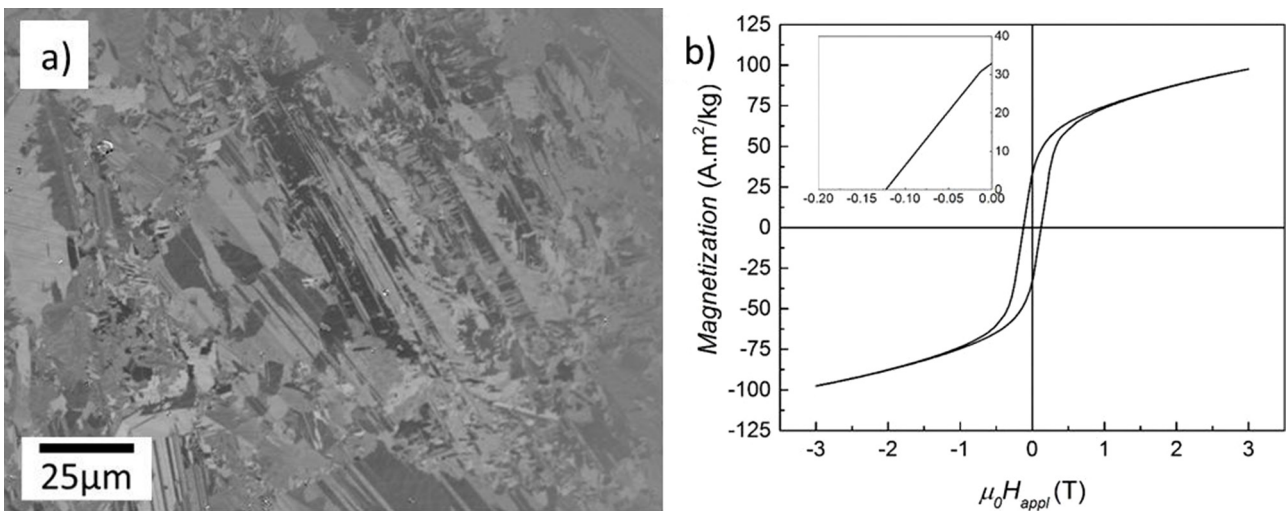


Fig. 6. Kerr micrograph of the hot-deformed sample (slightly extruded) Mn-Al-C sample (a) and the corresponding magnetization measurement (b).

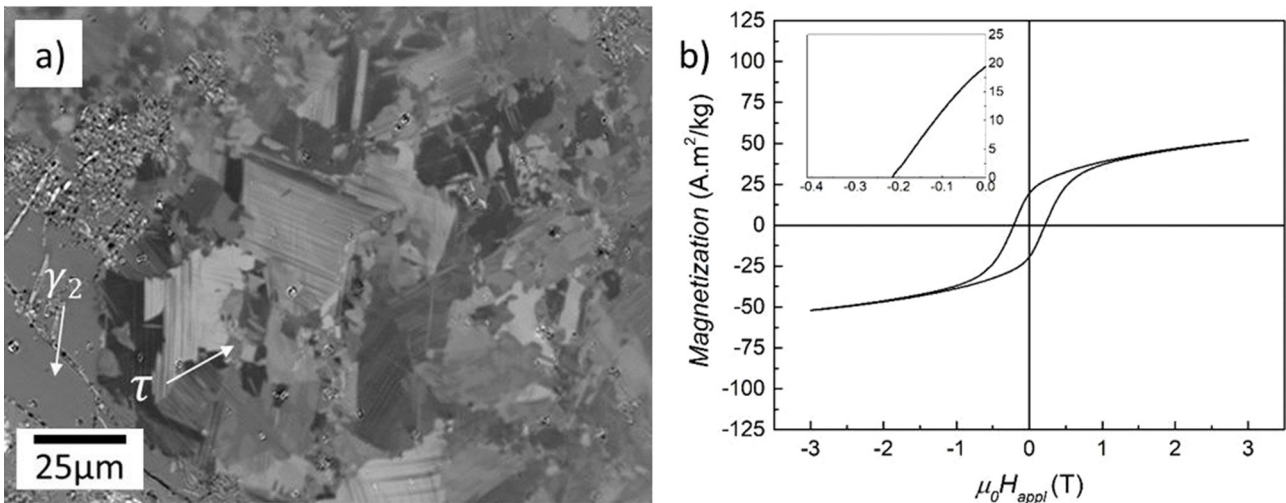


Fig. 7. Kerr image of the hot-pressed Mn-Al-C sample (a) showing the two present phases (γ_2 and τ -phases) and the magnetization measurement (b). The EDS of γ_2 -phase has shown $\text{Mn}_{49}\text{Al}_{51}$ composition.

chemical composition, process temperature, phase stabilization and magnetic properties would give an insight of the processing window for this material system, but this is beyond the scope of the present work.

Alternatively, with the aim to overcome the technical difficulties presented during the hot extrusion route and produce a refined τ -phase microstructure, the hot compaction of the produced ball milled powder has been performed. The obtained hot-compacted samples had the microstructure as shown in Figure 7a. As can be seen, the metastable phase partially was decomposed during the process, but the remaining τ -phase shows a refined microstructure when compared to VIM and suction casting processes. It is important to notice that was observed porosity in this sample, which led to a sample with density of $4,3\text{g/cm}^3$, around 83% relative to the theoretical density, measure by Archimedes' principle.

The magnetization curve of the hot-pressed sample, Figure 7b, shows a magnetization M_{3T} of $50\text{ A}\cdot\text{m}^2/\text{kg}$, related to a decrease of the ferromagnetic phase fraction. On the other hand, the coercivity has improved, reaching a value of 0.21 T , showing again, as in the case of hot extrusion, that grain refinement and defects induced during the process contribute to improve this property.

3.6 High pressure torsion – severe plastic deformation

Another deformation processing route that has been investigated in this work was high pressure torsion (severe plastic deformation), but different from the 295 previous ones, the deformation was carried out at room temperature. As can be seen from the magnetization measurements, Figure 8c, there is a gradient on the coercivity and magnetization values across the diameter. The increase in

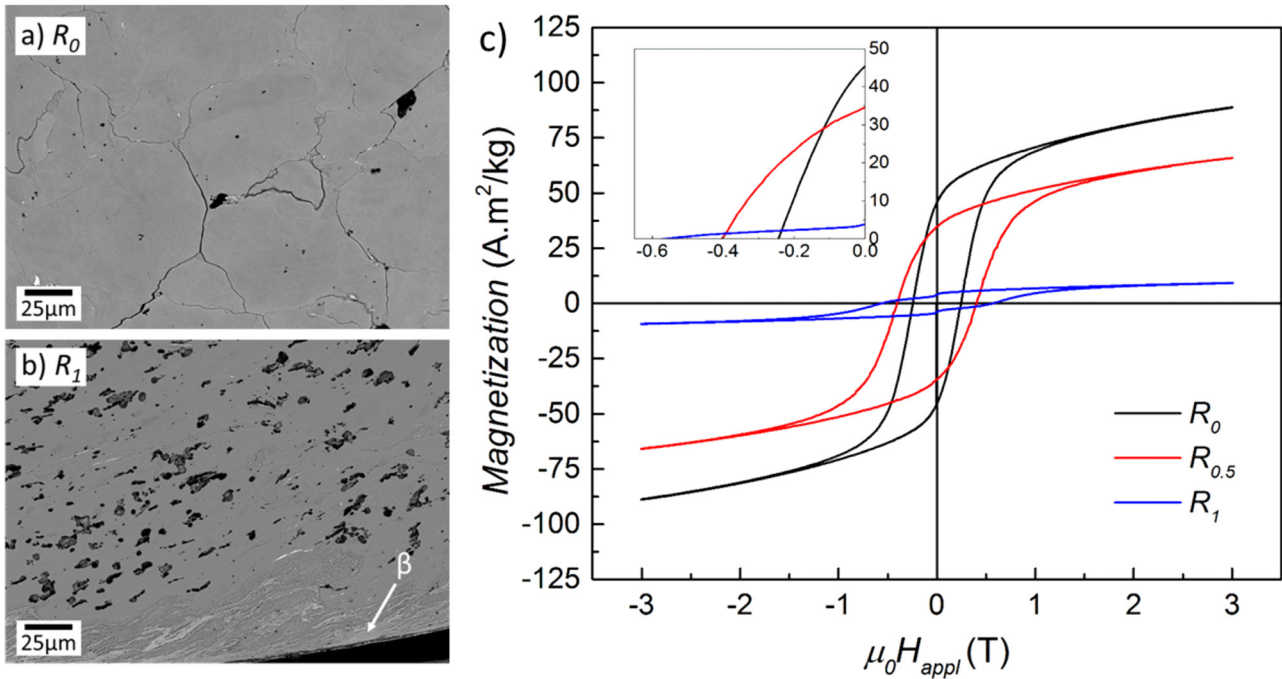


Fig. 8. SEM-BSE images showing the microstructure in the center (a)- R_0 and on the edge (b)- R_1 of high pressure deformed sample and magnetization measurements of different regions of the sample (c). The EDS of β -phase has shown $Mn_{64}Al_{36}$ composition.

the coercivity towards the edge of the sample (R_1), from 0.22 to 0.58 T, can be associated to the higher strain that this area is subjected during the HPT process and, consequently, higher defect density. The high values of coercivity obtained by HPT are similar to the ones reported by other authors and also similar for powders produced by high energy ball milling, in which the powder is also subjected to high a deformation degree.

On the other hand, the magnetization value decreases because of higher Mn-Mn antiferromagnetic interaction caused by internal stresses, which has been shown also for other processing routes [8]. In addition to the decrease in the absolute magnetization value, it is possible to notice a step-like decrease in the magnetization value. This behavior is related to the appearance of secondary phase caused by the stress-driven decomposition of the metastable τ - into β -phase, as confirmed by SEM-EDS (see Fig. 8b). The nucleated phase also contributes to the decrease in the absolute magnetization value since it is nonmagnetic.

To correlate the obtained magnetic results with microstructure, SEM analysis were made in the center (R_0 -Fig. 8a) and at the edges (R_1 -Fig. 8b), revealing a gradient on the microstructure morphology. Kerr microscopy was also used but it was not possible to distinguish features, like grain size or twins, as shown for the previous processing routes. For this reason, TEM analysis was carried in the as cast (VIM), powder precursor and in the HPT (R_1 region) states, as shown in Figure 9. In the as cast state (VIM), as shown previously in Figure 2a and also in Figure 9a, the microstructure is composed from coarse grains (micrometer range) with well-defined twins and twin

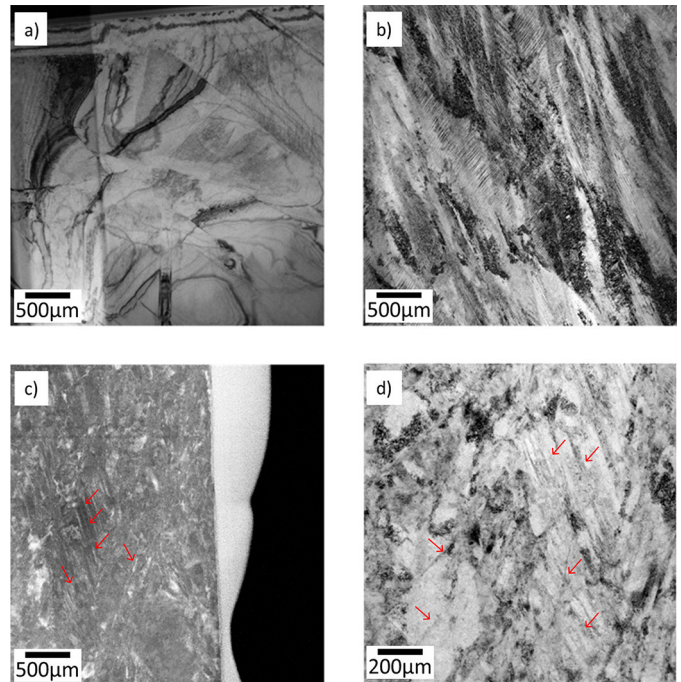


Fig. 9. HR-TEM of the Mn-Al-C samples in different states for comparison: (a) VIM, (b) powder precursor for HPT and (c, d) after HPT.

boundaries. As for the powder, Figure 9b, it is possible to notice a difference in the morphology and size of the grains along the presence with a higher density of defects.

Table 1. Various fabrication techniques of Mn-Al-based permanent magnets and their main magnetic characteristics.

Fabrication technique	H_c (kOe)	M_r (A · m ² /kg)	M_S (A · m ² /kg)	Ref.
Induction melting	0.3	17.5	100.0	This work
	0.2	23.0	120.0	[8]
Arc melting	–	–	–	This work
	0.1	5.0	n.i.	[38]
Suction cast	0.4	18	90	This work
	–	–	–	–
Hot compacted	2.2	20	50	This work
	3.3	28	50	[19]
Hot deformed	–	–	–	This work
	2.2	50	82	[19]
Hot extruded	1.2	32	97	This work
	3.2	85.7	111.2	[37]
Spark plasma sintered	–	–	–	This work
	2.4	12.0	28	[44]
FDM printed	–	–	–	This work
	1.53	35.8	80.0	[16]
EBM printed	0.6-1.2	3.1-26.3	10.7-111.3	This work and [15]
	–	–	–	–
High pressure torsion	2.5-5.8	5.0-45.0	10.0-90.0	This work
	5.9	15.0	40.0	[30]

The abbreviation “n.i.” means that this information was not provided by the authors.

The sample after HPT, Figure 9c and d, shows even further microstructural refinement and change in morphology, being difficult to distinguish individual grains. But it is noticeable the increase of defect density, including polytwinned microstructure with high density of dislocations. The high density of defects, especially dislocations, can hinder the domain wall motion leading to a higher coercivity, in accordance with the magnetic results presented in Figure 8c, and as previous reported by [30,31,41].

The results indicate that the coercivity is strongly related to the defects, and the density of such defects, that can pin the domain wall motion in the magnetization reversal process. Even though plastic deformation/severe plastic deformation is beneficial for this figure of merit, the magnetization value decreases due to internal stresses, as seen and explained previously. For this reason, a compromise between these two properties can be established by using HPT or even with the addition post annealing processing step. These possibilities can be further studied and explored to achieve a balanced magnet in terms of magnetization and coercivity, but the absence of texture coming from the HPT still remains a challenge for increasing remanence and, consequently, the energy-product BH_{max} .

Table 1 summarizes the magnetic characteristics of Mn-Al-C permanent magnets produced by various techniques that were found in literature. The results of the experimental findings presented in this work were also added to the Table 1 for comparison.

4 Conclusion

To investigate the influence of different production methods of bulk Mn-Al-C based permanent magnets on their magnetic properties, a batch of $Mn_{52}Al_{46}C_2$ precursor alloy was prepared by vacuum induction melting for further processing. MnAl based permanent magnets were produced by applying different degree of mechanical deformation and heat treatment. The resulting permanent magnets were studied with respect of the correlation between microstructure and magnetic properties.

It was clearly shown that the phase purity of the samples is important, but not the ultimate factor determining the magnetic properties of the MnAlC samples. Beside the amount of τ -phase, the density and the type of microstructural defects can significantly affect the extrinsic magnet properties of this material system. The samples that were subject of plastic deformation during the manufacturing process (hot extrusion, high pressure torsion and milling) have higher defects density. By having these higher defect density, especially dislocations, high coercivity values were obtained because these defects can act as pinning center than can hinder the reversal domains movement. On the other hand, the strain related to these processes can reduce magnetization due to Mn-Mn antiferromagnetic interaction and, in some cases, can also leads to a decomposition of the ferromagnetic metastable τ -phase.

Techniques related to melting with slow cooling (VIM) or with post annealing processing (suction casting) have

shown the highest magnetization values. Based on the obtained results, it can be concluded that introducing texture along the easy magnetization axis can (without negative effect on the magnetization) maximize the remanence and consequently the energy product BH_{max} of the magnets. From all investigated methods, as previously reported, only samples produced by hot extrusion has shown a significant degree texturing. Due to the experimental constraints (temperature and pressure), this could not be fully reproduced and therefore only isotropic samples are reported in this work.

Among the explored techniques, hot extrusion and high pressure torsion have shown promising possibilities to further develop Mn-Al-C as permanent magnets. However, it should be taken into account the challenges related to design a proper processing window for hot extrusion and the limitation of HPT regarding the absence of texture.

This work was supported by the European Union's Horizon 2020 NMBP232015 research No 686056 (NOVAMAG). F.Maccari acknowledges the funding provided by the Deutsche Forschungsgemeinschaft DFG (German Research Foundation) under the Priority Programme SPP1959-Fields Matter.

References

1. A.J.J. Koch, P. Hokkeling, M.G.v.d. Steeg, K.J. de Vos, New material for permanent magnets on a base of Mn and Al, *J. Appl. Phys.* **31** (1960) S75–S77
2. J. Cui, M. Kramer, L. Zhou, F. Liu, A. Gabay, G. Hadjipanayis, B. Balasubramanian, D. Sellmyer, Current progress and future challenges in rare-earth-free permanent magnets, *Acta Mater.* **158** (2018) 118–137
3. K. Patel, J. Zhang, S. Ren, Rare-earth-free high energy product manganese-based magnetic materials, *Nanoscale* **10** (2018) 11701–11718
4. K.P. Skokov, O. Gutfleisch, Heavy rare earth free, free rare earth and rare earth free magnets – Vision and reality, *Scr. Mater.* **154** (2018) 289–294
5. A.E. Berkowitz, J.D. Livingston, J.L. Walter, Properties of Mn-Al-C magnets prepared by spark erosion and other rapid solidification techniques, *J. Appl. Phys.* **55** (1984) 2106–2108
6. A. Chaturvedi, R. Yaqub, I. Baker, Microstructure and magnetic properties of bulk nanocrystalline MnAl, *Metals* **4** (2014) 20–27
7. H. Jian, K.P. Skokov, O. Gutfleisch, Microstructure and magnetic properties of Mn-Al-C alloy powders prepared by ball milling, *J. Alloys Compd.* **622** (2015) 524–528
8. F. Bittner, J. Freudenberger, L. Schultz, T.G. Woodcock, The impact of dislocations on coercivity in $L1_0$ -MnAl, *J. Alloys Compd.* **704** (2017) 528–536
9. J. Thielsch, F. Bittner, T.G. Woodcock, Magnetization reversal processes in hot-extruded τ -MnAl-C, *J. Magn. Mater.* **426** (2017) 25–31
10. S. Bance, F. Bittner, T.G. Woodcock, L. Schultz, T. Schrefl, Role of twin and anti-phase defects in MnAl permanent magnets, *Acta Mater.* **131** (2017) 48–56
11. F. Bittner, L. Schultz, T.G. Woodcock, The role of the interface distribution in the decomposition of metastable $L1_0$ - $Mn_{54}Al_{46}$, *J. Alloys Compd.* **727** (2017) 1095–1099
12. R. Madugundo, G.C. Hadjipanayis, Anisotropic Mn-Al-(C) hot-deformed bulk magnets, *J. Appl. Phys.* **119** (2016) 013904
13. A.M.G. Unalan, Development of rare-earth free permanent magnets, Ph.D. thesis, Graduate School of Natural and Applied Sciences of Middle East Technical University (2017). etd.lib.metu.edu.tr/upload/12621677/index.pdf/123456789/26977
14. V. Popov, A. Koptuyug, I. Radulov, F. Maccari, G. Muller, Prospects of additive manufacturing of rare-earth and non-rare-earth permanent magnets, *Procedia Manuf.* **21** (2018) 100–108
15. I.A. Radulov, V.V. Popov, A. Koptuyug, F. Maccari, A. Kovalevsky, S. Essel, J. Gassmann, K.P. Skokov, M. Bamberger, Production of net-shape Mn-Al permanent magnets by electron beam melting, *Addit. Manuf.* **30** (2019) 100787
16. E.M. Palmero, J. Rial, J. de Vicente, J. Camarero, B. Skärman, H. Vidarsson, P.O. Larsson, A. Bollero, Development of permanent magnet MnAlC/polymer composites and flexible filament for bonding and 3D-printing technologies, *Sci. Technol. Adv. Mater.* **19** (2018) 465–473
17. Z.W. Liu, C. Chen, Z.G. Zheng, B.H. Tan, R.V. Ramanujan, Phase transitions and hard magnetic properties for rapidly solidified MnAl alloys doped with C, B, and rare earth elements, *J. Mater. Sci.* **47** (2011) 2333–2338
18. J.M.D. Coey, Permanent magnets: plugging the gap, *Scr. Mater.* **67** (2012) 524–529
19. R. Madugundo, O. Koylu-Alkan, G.C. Hadjipanayis, Bulk Mn-Al-C permanent magnets prepared by various techniques, *AIP Adv.* **6** (2016) 056009
20. R.W. McCallum, L. Lewis, R. Skomski, M.J. Kramer, I.E. Anderson, Practical aspects of modern and future permanent magnets, *Ann. Rev. Mater. Res.* **44** (2014) 451–477
21. F. Bittner, L. Schultz, T.G. Woodcock, Twin-like defects in $L1_0$ ordered τ -MnAl-C studied by EBSD, *Acta Mater.* **101** (2015) 48–54
22. S. Zhao, Y. Wu, Z. Jiao, Y. Jia, Y. Xu, J. Wang, T. Zhang, C. Jiang, Evolution of intrinsic magnetic properties in $L1_0$ Mn-Al alloys doped with substitutional atoms and correlated mechanism: experimental and theoretical studies, *Phys. Rev. Appl.* **11** (2019) 064008
23. V. Öygarden, J. Rial, A. Bollero, S. Deledda, Phase-pure τ -MnAlC produced by mechanical alloying and a one-step annealing route, *J. Alloys Compd.* **779** (2019) 776–783
24. D. Palanisamy, D. Raabe, B. Gault, Elemental segregation to twin boundaries in a MnAl ferromagnetic Heusler alloy, *Scr. Mater.* **155** (2018) 144–148
25. J.M.K. Wiezorek, A.K. Kulovitz, C. Yanar, W.A. Soffa, Grain boundary mediated displacive-diffusional formation of τ -phase MnAl, *Metall. Mater. Trans. A* **42** (2011) 594–604
26. P.-Z. Si, H.-D. Qian, C.-J. Choi, J. Park, S. Han, H.-L. Ge, K. P. Shinde, In situ observation of phase transformation in MnAl(C) magnetic materials, *Materials* **10** (2017) 1016
27. H. Zijlstra, H.B. Haanstra, Evidence by Lorentz microscopy for magnetically active stacking faults in MnAl alloy, *J. Appl. Phys.* **37** (1966) 2853–2856
28. C. Yanar, J.M.K. Wiezorek, W.A. Soffa, V. Radmilovic, Massive transformation and the formation of the ferromagnetic $L1_0$ phase in manganese-aluminum-based alloys, *Metall. Mater. Trans. A* **33** (2002) 2413–2423

29. J. Landuyt, G. Tendeloo, J.J. Broek, H. Donkersloot, H. Zijlstra, Defect structure and magnetic properties of MnAl permanent magnet materials, *IEEE Trans. Magn.* **14** (1978) 679–681
30. P.Z. Si, J.T. Lim, J. Park, H.H. Lee, H. Ge, H. Lee, S. Han, H. S. Kim, C.J. Choi, High coercivity in MnAl disc prepared by severe plastic deformation, *Phys. Status Solidi (b)* **257** (2019) 1900356
31. Y. Jia, Y. Wu, S. Zhao, S. Zuo, K.P. Skokov, O. Gutfleisch, C. Jiang, H. Xu, L1₀ rare-earth-free permanent magnets: the effects of twinning versus dislocations in Mn-Al magnets, *Phys. Rev. Mater.* **4** (2020) 94402
32. P. Zhao, L. Feng, K. Nielsch, T.G. Woodcock, Microstructural defects in hot deformed and as-transformed τ -MnAl-C, *J. Alloys Compd.* **852** (2021) 156998
33. X.H. Tan, H. Xu, Q. Bai, W.J. Zhao, Y.D. Dong, Magnetic properties of Fe-Co-Nd-Y-B magnet prepared by suction casting, *J. Non Cryst. Solids* **353** (2007) 410–412
34. Z. Yuyong, P. Jing, J. Xiaoli, L. Xincai, D. Youren, X. Xiaoyan, Microstructure evolution and magnetic properties of the Nd₉Fe_{81-x}Ti₄C₂Nb₄B_x ($x = 11, 13, 15$) bulk magnets prepared by copper mold suction casting, *J. Rare Earths* **33** (2015) 1081–1086
35. F. Maccari, L. Schafer, I. Radulov, L.V.B. Diop, S. Ener, E. Bruder, K. Skokov, O. Gutfleisch, Rapid solidification of Nd_{1+x}Fe₁₁Ti compounds: phase formation and magnetic properties, *Acta Mater.* **180** (2019) 15–23
36. T. Ohtani, N. Kato, S. Kojima, K. Kojima, Y. Sakamoto, I. Konno, M. Tsukahara, T. Kubo, Magnetic properties of Mn-Al-C permanent magnet alloys, *IEEE Trans. Magn.* **13** (1977) 1328–1330
37. L. Feng, J. Freudenberger, T. Mix, K. Nielsch, T.G. Woodcock, Rareearth-free MnAl-C-Ni permanent magnets produced by extrusion of powder milled from bulk, *Acta Mater.* **199** (2020) 155–168
38. N. Singh, V. Mudgil, K. Anand, A.K. Srivastava, R.K. Kotnala, A. Dhar, Influence of processing on structure property correlations in τ -MnAl rareearth free permanent magnet material, *J. Alloys Compd.* **633** (2015) 401–407
39. J.Y. Law, J. Rial, M. Villanueva, N. Lopez, J. Camarero, L. G. Marshall, J.S. Blazquez, J.M. Borrego, V. Franco, A. Conde, L.H. Lewis, A. Bollero, Study of phases evolution in high-coercive MnAl powders obtained through short milling time of gas-atomized particles, *J. Alloys Compd.* **712** (2017) 373–378
40. Y. Jia, Y. Wu, S. Zhao, J. Wang, C. Jiang, Relation between solidification microstructure and coercivity in MnAl permanent-magnet alloys, *Intermetallics* **96** (2018) 41–48
41. M.V. Gorshenkov, D.Y. Karpenkov, R.V. Sundeev, V.V. Cheverikin, I.V. Shchetinin, Magnetic properties of Mn-Al alloy after HPT deformation, *Mater. Lett.* **272** (2020) 127864
42. A. Zhilyaev, T. Langdon, Using high-pressure torsion for metal processing: fundamentals and applications, *Prog. Mater. Sci.* **53** (2008) 893–979
43. A.G. Popov, V.S. Gaviko, V.V. Popov, O.A. Golovnia, A.V. Protasov, E.G. Gerasimov, A.V. Ogurtsov, M.K. Sharin, R. Gopalan, Structure and magnetic properties of heat-resistant Sm(Co_{0.796-x}Fe_{0.177}Cu_xZr_{0.027})₆₋₆₃ permanent magnets with high coercivity, *JOM* **71** (2018) 559–566
44. P. Saravanan, V.T.P. Vinod, M. Černík, A. Selvapriya, D. Chakravarty, S.V. Kamat, Processing of Mn-Al nanostructured magnets by spark plasma sintering and subsequent rapid thermal annealing, *J. Magn. Magn. Mater.* **374** (2015) 427–432

Cite this article as: Vladimir V. Popov Jr., Fernando Maccari, Iliya A. Radulov, Aleksey Kovalevsky, Alexander Katz-Demyanetz, Menahem Bamberger, Microstructure and magnetic properties of Mn-Al-C permanent magnets produced by various techniques, *Manufacturing Rev.* **8**, 10 (2021)

